INSTITUTO POTOSINO DE INVESTIGACIÓN CIENTÍFICA Y TECNOLÓGICA, A.C.

POSGRADO EN CIENCIAS AMBIENTALES

Carbon dioxide capture by carbonized bagasse fibers modified with carbon nanostructures and impregnated with liquid absorbents

Tesis que presenta

Luis Eduardo Rios Saldaña

Para obtener el grado de

Doctor en Ciencias Ambientales

Director de la Tesis:

Dr. José René Rangel Méndez

San Luis Potosí, S.L.P., Septiembre de 2024

Constancia de aprobación de la tesis

La tesis "**Carbon dioxide capture by carbonized bagasse fibers modified with carbon nanostructures and impregnated with liquid absorbents**" presentada para obtener el Grado de Doctor(a) en Ciencias Ambientales fue elaborada por **Luis Eduardo Rios Saldaña** y aprobada el **04 de septiembre de 2024** por los suscritos, designados por el Colegio de Profesores de la División de Ciencias Ambientales del Instituto Potosino de Investigación Científica y Tecnológica, A.C.

_____

Dr. José René Rangel Méndez
Director/Codirectores de la tesis

_____

Dr. Miguel Ávalos Borja
Miembro del Comité Tutoral

_____

Dr. Manuel Karim Sapag
Miembro del Comité Tutotal

_____

Dr. César Nieto Delgado
Miembro del Comité Tutoral

_____

Dr. Luis Felipe Cházaro Ruiz
Miembro del Comité Tutoral

_____

Dr. Miguel Ángel Ruiz Gómez

Miembro del Comité Tutoral

Créditos Institucionales

Esta tesis fue elaborada en el Laboratorio de Ingeniería Ambiental de la División de Ciencias Ambientales del Instituto Potosino de Investigación Científica y Tecnológica, A.C., bajo la dirección del Dr. José René Rangel Méndez.

Durante la realización del trabajo el autor recibió una beca académica del Consejo Nacional de Ciencia y Tecnología (823295) y del Instituto Potosino de Investigación Científica y Tecnológica, A. C.

El autor de esta tesis recibió recursos financieros por parte de la División de Ciencias Ambientales del Instituto Potosino de Investigación Científica y Tecnológica, A.C., para la divulgación de los resultados de esta investigación en congresos internacionales.

Dedicatorias

Esta tesis va dedicada a mi esposa Lorena Rodríguez que me ha acompañado durante todo este proceso llamado doctorado.

Eres la persona más importante en mi vida, a ti va dedicado el esfuerzo y sacrificio que significó esta tesis.

Agradecimientos

Primeramente, quiero agradecer al Dr. José René Rangel Méndez por darme la oportunidad de trabajar en su grupo de trabajo. Gracias por la gran cantidad de enseñanzas profesionales y personales, por su orientación, apoyo y paciencia.

Al Dr. Karim Sapag por dejarme ser, provisionalmente, parte de su grupo de trabajo durante mi estancia en Argentina, aprendí y disfruté mucho mi tiempo con ustedes.

Al Dr. César Nieto Delgado por sus valiosas enseñanzas y consejos profesionales y personales. Gracias por invitarme a sus posadas del grupo del "awita".

Al Dr. Miguel Ávalos por sus valiosos consejos durante estos 4 años, me ayudo a ser más crítico y darle otra perspectiva a nuestro trabajo.

Quiero agradecer a mi familia. A mi esposa Lorena Rodríguez por apoyarme incondicionalmente durante todo este proceso, por apoyarme y alentarme incluso cuando yo mismo menospreciaba lo que estaba haciendo. A mis padres Juana Saldaña Hernández y Luis Rios Constante por siempre estar ahí. A mis hermanas Nayeli y Fátima que, aunque estemos lejos, siempre sé que puedo contar con ustedes.

A mis amigos Christian, Gabino, Mario, Emilio, Jasso, Mau, Sammy, Do, Saldivar, Fortino por su gran amistad, por todos los buenos y malos momentos que hemos pasado y por su apoyo incondicional, son mi familia.

Al grupo de adsorción: Joel, Paola, Andrea, Charly, Jonathan, Quinik, Miguel, Mario, Esme, David, Anai, Amairani, Daniel, Diana, José Juan por sus valiosos comentarios durante el desarrollo de esta tesis.

A los técnicos de la división de Ciencias Ambientales y Materiales Avanzados: Elizabeth Isaacs, Ma. Del Carmen Rocha, Ana Iris Peña, Ignacio Becerril, Héctor Silva, Guillermo Vidríales y Beatriz Rivera.

Al grupo de solidos porosos de la UNSL Deicy, Dimar, Jhonny, Cristian, Octavio, Celene, Walter, Junior, Kiara por su apoyo y enseñanzas durante mi estancia.

Al Instituto Potosino de Investigación Científica y Tecnológica, en especial a la División de Ciencias Ambientales por la infraestructura y los recursos facilitados para la realización de este trabajo de investigación.

Contents

Constancia de aprobación de la tesis……ii
Créditos institucionales……...iii
Acta de examen……iv
Dedicatorias……..v
Agradecimientos……..vi
List of Tables……...xiii
List of Figures……xvi
Resumen……..….xxiii
Abstract……....xxvi
Structure of the thesis……..….xxix

Chapter 1: Introduction.

1.1 Global climate change……..2
1.1.1 Greenhouse gases ……..……2
1.1.2 Current situation and CO_2 projections……3
1.2 Physicochemical properties of CO_2……5
1.3 CO_2 capture systems and technologies ……6
1.3.1 Microbiological method……..……11
1.3.2 Hydrate method……...…12
1.3.3 Cryogenic separation……..……13
1.3.4 Separation by membranes……14
1.3.5 Chemical absorption in liquid absorbents……15
1.3.5.1 CO_2 capture with liquid amines……16
1.3.5.1.1 Tetraethylpentamine (TEPA) ……...…17
1.3.5.2 CO_2 capture with ionic liquids……..…18
1.3.5.2.1 1-butyl-3-methylimidazole acetate……...…21
1.3.6 Adsorption on solid materials……..…23
1.3.6.1 Zeolite……..…25
1.3.6.2 Metal organic framework (MOFs) ……..…25

1.3.6.3 Activated carbons……..…26
1.3.6.4 Biochars……..…27
1.3.6.4.1 Physicochemical properties of carbon materials……29
1.3.6.4.2 Agricultural residues as precursors for carbon materials……..…32
1.3.6.4.3 Agave bagasse carbonized fibers ……..…32
1.3.6.5 Carbon composites……...…33
1.3.6.5.1 Modification with nanostructures……..…34
1.3.6.5.1.1 Carbon nanotubes (CNT) ……35
1.3.6.5.1.2 Carbon nanofibers (CNF) ……36
1.3.6.5.1.3 Growth of carbon nanotubes and nanofibers……..……37
1.3.6.5.2 Impregnation with liquid sorbents ……41
1.4 State of the art……...…42
1.5 Motivation of this investigation……..……45
1.6 Hypothesis……...46
1.7 Objectives ……47
1.7.1 General objective……47
1.7.2 Specific objectives……..…47

Chapter 2: CO_2 capture capacity and kinetics of TEPA-impregnated macroporous biochar.

Abstract……49

2.1 Introduction ……..…50
2.2 Experimental Section……..…51
2.2.1 Reagents and precursor……..……51
2.2.2 Carbonization of bagasse fibers……51
2.2.3 Tetraethylenepentamine impregnation onto CBF……...51
2.2.4 Physicochemical characterization of impregnated carbons……..…52
2.2.5 CO_2 capture experiments……...…52

2.3 Results and Discussion……..54
2.3.1 Characterization of the carbonized bagasse fibers (CBF) ……54
2.3.2 Characterization of CNF impregnated with TEPA……..55
2.3.2.1 Thermal stability and impregnation level……58
2.3.3 CO_2 capture experiments……..…61
2.4 Conclusions……..…68

Chapter 3: Enhancing the CO_2 capture capacity of natural macroporous carbonized fibers by growing carbon nanotubes on their surface.

Abstract……71

3.1 Introduction……..72
3.2 Experimental Section……..…73
3.2.1 Reagents and precursor……..…73
3.2.2 Carbonization of bagasse fibers……73
3.2.3 Impregnation of iron nanoparticles in ACF……...74
3.2.4 CNT growth by CVD……75
3.2.5 Physicochemical characterization of CNT-modified ACF……..76
3.2.6 CO_2 capture experiments……..…77
3.3 Results and Discussion ……..…80
3.3.1 Characterization of the carbonized bagasse fibers and catalyst impregnation……80
3.3.2 Growth and characterization of CNT on ACF……..…83
3.3.2.1 Structural characterization of CNTs grown onto ACF……..…85
3.3.2.2 Texture proprieties and surface chemistry……..…90
3.3.3 CO_2 capture in pristine and modified ACF samples……... 94
3.4 Conclusions……...103

Chapter 4: Growth of carbon nanofibers on a macroporous biochar to improve its CO_2 capture capacity.

Abstract……106

4.1 Introduction……107
4.2 Experimental Section……108
4.2.1 Reagents and precursor……108
4.2.2 Carbonization of bagasse fibers……109
4.2.3 Impregnation of iron nanoparticles in MB……109
4.2.4 CNF growth by CVD……110
4.2.5 Physicochemical characterization of materials……110
4.2.6 CO_2 capture experiments……112
4.3 Results and Discussion……113
4.3.1 Characterization of the macroporous biochar (MB) and catalyst impregnation……113
4.3.2 Growth and characterization of CNF……115
4.3.2.1 Structural characterization of CNFs grown onto MB……115
4.3.2.2 Iron catalyst characterization in MB-CNF……121
4.3.2.3 Texture proprieties and surface chemistry……124
4.3.3 CO_2 capture of MB and MB-CNF……129
4.4 Conclusions……134

Chapter 5: Efficient use of ionic liquid in CO_2 capture through its dispersion in carbon nanofibers/macroporous biochar composite.

Abstract……137

5.1 Introduction……138
5.2 Experimental Section……140

5.2.1 Reagents and precursor……...140
5.2.2 Carbon composite synthesis……140
5.2.2.1 Macroporous biochar production……140
5.2.2.2 Carbon nanofibers growth……..…141
5.2.3 Impregnation of carbon composite with ionic liquid……..142
5.2.4 Physicochemical characterization of impregnated carbon composite...142
5.2.5 CO_2 capture experiments……143
5.3 Results and Discussion……144
5.3.1 Composite characterization……144
5.3.2 Characterization of the impregnated carbon composite……..…146
5.3.2.1 Thermal stability and impregnation level……...…149
5.3.3 CO_2 capture experiments……..…151
5.4 Conclusions……...156

Chapter 6: Highly selective separation of CO_2 from the CO_2/CH_4 gas mixture using carbonized bagasse fibers modified with carbon nanotubes.

Abstract……..……159

6.1 Introduction……160
6.2 Experimental Section……161
6.2.1 Physicochemical characterization of materials……162
6.2.2 CO_2 and CH_4 capture experiments……162
6.3 Results and Discussion……...…164
6.3.1 Physicochemical characterization……...…164
6.3.2 CO_2 adsorption capacity and selectivity……171
6.4 Conclusions……...178

Chapter 7: Final Remarks.

7 Final Remarks……180

Chapter 8: Final Conclusions

8.1 Final conclusions……189

Perspectives……192

Scientific products

Publications……194

Attendance to conferences……194

National……194

International……195

Others……196

References……198

Appendixes

Appendix A……242

List of Tables

Chapter 1

Table 1.1 *Physical and chemical properties of CO_2……..7*

Table 1.2 *Comparison of CO_2 capture technologies [20,23,36-43]……...9*

Table 1.3 *Physical and chemical properties of TEPA.……...17*

Table 1.4 *Physical and chemical properties of 1-butyl-3-methylimidazole acetate IL……....22*

Table 1.5 *Advantages and disadvantages of CO_2 solid adsorption materials [3,20,35,41,101-104].……24*

Table 1.6 *An overview of the capacity of some biomass productions.……32*

Table 1.7 *Comparative CO_2 adsorption capacities of different carbon materials, ionic liquids, amines, and composites.……..…42*

Chapter 2

Table 2.1 *TEPA and moisture concentration in impregnated CBF calculated from TGA analysis……....61*

Table 2.2 *CO_2 capture kinetics and capacities of CBF, TEPA and CBF impregnated with TEPA at 25 °C and pressure of 1 to 10 bar……...64*

Table 2.3 *CO_2 capture capacity of TEPA, CBF and CBF-TEPA5 and 10% at 25 °C and 10 bar…….……...66*

Chapter 3

Table 3.1 *Inorganic content of acid washed carbon before and after impregnation with magnetite nanoparticles……....82*

Table 3.2 *Textural properties of ACF, ACF1-CNT, ACF3-CNT and ACF3-CNT-AT1……...…91*

Table 3.3 *Kinetic constants for CO_2 capture by ACF, ACF3-CNT and ACF3-CNT-AT1……....95*

Table 3.4 *CO_2 capture capacity of different carbon materials……...99*

Table 3.5 *CO_2 capture kinetics and capacities of ACF and ACF3-CNT-AT1 at 25 °C, 1 bar and different CO_2 percentage……....102*

Chapter 4

Table 4.1 *Textural properties of MB and MB-CNF……...125*

Table 4.2 *Element composition (atomic %) of MB and MB-CNF……..…127*

Table 4.3 *Relative and absolute abundance (%) of the different peaks assigned to C1s, O1s and N1s from the XPS spectra deconvolution for MB and MB-CNF…....128*

Table 4.4 *CO_2 capture capacities of MB and MB-CNF at 0, 25, 50 and 75 °C and pressure of 1-10 bar……..130*

Table 4.5 *Kinetic constants for CO_2 capture of MB and MB-CNF……..133*

Chapter 5

Table 5.1 *Textural properties of MB and CC……146*

Table 5.2 *Ionic liquid and moisture concentration in impregnated CC calculated from TGA analysis……..151*

Table 5.3 *CO_2 capture kinetics and capacities of IL, CC and CC impregnated with IL at 25 °C and pressure of 1, 3, 5 and 8 bar……..153*

Table 5.4 *CO_2 capture capacity and regenerability of 3 sorption-desorption cycles of IL, CC and CC impregnated with IL at 25 °C and 8 bar……156*

Chapter 6

Table 6.1 *Textural properties of ACF and ACF3-CNT-AT1……167*

Table 6.2 *Element composition (atomic %) of ACF and ACF3-CNT-AT1……168*

Table 6.3 *Relative and absolute abundance (%) of the different peaks assigned from the deconvolution of the central energy level of C1, O1 and N1 for ACF and ACF3-CNT-AT1……....170*

Table 6.4 *Parameters of the Langmuir isotherms model for CO_2 and CH_4 adsorption of ACF and ACF3-CNT-AT1 at 25 °C and pressure up to 10 bar……....176*

Table 6.5 *IAST selectivity values at different CO_2/CH_4 ratios of ACF and ACF3-CNT-AT1 at 25 °C and pressure 1-10 bar……...178*

List of Figures

Chapter 1

Figure 1.1 *a) Global greenhouse gas emissions, modified from [4], and b) natural and human enhanced greenhouses effect, modified from [8]……..…...3*

Figure 1.2 *Global greenhouse gas emissions by economic sector, modified from [4]……4*

Figure 1.3 *Increased concentrations of CO_2, CH_4 and Nitrous oxide in the atmosphere since 1850 and, taken from [4]……...5*

Figure 1.4 a) *Lewis's structure of carbon dioxide (CO_2) and b) Stretching and bending oscillations of the CO_2 molecule……...6*

Figure 1.5 *Schematic diagram of CO_2 capture and utilization cycle, taken from [20]……...8*

Figure 1.6 *Typical diagram for the CO_2 capture process through hydration, taken from [47]……....13*

Figure 1.7 *Schematic diagram of gas separation membrane, taken from [43]……..15*

Figure 1.8 *Viscosity/diffusivity relationship for ionic liquids and conventional solvents, taken from [79]……20*

Figure 1.9 *Examples of types of anions and cations commonly used in ionic liquids……...….21*

Figure 1.10 *Chemical reaction between [BMIM][Ac] and CO_2 [85]……...23*

Figure 1.11 *Acidic and basic oxygen-containing functionalities of carbon surface, modified from [157]……..30*

Figure 1.12 *Types of nitrogen-containing functionalities on the carbon materials, modified from [157]……..31*

Figure 1.13 *Scanning electron microscope (SEM) micrographs of the macroporous channels of the carbonized bagasse fibers, taken from [184]……...33*

Figure 1.14 *Classification of 0D, 1D, 2D, and 3D nanostructures, modified from [190]……...……...35*

Figure 1.15 *Scheme of chirality in a plane of graphene and types of carbon nanotubes a) armchair, b) zigzag and c) chiral, modified from [197]……..…..35*

Figure 1.16 *a) Single-walled nanotubes (SWCNT) and b) Multi-walled nanotubes (MWCNT), taken from [199]……..36*

Figure 1.17 *Types of CNF, taken from [201]……..37*

Figure 1.18 *Common carbon precursors in CTS growth by CVD: carbon monoxide, methane, acetylene, ethylene, and ethanol from left to right (black: carbon, red: oxygen, white: hydrogen [208]……..39*

Figure 1.19 *Schematic representation of the basic steps of SWCNT growth on an Fe catalyst, as observed in ab initio simulations. a) Diffusion of individual C atoms (red spheres) on the catalyst surface. b) Formation of a sp^2 graphene sheet floating on the catalyst surface with edge atoms covalently bonded to the metal. c) Root incorporation of individual C atoms (or dimers) in diffusion, taken from [229]……41*

Figure 1.20 *Scheme of the CBF modification process a) catalyst impregnation b) CTS growth and c) Impregnation of the modified material with liquid absorbents….46*

Chapter 2

Figure 2.1 *a) 25 ml high pressure reactor 4704, Parr Instrument, adapted with an ASHCROFT DG25 digital pressure gauge, b) begining of the CO_2 capture process: opening and closing of the inlet valve c) CO_2 capture process until initial pressure (P_i) and equilibrium pressure (P_e) are equal or $\Delta P=0$, for 60 min and d) equilibrium and depressurization stage of the system……..53*

Figure 2.2 *SEM secondary electrons images of a) CBF tip b) and c) CBF surface.....55*

Figure 2.3 *SEM secondary electrons images of a), b) CBF-TEPA5%, c), d) CBF-TEPA10%, e), f) CBF-TEPA25% g) and h) CBF-TEPA50%.....56*

Figure 2.4 *FTIR spectra of CBF, pure TEPA and CBF impregnated with different TEPA mass ratio……..58*

Figure 2.5 *Non-isothermal thermogravimetric analysis under N_2 atmosphere at a heating rate of 10 °C/min until 700 °C, thermogravimetric (solid line) and differential thermogravimetric (dTG, dashed line) curves of CC (black) and TEPA (red)……..59*

Figure 2.6 *Non-isothermal thermogravimetric analysis under N_2 atmosphere at a heating rate of 10 °C/min until 400 °C, thermogravimetric curves of CBF impregnated with different TEPA mass ratio……...……...60*

Figure 2.7 *CO_2 capture kinetics of CBF, TEPA and CBF impregnated with TEPA at 25 °C and pressure of a) 1 bar, b) 3 bar, c) 5 bar, d) 8 bar and e) 10 bar……..63*

Figure 2.8 *Sorption-desorption cycles of CBF, TEPA and CBF impregnated with 5 and 10% of TEPA at 25 °C and 10 bar……..66*

Figure 2.9 *FTIR spectra of CBF-TEPA5% before and after CO_2 capture……...67*

Figure 2.10 *Scheme of the suggested CO_2 adsorption mechanism in TEPA impregnated CBF [261,266-269]……...68*

Chapter 3

Figure 3.1 *SEM backscattered electrons images of a) the macroporous channels of ACF, b) CBF and c) ACF……81*

Figure 3.2 *SEM secondary electrons images of a) and b) ACF3……..83*

Figure 3.3 *SEM secondary electrons images of a) ACF1-CNT, b) zoom of the marked area of ACF1-CNT, c) ACF2-CNT, d) zoom of the marked area of ACF2-CNT, e) ACF5-CNT, f) zoom of the marked area of ACF5-CNT, g) ACF3-CNT and h) zoom of the marked area of ACF3-CNT……...84*

Figure 3.4 *SEM secondary electrons images of a) ACF3-CNT and b) backscattered electrons image of ACF3-CNT……..85*

Figure 3.5 *Representative TEM images of CNT from ACF3-CNT: a) curved CNT, b) arrangement of two different CNT walls, c) and d) CNT from ACF3-CNT-AT1……..87*

Figure 3.6 *Raman spectrum of ACF, ACF3-CNT and ACF3-CNT-AT1……....89*

Figure 3.7 *a) Experimental N_2 adsorption isotherms at 77 K and b) pore size distribution of ACF, ACF1-CNT, ACF3-CNT and ACF3-CNT-AT1 calculated with Quenched solid density functional theory (QSDFT)……...91*

Figure 3.8 *FTIR (a) and proton binding curves (b) of ACF and ACF3-CNT-AT1 samples……....92*

Figure 3.9 *SEM secondary electrons images of a) ACF, b) ACF3-CNT and EDS analysis of c) ACF and d) ACF3-CNT-AT1 of presented images……...93*

Figure 3.10 *CO_2 capture kinetics of ACF, ACF3-CNT and ACF3-CNT-AT1 at 25° C and 1 bar, using a pure CO_2 flow of 30 mL/min. Experimental data (solid lines) and the pseudo first-order model fit (dotted lines)……..…..95*

Figure 3.11 *Suggested CO_2 capture mechanism of CNT-modified ACFs [284,285,295,296]……..…96*

Figure 3.12 *a) CO_2 adsorption isotherms at 25 °C and pressures up to 10 bar from ACF and ACF3-CNT-AT1……..97*

Figure 3.13 *a) CO_2 adsorption isotherms at different temperatures (25, 50 and 75°C) and pressures up to 10 bar for ACF (solid points) and ACF3-CNT-AT1 (empty points) and b) Isosteric heat of adsorption……....98*

Figure 3.14 *Sorption (black arrow)-desorption (red arrow) cycles of ACF and ACF3-CNT-AT1 at 25 °C and 1 bar using a flowrate of pure CO_2 of 30 mL/min……...100*

Figure 3.15 *a) Capture kinetics of CO_2 (flowrate of pure CO_2 of 30 mL/min) at 25 °C (solid line) and 80 °C (dotted line) of ACF and ACF3-CNT-AT1 and b) CO_2 capture kinetics at concentrations of 100%, 50%, 25% and 0.04% (air) of ACF (dotted lines) and ACF3-CNT-AT1 (solid lines) at 1 bar and 25 °C……...101*

Chapter 4

Figure 4.1 *SEM secondary electrons images of a) MB tip and b) MB surface…….114*

Figure 4.2 *SEM secondary electron images of a, b) catalyst-impregnated MB and c) size histogram of impregnated catalyst (n=60)……115*

Figure 4.3 *Secondary electron SEM images of a-f) different zones and magnifications of MB-CNF……...117*

Figure 4.4 *Representative TEM images of CNF from a) and b) MB-CNF……118*

Figure 4.5 Representative TEM images of CNF from MB-CNF: a) CNF tip and b) CNF tail (**red line**= direction of graphic planes of CNF and **red arrow**= direction of fiber axis)……...119

Figure 4.6 *Raman spectrum of MB and MB-CNF……120*

Figure 4.7 *SEM secondary electrons images of the catalyst in the tip of CNF grown in MB and EDS of the two areas marked with yellow boxes……..……...121*

Figure 4.8 *X-ray diffraction patterns of MB-CNF and catalyst-impregnated MB….122*

Figure 4.9 *Deconvolution high-resolution XPS of Fe $2p_{1/2}$ and Fe $2p_{3/2}$ spectra of MB-CNF……123*

Figure 4.10 *a) Experimental N_2 adsorption isotherms at 77 K and b) pore size distribution of MB and MB-CNF calculated with Quenched solid density functional theory (QSDFT)……124*

Figure 4.11 *Proton binding curves of MB and MB-CNF samples……..125*

Figure 4.12 *XPS survey spectra of MB and MB-CNF……..126*

Figure 4.13 *Deconvolution of high-resolution XPS spectra of samples MB and MB-CNF: a) and b) for C1s, c) and d) for O1s, e) and f) for N1s……128*

Figure 4.14 *a) CO_2 adsorption isotherms at different temperatures (25, 50 and 75°C) and pressures up to 10 bar for MB (solid points) and MB-CNF (empty points) b) CO_2 adsorption isotherms at 25 °C and 1 bar……....130*

Figure 4.15 *Suggested CO_2 capture mechanisms of MB-CNF [155,162,164]…...131*

Figure 4.16 *a) Isosteric heat of adsorption and b) CO_2 capture kinetics (1 bar, CO_2 flowrate of 30 mL/min) of MB and MB-CNF. Experimental data (solid lines) and the pseudo first-order model fit (dotted lines)……..132*

Figure 4.17 *Multi-cycles of CO_2 adsorption isotherms of MB-CNF at 25 °C……134*

Chapter 5

Figure 5.1 *SEM secondary electrons images of a) MB surface, b) CC surface, c) and d) CNF grown on the surface of MB……145*

Figure 5.2 *Experimental isotherms of N_2 adsorption at 77 K of MB and CC calculated with Quenched solid density functional theory (QSDFT)……146*

Figure 5.3 *SEM secondary electrons images of a) CC-IL1:0.05, b) CC-IL1:0.075, c) CC-IL1:0.1, zoom of the IL-impregnated CNF of d) CC-IL1:0.05, e) CC-IL1:0.075 and, CC-IL1:0.1……147*

Figure 5.4 *FTIR spectra of CC, pure [BMIM][Ac] IL and CC impregnated with different IL mass ratio……...148*

Figure 5.5 *Non-isothermal thermogravimetric analysis under N_2 atmosphere at a heating rate of 10 °C/min until 700 °C, thermogravimetric (solid line) and differential thermogravimetric (dTG, dashed line) curves of CC (black) and [BMIM][Ac] IL (orange)……..……...149*

Figure 5.6 *Non-isothermal thermogravimetric analysis under N_2 atmosphere at a heating rate of 10 °C/min until 350 °C, thermogravimetric (solid line) and differential thermogravimetric (dTG, dashed line) curves of CC impregnated with different IL mass ratio……..…...150*

Figure 5.7 *CO_2 capture kinetics of CC, IL and CC impregnated with IL at 25 °C and pressure of a) 1 bar, b) 3 bar, c) 5 bar and d) 8 bar……...152*

Figure 5.8 *Suggested CO_2 capture mechanism of impregnated IL [92,185,371,372].....154*

Figure 5.9 *Sorption-desorption cycles of CC, IL and CC impregnated with IL at 25 °C and 8 bar……...155*

Chapter 6

Figure 6.1 *SEM secondary electrons images of a) and b) ACF, d)-e) ACF3-CNT-AT1 and f) representative TEM image of CNT from ACF3-CNT-AT1……....165*

Figure 6.2 *a) Experimental N_2 adsorption isotherms at 77 K and b) pore size distribution calculated from N_2 isotherms with Quenched solid density functional theory (QSDFT), c) Experimental CO_2 adsorption isotherms at 273 K and d) pore size distribution calculated from CO_2 isotherms with nonlocal density functional theory (NLDFT)……..166*

Figure 6.3 *XPS survey spectra of ACF and ACF3-CNT-AT1……168*

Figure 6.4 *Deconvolution of high-resolution XPS of samples ACF and ACF3-CNT-AT1: a) and b) for C1s, c) and d) for O1s and e) for N1s high resolution spectra….170*

Figure 6.5 *CO_2 and CH_4 adsorption isotherms at 25 °C and pressures up to 10 bar of ACF and ACF3-CNT-AT1……....172*

Figure 6.6 *Schematic representation of the interaction between gas molecules and charged atoms in the functional groups, modified from [415]……..…174*

Figure 6.7 *a) CO_2 (empty points) and CH_4 (solid points) adsorption isotherms at 25, 50 and 75 °C and pressure up to 10 bar and b) Isosteric heat of adsorption of CO_2 and CH_4 of ACF3-CNT-AT1……175*

Figure 6.8 *CO_2 and CH_4 adsorption isotherms of a) ACF and b) ACF3-CNT-AT1, curves were fit to the Langmuir model (solid line)…….....175*

Figure 6.9 *IAST selectivity values of ACF and ACF3-CNT-AT1 for a CO_2/CH_4 binary mixture of a) 10:90, b) 30:70 and c) 50:50 at 25 °C and pressure up to 10 bar……...177*

Resumen

Captura de dióxido de carbono mediante fibras de bagazo carbonizado modificadas con nanoestructuras de carbono e impregnadas con absorbentes líquidos.

Las emisiones de gases de efecto invernadero han incrementado considerablemente en las últimas décadas, donde el dióxido de carbono o CO_2 representa más del 70% de las emisiones de gases de efecto invernadero seguido del metano. Dentro de las metodologías que se han investigado para reducir la concentración y emisiones de CO_2 resalta la captura de CO_2. La impregnación de absorbentes líquidos en carbones poroso ha demostrado tener un efecto sinérgico y capacidades de captura de CO_2 superiores a los materiales prístinos por separado. Debido a esto, en este trabajo se impregnaron dos absorbentes líquidos con diferentes propiedades (amima líquida tetraetilenepentamina (TEPA) y líquido iónico acetato de 1-butil-3metilimidazolio [BMIM][Ac]) sobre fibras de bagazo carbonizadas (FBC) modificadas con nanoestructuras tubulares de carbono como nanotubos de carbono (CNT) y nanofibras de carbono (CNF). Se probó la capacidad de captura de CO_2 mediante isotermas y cinéticas de adsorción a diferentes condiciones de temperatura y presión, y las propiedades fisicoquímicas de los materiales se caracterizaron mediante diversas técnicas.

La impregnación de una pequeña cantidad de TEPA sobre FBC resultó en una considerable mejora en la capacidad de captura de CO_2 y cinética, y en una mayor capacidad de regeneración durante ciclos de sorción-desorción.

Por otra parte, el crecimiento de CNT y CNF sobre FBC aumentó considerablemente el área superficial especifica donde se impregnó el líquido iónico. Mediante la impregnación de una baja concentración de hierro (0.3%) se lograron crecer uniformemente CNT y CNF a través de deposición química de vapor, lo que les confirió una naturaleza básica a las FBC. Los cambios en la química superficial y las propiedades texturales permitieron mejorar hasta en un 40% la capacidad de captura de CO_2 para las diferentes condiciones de temperatura (0 a 75 °C) y presión (1 a 10 bar) probadas sin afectar la rápida cinética de adsorción del biocarbon macroporoso prístino.

Mediante la impregnación de una pequeña cantidad del líquido iónico [BMIM][Ac] sobre FBC modificadas con CNF se logró aumento alrededor del doble la capacidad de captura de CO_2 (de 0.41 y 1.37 mmol/g a 0.81 y 2.46 mmol/g a 1 y 8 bar, respectivamente) sin afectar la rápida cinética del material de carbono, y se mejoró la capacidad de regeneración del líquido iónico, de 84.33% a 90.32%, una vez impregnado en las FBC modificadas.

Finalmente, las FBC modificadas con CNT presentaron una notable selectividad CO_2/CH_4 (10:90 a 1 bar) de 330.3 respecto al material prístino (22.8) o al modificado con CNF (22.9). La gran afinidad de este material por el CO2 se atribuyó a la mayor abundancia relativa de grupos C=O, el mayor carácter hidrofóbico, la disponibilidad de grupos oxigenados, el área superficial específica expuesta y la distribución del

tamaño de poro (menor volumen de poros <0,42 nm), lo que le proporciona mayor capacidad de polarizar la molécula de CO_2. Las propiedades de este material lo hacen altamente viable para su aplicación en la purificación de gas natural.

Los resultados presentados en esta tesis doctoral demostraron el gran potencial que tiene la modificación de FBC con nanoestructuras de carbono para la captura selectiva de CO_2, así como su utilidad para impregnar liquido iónico y generar un composito con excelente capacidad de captura de CO_2 y rápida cinética. Esto representa un gran avance en el desarrollo de materiales altamente eficientes para la captura selectiva de CO_2.

Palabras clave: absorbentes líquidos, tetraetilenepentamina, acetato de 1-butil-3-metilimidazolio, biochar macroporoso, nanotubos de carbono, nanofibras de carbono, captura de CO_2, separación de CO_2/CH_4.

Abstract

Carbon dioxide capture by carbonized bagasse fibers modified with carbon nanostructures and impregnated with liquid absorbents.

Greenhouse gas emissions have increased considerably in recent decades, with carbon dioxide (CO_2) representing more than 70% of greenhouse gas emissions followed by methane. Among the methodologies that have been investigated to reduce the concentration and emissions of this gas, CO_2 capture stands out. The impregnation of liquid absorbents in porous carbons has been shown to have a synergistic effect and superior CO_2 capture capacities than pristine materials separately. Due to this, in this work two liquid absorbents with different properties (liquid amine tetraethylenepentamine (TEPA) and ionic liquid 1-butyl-3-methylimidazolium acetate [BMIM][Ac]) were impregnated on carbonized bagasse fibers (CBF) modified with tubular carbon nanostructures such as carbon nanotubes (CNT) and carbon nanofibers (CNF). The CO_2 capture capacity was tested by adsorption isotherms and kinetics at different temperature and pressure conditions and the physicochemical properties of the materials were characterized through various techniques.

The impregnation of a small amount of TEPA on CBF resulted in a considerable improvement in the CO_2 capture capacity and kinetics, and in better regeneration capacity during sorption-desorption cycles.

On the other hand, the growth of CNT and CNF on CBF considerably increased the specific surface area where the ionic liquid was impregnated. By the impregnation of a low concentration of iron (0.3%), CNTs and CNFs were able to grow uniformly through chemical vapor deposition, which gave a basic nature to the CBF. The changes in the surface chemistry and textural properties allowed to improve up to 40% the CO_2 capture capacity for the different temperature (0 to 75°C) and pressure (1 to 10 bar) conditions tested without affecting the rapid adsorption kinetics of the pristine macroporous biochar.

A small amount of the ionic liquid [BMIM][Ac] on CNF-modified CBF was impregnated and the CO_2 capture capacity was approximately doubled (from 0.41 and 1.37 mmol/g to 0.81 and 2.46 mmol/g at 1 and 8 bar, respectively) without affecting the rapid kinetics of the carbon material. Also, the regeneration capacity of the ionic liquid was improved, from 84.33% to 90.32%, once impregnated in the modified CBF.

Finally, the CNT-modified CBF presented a notable CO_2/CH_4 selectivity (10:90 at 1 bar) of 330.3 with respect to the pristine material (22.8) or the one modified with CNF (22.9). The high affinity of this material for CO_2 was attributed to the greater relative abundance of C=O groups, the greater hydrophobic character, the availability of oxygenated groups, the specific exposed surface area and the pore size distribution (smaller pore volume <0.42 nm), which provides it a higher capacity to polarize the CO_2 molecule. The properties of this material, make it highly viable for its application in the purification of natural gas.

The results presented in this doctoral thesis demonstrated the excellent potential of the modification of CBF with carbon nanostructures for the selective capture of CO_2, as well as its usefulness to impregnate ionic liquid to generate a composite with enhanced CO_2 capture capacity and fast kinetics. This represents an important advance in the development of highly efficient materials for the selective capture of CO_2.

Keywords: Liquid sorbents, tetraethylenepentamine, 1-butyl-3-methylimidazolium acetate, macroporous biochar, carbon nanotubes, carbon nanofibers, CO_2 capture, kinetics, CO_2/CH_4 separation.

Structure of this thesis

This doctoral thesis was organized as follows:

Chapter 1 Reports an overview of the problem of increasing CO_2 emissions and methodologies for CO_2 capture, emphasizing on the absorption and adsorption processes. Also, the physicochemical characteristics of carbons are presented, as well as their modification with tubular nanostructures or impregnation with liquid absorbents as a strategy to improve the CO_2 capture capacity. At the end of the chapter, a description of the state of the art in CO_2 capture with carbon materials, liquid absorbents and impregnated absorbents was included.

Chapter 2 reports the impregnation of liquid amine TEPA on carbonized bagasse fibers (CBF) to improve the CO_2 capture capacity. The capture kinetics at different pressures, sorption-desorption cycles, and the ideal concentration of impregnated TEPA to obtain the best CO_2 capture capacity and regeneration without affecting the kinetics were reported.

Chapter 3 presents the enhance in CO_2 capture through the synthesis of carbon nanotubes on CBF. The CO_2 capture capacity at different conditions of temperature, pressure, and CO_2 concentration were reported. Also, the kinetics, isosteric heat of adsorption and regeneration capacity were also included. Finally, a CO_2 capture mechanism was proposed.

Chapter 4 reports the growth of fishbone carbon nanofibers on CBF and the increase in CO_2 capture capacity. The physicochemical properties of the material and the CO_2 capture capacity analyzed through adsorption isotherms at different pressures and

temperatures, kinetics and sorption-desorption cycles at standard conditions were included. The effect of CNFs on CO_2 capture and the adsorption mechanism was proposed.

Chapter 5 includes the effect of the impregnation of the liquid ionic on CNF-modified CBF on the CO_2 capture capacity. It is reported the effect of different concentrations of impregnated ionic liquid on the CO_2 capture kinetics at different pressures and on the sorption-desorption cycles. Finally, a CO_2 capture mechanism was proposed.

Chapter 6 presents the possible application of CNT-modified CBF in the selective separation of CO_2/CH_4. Adsorption isotherms of CO_2 and CH_4 at different pressures and temperatures, the isosteric heat of adsorption calculated for both gases, and the CO_2/CH_4 selectivity, calculated by using the ideal adsorbed solution theory (IAST) for different CO_2/CH_4 ratios, were reported. Finally, the phenomena related to the high selectivity towards CO_2 of the material were proposed.

Chapter 7 reports a general discussion of the results obtained in Chapters 2 to 6, and Chapter 8 provides the final conclusions of this work as well as the perspectives, a list of scientific products and attendance at national and international conferences.

Chapter 1:

Introduction

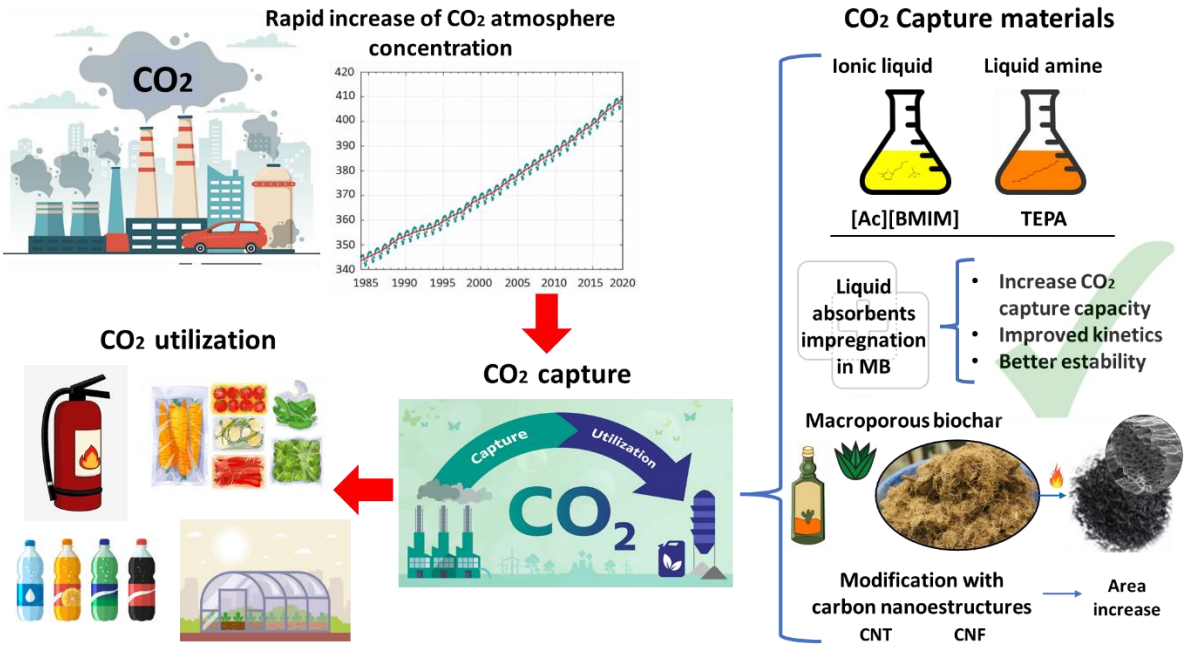

1.1 Global climate change

1.1.1 Greenhouse gases

Climate change is the greatest challenge of our time, and we are at a decisive moment; if drastic measures are not taken today, it will be more difficult and costly to adapt and face these effects in the future. Since the beginning of the industrial revolution, global emissions of greenhouse gases have been increasing and therefore, the negative effects that the excess of these gases produce in the atmosphere [1,2]. It has been reported that CO_2 is the main gas causing the greenhouse effect, which represents more than 70% of global greenhouse gases, followed by methane, nitrous oxide, fluorinated gases, among others (Figure 1.1 a) [3].

Naturally, the greenhouse effect is a process in which thermal radiation from the sun passes through the atmosphere and reaches the Earth's surface, where it is absorbed by plants, soil, bodies of water, etc. A fraction of the incident radiation is re-emitted as infrared light, which is absorbed by greenhouse gases, such as CO_2, causing the Earth's surface to warm (Figure 1.1 b). When the planet's temperature increases, mainly due to human activity, the climate system responds at various scales of space and time [4]. These temperature changes alter the circulation of the sea and the atmosphere and, consequently, the hydrological cycle, resulting in changes in precipitation and temperature on the Earth's surface, which has caused the melting of glaciers and the rise in sea level [5,6]. Furthermore, in the particular case of CO_2, it has been reported that it causes ocean acidification [6,7].

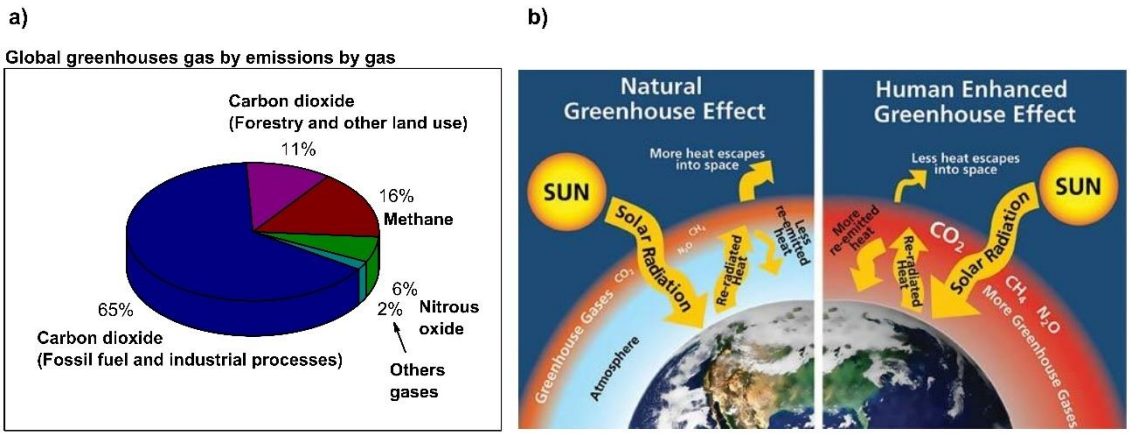

Figure 1.1 *a) Global greenhouse gas emissions, modified from [4], and b) natural and human enhanced greenhouses effect, modified from [8].*

1.1.2 Current situation and CO_2 projections

Since the beginning of the industrial era, the burning of fossil fuels to generate energy, livestock processes, industrial processes, waste management and oil, gas and mineral extraction have contributed to most of the emission of CO_2 and other greenhouse gases (Figure 1.2) [9]. Since 1970, CO_2 emissions have been increasing by approximately 90%, rising from 16 GT to reach 37.5 GT (1 GT= $1x10^{12}$ kg of CO_2) by 2018 [10]. For the year 2020, it has been reported that, despite the climate crisis, the use of fossil fuels has been maintained and its use is expected to continue with an increase of 2% annually until 2030 [11]. Furthermore, energy demand is expected to increase by up to 30% from 2019 to 2040, of which fossil fuels are expected to supply more than 70% of this demand [12,13]. In this sense, the largest contribution to the emission of CO_2 into the atmosphere is mainly from China, the United States, the European Union and India with approximately 30 and 15, 9 and 7%, respectively [14].

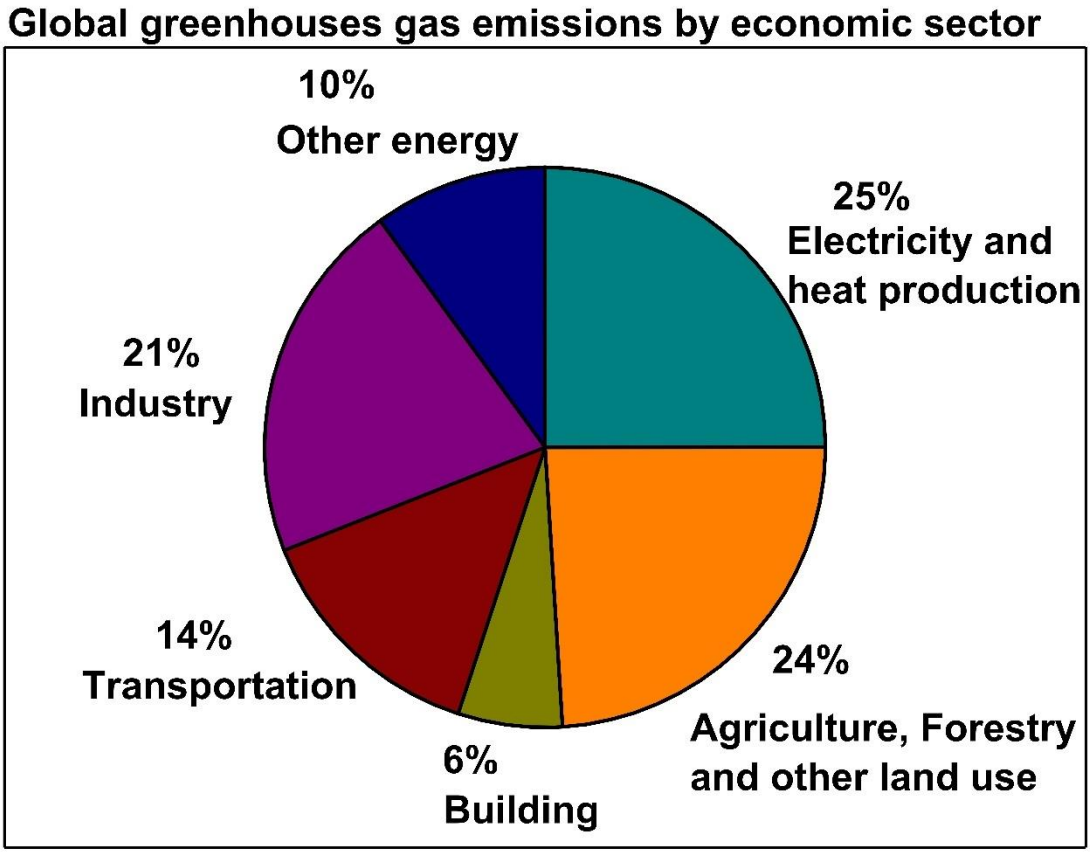

Figure 1.2 *Global greenhouse gas emissions by economic sector, modified from [4].*

It is estimated that there is around 805 PgC in the atmosphere (~109 metric units=1015 grams), which represents that the concentration of CO_2 in the atmosphere reach more than 400 ppm (Figure 1.3) [4,15]. According to the assessment of the Intergovernmental Panel on Climate Change (IPCC) in 2019, it is recommended to restrict CO_2 emissions to limit warming to 1.5 °C. This means achieving zero emissions within the next 30 years, which requires urgent actions from all the global community [4].

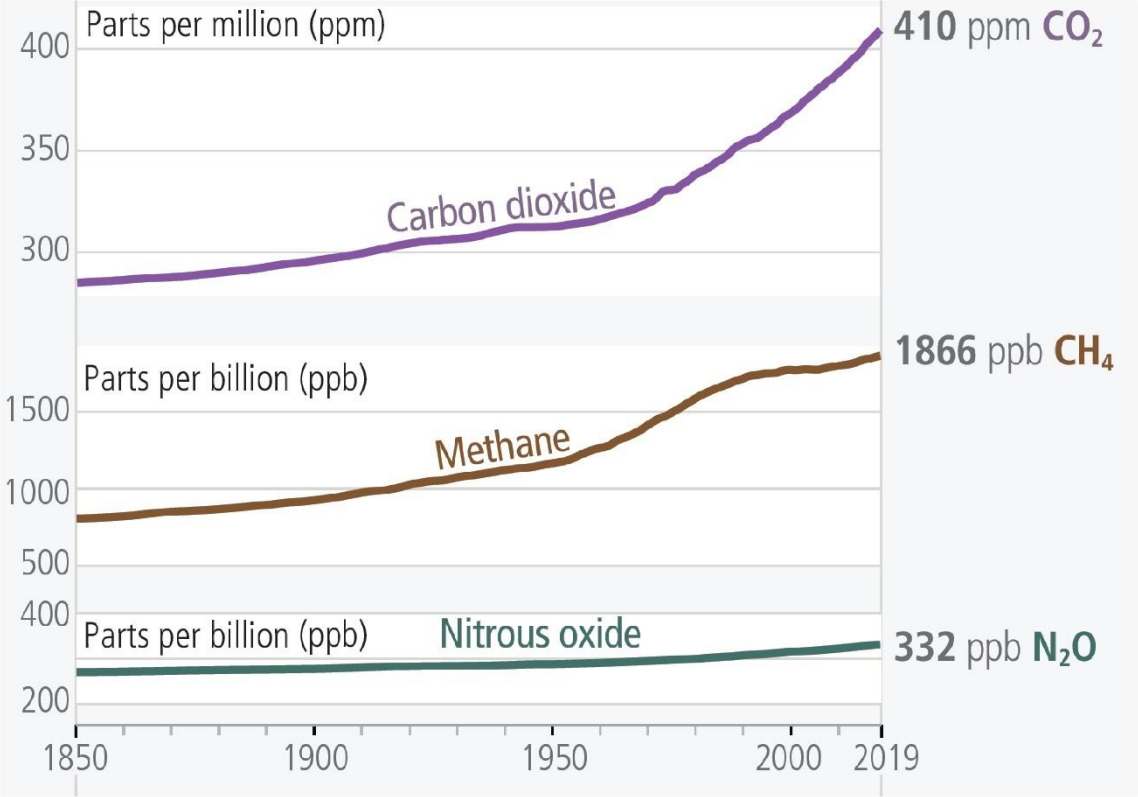

Figure 1.3 *Increased concentrations of CO_2, CH_4 and Nitrous oxide in the atmosphere since 1850, taken from [4].*

1.2 Physicochemical properties of CO_2

Carbon dioxide or CO_2 is a molecule composed of a central carbon atom linked to two oxygen atoms through an α bond and a π bond for each O atom [16]. CO_2 is a non-polar molecule (despite having polar bonds), presents a linear and symmetric geometry due to the *sp* hybridization of the carbon atom, and its Lewis structure can be seen in Figure 1.4 a). The length of the C-O bond in carbon dioxide is 1.16 Å, shorter than the approximate length of a C-O single bond of 1.4 Å [17]. The non-polarity of this molecule is attributed to the fact that, although the C-O bonds are polar, it has equal electric dipoles, but in opposite directions. On the contrary, the charge distribution of CO_2 gives it a quadrupole moment with a partial negative

charge on the oxygen atoms (-0.19 each) and a partial positive charge on the central carbon atom (+0.38). CO_2 molecule has 4 vibration modes as shown in Figure 1.4 b), two symmetric and asymmetric stretching modes, two degenerate bending modes (same frequency and same energy) due to the symmetry of the molecule [18].

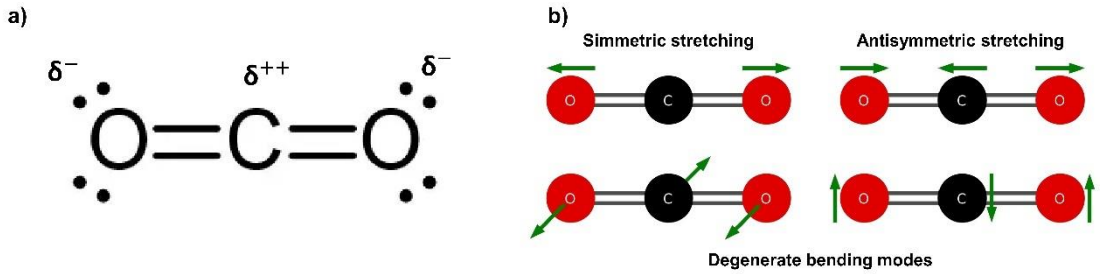

Figure 1.4 a) *Lewis's structure of carbon dioxide (CO_2) and* ***b)*** *Stretching and bending oscillations of the CO_2 molecule.*

CO_2 is considered slightly acidic (weak Lewis's acid) with a kinetic diameter of 3.3 Å. Furthermore, this molecule exists in the form of a colorless and odorless gas (at low concentrations) at 0 °C and 1 bar, has very low melting and boiling points, is non-flammable and has a density of 1.98 kg/m^3 (Table 1.1). In addition, CO_2 is transparent to visible light, but absorbs infrared radiation and is soluble in water, forming carbonate and bicarbonates [16,18].

Table 1.1 *Physical and chemical properties of CO_2.*

Properties			
Chemical formula	CO_2	**Water solubility**	1.45 g/L at 25 °C and 1 bar
Molar mass	44.01 g/mol	**Triple point (T, P)**	-56.5 °C, 5.185 bar
Appearance	Colorless gas	**Vapor pressure**	57.3 bar at 20 °C
Density	1.98 kg/m^3 at 0°C and 1 bar	**Acidity (pK_a)**	6.35, 10.33
Critical point (T, P)	30.9 °C, 73.76 bar	**Viscosity**	0.0137 cP at 0 °C and 1bar 0.015 at 25 °C and 1 bar
Sublimation point	-78.5 °C at 1 bar	**Quadrupole moment**	$13.4x10^{-40}$ Cm^2

1.3 CO_2 capture systems and technologies

Due to the environmental problems presented by CO_2, systems have been developed in recent years to capture it from stationary sources, like power plants, refineries, and manufacturing plants. By CO_2 capture, the aim is to concentrate this gas to be stored in geological and marine systems, in forest biomass, among others [19]. In addition, the captured CO_2 could be reintroduced to the production system since it is widely used in various industrial processes (Figure 1.5) as inert gas in welding, fire extinguishers, for beverages carbonation, as a preservative agent for packaged vegetables, as pressurized gas for weapons, compressed air, and oil recovery [19,20]. Likewise, it is used in enrichment systems for intense vegetable production crops at concentrations between 600 and 1000 ppm of CO_2 [21].

Figure 1.5 *Schematic diagram of CO_2 capture and utilization cycle, taken from [20].*

CO_2 capture has been divided into 3 different systems: postcombustion, precombustion and oxycombustion.

- In post-combustion, systems are installed to treat the gas flows produced from the combustion of coal, gas or biomass. These systems require the use of sorbents and due to this, the amount of impurities contained in the carbon

source must be considered since this intervenes in the regeneration capacity of the sorbent, and therefore the efficiency and cost of the post combustion system in industrial gas streams [15].

- In pre-combustion systems, the main objective is to obtain H_2, this by reacting carbon monoxide from the combustion of coal or biomass with a stream of oxygen or gas to produce synthesized gas or syngas composed of CO_2 and H_2 [15].
- In oxy-combustion systems, oxygen is produced through a process of air separation, where it is reacted in a combustion chamber to produce CO_2 and H_2O that will be stored. The reaction of gas streams from power plants with pure oxygen can be used as energy for boilers [19].

In addition to the capture systems mentioned, direct air capture has been tested. However, the low concentration of CO_2 in the air (~400ppm) represents the greatest limitation in these systems [22]. Regarding the proposed technologies for CO_2 capture, various methodologies have been investigated (Figure 1.5), such as microbiological method [23,24], hydration [25,26], cryogenic separation [27,28], membrane separation [29,30], chemical absorption [31,32] and adsorption using solid materials [33-35]. Some of the advantages, disadvantages, and perspectives of the different technologies for CO_2 capture are mentioned in Table 1.2 and will be discussed in more detail below.

Table 1.2 *Comparison of CO_2 capture technologies [20,23,36-43].*

Technology	Advantages	Disadvantages	Perspectives
Microbiological method	No pollution, low cost, high return value, simple process, direct conversion of CO_2 to organic matter.	Little research, it is in the theoretical stage.	More experimental studies, more immature technology.
Hydrate method	Low energy consumption, non-corrosive and non-polluting, simple process.	Immature technology and few practical applications, CO_2 separation efficiency depends on hydrate formation method.	Improve separation efficiency, development of new equipment and process.
Cryogenic separation	Suitable for concentrated CO_2 capture, excellent separation purity.	High operating cost, complex process, CO_2 solidification, not suitable for CO_2 capture at low concentration.	Efficient processes at low temperature, avoid solidification of CO_2 in pipes.
Membrane separation	Low cost and energy consumption, simple operation, high separation capacity, environmentally friendly	Easily damaged, short useful life, sensitive to humidity in polymeric membranes, low separation efficiency, low membrane area for industrial application.	Modification of membranes to improve separation efficiency and humidity resistance, scale the technology to a pilot scale.

Table 1.2 (Continuation)			
Chemical absorption	High CO_2 capture performance, high CO_2 selectivity, mature technology.	Equipment corrosion, high energy consumption and operating cost, use of solvents.	New fewer corrosive solvents, impregnate solvents in solid matrices, develop more efficient processes to reduce energy consumption
Solid adsorption	Low energy consumption for regeneration, non-corrosive, low cost, high regeneration capacity, fast kinetics, good selectivity, high chemical, thermal and water stability, simple operation.	Lower capture capacity than chemical absorption, relatively immature technology.	Modify materials to improve CO_2 capture capacity, combination of adsorption technologies.

1.3.1 Microbilogical method

For microbial CO_2 capture, the fundamental principle is that, through photosynthesis, microorganisms absorb and fix CO_2, converting it into biomass or into some value-added compound. This CO_2 capture technology has the advantages of low energy consumption, non-corrosive, and environmentally friendly, but it has the disadvantages of requiring large-scale cultivation to be profitable [20]. It has been reported that this technology can reach approximately 7 billion tons per year, which makes it an effective methodology to reduce the CO_2 concentration in the atmosphere [23]. In addition to microorganisms, microalgae have been shown to be

a good option for microbial CO_2 capture due to their rapid reproductive capacity, rapid photosynthetic rate, and short growth cycle [20]. Finally, hybrid processes have been reported where chemical absorption is coupled with microbial capture, which improves the CO_2 capture rate [38].

1.3.2 Hydrate method

CO_2 capture by hydration is a gas separation technology in which the gas is enclosed in a crystalline envelope under the action of hydrogen bonds in water [25,26]. Hydrate method is carried out by the difference in pressures of gas hydrates formed by various gases and hydrates, that is, the components with low pressure favor the formation of the hydrated phase and the gases with higher pressure remain in the gas phase [39,44]. Figure 1.6 presents a typical diagram for the CO_2 capture process through hydration. For CO_2, the hydrate formation pressure is 5.2 bar at 0 °C, conditions in which this gas is enclosed in cage-shaped pores, where each pore can only encapsulate one molecule of CO_2. This relatively new technology has the advantages of being non-polluting, non-corrosive, a simple process and relatively low energy consumption [40,45]. Additionally, it has been reported that by adding SiO_2 or Al_2O_3 nanoparticles to additives to form hydrates, such as tetra-n-butyl ammonium bromide (TBAB), hydrate formation can be accelerated and improved the CO_2 capture capacity [46].

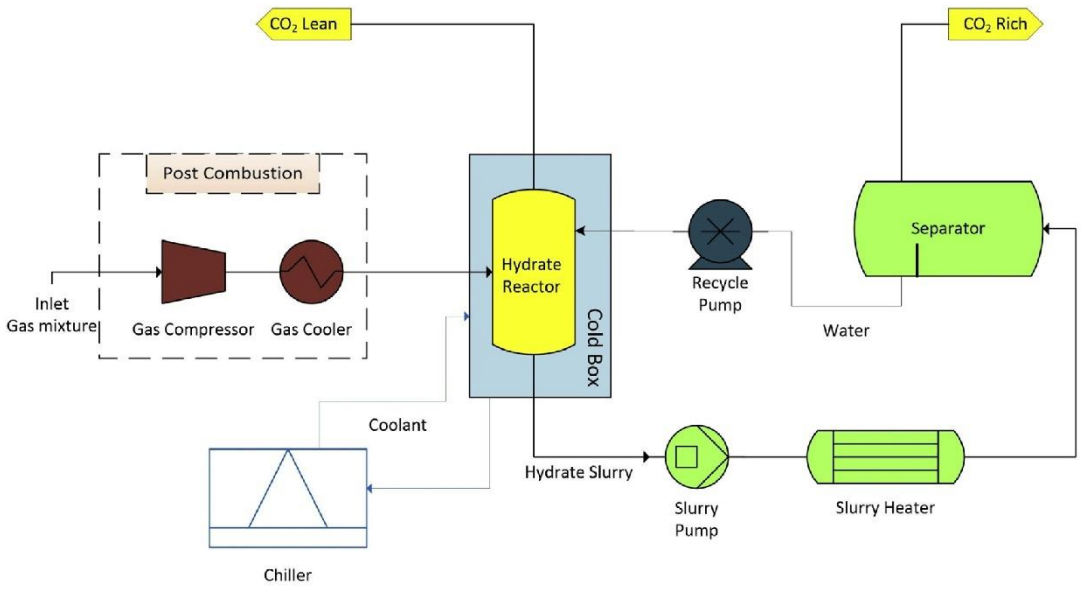

Figure 1.6 *Typical diagram for the CO_2 capture process through hydrate method, taken from [47].*

1.3.3 Cryogenic separation

Cryogenic separation is a low temperature physical separation or CO_2 capture process where the gas is brought to sublimation conditions, -56.6 °C or 100-135 °C and 10-20 MPa, to solidify the CO_2 in a pipe [27,28,48]. This gas separation process can recover between 90-95% of the CO_2 from a combustion stream by separating the gases with respect to their boiling points [48]. Using this technique, solid CO_2 can be melted and recovered in high-purity liquid form, which can be stored or used in oil recovery [43,49]. However, this process can only be used with very high CO_2 concentrations, combustion gases of relatively low temperature or high partial pressure [30]. Furthermore, this process consumes a lot of energy, requires cryogenic temperatures or high pressures and when CO_2 solidifies it causes the pipes to become blocked, affecting gas separation [48,50,51].

1.3.4 Separation by membranes

Gas separation by membranes is a relatively mature technology, as this has been used since the 1980s for air separation, biogas improved, hydrogen production, natural gas sweetening and combustion processes [52,53]. The principle of gas separation using membranes is based on the difference in the permeation rate of the gas components on the surface of the membrane (Figure 1.7) [29]. Membranes can be classified into two main categories: polymeric membranes and inorganic membranes [20]. In general, inorganic membranes have better stability, corrosion resistance and greater separation performance; however, they are considerably more expensive, which makes them difficult to implement at an industrial level [3,30]. Membrane separation is considered an economical process due to the low energy requirement compared to other methods such as solvent absorption [54]. However, this technology presents several challenges such as its low selectivity for CO_2 [30]. Unfortunately, the selectivity and permeability of membranes often have an inverse relationship, presenting a fundamental barrier to obtain high selectivity and permeability [48]. Therefore, few commercial membranes exist specifically for CO_2 capture [42]. Currently, research has focused to improve the CO_2 capture and separation capacity of membranes through doping, pore size control, surface functionalization, etc. [48].

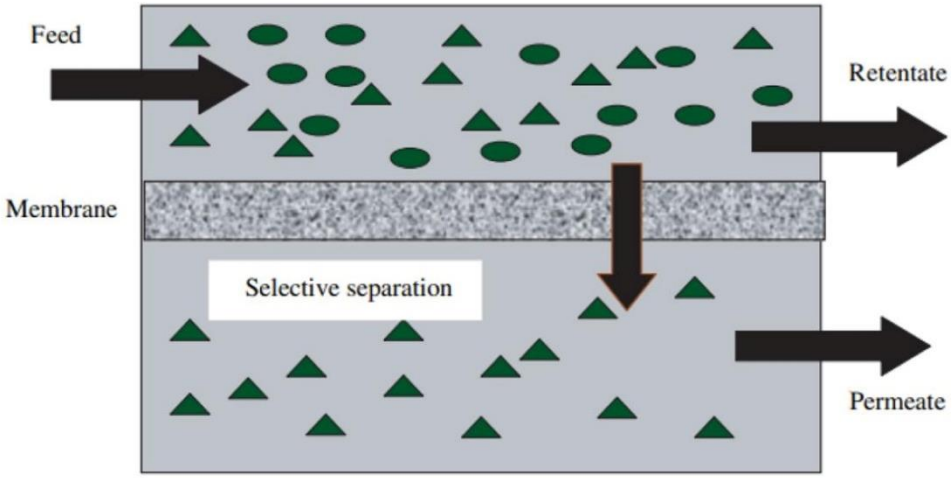

Figure 1.7 *Schematic diagram of gas separation membrane, taken from [43].*

1.3.5 Chemical absorption in liquid absorbents

Chemical absorption is the most widely used method for CO_2 capture despite being a relatively expensive technology, high energy consumption, highly corrosive [48]. This method has received great attention for more than 50 years because it can absorb large volumes of gas emissions with high CO_2 recovery efficiencies between 70-95% [48,55,56]. Chemical absorption is a method where chemical solvents are used and react with CO_2, subsequently the gas will be desorbed by a change in pressure or temperature and in consequence, the absorbent can be reused during many sorption-desorption cycles [31]. Currently there is a wide variety of absorbents such as organic amines, ammonia solutions, sodium hydroxide solution, amino acid salts, carbonate systems, ionic liquids, and eutectic solvents to mention the main ones [20,57]. Because in this work we will work with liquid amines and ionic liquids, in the following sections both compounds will be discussed more broadly.

1.3.5.1 CO_2 capture with liquid amines

Liquid amines are the most used materials for CO_2 capture at an industrial level due to the reasonable maturity of the technology, their reactions are highly reversible, and they have high capture capacity and selectivity towards CO_2 [58]. The CO_2 absorption process involves subjecting the low-volatility liquid amine to a stream of combustion gas at conditions close to ambient conditions. Subsequently, the solution is regenerated by extraction of water vapor at a temperature between 100-120 °C, the released CO_2 is compressed to more than 15 MPa and stored [48]. However, the desorption process consumes a lot of energy, representing between 70 and 80% of the total energy consumption for CO_2 capture [20]. The most widely used amines for chemical CO_2 absorption include diethanolamine (DEA), monoethanolamine (MEA) due to their high reaction rate compared to primary or secondary amines [59-61]. However, they have disadvantages such as low thermal stability, high volatility, low CO_2 capture capacity, easy degradation in the presence of SO_x, NO_x and oxygen and high corrosion rate of the equipment [57,61,62]. Another of the most commonly used amines includes piperazine (PZ) and its derivatives, which have better thermal stability and better CO_2 capture capacity than MEA, but have higher vapor pressure, which limits its practical application [48]. On the other hand, conventional amines with amino acid salts (AAS) solutions have been mixed and demonstrated high CO_2 absorption efficiency. AAS have various advantages such as high CO_2 absorption rates, low toxicity, greater resistance to degradation, high thermal stability, low volatility, and high biodegradability [63]. Finally, the search for amines with better properties in CO_2 absorption continues, so

in the next section tetraethylenepentamine or TEPA, which we studied in this thesis, will be described in more depth. This amine has interesting properties for CO_2 capture, such as high density of amino groups, high thermal stability, low volatility, and lower viscosity compared to other amine compounds [64].

1.3.5.1.1 Tetraethylpentamine (TEPA)

Tetraethylenepentamine (TEPA) is a polyamine with a linear structure that contains two primary and three secondary amino groups in its structure [65]. It is a viscous yellow liquid with a pungent ammoniacal odor. It has a high boiling point of 340 °C, a solidification point of -40 °C and in the liquid phase and it has a density practically equal to that of water (ρ = 0.998 g/cm³). It is soluble in water and organic solvents and is a hygroscopic compound, and it has a low viscosity of 96.2 cP at 20 °C [66,67]. Table 1.3 lists some of the most significant properties of TEPA.

Table 1.3 *Physical and chemical properties of TEPA*.

Properties			
Structure	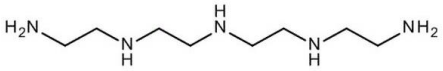		
Chemical formula	$C_8H_{23}N_5$	**Boiling point**	340 °C
Molar mass	189.3 g/mol	**Water solubility**	$1x10^3$ g/L
Appearance	Yellow viscous liquid	**Viscosity**	96.2 cP at 20 °C
Density	998 kg/m^3	**Vapor pressure**	1.3 mmHg at 20 °C
Melting point	-40 °C	**Acidity (pK_a)**	9.68/ 9.1/ 8.08/ 4.72/ 2.98

TEPA has been extensively investigated for CO_2 capture mostly by impregnating it into porous materials, where it has shown excellent properties and stability, which

will be discussed furthermore in section 1.3.6.5.2. Regarding the reaction mechanism of amines during CO_2 capture, it has been studied extensively [68,69]. For primary and secondary amines, such as TEPA, the most widely recognized reaction mechanism is “zwitterionic”, where the reaction between anima and CO_2 first produces zwitterionic (a neutral molecule containing negatively and positively charged groups), then the amine reacts to form a protonated amine and carbamate ions, as shown below [68].

$$\mathrm{AmineH} + \mathrm{CO_2} \rightleftharpoons \mathrm{AmineH^+COO^-} \quad (1)$$

$$\mathrm{AmineH} + \mathrm{AmineH^+COO^-} \rightleftharpoons \mathrm{AmineH_2^+} + \mathrm{AmineCOO^-} \quad (2)$$

$$2\mathrm{AmineH} + \mathrm{CO_2} \rightleftharpoons \mathrm{AmineH_2^+} + \mathrm{AmineCOO^-} \quad (3)$$

According to this zwitterionic reaction mechanism, the theoretical CO_2 absorption of primary and secondary amine solutions is 0.5 mol of CO_2/mol of amine. However, in the presence of water, this value can be higher due to hydrolysis reactions with CO_2 absorption, as shown in equation (4), where free amines and bicarbonates are produced [70].

$$\mathrm{AmineCOO^-} + \mathrm{H_2O} \rightleftharpoons \mathrm{AmineH} + \mathrm{HCO_3^-} \quad (4)$$

1.3.5.2 CO_2 capture with ionic liquids

Ionic liquids (IL) are liquid salts at room temperature composed of a cation, often organic, and an anion that is a weak inorganic or organic base, which has a diffuse negative charge [71,72]. ILs are considered viable alternatives for CO_2 capture since

they present interesting properties such as high CO_2/N_2 selectivity, good chemical and thermal stability, very low vapor pressure, non-flammable, recyclability, high polarity, and low toxicity [72- 75]. Most of the characteristics of an IL are determined by its degree of viscosity, melting point, and miscibility with other solvents [72,76]. Furthermore, the type of anion that conformed the IL influences its thermal stability, hygroscopic properties (ability to absorb moisture from the medium), surface tension and ability to form hydrogen bonds [77]. However, ILs have some disadvantages, one of the main ones is their high viscosity that can range between 66 and 1100 cP at room temperature [78]. The high viscosity of these materials is usually much higher than that of other common solvents, which represents that the diffusion of CO_2 towards the IL is limited. Figure 1.8 shows the relationship between the self-diffusion coefficient of CO_2 in various solvents and ionic liquids with respect to their viscosities [48,79], whereas the viscosity of the solvent is bigger, there is a reduction in the coefficient of diffusivity in a proportion of ~0.43 (depending on the slope of the line). Another main disadvantage of ILs is their high cost, which can reach ~$1000 USD/kg [79].

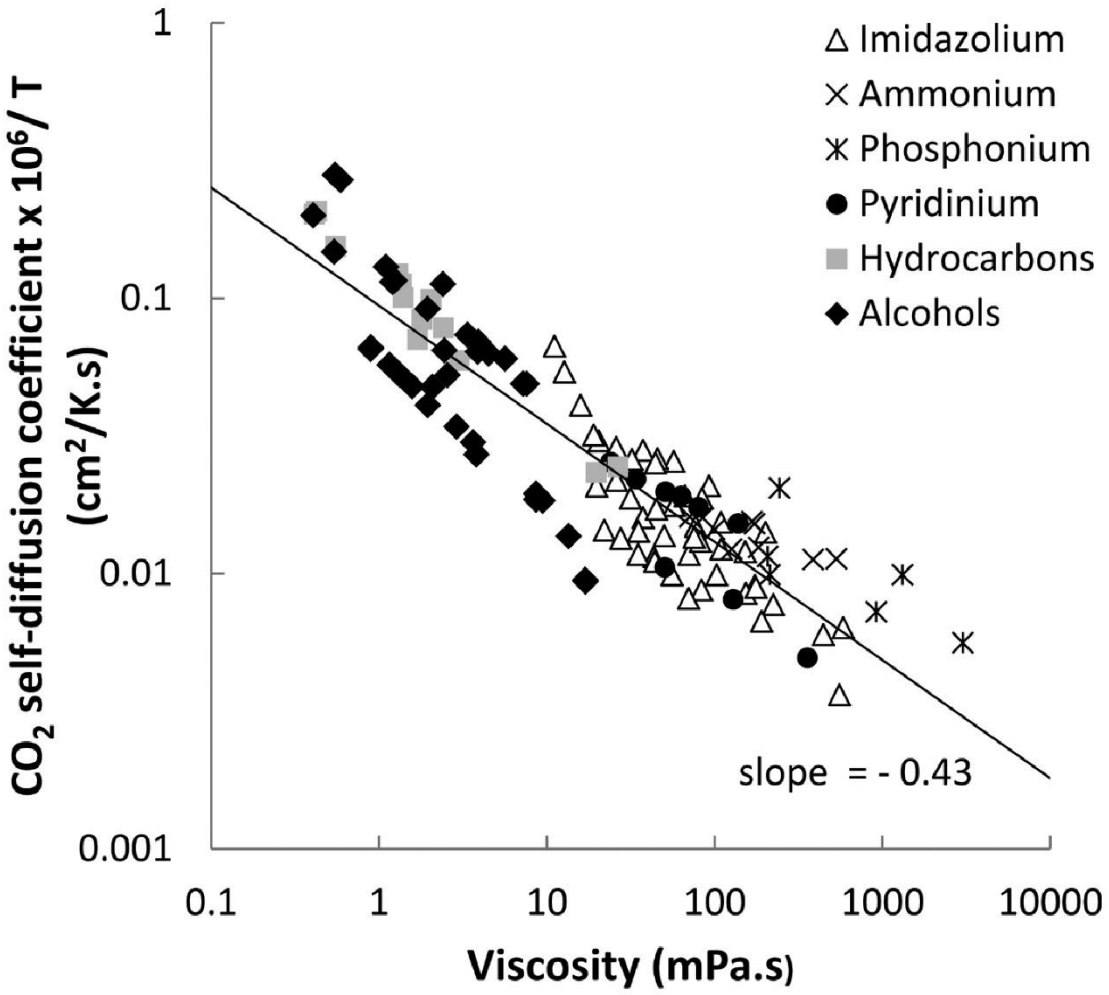

Figure 1.8 *Viscosity/diffusivity relationship for ionic liquids and conventional solvents, taken from [79].*

Despite the disadvantages that ILs present, the variety that exists is very large and their properties will depend on the choice of ions that make it up, so ILs can be adjusted relatively easily to obtain the desired properties for the capture of CO_2 [79,80]. Figure 1.9 shows some of the anions and cations that most commonly conformed an IL. Among the large number of ILs, those formed by cation based on imidazolium stand out due to their high solubility for CO_2 [80,81]. 1-Methoxyethyl-3-methylimidazolium hexafluoroborate and 1-methoxyethyl-3-methylimidazolium

bis(trifluoro-methylsulfonimide) have been tested to capture CO_2 in mixtures with N_2 and O_2 at room temperature [82]. Also, the high capacity of 1-methoxyethyl-3-methylimidazolium bis (trifluoro-methylsulfonimide), in combination with a base, to capture CO_2 has also been reported [83]. Moreover, 1-butyl-3-methylimidazole acetate or [BMIM][Ac] has been reported in CO_2 capture because it is highly selective for this gas [84,85].

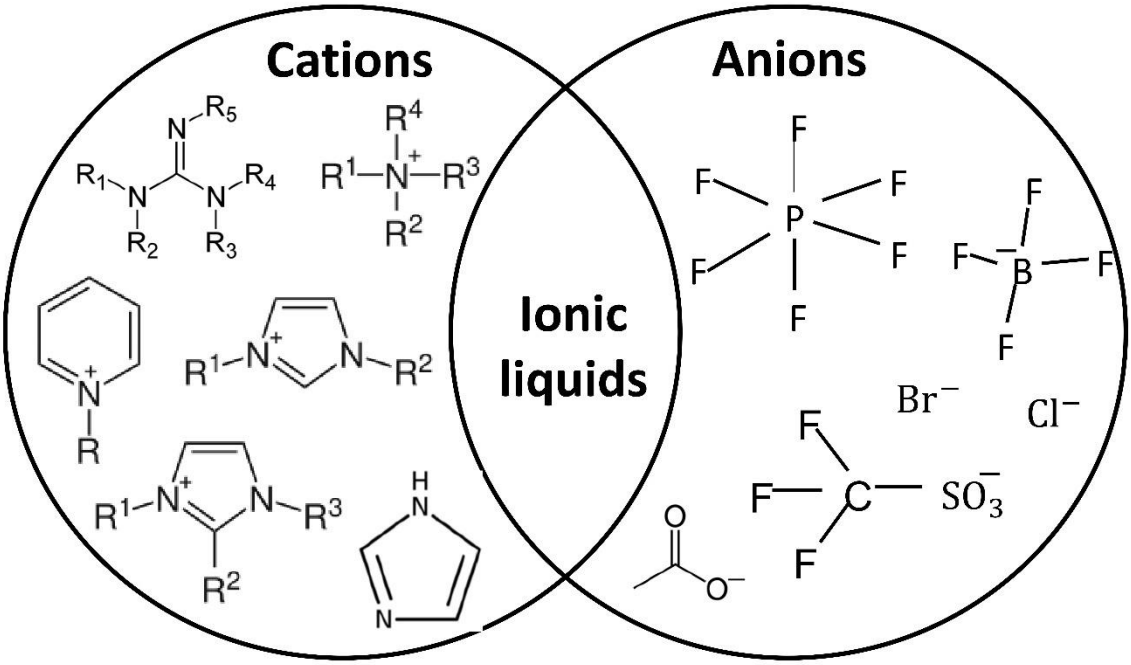

Figure 1.9 *Examples of types of anions and cations commonly used in ionic liquids.*

1.3.5.2.1 1-butyl-3-methylimidazole acetate

1-Butyl-3-methylimidazole acetate or [BMIM][Ac] is an ionic liquid with a density slightly greater than that of water (1.0578 g/cm^3 at 25 °C) and high viscosity (393.3 cP at 25 °C). This is considered an IL of basic nature, aprotic and miscibility in water (Table 1.4) [19]. The acetate anion that makes up this IL shows high basicity and solubility, which gives it a high CO_2 capture capacity [84,86]. Furthermore, it has

been reported that imidazolium based ILs with the acetate anion allow to increase the CO_2 capture by an order of magnitude at 1 bar and 25 °C with respect to common inorganic anions such as PF_6 and BF_4 [87].

Table 1.4 *Physical and chemical properties of 1-butyl-3-methylimidazole acetate IL.*

Properties			
Ionic Structure	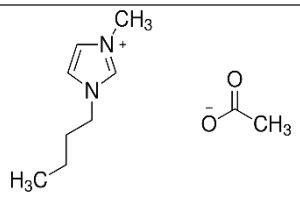		
Chemical formula	$C_{10}H_{18}N_2O_2$	**Density**	1.055 g/cm^3
Molar mass	198.26 g/mol	**Melting point**	-20 °C
Appearance	Yellow high viscous liquid	**Viscosity**	393.3 cP at 25 °C and 1 bar
Water content	<2%		

The chemical reaction between [BMIM][Ac] and CO_2 has been widely investigated using different techniques such as X-ray diffraction [88], Raman spectroscopy [89], infrared spectroscopy [90], nuclear magnetic resonance [91] and computational methods [89,90,92], where CO_2 reacts with the imidazole ring and a carboxylate is formed (Figure 1.10). $[BMIM]^+$ donates an H^+, which produces the deprotonation of carbon atom 2 (acid site), which interacts with CO_2. Furthermore, the $[acetate]^-$ anion accepts the released H^+, forming acetic acid [81,88-90]. This reaction is considered thermodynamically favorable and reversible, so it has a good capacity to capture CO_2 at ambient conditions.

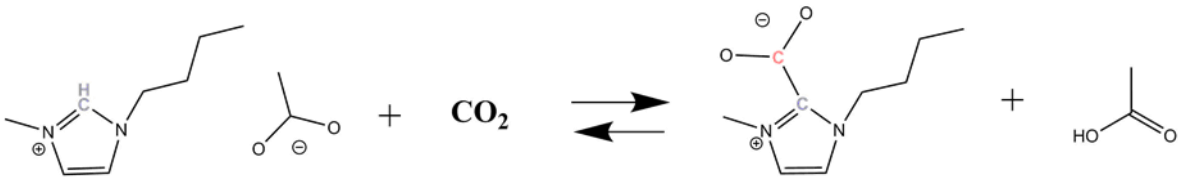

Figure 1.10 *Chemical reaction between [BMIM][Ac] and CO_2 [85].*

1.3.6 Adsorption on solid materials

Adsorption with solid materials is considered a potential CO_2 capture method because it presents great advantages such as its high adsorption capacity, low regeneration cost, chemically stable, no-corrosive, and low energy consumption [34,35]. In this CO_2 capture method, the gas is captured in a porous solid, generally with high specific surface area, by Van der Waals forces or electrostatic forces [33]. It has been reported that the selective adsorption of CO_2 against other gases such as N_2 and CH_4 is governed by the Van der Waals interaction between the polar sites of the adsorbent surface and the high quadrupole moment of CO_2 ($13.4x10^{-40}$ Cm^2) compared to that of N_2 ($4.65x10^{-40}$ Cm^2) [93]. Furthermore, solid sorbents can also capture CO_2 through chemisorption, where the adsorbate binds to the active sites present on the surface of the sorbent through covalent bonds [94]. The main difference between physisorption and chemisorption in porous solids is the bond strength or heat of adsorption, where the physisorption of gases in solids is usually below 50 kJ/mol, while for chemisorption it ranges between 60 and 90 kJ/mol. [95]. Therefore, the higher interaction strength has been correlated directly with higher energy consumption for gas desorption, but inversely proportional to the CO_2 selectivity [48].

It is considered that an ideal adsorbent must have high adsorption capacity, selectivity for CO_2, rapid adsorption/desorption kinetics, operating temperatures and pressures compatible with combustion gases, high chemical and thermal stability against other gase like SO_x, H_2O, NO_x and easy regeneration to make it economically viable [48,96,97]. Because no adsorbent has all these properties, different materials have been investigated such as activated carbons, zeolites, metal-organic structures (MOFs), metal oxides, hydrocalcites, geopolymers, mesoporous materials, biocarbons, among others [41,98-100]. Table 1.5 lists the main advantages and disadvantages of these materials for CO_2 adsorption.

Table 1.5 *Advantages and disadvantages of CO_2 solid adsorption materials [3,20,35,41,101-104].*

Adsorbent material	Advantages	Disadvantages
Zeolites	High adsorption capacity, long service life, uniform porosity.	Low selectivity, adsorption capacity effected by temperature and water vapor.
MOFs	Modifiable porous structure, high capacity at high pressure.	Complex synthesis, low capacity at low pressures, sensitive to water, high cost.
Mesoporous materials	High specific area, developed porous structure, easily modifiable.	Low adsorption capacity, sensitive to water vapor.
Activated carbons	High thermal stability and surface area, low cost, easy regeneration, Low sensitivity to humidity.	Low selectivity, CO_2 partial pressure significantly affects capture capacity, moderate adsorption capacity.
Biochars	Low-cost adsorbents, easy regeneration, modifiable, fast kinetics.	Low adsorption capacity, undeveloped porosity, sensitive to temperature.

1.3.6.1 Zeolites

Zeolites are materials made of crystalline aluminosilicates, where the crystalline structure is composed of the periodic arrangement of tetrahedra of SiO_4 and AlO_4 with pores of well-defined size [48]. According to the structures commission of the international zeolite association (IZA-SC) there are more than 170 unique approved topologies [105]. Some of the important characteristics of zeolites are attributed to the nature and size of the cations (generally alkaline metals), which are exchangeable and easily adjust the acid-base properties and porosity (generally less than 1 nm) to react with CO_2 [48,106,107]. Zeolites have a strong interaction with CO_2, due to the structural cations in their pores, they have a long useful life, and their uniform porosity makes them good materials for gas separation through molecular sieving [108]. However, these materials have important disadvantages such as their high affinity for water, which makes them difficult to use for CO_2 capture in humid environments, and the strong interaction between CO_2 and the zeolite makes it more difficult and expensive to desorb CO_2 during its regeneration [41].

1.3.6.2 Metal-organic framework (MOFs)

Metal-organic framework or MOFs are porous crystalline structures made up of one or several transition metal ions (such as Cu and Zn) and an organic ligand (for example: carboxylates, azolates and phosphonates) that connects them [109]. The structure and shape of the MOF is governed mainly by the nature of the metal ions, the organic ligands, and how they linked together in the structure [110]. The length of the organic ligand mainly affects the specific surface area and porosity which can improve the adsorption capacity of the material. However, long ligands generate

MOFs with more fragile structures. MOFs have the great advantage of being modifiable depending on the unitary elements that compose them, resulting in diverse topological structures, functional groups, and different pore sizes [102,110,111]. Actually, MOFs have been reported with very large surface areas of up to 10,000 m^2/g [112] and high adsorption capacities of 8.29 mmol/g obtained at standard conditions [113]. These extremely high areas, adjustable pore size, and the ability to tune their properties, make MOFs excellent candidates for CO_2 capture. However, MOFs have some disadvantages such as their high cost, instability in the presence of water and other contaminants, relatively low thermal and mechanical stability, and like most solids, their CO_2 adsorption capacity decreases as the temperature increases [48,114].

1.3.6.3 Activated carbons

Activated carbon (AC) is one of the oldest solid adsorbents used in industrial processes due mainly to its low cost [115]. Its large-scale use began in the Second World War in gas masks [116]. These carbonaceous materials are of great interest in CO_2 capture because of their excellent thermal, chemical, and mechanical stability, low sensitivity to water vapor, low production cost and easy regeneration [35,101]. AC has a mainly microporous structure and a high specific surface area in the range from 500 to 3000 m^2/g [20,117]. However, CO_2 is usually weakly adsorbed on ACs resulting in low selectivity and relatively low adsorption capacity compared to other materials such as MOFs [48]. Therefore, attempts have been made to include heteroatoms on its surface, such as N, to increase the alkalinity of the active sites and improve the CO_2 capture capacity [118].

For the activation process there are two main methods, physical and chemical activation. In physical activation, gases such as CO_2, air or water vapor are used [119]. This process is usually considered more environmentally friendly as it does not use chemical reagents. However, this process requires higher energy and higher temperatures (700-1000 °C) for a longer time [120]. On the other hand, during chemical activation the material is impregnated with an activating agent that can be acidic, basic, or metallic salt and is subsequently thermally treated in an inert atmosphere for the AC formation. The most commonly used activating agents are KOH, NaOH, K_2CO_3 as alkali agents, H_3PO_4 and H_2SO_4 as acidic agents and alkali metal salts such as $ZnCl_2$ [121,122]. Chemical activation has the main advantage of using lower temperatures (400-800 °C). Furthermore, activation can be carried out in a single step (pyrolysis and activation) and chemically activated carbons have been observed to have higher porosity and surface area [121,123-125]. However, the main disadvantages of chemical activation are the use of products that can be toxic, dangerous, or difficult to recycle and the use of agents such as HCl to wash the material after the activation process [120,126].

1.3.6.4 Biochars

Biochar is a carbonaceous material where its main characteristic is that the precursor is biomass. Biomass generally refers to organic matter of plant origin, but it can also be animal excrement, industrial and agricultural waste, and municipal solid waste [127-134]. To produce biochar, the pyrolysis process is necessary, where the main reaction is the thermal degradation of the biomass components and the release of volatile compounds at temperatures between 300 and 900 °C in an inert atmosphere

[135]. In this process, volatile compounds are released in the form of CO, CO_2 and H_2O and result in the reduction of sample mass and new porosity [136]. The composition of hemicellulose, cellulose and lignin of each precursor, the evaporation rate of volatiles and mass loss can modify the textural properties of each biochar [125]. During a typical pyrolysis process, 4 main stages have been described [137]; 25-150 °C eliminates moisture, 150 to 400 °C usually shows the greatest mass loss due to primary carbonization. At temperatures of 180-270 °C, hemicellulose begins to degrade and between 240 and 350 °C, cellulose begins to degrade [138]. The third stage occurs around 400-550 °C, where the lignin begins to decompose [139] and finally, as the temperature increases above 550 °C up to 900 °C, the remains of cellulose, hemicellulose and lignin continue to decompose. This type of pyrolysis usually has a yield of around 30% [140,141].

Biochar has been used in various applications such as environmental remediation and energy storage and conversion [141-143]. Furthermore, it is considered a sustainable resource due to its high availability, low cost, relatively easy synthesis, less pollution, and renewability [144,145]. Due to this, in recent years there has been greater interest in carbons derived from biomass for CO_2 capture [142,143]. On the other hand, the use of biomass to produce biochars is beneficial to mitigate climate change and pollution caused by mismanagement of biomass [146]. However, to develop greater porosity and specific area for a biochar, an activation and/or modification process of the surface is necessary [147]. Biochar alone usually has low to moderate CO_2 capture capacities.

1.3.6.4.1 Physicochemical properties of carbon materials

The CO_2 capture capacity has been highly correlated with the textural properties of the materials, specifically with the microporosity smaller than 0.7 nm [148-150] and with the content of heteroatoms on the surface [151-153]. The most common strategies used to improve the CO_2 capture capacity and selectivity of a carbon material is through the modification of the surface chemistry and increasing the specific surface area and porosity [154]. It has been reported that surface chemistry plays an important role at low pressure (<5 bar) and this effect gradually disappears with increasing pressure, where the pore volume becomes more important [155].

Carbon materials exhibit a high carbon content with sp^2 hybridizations which is arranged in lamellar layers (graphene) that are stacked on top of each other through Van der Waals interactions orderly (graphite or graphitizable carbons) or with a higher degree of disorder, called turbostratic carbon (activated carbon or carbon black) [156,157]. The arrangement of graphitic sheets is responsible of most of the physicochemical properties of carbon materials and two different types of sites can be identified: basal or edge carbon atoms [158]. Generally, disordered carbon contains a higher number of imperfections and defects such as vacancies in graphitic sheets and non-aromatic rings. These sites, together with the edge sites of the carbon layers (called active sites), have a greater number of unpaired electrons, which present more reactivity and functionality through interaction with heteroatoms such as oxygen, hydrogen, nitrogen, and sulfur [159,160]. The amount of heteroatoms that the material has can be naturally from the precursor or can be introduced during a post-treatment. The type of atom and/or functional group

determine the acidic or basic character of the material [161,162]. The most abundant heteroatom is O, which is distributed in the peripheries of the basal planes, in the defects or vacancies of the graphitic sheets (Figure 1.11) [158,163]. Oxygen occurs in the form of acidic groups such as carboxylic, lactone and phenolic hydroxyls or basic groups such as chromene, quinone, ketone and pyrone [161,162]. It has been reported that functional groups of an acidic nature can improve the capture of CO_2 due to the increase in electronegativity, resulting in an attraction through a dipole induced with the quadrupole moment of CO_2 [164].

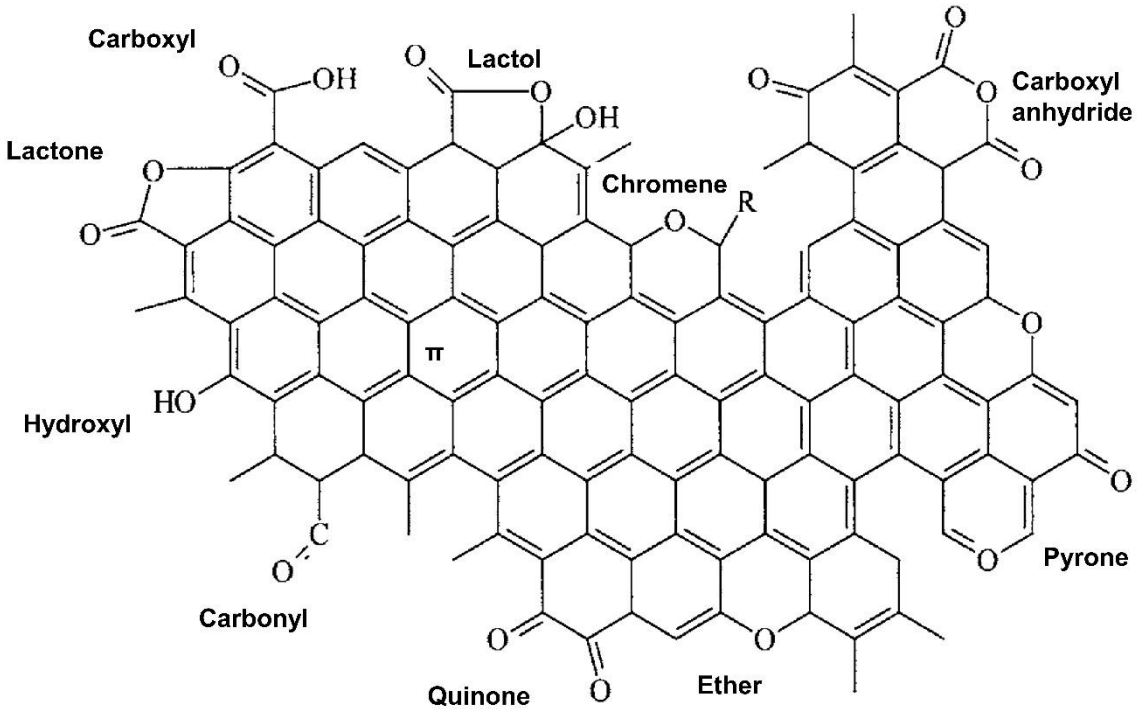

Figure 1.11 *Acidic and basic oxygen-containing functionalities of carbon surface, modified from [157].*

On the other hand, there are two main treatments to introduce N atoms into the carbon structure (Figure 1.12), one is through nitrogen-containing reagents at low

temperatures, which results in the formation of lactams, imides, and amines of a slightly acidic character. Also, through high temperature treatments, quaternary N-type structures (N incorporated into the graphitic sheet replacing C atoms), pyridine and pyrrole [165] can be introduced, which can polarize the carbon surface giving it a basic character. [166,167]. In the same way, it has been reported that by doping with atoms such as sulfur (S) or boron (B), the polarization of graphitic sheets can be improved, which provides active sites for the capture of CO_2 [168]. The CO_2 capture through basic surfaces has been reported through Van der Waals and electrostatic interactions originated by the charge of functional groups, surface defects, edge sites and delocalized electrons in the basal plane due to the slightly acidic nature of CO_2 [155,162].

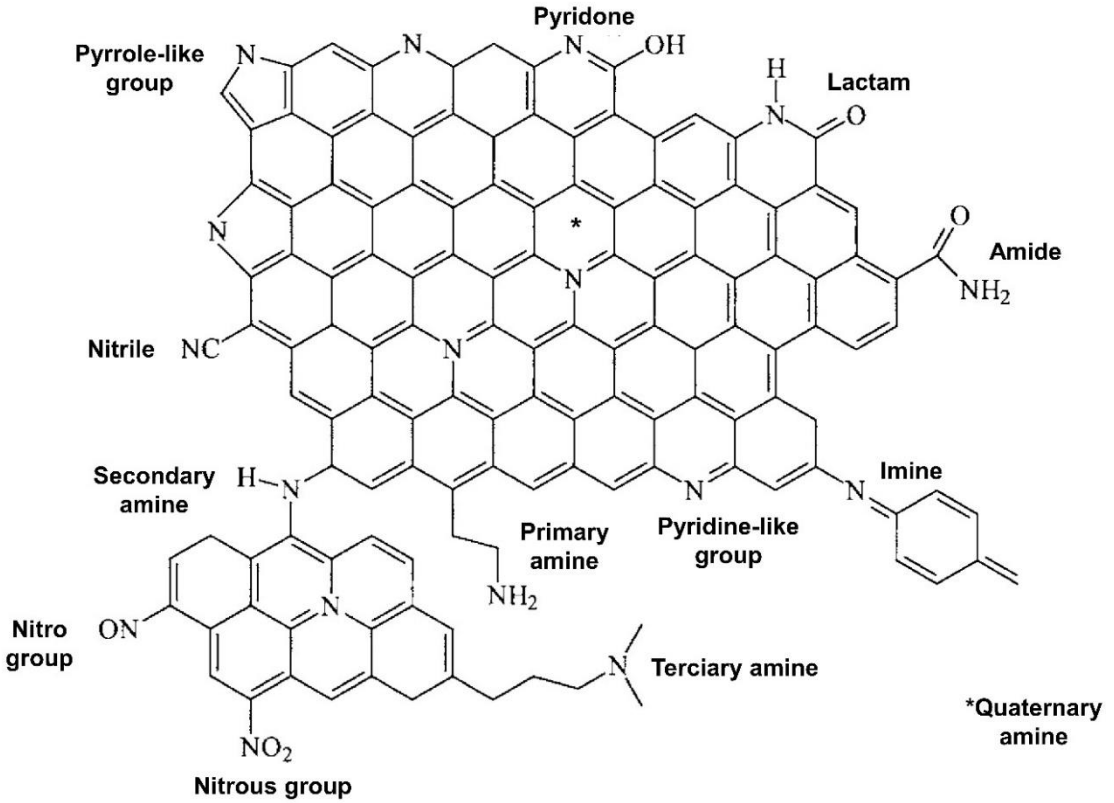

Figure 1.12 *Types of nitrogen-containing functionalities on the carbon materials, modified from [157].*

1.3.6.4.2 Agricultural residues as precursors for carbon materials

Agricultural waste has been of great importance for the synthesis of low-cost carbon materials for different environmental applications such as water treatment or gas adsorption [104,127,131,132,147]. These carbons are considered of great value because they mainly respond two problems, the accumulation of agricultural waste, as well as the challenges presented by commercial coals [169,170]. Table 1.6 presents an overview of the biomass production capacity in the world.

Table 1.6 *An overview of the capacity of some biomass productions.*

Type of Sample	Country/ Region	Production Capacity (tons/year)	Year	Reference
Agave bagasse	México	377,000	2016	[171]
Pine sawdust	México	280,000	2019	[172]
Olive	Spain	6,559,000	2020	[173]
Lignin	Global	100,000,000	2019	[174]
Coconut	Indonesia	17,130,000	2019	[175]
Almond	United States of America	2,000,000	2020	[176]
Oil tea	China	56,250,000	2018	[177]
Rice	China	148,500,000	2020	[178]
Palm	Indonesia	25,400,000	2012	[179]
Bagasse	Brazil	758,000,000	2020	[180]
Bagasse	India	306,000,000	2020	[181]
Wood ash	Germany	12,000,000	2008	[182]

1.3.6.4.3 Agave bagasse carbonized fibers

Agave bagasse fibers are a lignocellulosic waste from the mezcal and tequila industry, which generates 332,000 tons of waste per year [171], distributed in the states of Oaxaca, Guerrero, Durango, Michoacán, Puebla, Guanajuato, Zacatecas,

and San Luis Potosí [183]. These wastes represent an environmental and economic problem because they do not have any direct application. One of the ways to utilize this waste is through its carbonization. In this method, the material is dehydrated and compounds such as cellulose and hemicellulose are volatilized, developing a rigid structure, with high mechanical, chemical and thermal resistance, composed of macro and mesopores that go from end to end of the fiber (Figure 1.13), with a specific area of 3 m^2/g [184]. Carbonized bagasse fibers have been used in CO_2 adsorption due to their low-cost, high availability, high hydrophobicity and, due to their macroporous channels (2-30 um), rapid CO_2 capture kinetics (50 min) and acceptable CO_2 capture capacity (1.26 mmol/g) [185].

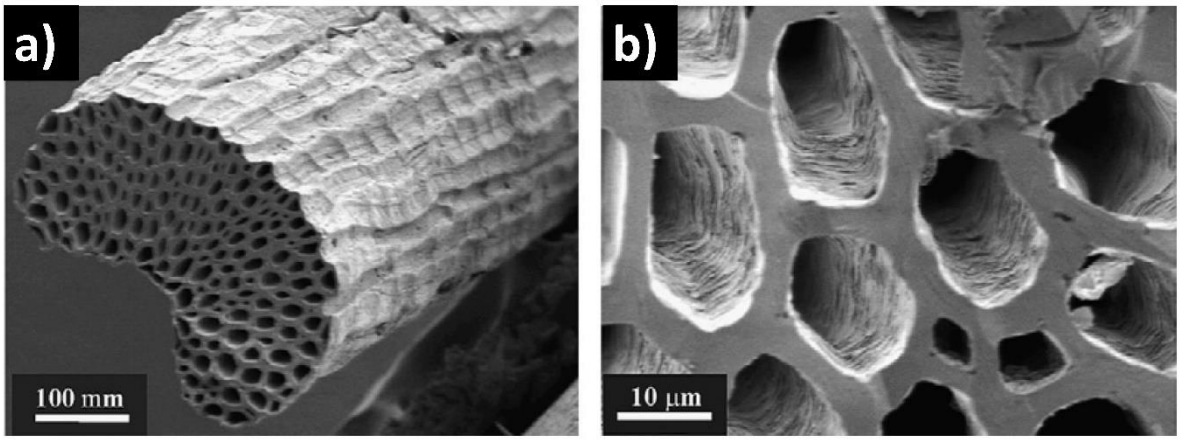

Figure 1.13 *Scanning electron microscope (SEM) micrographs of the macroporous channels of the carbonized bagasse fibers, taken from [184].*

1.3.6.5 Carbon composites

As mentioned in Table 1.5, all solid materials for CO_2 capture present some disadvantage which limits their application on a pilot or industrial scale. Specifically, carbon materials present disadvantages such as low selectivity or relatively low CO_2 capture capacity [48], therefor attempts have been made to generate efficient

composites. Among the materials and chemical used to generate carbon-based composites are amines [64,66], ionic liquids [77,85,185] and nanostructures [186-188]. Through the generation of a composite, the aim is to solve the disadvantages that the separate components present and, consequently, generate a material with better properties for CO_2 capture.

1.3.6.5.1 Modification with carbon nanostructures

Carbon nanostructures are considered structures smaller than 100 nm and can be classified as 0D, 1D, 2D and 3D materials (Figure 1.14). 0D structures are those whose 3 dimensions are below 100 nm (Fullerenes, quantum dots, nanoclusters), 1D two of their dimensions (nanotubes, nanofibers, nanowires), 2D one of their dimensions (nanolamines, nanoplates, sheets of graphene) and 3D none of its dimensions (nanostructured materials or nanocomposites, MOFs) [189,190]. In general, all carbon nanostructured materials have been considered excellent candidates for environmental remediation [191,192]. In particular, tubular nanostructures like carbon nanotubes and nanofibers are of great interest since they have excellent specific surface area quickly available for rapid adsorption. Furthermore, they can be functionalized with relative ease to improve their selectivity towards a certain pollutant, such as CO_2 [193-195].

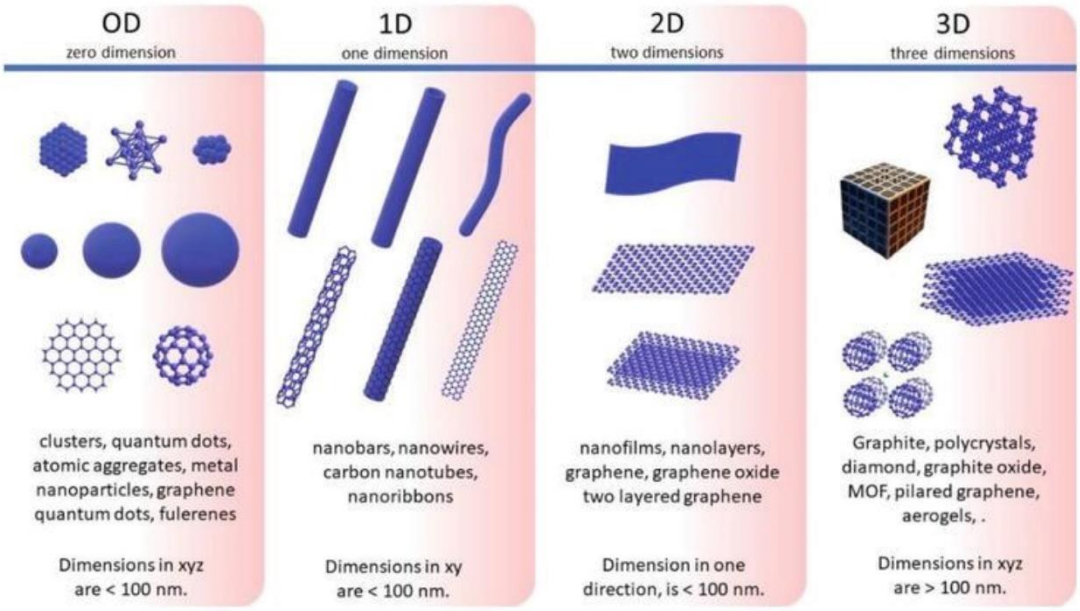

Figure 1.14 *Classification of 0D, 1D, 2D, and 3D nanostructures, modified from [190].*

1.3.6.5.1.1 Carbon nanotubes (CNT)

Carbon nanotubes (CNTs) are allotropic tubular structures of carbon. They can be found in 3 specific coiling angles, which dictates their morphology, being of the saddle, zigzag or chiral type (Figure 1.15) [196,197].

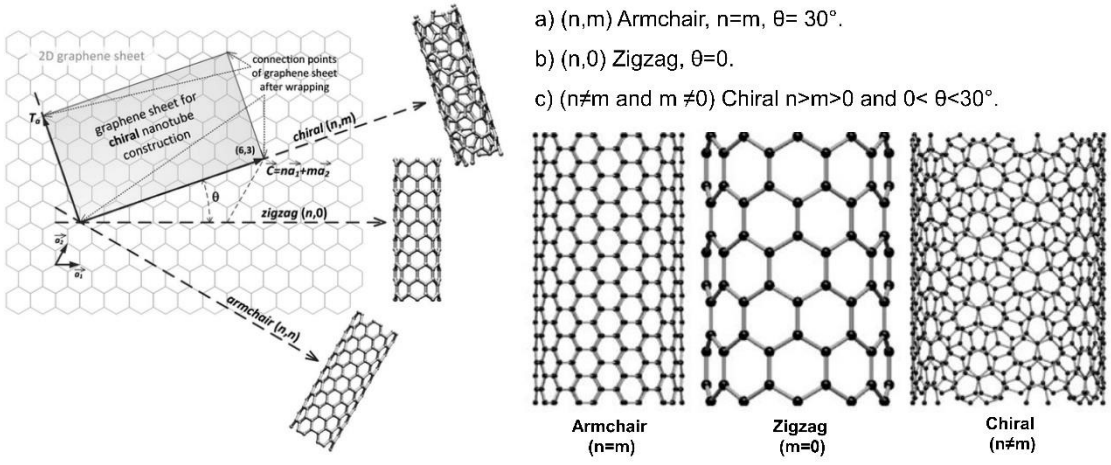

Figure 1.15 *Scheme of chirality in a plane of graphene and types of carbon nanotubes a) armchair, b) zigzag and c) chiral, modified from [197].*

CNTs can be single-walled (SWCNT) formed from a single rolled graphitic sheet or multi-walled (MWCNT) made up of layers of concentrically formed cylinders (Figure 1.16) [198]. Generally, the production of CNTs is by chemical vapor deposition or CVD, where various parameters can affect the quality of CNTs, such as catalyst, carbon source and substrate.

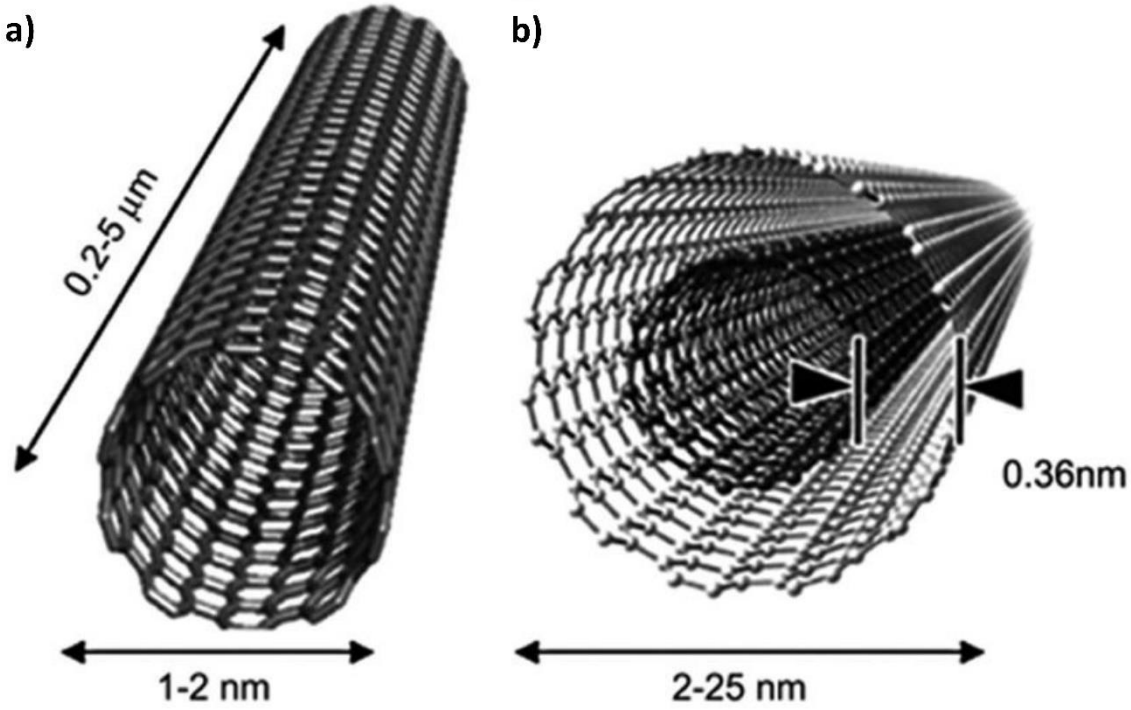

Figure 1.16 *a) Single-walled nanotubes (SWCNT) and b) Multi-walled nanotubes (MWCNT), taken from [199].*

1.3.6.5.1.2 Carbon nanofibers (CNF)

Carbon nanofibers (CNF) are tubular structures very similar to CNTs, with the main difference that they do not contain a hollow core. The unit structures of CNFs and CNTs show a hexagonal carbon arrangement similar to the structure of graphite [200]. CNFs are classified into three main types depending on the nature and shape of the catalyst, and the orientation of the graphene layers relative to the central axis

of the fibers (Figure 1.17) [201-203]. The different categories are fishbone, platelet, and ribbon type [204]. In fishbone CNFs, graphene sheets form cones with apical angles between 0 and 90° with respect to the filament growth direction. The growth of this type of structure is still not clear, but it is believed that the diffusion of C under different concentrations can result in the deformation of the catalyst and, consequently, the cone angle of the fishbone CNFs [205]. In platelet-type CNFs, the graphene layers are placed perpendicular to the central axis of the fiber. Finally, in ribbon or tubular CNFs, the graphene layers are arranged parallel to the growth axis [204].

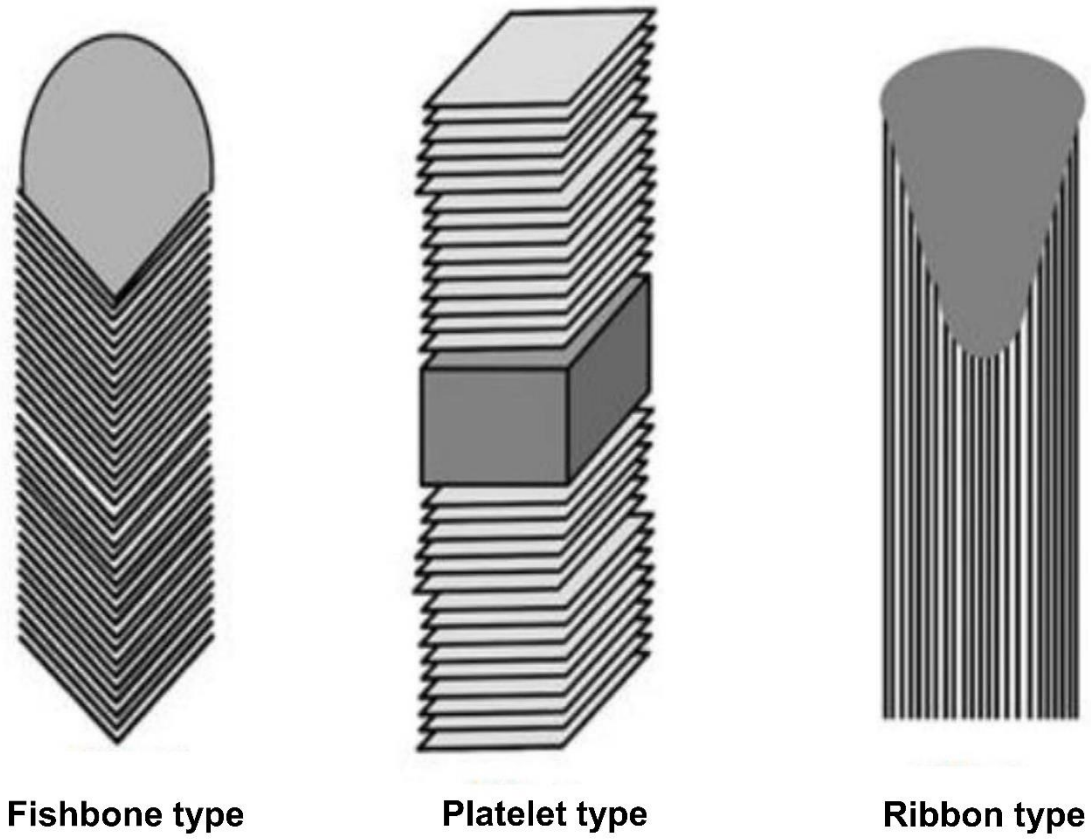

Figure 1.17 *Types of CNF, taken from [201].*

Although CNTs and CNFs could be considered to be very similar, the diameter of CNTs is usually lower (0.6-50 nm) compared to that of CNFs (50-200 nm), which makes their mechanical, electrical and thermals differ. Furthermore, their surface composition is different since in CNFs the graphene layers are inclined with respect to the axis of the fiber, which gives them higher reactivity trough their edge sites exposed [200].

1.3.6.5.1.3 Growth of carbon nanotubes and nanofibers

The most commonly used method to grow carbon tubular structures (CTS), i.e. CNT or CNF, is chemical vapor deposition (CVD), which comprises 3 key factors: support, catalyst and carbon source or precursor [206].

Precursor. Through the proper selection of the carbon precursor and its vapor pressure, the catalyst lifetime and the CTS growth rate can be significantly increased, resulting in improved CTS performance and quality [207,208]. Within the large number of precursors that exist, these can be divided into linear or cyclic, where the most used precursors are methane [208,209], ethylene [210,211], acetylene [212], benzene [213], xylene [214] and carbon monoxide [215] (Figure 1.18). The molecular structure of the precursor has an important effect on the morphology of CTS. Linear hydrocarbons like methane, ethylene, acetylene thermally decompose into atomic carbons or linear carbon dimers/trimers and generally produce straight, hollow CTS. On the other hand, cyclic hydrocarbons such as benzene, xylene, cyclohexane, fullerene produce relatively curved CTS with the tube walls joined together on the inside [216,217]. Linear precursors, such as acetylene, are more effective at low

temperatures, since at higher temperatures they are unstable and lead to the deposition of large amounts of carbonaceous compounds [218].

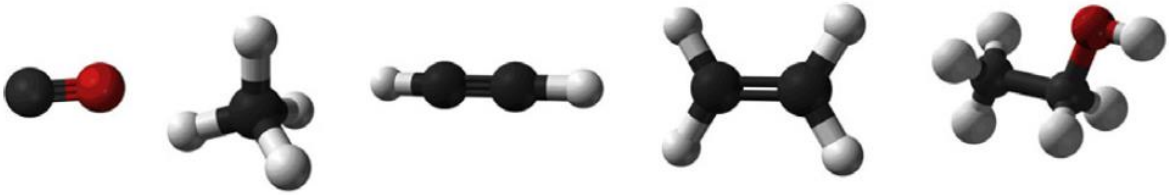

Figure 1.18 *Common carbon precursors in CTS growth by CVD: carbon monoxide, methane, acetylene, ethylene, and ethanol from left to right (black: carbon, red: oxygen, grey: hydrogen [208].*

Support. The support is another parameter of great relevance in the growth of CTS through CVD, this is because the same catalyst can function differently on different materials [211]. Supports commonly used in CVD process are graphite [219], quartz [220], silicon [198], silica [221], alumina [222], aluminosilicate (zeolite) [223], magnesium oxide [224] and more recently carbonized biomass [225,226]. For efficient CTS growth, there must be a good metal-support interaction that allows good metal dispersion and, therefore, a high density of catalytic sites [227]. These interactions prevent metal species aggregating and forming of large unwanted clusters which leads to the formation of graphite, amorphous carbon or turbostratic particles [228]. Therefore, the chemical properties, surface morphology and texture properties of the support affect the performance and quality of CTS [210,211].

Catalyst. Typically, nanometer-sized metal particles are required to allow hydrocarbons decomposition at a lower temperature than the spontaneous decomposition of this. It is a widespread consideration that the catalyst particles size dictates the diameter of the structure [217]. Small particles (1–2 nm) have steep sharp edges (atomic steps); Therefore, they have high catalytic activity and can form

SWCNT. With increasing particle size (5–20 nm), the sharpness of the atomic steps at the boundary decreases and so does its catalytic activity, forming MWCNT or CNF. Clusters that are too big (>100 nm) acquire an almost spherical boundary without sharp steps, so it is not common for them to form CNTs but CNFs can still form [229,230]. Therefore, size-controlled metal nanoparticles, pre-synthesized by other reliable techniques, can be used to grow CTS of controlled diameter [231].

The most commonly used metals as catalysts for CTS growth are Fe, Co, Ni, due to two main reasons: (i) high solubility of carbon at high temperatures; and (ii) high carbon diffusion rate [211]. Also, the high melting point and low vapor pressure of these metals offer a wide CVD temperature window for working with a wide range of carbon precursors. Moreover, these catalysts exhibit strong adhesion to growing CTS compared to other transition metals and are therefore more efficient in CTS formation [209,232]. In general, the solubility or surface diffusion of carbon in metal particles has been described as follows: At first, a cap of graphene forms that floats on the metal, while the atoms at the edge of the cap remain anchored to the metal. Subsequently, more C atoms bond to the edge atoms pushing the cap upwards and thus forming a cylindrical wall (Figure 1.19) [229,230].

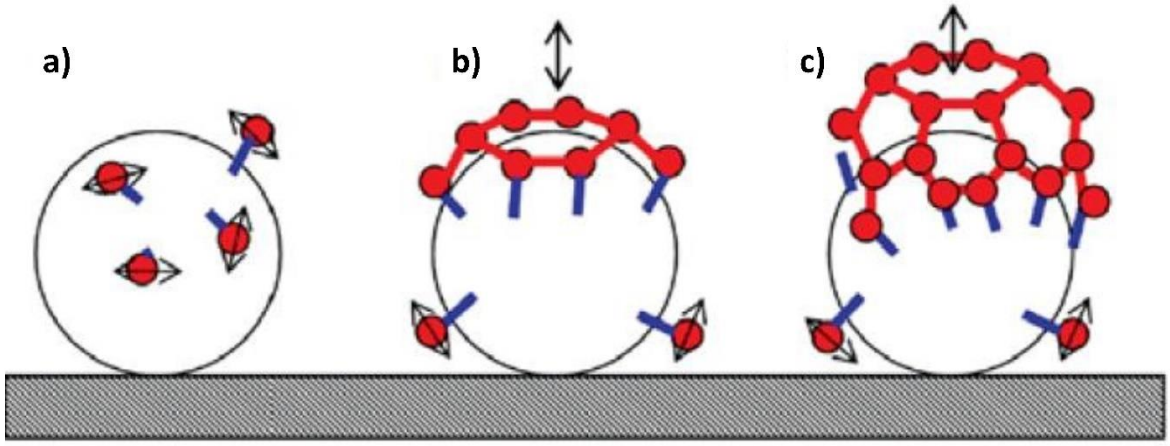

Figure 1.19 *Schematic representation of the basic steps of SWCNT growth on an Fe catalyst, as observed in ab initio simulations. a) Diffusion of individual C atoms (red spheres) on the catalyst surface. b) Formation of a sp^2 graphene sheet floating on the catalyst surface with edge atoms covalently bonded to the metal. c) Root incorporation of individual C atoms (or dimers) in diffusion, taken from [229].*

1.3.6.5.2 Impregnation with liquid sorbents

Impregnation with liquid absorbents, such as animas or ionic liquids, is a strategy to further improve the adsorption properties of solid adsorbents. Through the impregnation of the liquid absorbent in the pores of solid materials, it is sought to improve the capacity and CO_2 selectivity of these composite materials, even at low partial pressures of CO_2, which makes them suitable for direct capture of CO_2 in the air [233]. The principle for improving CO_2 capture by impregnation with liquid sorbents is the increase in the interaction of CO_2, of acidic nature, with the active sites of the amine or IL, which are usually of basic nature [48]. Furthermore, by impregnating liquid absorbents into porous solids, the stability, recyclability, and CO_2 capture kinetics of these materials have been improved. Among the most used liquid absorbents to impregnate porous solids are amines, such as polyethyleneimine (PEI), diethanolamine (DEA) and tetraethylenepentamine (TEPA), and ILs formed by cations based on the imidazolium ring [80-82, 234].

1.4 State of the art

Impregnation with liquid absorbents (amines and IL) has been studied more widely [77,79,84,85,185], unlike modification with nanostructures, where most of the works have focused on the modification of nanostructures [186-188,194] but not on their addition to porous solid materials, mainly due to their relative difficulty to grown them on non-homogeneous surfaces such as carbons materials. Table 1.7 compiles some of the works related to CO_2 capture at different pressure and temperature conditions**.**

Table 1.7 *Comparative CO_2 adsorption capacities of different carbon materials, ionic liquids, amines, and composites.*

Material	**Specific surface area (m^2/g)**	**Adsorption conditions**	**Capture capacity (mmol/g)**	**Selectivity**	**Heat of adsorption (kJ/mol)**	**Ref.**
Meso-carbon	789	25 °C	1.50	-	-	[234]
SWCNT	1587	35 °C	4.02	-	-	[234]
MWCNT	407	35 °C	1.73	-	-	[234]
Graphene	1550	-78 °C	7.95	-	-	[234]
Rotten strawberries AC N-doping	1117	25 °C, 1 bar	4.49	16 (CO_2/N_2 10/90)	-	[235]

Material	Specific surface area (m^2/g)	Adsorption conditions	Capture capacity (mmol/g)	Selectivity	Heat of adsorption (kJ/mol)	Ref.
Carrot peel AC	1379	25 °C, 1 bar	4.18	8 (CO_2/N_2 15/85)	-	[236]
Pineapple waste AC N-doping	1076	25 °C 1 bar	4.25	18 (CO_2/N_2 10/90)	-	[237]
Coconut shell AC N-doping	1535	25 °C, 1 bar	4.80	15 (CO_2/N_2 10/90)		[238]
Data seeds AC	798	25 °C, 1 bar	10.8	-	13.15	[125]
Olive stones biochar	629	25 °C, 1 bar	1.98	36 (CO_2/N_2 10/90)	31.5	[239]
Almond shell biochar	511	25°C, 1 bar	2	47(CO_2/N_2 10/90)	32.2	[239]
Peanut shell AC	1713	25 °C, 1 bar	4.41	7.9	24-25	[240]
Rice husk AC/chitosan composite	1496	25 °C, 1 bar	3.68	20 (CO_2/N_2 15/85)	30.2	[242]
Rice husk AC	1475	25 °C, 1 bar	2	3.4 (CO_2/N_2 15/85)	14.4	[242]

Material	Specific surface area (m^2/g)	Adsorption conditions	Capture capacity (mmol/g)	Selectivity	Heat of adsorption (kJ/mol)	Ref.
MWCNT /TEPA	-	70°C, 1 bar (10% CO_2/90% N_2)	3.09	-	-	[243]
MWCNT /TEPA	-	25 °C, 1 bar (2% CO_2/98% N_2)	2.97	-	-	[244]
MOF-808-TEPA	475	25 °C, 1 bar	1.3	256 (CO_2/N_2 15/85)	46	[245]
Wood ash/TEPA	0.7	60 °C,1 bar (5% CO_2/ 5% H_2O y 90% N_2)	2.02	-	-	[246]
ADS-17/TEPA	26	25-70 °C, 1 bar (35% CO_2/ 65% CH_4)	5.7 at 60 min	14.1 (CO_2/CH_4 35/65)	-	[247]
MgO/TEPA	19	30 °C, 1 bar (40% CO_2/ 60% CH_4)	4.98	-	-	[248]
Agave bagasse fibers (ABF) biochar	75	25 °C, 1 bar	1.26-1.42 at 50 min	-	-	[185, 249]
ABF biochar/ [BMIM][Ac]	2	25 °C, 1 bar	1.29-1.47 at 30-50 min	-	-	[185, 249]
[BMIM][Ac]	-	30 °C, 1 bar	1.7 at 20 hrs	-	-	[85]
MCM-4/[BMIM][Ac]	1	25 °C, 1 bar	1.18 at 30 min	-	40	[250]

Material	Specific surface area (m^2/g)	Adsorption conditions	Capture capacity (mmol/g)	Selectivity	Heat of adsorption (kJ/mol)	Ref.
SBA-15/[BMIM][Ac]	7	30 °C, 1 bar	0.89 at 30 min	-	70	[250]
Porous material/[BMIM][Ac]	-	30 °C, 1 bar	3.88 at 90 min	-	-	[251]
MOF/[BMIM][Ac]	-	30 °C, 1 bar	1.15 at 60 min	-	-	[252]

1.5 Motivation of this investigation

The increase in greenhouse gases in the environment, such as CO_2, has led to the development of new materials that can remove this gas from the environment. Currently, liquid adsorbents, such as liquid amines and ionic liquids, are of great interest due to their great CO_2 capture capacity and selectivity. However, liquid amines have disadvantages like low thermal stability. On the other hand, ionic liquids have slow capture kinetics due to their high viscosity (66-1100 cP). In this way, using a support material with a high specific surface area, where liquid absorbents can be dispersed, is a viable option to solve these disadvantages. Therefore, in this research project it was proposed to synthesize carbon tubular nanostructures (CTS), such as CNTs and CNFs, in the macropores of carbonized bagasse fibers (CBF) to generate a carbon composite (CC) with high specific surface area available. Moreover, ionic liquid (IL) 1-butyl-3-methylimidazole acetate or liquid amine (LA) TEPA (Figure 20) was impregnated on the carbon-based composite, and then the capacity and kinetics of CO_2 sorption-desorption were evaluated. In addition, we

sought to elucidate the interactions between carbon materials and IL/TEPA, as well as the CO_2 capture mechanism. Finally, it should be noted that until now no studies have been carried out on CO_2 capture by using a composite such as the one proposed in this study.

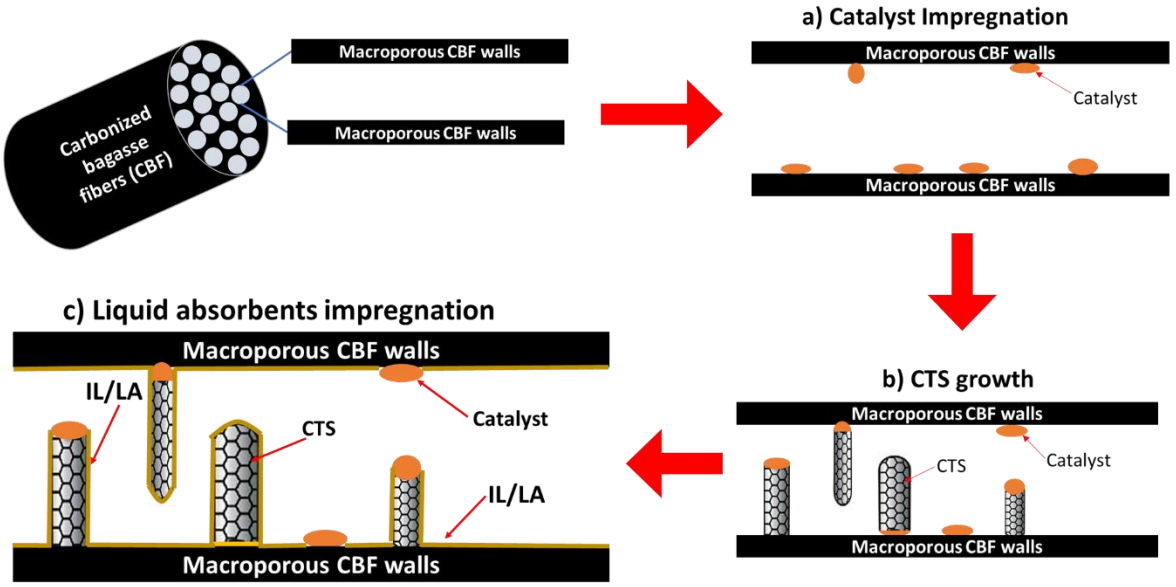

Figure 1.20 *Scheme of the CBF modification process: a) catalyst impregnation, b) CTS growth, and c) Impregnation of the modified material with liquid absorbents.*

1.6 Hypothesis

By modifying the macroporous channels of carbonized bagasse fibers (CBF) through growing carbon tubular nanostructures (CTS), such as carbon nanotubes (CNT) or carbon nanofibers (CNF), their exposed specific surface area will increase and with this, more liquid absorbents [BMIM][Ac] and TEPA can be impregnated. This will result in an increase in the mass transfer of CO_2 towards the liquid absorbent, allowing to improve the kinetics and CO_2 sorption-desorption capacity.

1.7 Objectives

1.7.1 General objective

To synthesize CTS on the macroporous channels of the carbonized bagasse fibers to increase their specific surface area and to impregnate it with liquid sorbents ([BMIM][Ac] and TEPA) to improve their CO_2 kinetics and sorption-desorption capacity.

1.7.2 Specific objectives

Establish the optimal synthesis conditions for the CNT/CNF growth by CVD using CBF as a support matrix to obtain a material with high specific surface area, where liquid absorbents can be impregnated.

Study the physicochemical properties of CBF, CNT/CNF modified CBF and CNT/CNF modified CBF impregnated with liquid absorbents through nitrogen physisorption, surface charge distribution, ash content, functional groups, crystalline phases, and scanning electron microscopy.

Determine the CO_2 capture and desorption capacity of CBF, CNT/CNF modified CBF and CNT/CNF modified CBF impregnated with liquid absorbents at different temperature, pressure, and CO_2 concentration.

Elucidate the CO_2 capture mechanism in CBF and liquid absorbents, as well as the effect of CTS on CO_2 capture.

Chapter 2:

CO_2 capture capacity and kinetics of TEPA-impregnated macroporous biochar

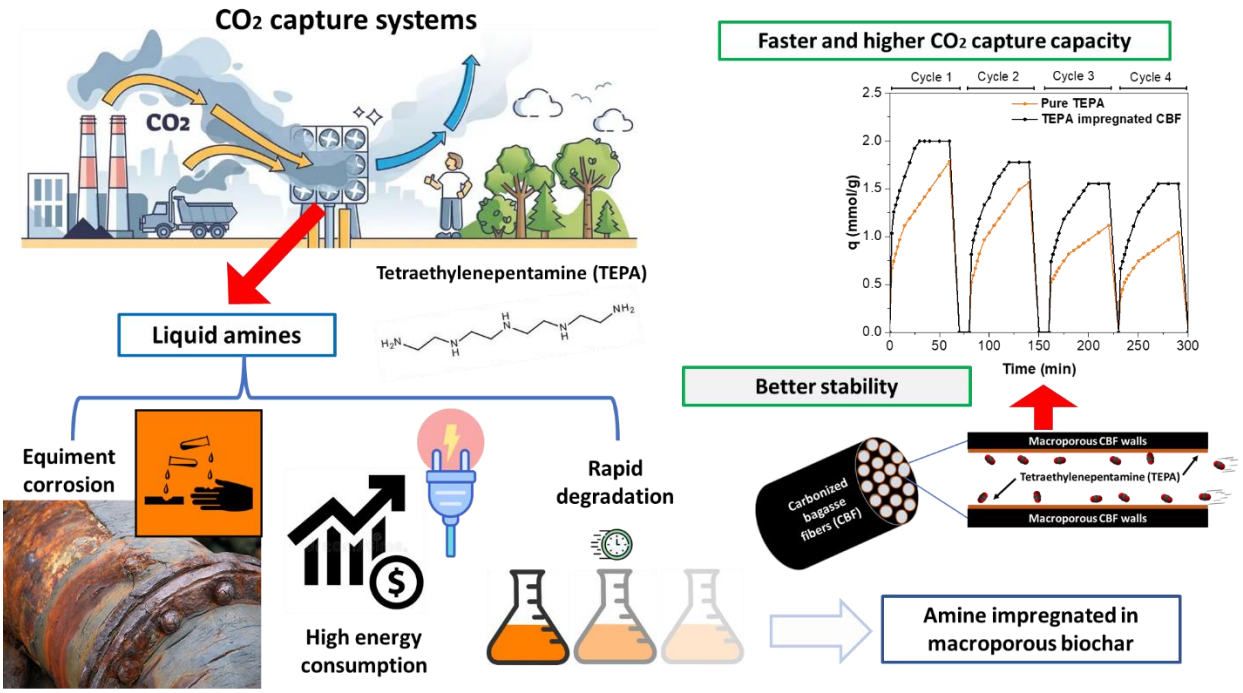

ABSTRACT

The increasing CO_2 emissions have led to search strategies to reduce its concentration and emission into the atmosphere. The CO_2 capture by liquid amines is one of the most used methods. However, its high energy consumption and corrosive effect are important limitations. Therefore, in this research, a new hybrid material consisting of carbonized agave bagasse fibers (CBF) impregnated with the liquid amine tetraethylenepentamine (TEPA) was synthesized to improve its CO_2 capture capacity and regeneration. The materials were characterized by scanning electron microscopy (SEM), thermogravimetric analysis (TGA) and Fourier transform infrared spectroscopy (FTIR). In addition, the CO_2 capture capacity was evaluated in static mode at different pressures (1-10 bar) and sorption-desorption cycles were conducted at 10 bar for pure TEPA, CBF and CBF impregnated with 5, 10, 25 and 50 wt.% of TEPA. The samples with the lowest degree of impregnation (5 and 10 wt.%) showed the best performance in CO_2 capture capacity and CBF-TEPA5% presented the shortest time to reach equilibrium (30 min) for all the pressures tested. The CO_2 capture capacity improved from 0.21 to 0.28 mmol/g and from 1.3 to 1.99 mmol/g at 1 and 10 bar, respectively. Finally, regeneration capacities of 88.9, 77.8 and 77.8% for CBF-TEPA5% were achieved for the 2nd, 3rd and 4th cycle, which represents an improvement of up to 15.3% with respect to the regeneration capacity of pure TEPA. The considerable improvement in CO_2 capture capacity, kinetics, and regeneration capacity of TEPA-impregnated CBFs demonstrated the feasibility of using carbon derived materials from an agro-industrial waste in CO_2 capture systems.

2.1 Introduction

The increase in the concentration of greenhouse gases has caused a significant increase in the earth's temperature, which has caused significant environmental problems [4.6]. Carbon dioxide (CO_2) is considered the main greenhouse gas, which has increased its concentration drastically in the atmosphere in recent years, reaching more than 400 ppm [5,6]. The growing attention to the problems caused by global warming has led to the search of different strategies to reduce emissions and concentration of CO_2 in the atmosphere, including CO_2 capture [253]. The CO_2 capture through liquid amines is the most used method at an industrial level due to its rapid absorption, excellent capture capacity and low cost [58,60]. Specifically, tetraethylenepentamine (TEPA) has shown excellent performance in CO_2 capture due to the high density of amine groups and relatively low viscosity, compared to other liquid absorbents [64,65]. However, these materials have some disadvantages such as rapid degradation, equipment corrosion, and high energy consumption for regeneration [61,62]. One of the proposals to overcome these deficiencies is to impregnate liquid amines in porous materials [64,80,233,254]. In our work group, bagasse waste from the tequila and mezcal industry has been carbonized resulting in a carbon with macroporous channels that go from end to end of the structure. Carbonized bagasse fibers (CBF) have shown moderate CO_2 capture capacity and fast kinetics [185,249]. Therefore, in this work it is proposed to impregnate carbonized bagasse fibers with tetraethylenepentamine amine (TEPA) to improve the CO_2 capture capacity of the material, as well as its stability during sorption-desorption cycles.

2.2 Experimental Section

2.2.1 Reagents and precursor

The *Agave salmiana* bagasse fibers come from the waste of a mezcalera located in the state of San Luis Potosí, Mexico. Furthermore, all chemical reagents used were purchased from Sigma Aldrich.

2.2.2 Carbonization of bagasse fibers

The agave bagasse was rinsed with deionized water, dried at 90 °C for 48 h and then fractionated to ~0.5 cm. The agave fibers were carbonized in a Barnstead Thermolyne 21100 model tubular furnace under an inert atmosphere of N_2 at a temperature of 600 °C for 2 h, this sample was named carbonized bagasse fibers (CBF).

2.2.3 Tetraethylenepentamine impregnation onto CBF

First, 4 mL of ethanol was mixed with the corresponding mass of TEPA to obtain an impregnation ratio of 1:0.05 to 1:0.5 and vortexed for 2 min at 1500 rpm. Subsequently, the ethanol/TEPA mixture was stirred using a magnetic bar at 700 rpm for 5 min at 80 °C and then 50 mg of CBF were added: stirring was maintained for 1 h. Subsequently, the samples were stirred at 90 rpm on an orbital incubator at 25 ^{o}C for 24 h. Finally, the solvent was removed by evaporation at 80 °C for 24 h and the material was stored in a N_2 atmosphere. The samples were named as CBF-TEPAx, where x is the percentage of the mass ratio of TEPA used (5-50%).

2.2.4 Physicochemical characterization of impregnated carbons

The morphology of the samples was analyzed by using a HELIOS NANOLAB 600i scanning electron microscope (SEM) with high-resolution field emission source, secondary electron detector, and backscattered electron detector. Before analysis, samples were immobilized on a carbon tape retained in an SEM sample holder. The degree of TEPA impregnation was determined in a thermogravimetric analyzer (SETSYS Evolution TGA-DTA/DSC, SETARAM Instrumentation) by using a heating ramp of 10 °C/min from 25 to 700 °C in an N_2 atmosphere and atmospheric pressure. Furthermore, the degree of impregnation of the CBF was estimated from the percentage of mass loss in a range of 140 to 400 °C for the TEPA amine, based on the resulting thermogravimetric curve of the pure TEPA. For the identification of functional groups in the materials impregnated with TEPA, FTIR analyses were conducted in a Nicolet 1S50 FTIR equipment from Thermo Scientific in the spectral range of 500 to 4000 cm^{-1}, in attenuated total reflectance (ATR) mode with 64 scans of a resolution of 4 cm^{-1}.

2.2.5 CO_2 capture experiments

The kinetics and CO_2 capture capacity experiments at room temperature and different pressures were carried out in a 25 ml high-pressure reactor (4704, Parr Instrument), adapted with a digital manometer (ASHCROFT DG25). The reactors configuration is shown in Figure 2.1 and the applied methodology was previously reported by our research group [249]. In short, for the CO_2 capture experiments, it began with the opening and closing of the inlet valve until the established initial pressure was reached. Subsequently, the pressure change was recorded until $P_i=P_e$

or ΔP=0, for 60 min. At the end of this stage, the equipment was depressurized, and the CO_2 capture kinetics end. For the capture cycles, the reactor containing the saturated sample was heated up to 80 °C for 10 min after depressurization of the equipment and allowed to cool down to room temperature to repeat the CO_2 capture process.

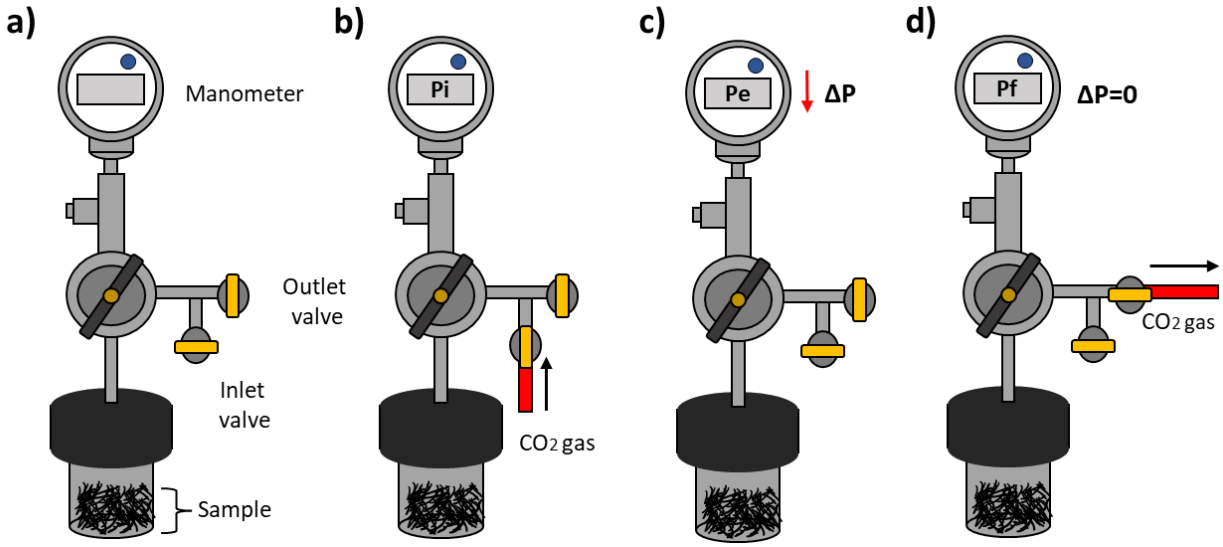

Figure 2.1 *a) 25 ml high pressure reactor 4704, Parr Instrument, adapted with an ASHCROFT DG25 digital pressure gauge, b) beginning of the CO_2 capture process: opening and closing of the inlet valve, c) CO_2 capture process until initial pressure (P_i) and equilibrium pressure (P_e) are equal or ΔP=0, for 60 min, and d) equilibrium and depressurization stage of the system.*

CO_2 capture kinetics were carried out at 1, 3, 5, 8 and 10 bar on the impregnated materials with TEPA and CBF. A mass of 0.1 g was used, where the amount of gas captured was attributed to the pressure change during the CO_2 capture experiments. To calculate the CO_2 capture capacity, the ideal gas law was employed, taking into account the compressibility constant of CO_2 (ζ_{CO_2}).

$$q_{CO_2} = \frac{(V)(\Delta P)}{(\zeta_{CO_2})(R)(T)(m_0)} \qquad \textit{(Equation 2.1)}$$

Where, q_{CO_2} is the CO_2 capture capacity (mmol of CO_2/ g of material), P is the difference between the initial pressure and the equilibrium pressure (bar), R is the ideal gas constant (0.083 L bar/ K mol), V is the volume of equipment (mL), T is the temperature (K) and ζ_{CO_2} is the compressibility constant.

2.3 Results and Discussion

2.3.1 Characterization of the carbonized bagasse fibers (CBF)

The morphological analysis of the CBF was carried out by scanning electron microscopy (SEM). Figure 2.2 a) shows the tip of a carbonized fiber, where the characteristic macropores with a size of 2 to 30 µm can be observed, as previously reported by our working group [184]. Furthermore, Figure 2.2 b) and c) show the rough surface formed with channels parallel to the fiber and inorganic particles of calcium and sodium (identified by EDS), typical of bagasse.

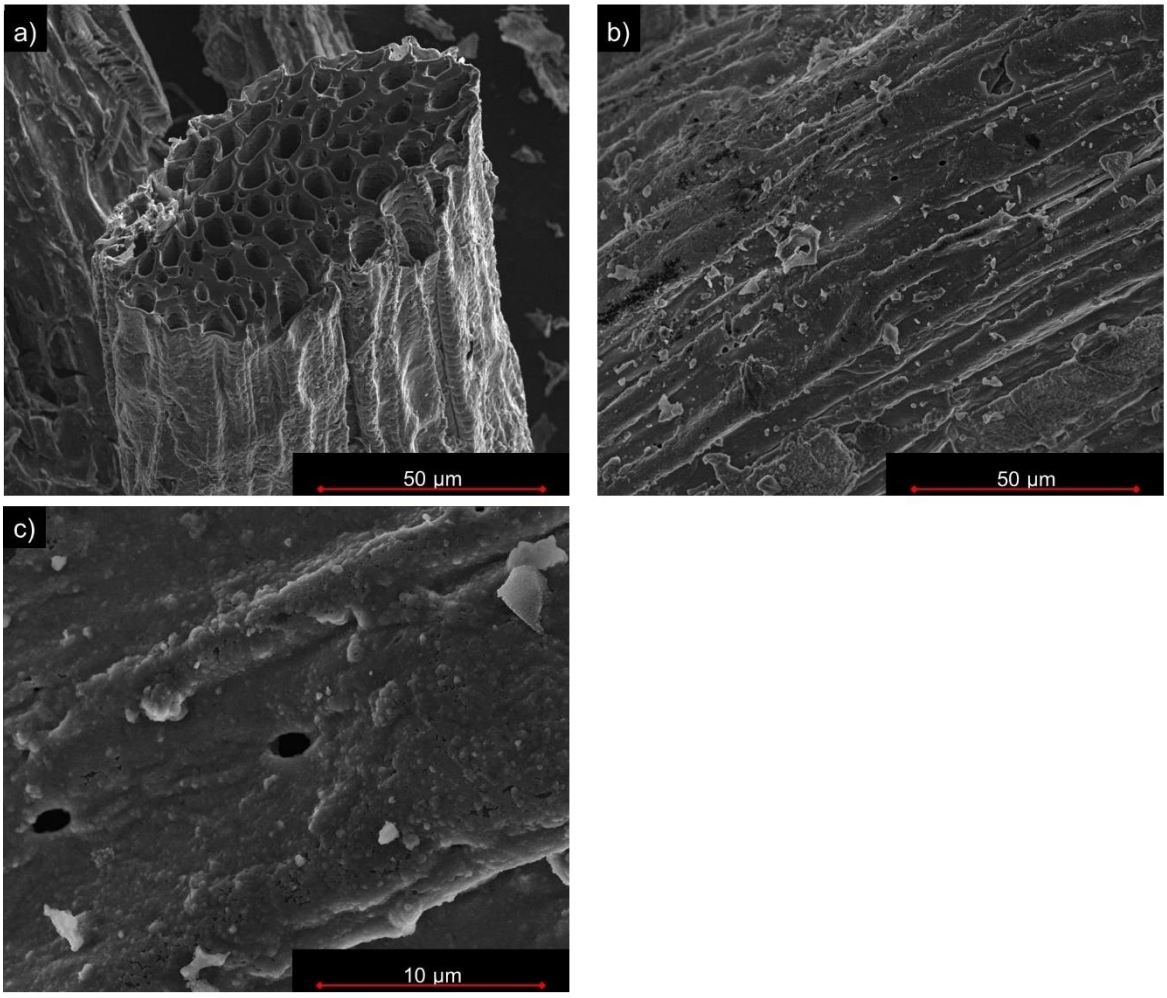

Figure 2.2 *SEM secondary electrons images of a) CBF tip, b) and c) CBF surface.*

2.3.2 Characterization of CBF impregnated with TEPA

Figure 2.3 shows the SEM images corresponding to the CBF impregnated with TEPA. Sample CBF-TEPA5% (Figure 2.3 a) and b)) did not show significant change in the surface with respect to the pristine CBF, only a slight change in the roughness of the fibers attributed to the low amount of TEPA impregnated. For CBF-TEPA10% (Figure 2.3 c) and d)) and CBF-TEPA25% (Figure 2.3 e) and f)), the material channels were less noticeable, and some clusters attributed to TEPA were identified. Finally, for CBF-TEPA50% (Figure 2.3 g) and h)) the surface roughness of the pristine material was practically imperceptible, and a dense coverage and clusters

of TEPA can be seen on the surface of the material. From these results, we can say that the TEPA impregnation on CBF was carried out homogeneously at low concentrations.

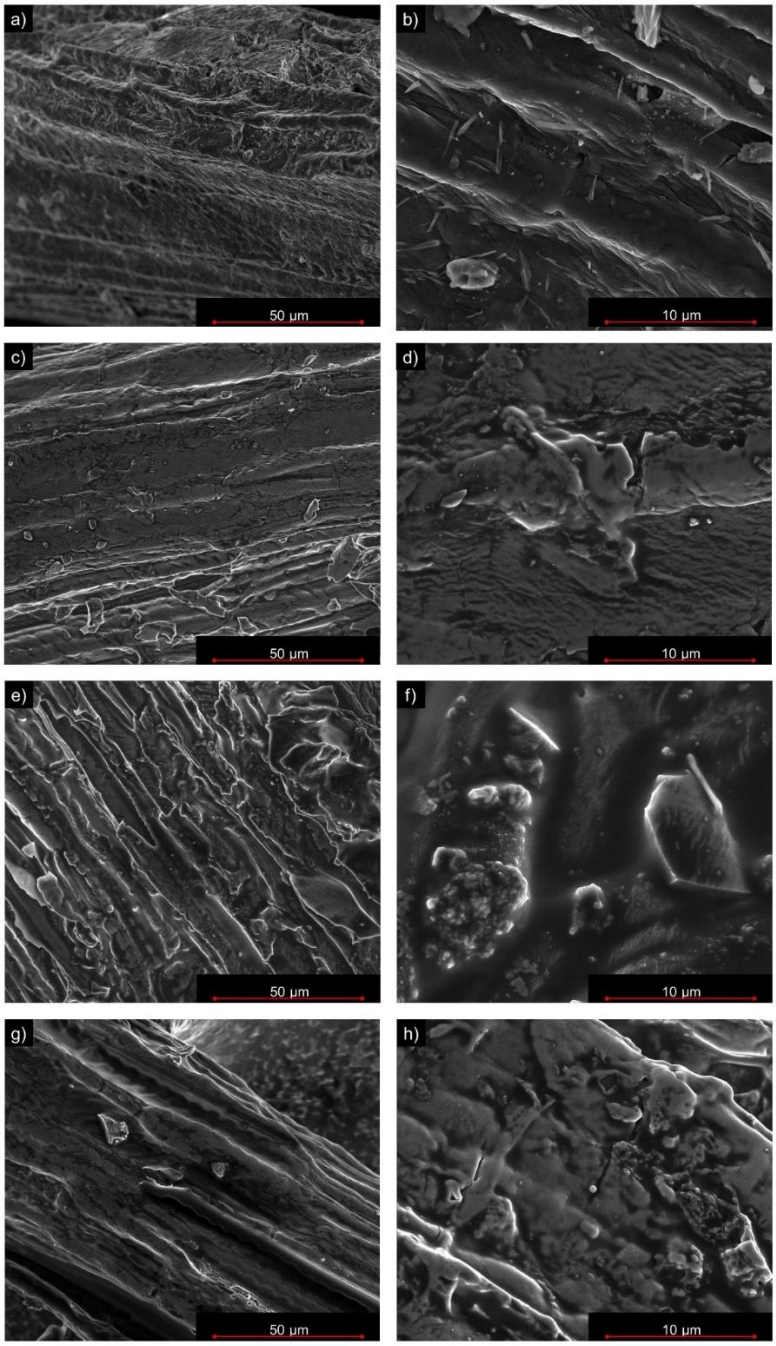

Figure 2.3 *SEM secondary electrons images of a) and b) CBF-TEPA5%, c) and d) CBF-TEPA10%, e) and f) CBF-TEPA25%, g) and h) CBF-TEPA50%.*

Through FTIR, the functional groups related to the TEPA impregnated on the CBF were identified (Figure 2.4). From the pristine material (CBF), bands were identified between 600 and 950 cm^{-1} corresponding to -OH and =CH stretching of phenolic groups, bands between 1000 and 1300 cm^{-1} corresponding to C-O and C-OH vibrations of phenolic structure groups and bands between 1550 and 1750 cm^{-1} corresponding to C=C vibrations of the aromatic ring [255,256]. What corresponds to the TEPA, it was identified with the main bands between 3350-3200 and 1320 cm^{-1} attributed to N-H vibrations, and bands between 2950 and 2800 cm^{-1} were attributed to C-H vibrations. Signals of NH_2- related to asymmetric and symmetric bending vibration were also identified between 1550 and 1450 cm^{-1} and at 1125 cm^{-1} CN- vibrations [257,258]. Furthermore, in the materials impregnated with TEPA, the appearance of a new band around 1650 cm^{-1} was observed, which corresponds to N-H bending vibrations, which has been attributed to the good impregnation of TEPA on some materials [259,260]. Finally, it can be observed that as the concentration of TEPA increased on the support, its signal became more assimilated to those of TEPA and the bands related to the support became less evident, which indicates a good distribution of the TEPA on CBF [254,261].

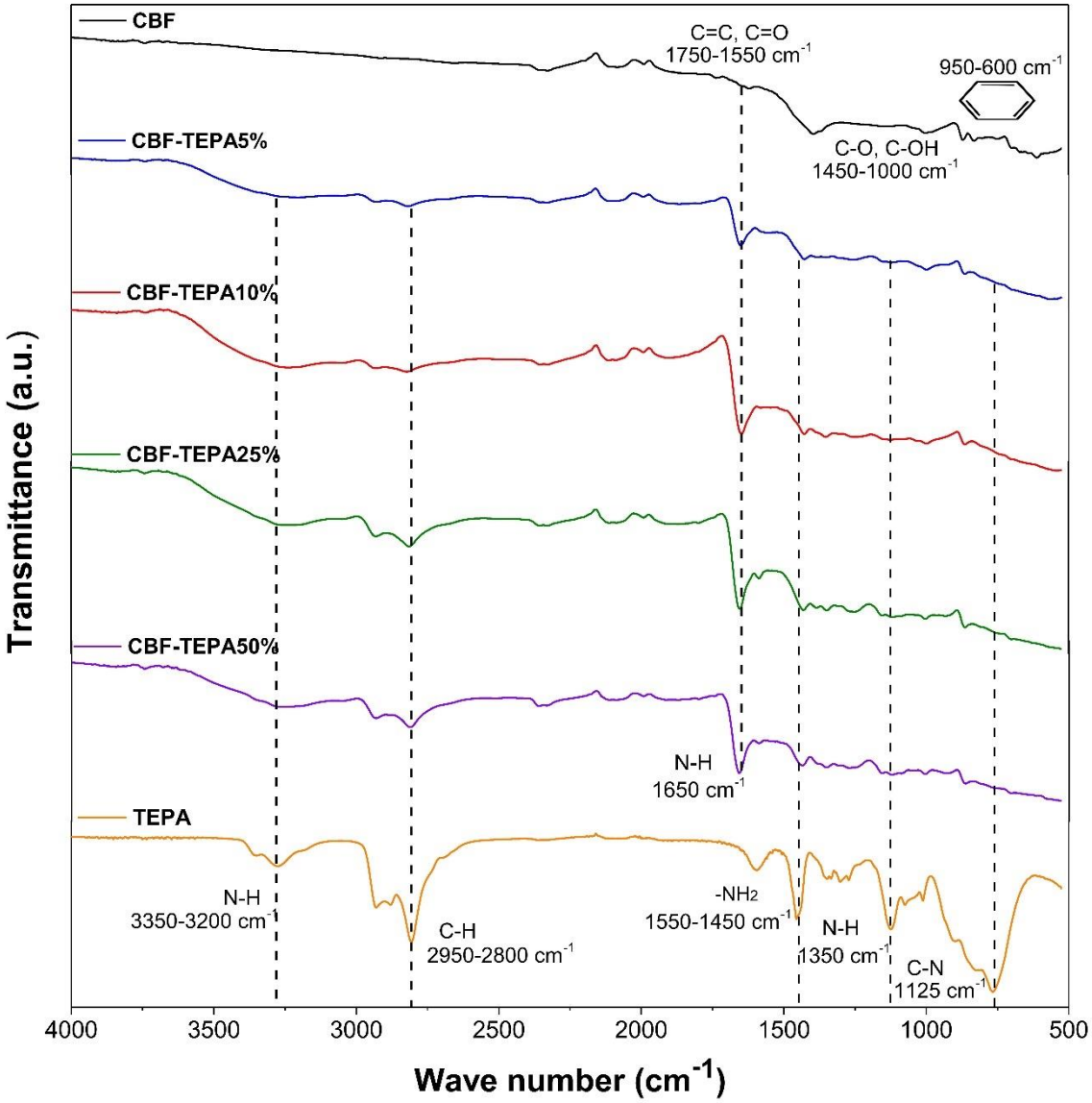

Figure 2.4 *FTIR spectra of CBF, pure TEPA and CBF impregnated with different TEPA mass ratios.*

2.3.2.1 Thermal stability and impregnation level

Thermal stability tests were carried out on CBF and TEPA, as seen in Figure 2.5. The CBF showed a mass loss of 7.21% below 140 °C mainly attributed to adsorbed moisture. Furthermore, there was a mass loss of 2.96% up to 400°C and from there the mass loss increased as the temperature increased, until reaching a total loss of

37% at 700°C. This indicate that CBFs have good thermal stability up to 400 °C, where phenol, carbonyl and quinone groups begin to volatilize and subsequently gasify graphitic sheets [262,263]. For TEPA, there was a mass loss below 140 °C of 3.57% attributed to moisture. Furthermore, after 140 °C it began to degrade, presenting the highest mass loss around 230 °C until obtaining a residual mass of 8.19 % at 400 °C. These results were used to calculate the degree of impregnation in the CBF.

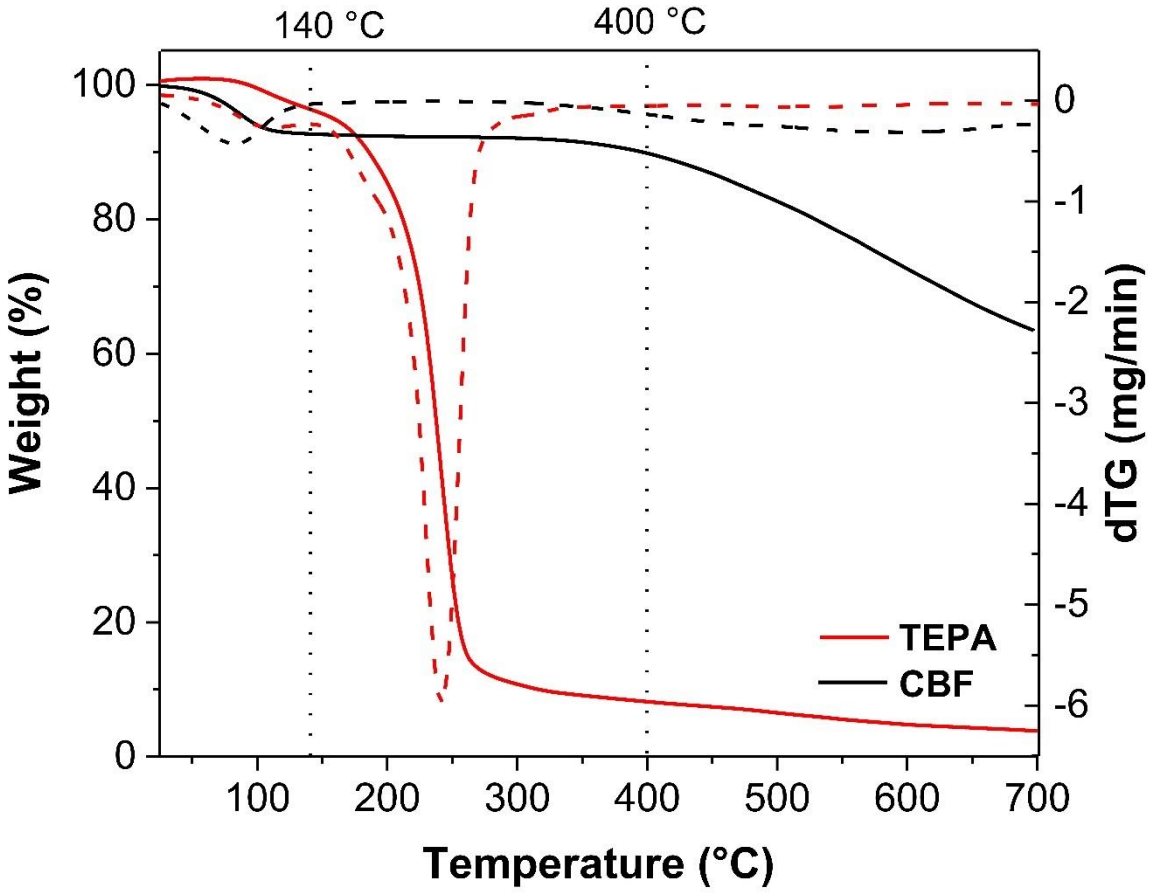

Figure 2.5 *Non-isothermal thermogravimetric analysis under N_2 atmosphere at a heating rate of 10 °C/min until 700 °C, thermogravimetric (solid line) and differential thermogravimetric (dTG, dashed line) curves of CBF (black) and TEPA (red).*

For TEPA impregnations on the CBF, different mass ratios were tested, from 5% to 50%, and Figure 2.6 shows the thermogravimetric curves of the impregnated materials. For all samples, a mass loss was found between 25-140 °C attributed to moisture of CBF and TEPA. Regarding the amount of TEPA impregnated, the data were condensed in Table 2.1, where it can be seen that for the lowest TEPA ratios (5, 10 and 25%) the impregnation was carried out adequately. For CBF-TEPA50% the amount of TEPA impregnated was less than expected, which coincides with what was observed in the SEM micrographs, where a homogeneous impregnation was not observed on the surface of the CBF.

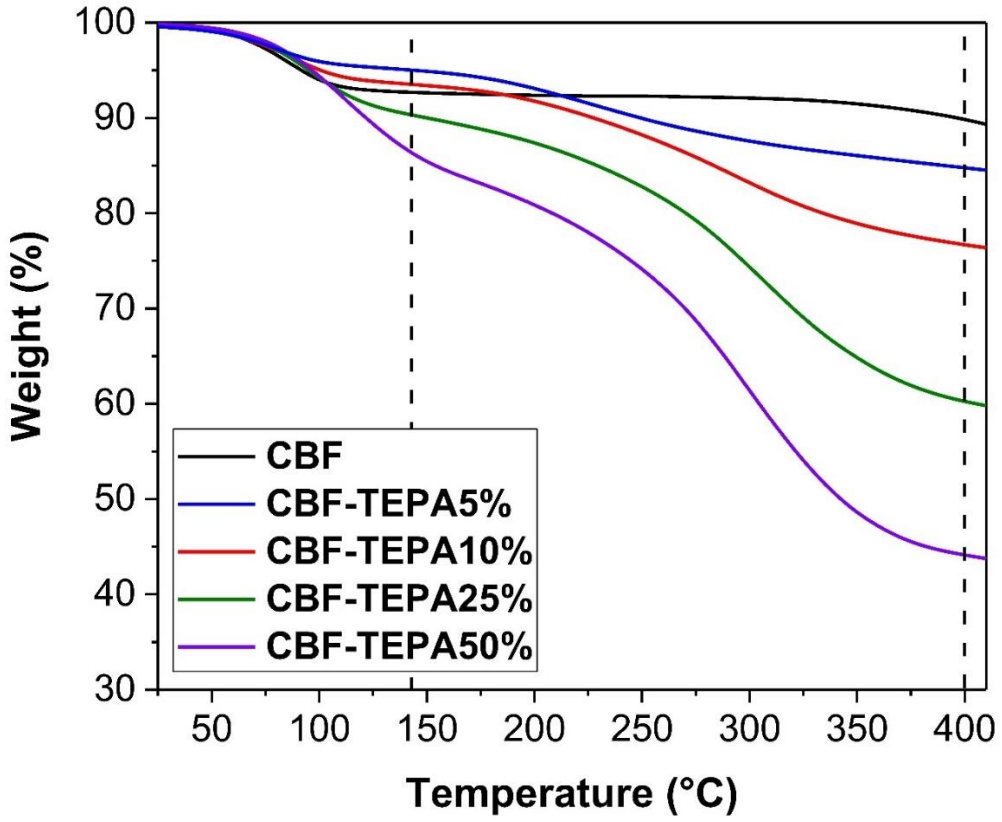

Figure 2.6 *Non-isothermal thermogravimetric analysis under N_2 atmosphere at a heating rate of 10 °C/min until 400 °C, thermogravimetric curves of CBF impregnated with different TEPA mass ratio.*

Table 2.1 *TEPA and moisture concentration in impregnated CBF calculated from TGA analysis.*

Samples	Moisture (%)*	TEPA content (%)+	
		Calculated from mass ratio	Measured in TGA
CBF	7.21	-	-
CBF-TEPA5%	4.94	5	3.09
CBF-TEPA10%	6.43	10	9.67
CBF-TEPA25%	9.56	25	22.98
CBF-TEPA50%	13.17	50	35.44

*** mass loss up to 140 °C**
+ mass loss from 140 to 400 °C

2.3.3 CO_2 capture experiments

Figure 8 shows the CO_2 capture kinetics of CBF, TEPA and the CBF impregnated with TEPA with different mass ratios at 1, 3, 5, 8 and 10 bar. The CO_2 capture capacities, the kinetics and capture rate were condensed in Table 2.2. It was observed that the CO_2 capture capacity improved for all impregnated CBF, except for CBF-TEPA50%. Also, it was found that as the amount of TEPA was lower, the CO_2 capture capacity was improved for all pressures tested, which indicated that low concentrations of impregnated TEPA results in a better CO_2 capture capacity. The CBF-TEPA5% sample showed CO_2 capture capacities of 0.28, 0.57, 0.86, 1.56 and 1.99 mmol/g at 1, 3, 5, 8 and 10 bar, respectively. This represents an improvement of around 35% at 1, 3 and 5 bar, and approximately 55% at 8 and 10 bar compared to the pristine material. Furthermore, the CO_2 capture capacity of CBF-TEPA5% was very similar to that of pure TEPA at 60 min, with the difference that, for the impregnated material, this capacity was obtained in half the time (30 min). The great

dispersion of TEPA onto CBF, especially at low mass ratios (5 and 10 wt.%), led to a significant improvement in the CO_2 mass transfer rate due to the increase in the gas-liquid contact area. The CO_2 capture rate improved 50% at 1 bar, from 0.006 to 0.009 mmol/g·min for CBF and CBF-TEPA5%, respectively. While at the highest pressures tested, the CO_2 capture rate was double, reaching values of 0.053 and 0.066 mmol/g·min for CBF-TEPA5% at 8 and 10 bar, respectively. Finally, it was observed that CBF-TEPA5% and CBF-TEPA10% presented very similar capture capacities with the difference that, in some cases, the saturation time of CBF-TEPA10% was slower (in 40 min). These results showed the feasibility of considerably improving the CO_2 capture capacity of CBF by impregnating a relatively small amount of TEPA on its surface.

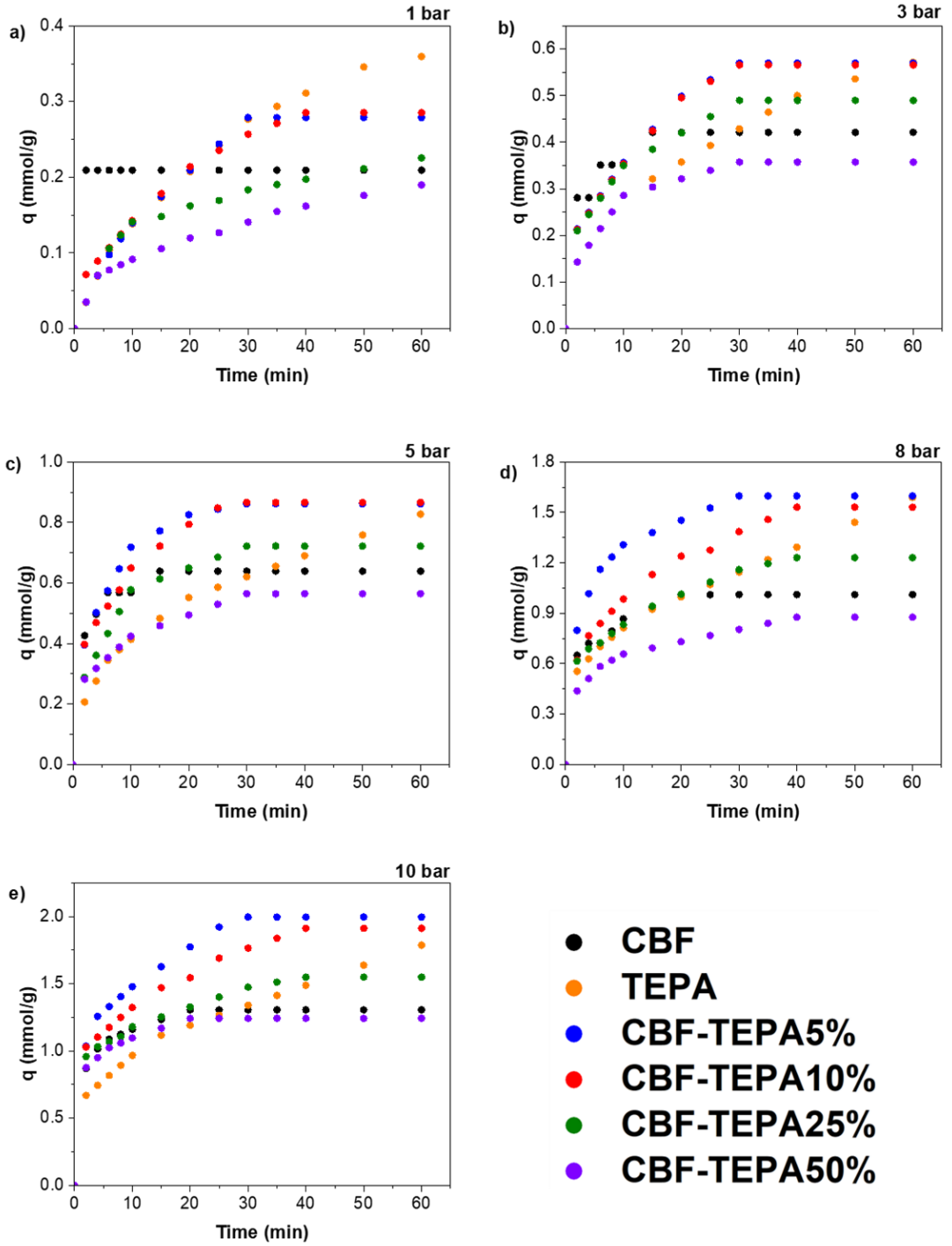

Figure 2.7 *CO_2 capture kinetics of CBF, TEPA and CBF impregnated with TEPA at 25 °C and pressure of a) 1 bar, b) 3 bar, c) 5 bar, d) 8 bar and e) 10 bar.*

Table 2.2 *CO_2 capture kinetics and capacities of CBF, TEPA and CBF impregnated with TEPA at 25 °C and 1 to 10 bar.*

Samples	Pressure (bar)	q (mmol/g)	Saturation time (min)	Capture rate at saturation time (mmol/g·min)
CBF	1	0.21	2	0.105
	3	0.42	15	0.028
	5	0.64	15	0.043
	8	1.01	20	0.051
	10	1.30	20	0.065
TEPA	1	0.36	60	0.006
	3	0.57	60	0.010
	5	0.86	60	0.014
	8	1.59	60	0.027
	10	1.99	60	0.033
CBF-TEPA5%	1	0.28	30	0.009
	3	0.57	30	0.019
	5	0.86	30	0.029
	8	1.59	30	0.053
	10	1.99	30	0.066
CBF-TEPA10%	1	0.29	40	0.007
	3	0.56	30	0.019
	5	0.86	30	0.029
	8	1.53	40	0.038
	10	1.91	40	0.048
CBF-TEPA25%	1	0.22	60	0.004
	3	0.49	30	0.016
	5	0.72	30	0.024
	8	1.23	40	0.031
	10	1.55	40	0.039
CBF-TEPA50%	1	0.19	60	0.003
	3	0.35	30	0.012
	5	0.56	30	0.019
	8	0.87	40	0.022
	10	1.24	20	0.062
For TEPA, the capture capacity was taken at 60 min.				

Sorption-desorption cycles were carried out at 10 bar to obtain the regeneration capacity of the TEPA-impregnated materials that presented better CO_2 capture capacities (CBF-TEPA5% and CBF-TEPA10%) as well as TEPA and CBF (Figure 2.8). The results of these sorption-desorption tests were condensed in Table 2.3. For TEPA, capacities of 1.78, 1.56, 1.11 and 1.11 mmol/g were obtained with regeneration capacity of 87.5, 62.5 and 62.5% for the 2nd, 3rd and 4th cycle, respectively. The CBF had a regeneration capacity of 100% and CO_2 capture capacities of 1.30 mmol/g. Regarding the materials impregnated with TEPA, the material that presented the best performance was CBF-TEPA5% with CO_2 capture capacities of 1.99, 1.77, 1.55 and 1.55 mmol/g with regeneration capacities of 88.9, 77.8 and 77.8% for the 2nd, 3rd and 4th cycle, respectively. The regeneration capacity of CBF impregnated with TEPA improved slightly in the second cycle (1.4%), considerably in the third cycle (from 62.5 to 77.8%) and remained constant in the fourth cycle (77.8%), regarding pure TEPA.

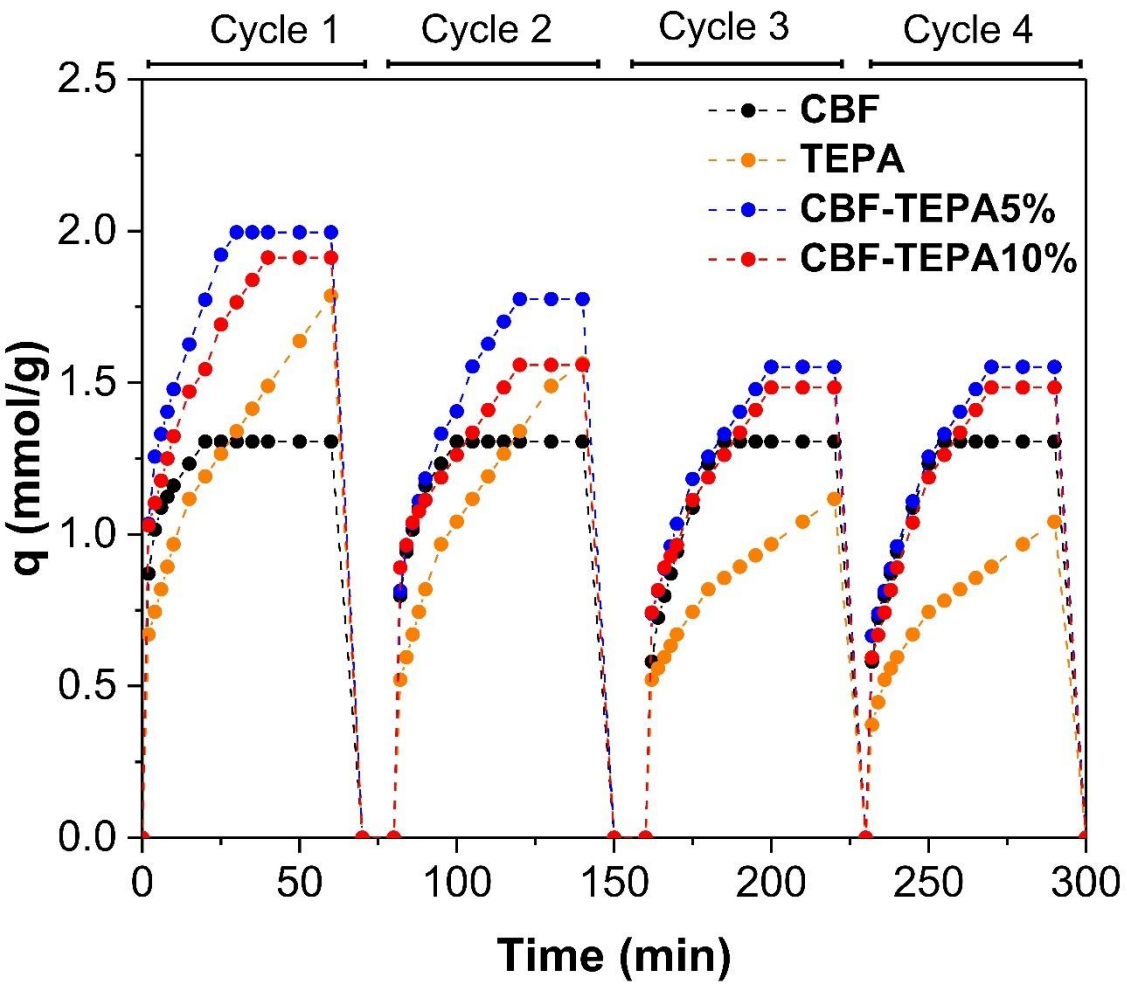

Figure 2.8 *Sorption-desorption cycles of CBF, TEPA and CBF impregnated with 5 and 10% of TEPA at 25 °C and 10 bar.*

Table 2.3 *CO_2 capture capacity of TEPA, CBF and CBF-TEPA5 and 10% at 25 °C and 10 bar.*

	CO_2 capture capacity (mmol/g)				**Regeneration capacity (%)**		
Sample	**C1**	**C2**	**C3**	**C4**	**C2**	**C3**	**C4**
CBF	1.30	1.30	1.30	1.30	100	100	100
TEPA	1.78	1.56	1.11	1.11	87.5	62.5	62.5
CBF -TEPA5%	1.99	1.77	1.55	1.55	88.9	77.8	77.8
CBF -TEPA10%	1.91	1.56	1.48	1.48	81.5	77.6	77.6

C means Cycle

FTIR analysis was carried out before and after CO_2 capture to elucidate the sorption mechanism (Figure 2.9). For the spectrum after CO_2 capture, the previously defined bands were found in addition to small bands between 1480-1580 cm^{-1} which can be attributed to tension and stretching vibrations of COO- in the $N\text{-}COO^-$ group [264,265].

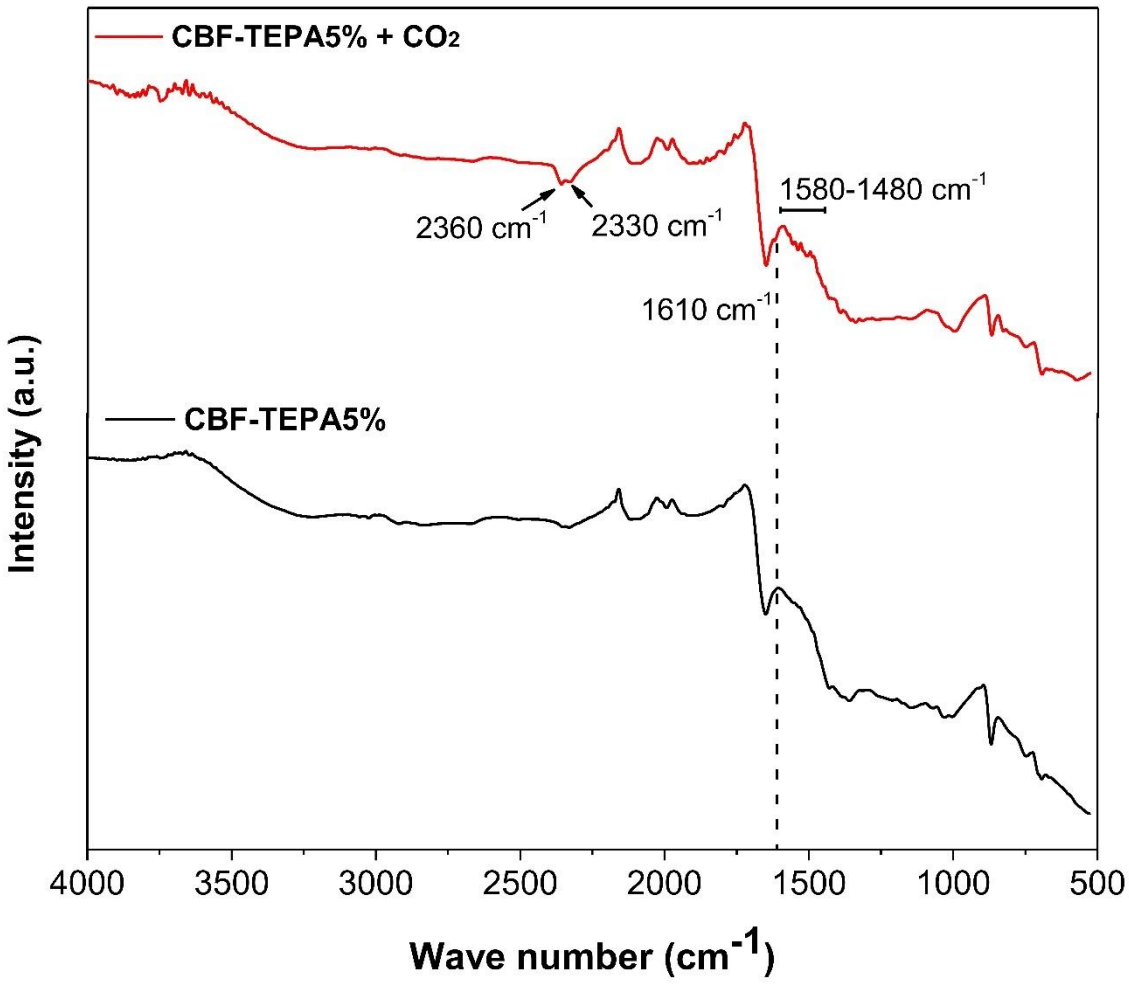

Figure 2.9 *FTIR spectra of CBF-TEPA5% before and after CO_2 capture.*

A band was also found around 1610 cm^{-1} which is attributed to the formation of carbamic acid [266]. This is because when the amine is exposed to high concentration of CO_2, the CO_2 adsorbs on the individual amine sites, thus forming

carbamic acid, as expressed in Figure 2.10 [261,267,268]. Finally, two bands were identified at 2330 and 2360 cm^{-1} which have been attributed to the physical adsorption of CO_2 in TEPA [269]. These results indicated that the CO_2 capture by the impregnated materials was carried out through chemisorption and physisorption.

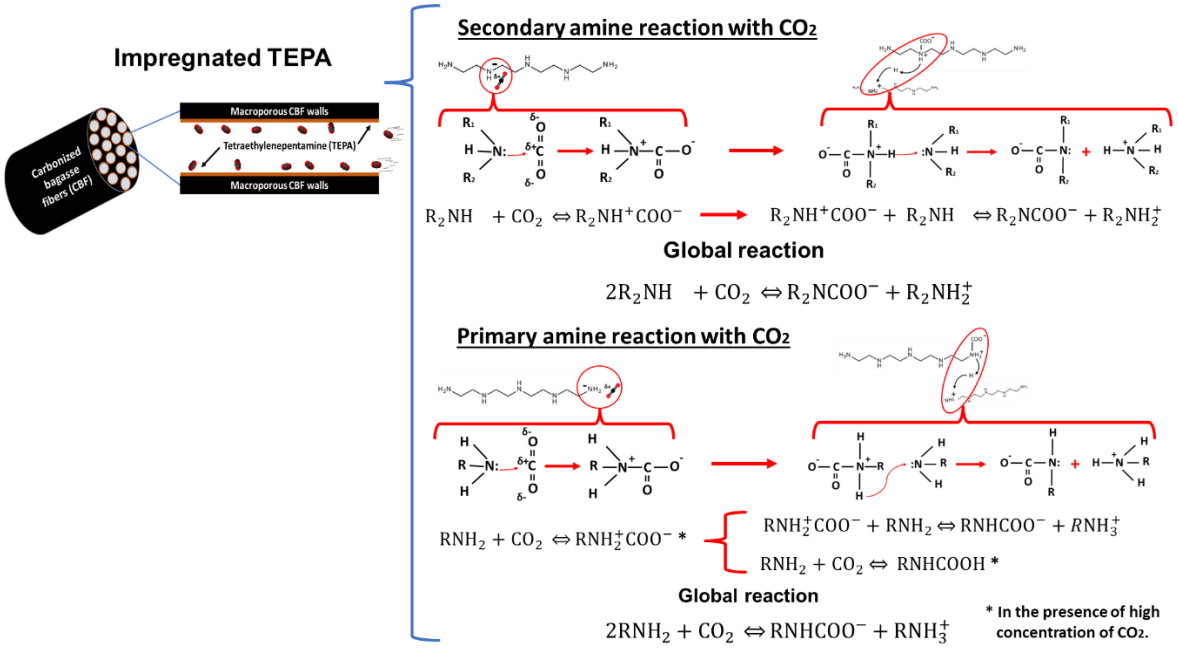

Figure 2.10 *Scheme of the suggested CO_2 adsorption mechanism in TEPA impregnated CBF [261,266-269].*

2.4 Conclusions

In this work, it was demonstrated the feasibility of improving the CO_2 capture capacity of carbonized agave bagasse fibers (CBF) by impregnating them with the liquid amine tetraethylenepentamine (TEPA). The TGA results showed that the methodology used to impregnate CBF with TEPA was appropriate for concentrations lower than 25%, since at higher concentrations the impregnated amount was less than estimated. Through SEM, a homogeneous distribution of TEPA was observed, mainly for CBF-TEPA5%, where the amine distribution was more homogeneous. The samples with low impregnation ratio explored (5 and 10 wt.%) exhibited the

highest CO_2 capture capacity and kinetics improvement. The CO_2 capture capacity of CBFs increases from 0.21 and 1.3 mmol/g to 0.28 and 1.99 mmol/g of CBF-TEPA5% at 1 and 10 bar, respectively. The CO_2 capture rate of TEPA is doubled due to its impregnation (from 0.033 to 0.066 mmol/g·min for CBF and CBF-TEPA5% at 10 bar, respectively). Furthermore, the maximum CO_2 capture capacities are obtained in less than 30 min for all pressures tested, where a similar capture capacity was obtained for pure TEPA in about 60 min. For the sorption-desorption cycles, CBF-TEPA5% regeneration capacities of 88.9, 77.8 and 77.8% are achieved for the 2nd, 3rd and 4th cycle, which represent an improvement of 1.4, 15.3 and 15.3% compared to pure TEPA, respectively. Finally, FTIR studies suggest that the CO_2 capture mechanism is through both chemisorption (carbamate formation) and physisorption (electrostatic interactions). The considerable improvement in the CO_2 capture capacity, kinetics, and regeneration capacity of CBF impregnated with TEPA demonstrate the great advantage of dispersing a liquid absorbent in a macroporous material for its application in CO_2 capture systems.

Chapter 3:

Enhancing the CO_2 capture capacity of natural macroporous carbonized fibers by growing carbon nanotubes on their surface

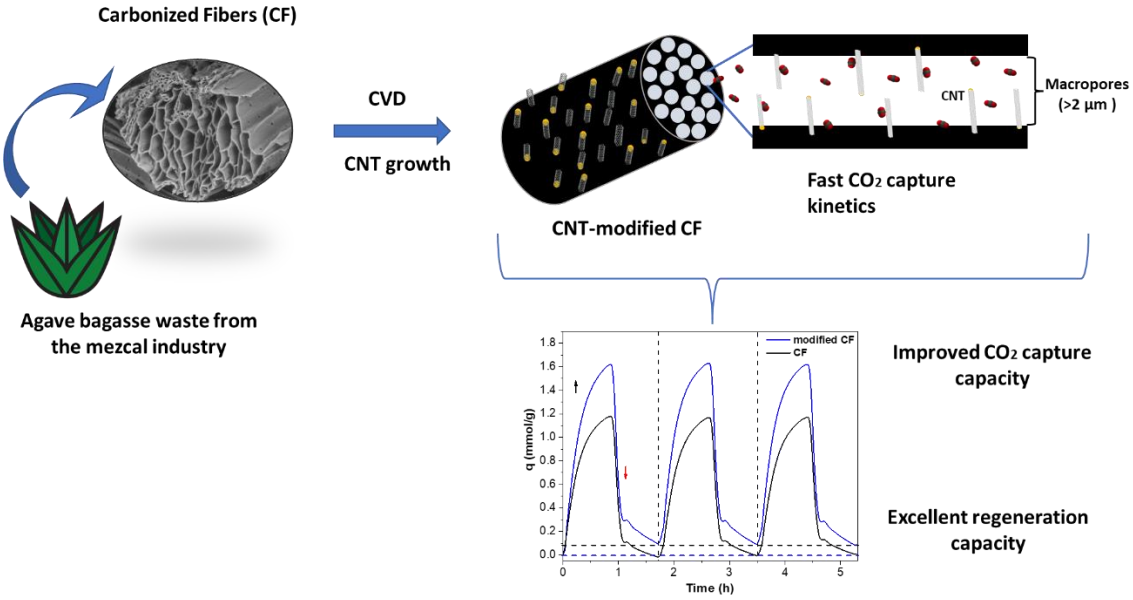

This chapter was adapted from: *Enhancing the CO_2 capture capacity of natural macroporous carbonized fibers by growing carbon nanotubes on their surface*, Colloids and Surfaces A: Physicochemical and Engineering Aspects 669 (2023) 131524.

ABSTRACT

The capture of CO_2 is one of the strategies proposed to reduce the emission and concentration of this gas in the atmosphere. Porous carbon materials from agro-industrial waste have important advantages for CO_2 capture, such as their low cost but they have limited CO_2 capture capabilities. Therefore, in this study a new hybrid material with superior CO_2 sorption capacity was prepared by the growth of carbon nanotubes (CNT) into the macroporous structure of acid carbonized fibers (ACF). The growth of CNT was carried out by chemical vapor deposition using acetylene as a carbon source for 3.5 min at 700 °C. Selected materials were characterized by N_2 physisorption, FTIR, potentiometric titrations, acid digestions, Raman spectroscopy, scanning and transmission electron microscopy. The CO_2 capture was measured in static mode at pressure up to 10 bar in a sorptometer and in dynamic mode in a thermogravimetric analyzer at pressure of 1 bar. CNTs were homogeneously grown on the entire surface of ACF. The specific surface area of carbonized fibers increased from 2 to 452 m^2/g after CNT growth and treatment at 300 °C for 1 min in air. The CO_2 capture capacity of the ACF increased from 2.30 to 3.51 mmol/g at 25 °C and 10 bar after CNTs growth and air treatment (ACF3-CNT-AT1). The CO_2 capture rate was also higher, from 0.023 to 0.032 mmol/g·min for ACF and ACF3-CNT-AT1 at 25°C and 1 bar, respectively. These results were mainly attributed to the increase in basic groups and highly reactive edge sites. In addition, regeneration capacities of 99% and 95% were obtained for the first 3 sorption-desorption cycles and an apparent selectivity (Q_{CO_2}/Q_{N_2}) of 1.65 and 2.48 for ACF and ACF3-CNT-AT1, respectively. The rapid sorption-desorption kinetics, coupled with the high

reversibility of CNT-modified ACFs, makes this hybrid material viable for use in CO_2 capture systems.

3.1 Introduction

Climate change is the greatest challenge of our time, and we are at a decisive moment. As populations, economies, products, and demand for services grow, so does the concentration of greenhouse gas emissions [1-2]. The combustion of fossil fuels has raised CO_2 levels in the atmosphere to more than 400 ppm, causing negative effects on the environment. Various methodologies have been proposed to reduce CO_2 emissions, one of them is to selectively capture this gas from combustion streams or directly from the atmosphere [4,19].

Absorption-regeneration processes have been recognized as one of the most established technologies in the CO_2 capture field, using mostly ammonia-based materials, due to their high CO_2 sorption capacity even at low partial pressures [194,270,271]. In recent years, carbon-based adsorbent materials have been tested and shown to have superior ability to capture CO_2 [104,272]. Gas adsorption on carbon materials has a lower heat of adsorption than on other adsorbents [273], which makes them excellent candidates for adsorption-desorption processes [274]. In addition, these kinds of adsorbents can be considered low cost, since they can be obtained from various sustainable sources, such as agricultural waste [104].

Particularly, our research group has explored the use of carbonized bagasse fibers (CBF) for CO_2 capture. These CBFs are characterized by having macroporous channels that go from end to end of the fiber. This macroporous structure provides

an accessible surface for CO_2 capture, resulting in an acceptable CO_2 capture capacity and fast adsorption/desorption kinetics, mainly by the elimination of gas diffusion through micro and mesopores that characterize adsorbent materials (i.e., activated carbon) [185]. Previous works have shown the kinetics advantages of using CBFs for CO_2 capture, however, their adsorption capacity is still limited. This can be improved by increasing the specific surface area of CBFs with nanostructures, such as carbon nanotubes (CNT), which have reported significant CO_2 capture capacity [275,276]. As a result, in this study the growth of carbon nanotubes on carbonized bagasse fibers is proposed to improve their CO_2 capture capacity while maintaining fast CO_2 capture kinetics.

3.2 Experimental Section

3.2.1 Reagents and precursor

All the chemicals used in this research were reagent grade. $FeCl_3 \cdot 6\ H_2O$, $FeCl_2 \cdot 4\ H_2O$, HNO_3, H_2SO_4, 0.1 N NaOH and 0.1 N HCl were obtained from Sigma Aldrich. Deionized water was used for the preparation of all solutions. The precursor (agave bagasse fibers from *Agave salmiana* plant) was provided by a distillery located in San Luis Potosi, Mexico.

3.2.2 Carbonization of bagasse fibers

The methodology used for the carbonization of the bagasse fibers was a modification of a previous study [184]. The agave bagasse fibers were washed, dried at 90 °C for 48 h and evenly fractionated at ~ 0.5 cm. Subsequently, the fibers were carbonized in a Barnstead Thermolyne 21100 tube furnace under an inert atmosphere of N_2 at

a temperature of 600 °C for 2 h to favor the formation of macroporous channels in the bagasse fibers [184]. The carbonized bagasse fibers (CBF) were then sieved (35x60 USA Standard test sieve) and washed with HCl to reduce ash content as mentioned below. 1 g of CBF was placed in a polypropylene tube, then 40 mL of 3M HCl solution was added and stirred at 100 rpm on an orbital incubator for 72 h. Subsequently, the residue was decanted, and the CBF were rinsed with deionized water until no variations in pH were measured, to obtain the sample named acid carbonized fibers (ACF). Finally, the fibers were dried at 90 °C for 48h and stored in a N_2 atmosphere to avoid the oxidation of the material.

3.2.3 Impregnation of iron nanoparticles in ACF

Chemical vapor deposition (CVD) was used to grow CNT onto the ACF surface. Impregnation tests were carried out from iron salts ($FeCl_3$ and $FeCl_2$) to obtain magnetite nanoparticles (Fe_3O_4) of particle size <25 nm, as previously reported [206,218]. The methodology used was a modification of the chemical precipitation of iron salts in an alkaline environment known as the Massart process [277,278]. The chemical reaction to synthesize magnetite (Fe_3O_4) can be formulated according to Equation 3.1 [279].

$$Fe^{2+} + 2Fe^{3+} + 8OH^- \rightarrow Fe_3O_4 + 4\ H_2O \qquad (Equation\ 3.1)$$

For the synthesis of the magnetite nanoparticles (MN), 5 mL of solutions of $FeCl_3 \cdot 6\ H_2O$ and $FeCl_2 \cdot 4\ H_2O$ were mixed in a 2:1 ratio respectively, with different concentrations (2:1, 4:2, 6:3 and 10:5 g/L), and then 100 mg of ACF were added. The suspension was mixed under a N_2 atmosphere, and the pH was adjusted to 12. It was then placed in a microwave reactor (Anton Paar model "Monowave 400") at

160 °C for 10 min. Finally, the MN impregnated fibers were washed with deionized water and dried at 90 °C for 48 h. These samples were named as ACFx, where “x” indicates the concentration of $FeCl_2$ iron salts used (x=1, 2, 3, 5).

3.2.4 CNT growth by CVD

The growth of CNTs on the ACF was carried out by duplicate: approximately 32 mg of each sample were placed in a thermogravimetric analyzer (Versa Therm) with a vertical quartz furnace as reactor, where the temperature was raised from room temperature to 700 °C with a heating ramp of 10 °C/min and a N_2 flowrate of 20 mL/min. Once the temperature was reached, acetylene (carbon source) was introduced for 3.5 min at a constant flow of 5 mL/min. After completing the CVD process, to synthesize CNTs, the temperature, and the N_2 flow were kept constant until the sample weight remained stable (around 10 min). "CNT" was added to these samples in the nomenclature (i.e. ACF1-CNT)

Subsequently, with the intention of removing the amorphous carbon deposited during the CVD process and improving the CO_2 capture capacity, a heat treatment was performed on selected materials (labeled as AT1). Briefly, the samples were heated up in a gravimetric analyzer from room temperature to 300°C with a heating ramp of 10 °C/min and a N_2 flowrate of 20 mL/min. Once the temperature was reached, the reaction gas was changed to air, flowing at 10 mL/min for 1 min. Finally, the sample was cooled down under nitrogen atmosphere.

3.2.5 Physicochemical characterization of CNT-modified ACF

The specific surface area and pore size distribution were determined from the nitrogen adsorption isotherm at 77 K using a Micromeritics ASAP 2020 physisorption equipment. The specific surface area was determined using the Breunaer-Emment-Teller (BET) equation and the pore size distribution was obtained using the density functional theory (DFT). The iron content of impregnated samples was determined by means of an acid digestion following the methodology reported by Nieto-Delgado and Rangel-Méndez, 2012 [184]: 0.05 g of sample were placed in a Teflon reactor and 20 mL of an acidic solution (HNO_3:H_2SO_4 5:1) were added. Then, the samples were heated up to 150 °C for 45 min. After digestion, the volumetric solutions were diluted to 50 mL and analyzed in an inductively coupled plasma atomic emission spectrometer (ICP-AES) (Varian 730-ES).

The surface charge distribution and the point of zero charge (pH_{pzc}) were determined by potentiometric titration using a METTLER TOLEDO T70 automatic titrator, with 0.1 N NaOH and 0.1 N HCl as the titration system. The values obtained in the potentiometric titration were analyzed using the SAEIUS-pK-dist program © 1994 software.

The CNTs structure was analyzed by Raman spectroscopy (Renishaw with Leica DM LM), which was performed between 500 and 3500 cm^{-1}, with a scan duration of 60 s and a microscope magnification of 50x, providing a spatial resolution of 1 μm.

For the identification of functional groups, FTIR studies were conducted in a Nicolet 1S50 FTIR equipment, from Thermo Scientific, in the spectral range of 500 to 4000

cm^{-1}, in attenuated total reflectance (ATR) mode with 64 scans with a resolution of 4 cm^{-1}.

The morphology of the CBF and ACF were analyzed by an environmental scanning electron microscope (SEM), FEI QUANTA 250. Also, CNT-modified ACFs were observed under a HELIOS NANOLAB 600i SEM with high resolution field emission source and secondary electron detector. Before analysis, the samples were immobilized on a carbon tape retained in an SEM sample holder. In addition, a transmission electron microscope (TEM, FEI´s Tecnai F-30 operated at 300 kV) was used to analyze in more detail the CNT morphology. The sample was suspended in isopropanol and then sonicated for 10 min. Finally, the sample was mounted onto a lacey carbon coated copper grids.

3.2.6 CO_2 capture experiments

The CO_2 capture isotherms (at 25, 50 and 75 °C) of the selected materials were studied in a Micromeritics ASAP 2050 automatic manometric sorptometer up to a pressure of 10 bar. Before measurements, the materials were degassed at 150 °C for 8 hours under vacuum.

In addition, the isosteric heat of adsorption (q_{st}) was calculated, which is a value that characterizes the adsorbate-adsorbent interaction strength, the type of adsorption (chemisorption or physisorption) and the degree of heterogeneity of the material surface. This study was carried out from the analysis of the q_{st} curve (kJ/mol) vs. amount of CO_2 adsorbed (mmol/g), where the q_{st} values were obtained from the data

of the CO_2 adsorption isotherms measured at different temperatures and using the Clausius-Clapeyron equation:

$$q_{st} = R\left[\frac{\delta \ln p}{\delta\,(1/T)}\right]_{n_{ads}} \quad \textit{(Equation 3.2)}$$

where p (kPa) is the equilibrium pressure, T (K) is the adsorption temperature and R (8.314 kJ/mol·K) is the ideal gas constant. The equilibrium pressure (p) for each amount of CO_2 adsorbed (n_{ads}) was estimated by non-linear interpolation from the data of the experimental isotherms at different temperatures. The slope of the straight line of adsorption (ln p vs. 1/T) corresponds to the isosteric enthalpy of CO_2 adsorption for a defined amount of CO_2 adsorbed.

CO_2 capture kinetics was quantified with a thermogravimetric analyzer (TGA) model SETSYS EVOLUTION TGA-DTA / DSC from Setaram Instrumentation. During the stabilization stage, the sample was exposed to a flow of 30 mL/min of N_2, while the temperature was increased to 105 °C for 30 min and then decrease to the desired temperature. This, to eliminate water and volatile organic compounds that can interfere with the determination of CO_2 capture. Then, in the CO_2 capture stage, tests were carried out at 25 and 80 °C, and CO_2 of 99.98% purity was used at a flowrate of 30 mL/min for 90 min. In addition to this, tests were also carried out with different concentrations of CO_2 (50%, 25% and air (400ppm)). The samples weight change during CO_2 exposure was attributed to the mass of CO_2 captured, and this was estimated per gram of material (Equation 3.3). In addition, the time in which the sample reached equilibrium was determined.

$$\mathrm{Q} = \frac{\mathrm{m_t} - \mathrm{m_i}}{\mathrm{m_0}(PM)} \quad \textit{(Equation 3.3)}$$

Where Q is the CO_2 capture capacity (mmol/g material), m_t and m_i is the difference in mass (mg), m_0 (g) the initial mass of the adsorbent material and PM is the molecular weight of CO_2 (mg/mmol).

Under the same analytical conditions, the pure N_2 capture capacity of the ACF and CNT-modified ACFs at 25 °C was evaluated, since CO_2 was diluted in N_2, to determine the degree of affinity of CO_2 over N_2 [280] (Equation 3.4).

$$\text{Apparent selectivity} = \frac{Q_{CO_2}}{Q_{N_2}} \qquad \textit{(Equation 3.4)}$$

Where Q_{CO_2} and Q_{N_2} represents the capture capacity of pure CO_2 or N_2 calculated with equation 3, respectively. It should be noted that the apparent selectivity represents a practical approximation of selectivity from a kinetic point of view [281]. Adsorption rate parameters were determined for pseudo-first, pseudo-second intraparticle diffusion models. The pseudo first order kinetic equation is given by:

$$\ln(q_e - q_t) = \ln(q_e - k_1)t \qquad \textit{(Equation 3.5)}$$

where, q_t (mmol/g) and q_e (mmol/g) are the adsorption capacities at time t (min) and equilibrium, respectively, and k_1 (min^{-1}) is the pseudo-first order rate constant. The pseudo second order kinetics is represented by the following equation:

$$\frac{t}{q_t} = \frac{1}{k_2 q_e^2} + \frac{1}{q_e}t \qquad \textit{(Equation 3.6)}$$

where k_2 (mmol/(g·min)) is the second order adsorption rate constant, q_e (mmol/g) is the amount of contaminant adsorbed at equilibrium, and q_t (mmol/g) is the amount of contaminant adsorbed at any time t (min).

To evaluate the reversibility of captured CO_2, CO_2 sorption-desorption cycles were performed on the ACF and CNT-modified ACFs. The capture stage began, when the temperature was dropped to 25 °C and remained constant for 50 min with a flowrate of 30 mL/min of CO_2. During the desorption stage, the temperature was raised to 80 °C with a flowrate of 30 mL/min of N_2 for 30 min.

The reversibility was calculated based on the following equation:

$$Reversibility = \left(\frac{Q_{i+1}}{Q_i}\right)(100\%) \qquad \textit{(Equation 3.7)}$$

Where Q is the capture capacity (mmol of CO_2/g of material) obtained at 50 min in the sorption-desorption cycle number i = 1 to 3.

3.3 Results and Discussion

3.3.1 Characterization of the carbonized bagasse fibers and catalyst impregnation

Firstly, the carbonization yield of the bagasse fibers was calculated by using the following equation: $\left(\frac{final\ mass}{initial\ mass}\right)x100$. Ten repetitions were performed and an average yield of 22.1 % was obtained. Representative SEM images of CBF and ACF samples are presented in Figure 3.1. Being a natural residue, bagasse fibers present different diameters and sizes, and once carbonized their transversal section is characterized by macroporous channels with a diameter between 2 to 30 µm.

These channels were related to its different vascular layers [184] (Figure 3.1 a). In addition, rectangular bars were observed on the CBF (Figure 3.1 b), which have been attributed to calcium carbonate from the bagasse fibers [225,282]. On the other hand, ACF, reported in Figure 3.1 c), did not show calcium bars, just cavities where these were deposited. This was also corroborated with the calcium content of CBF and ACF samples, 1.34 and 0.3 % respectively.

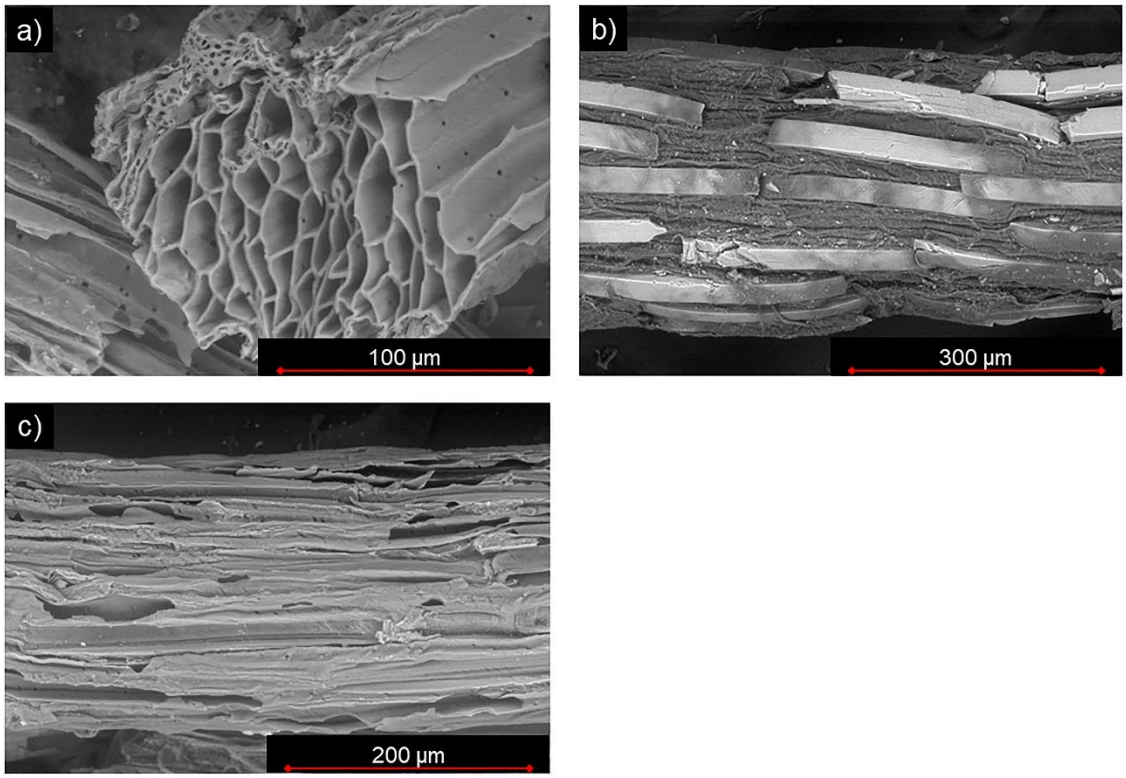

Figure 3.1 *SEM backscattered electrons images of a) the macroporous channels of ACF, b) CBF and c) ACF.*

Different concentrations of catalyst (magnetite nanoparticles) were used to study its effect on the CNT growth synthesis. The iron concentration in ACF samples was reported in Table 3.1. An iron concentration of 0.05% was obtained for the ACF1 sample, double (0.11%) for ACF2, six times more (0.3%) for ACF3 and almost 17 times more (0.84%) for ACF5.

Table 3.1 *Inorganic content of acid washed carbon before and after impregnation with magnetite nanoparticles*.

Material	Fe (%)	Ca (%)	Mg (%)	Na (%)	B, Ba, Al and P (%)
ACF	0.01	0.30	0.08	0.05	0.02
ACF1	0.05	0.30	0.08	0.09	0.03
ACF2	0.11	0.46	0.06	0.09	0.02
ACF3	0.30	0.41	0.06	0.07	0.02
ACF5	0.84	0.33	0.06	0.10	0.02
ACFx: Acid wash carbonized sample. The number (x) indicates the concentration of $FeCl_2$ iron salts employed for impregnation					

To have a better understanding of the growth process of CNT in the iron impregnated ACF materials, the ACF3 sample was analyzed in detail to measure the size and distribution of MN particles. Particularly, the ACF3 sample showed the best conditions in CNT growth, which will be discussed in detail in the next section. Accordingly, the ACF3 sample was characterized by having a uniform distribution of MN (see Figure 3.2 a). This can be translated into a high density of catalytic sites for the growth of CNTs [227]. In addition, a good interaction between the substrate (acid carbonized bagasse fibers) and the catalyst (magnetite nanoparticles) can be assumed, because the SEM micrographs did not show aggregation of particles. The particles aggregation has been reported as consequence of the magnetic interaction between the metallic particles [283]. Formation of large MN particle clusters is something to be avoided since it could lead to the formation of carbon deposits rather than the carbon nanotubes growth during CVD [228].

On the other hand, from Figure 3.2 b) the average nanoparticle size was estimated, which was less than 25 nm, suitable (5 and 25 nm) for the growth of multilayer carbon

nanotubes (MWCNT) [229,230]. In addition to the fact that the catalyst size dictates the CNTs diameter [217].

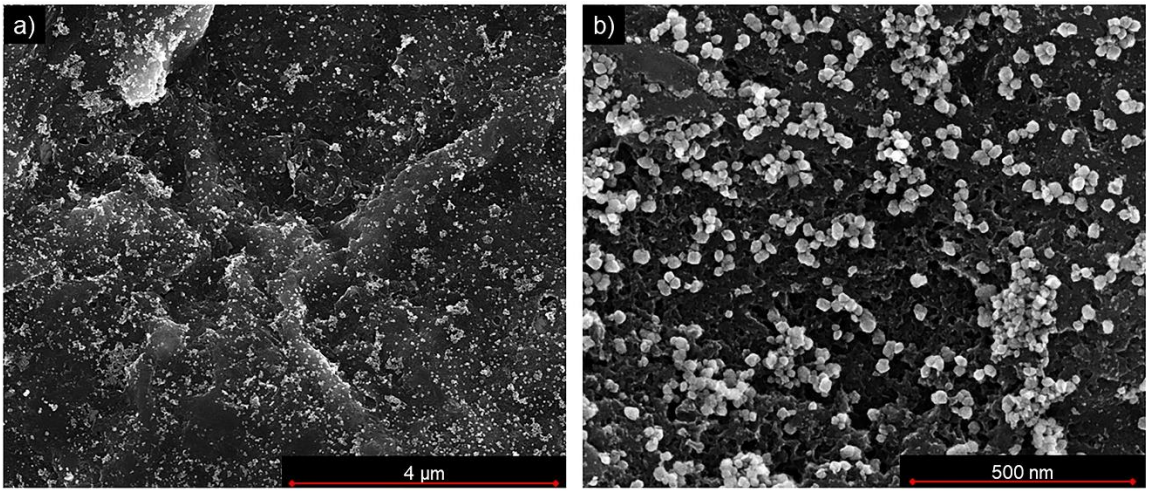

Figure 3.2 *SEM secondary electrons images of a) and b) ACF3.*

3.3.2 Growth and characterization of CNT on ACF

All ACF samples reported in Table 3.1 were modified according to the CVD protocol. Representative SEM images of those samples are presented in Figure 3.3. Accordingly, the sample with the lowest catalyst concentration (ACF1-CNT), is characterized by having long CNTs and clusters of CNTs in certain areas of the ACF (see Figure 3.3 a) and b). On ACF2-CNT sample, a considerable increase in CNT growth was observed, however, carbon shoot and some areas without CNT were observed (Figure 3.3 c) and d). On the other hand, for the ACF5-CNT sample, low growth of CNT and clusters of carbon spheres were observed (Figure 3.3 e) and f), mainly attributed to the excess of condensed carbon that did not react with the catalyst [225]. Finally, ACF3-CNT sample exhibited a homogeneous CNT coverage in most of the surface with low presence of carbon spheres or other carbon nanostructures different from CNTs (Figure 3.3 g) and h), hence, subsequent experiments were conducted with this sample.

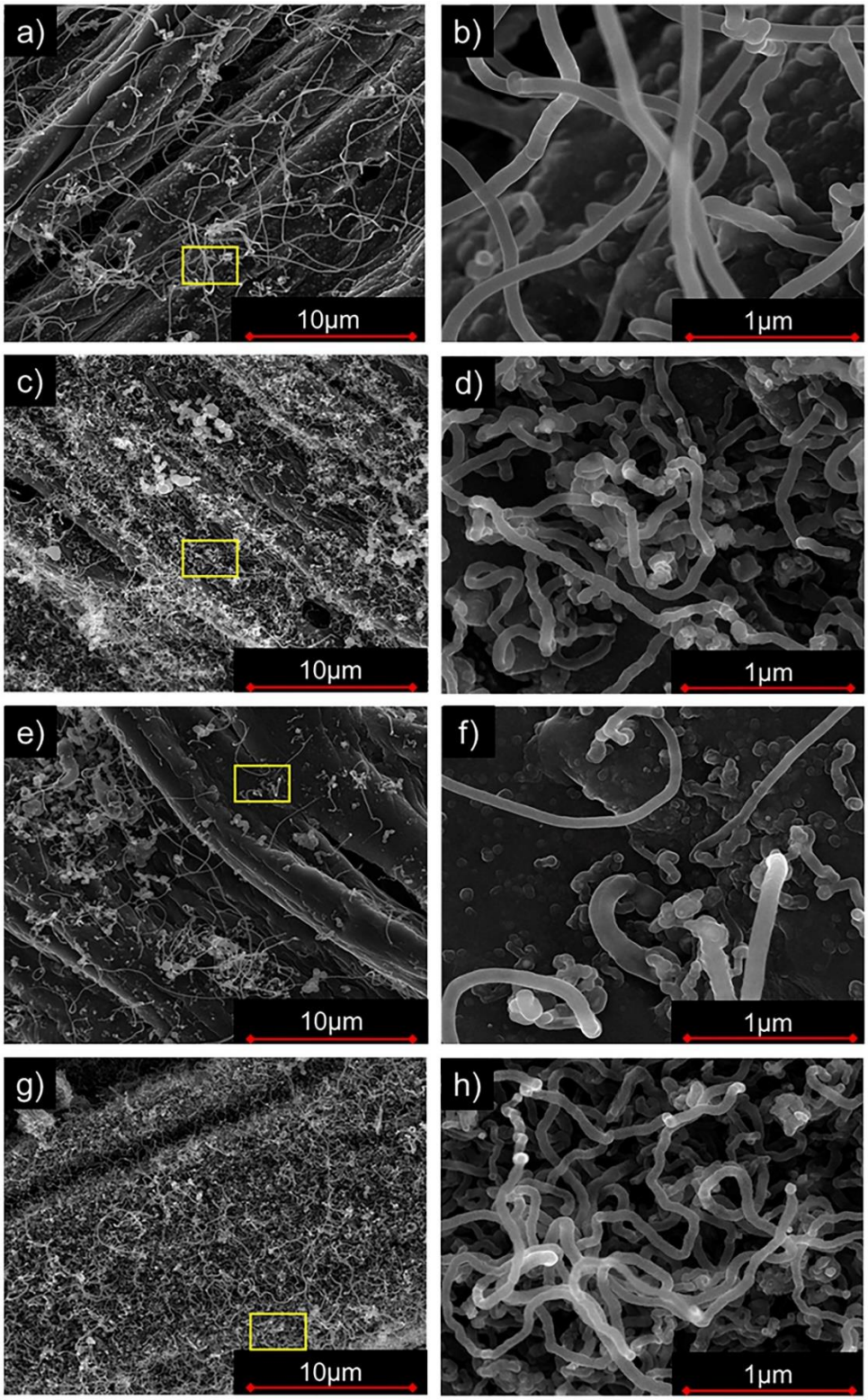

Figure 3.3 *SEM secondary electrons images of a) ACF1-CNT, b) zoom of the marked area of ACF1-CNT, c) ACF2-CNT, d) zoom of the marked area of ACF2-CNT, e) ACF5-CNT, f) zoom of the marked area of ACF5-CNT, g) ACF3-CNT and h) zoom of the marked area of ACF3-CNT.*

3.3.2.1 Structural characterization of CNTs grown onto ACF

CNTs grown on sample ACF3 were characterized by electron microscopy (scanning and transmission). Curved CNTs with similar outer diameter formed a complex array, as presented in Figure 3.4 a) and Figure 3.3 h). In addition, MN was identified at the tip of CNTs (yellow circles on Figure 3.4 b), which suggests a tip-growth model, where the carbon atoms displace the catalyst during the growth of the CNTs by CVD process [218].

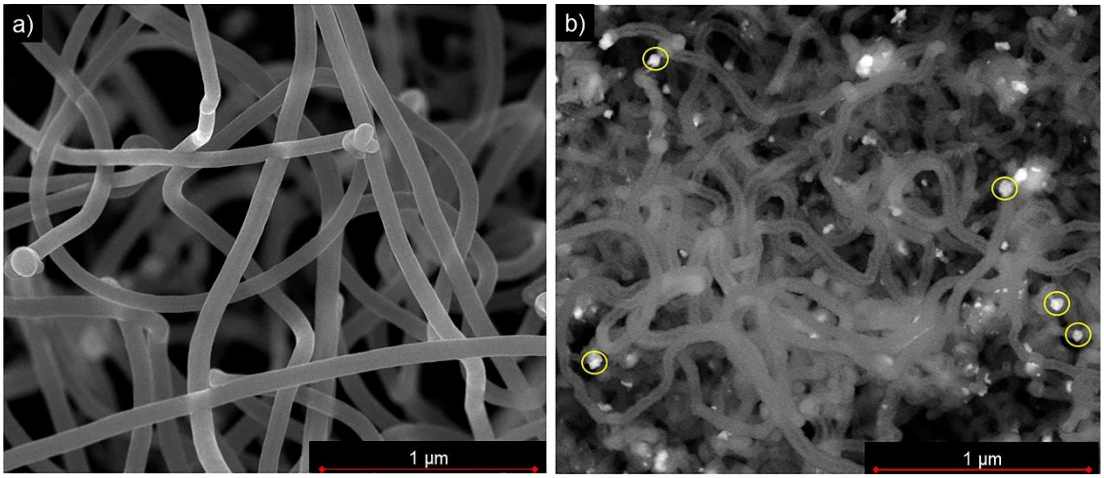

Figure 3.4 *SEM secondary electrons images of a) ACF3-CNT and b) backscattered electrons image of ACF3-CNT.*

Through the transmission electron microscopy (TEM) images, the growth of curved CNTs with an inner diameter of 20-30 nm was corroborated (Figure 5 a). CNTs could be conformed by two different types of wall arrangements (Figure 5 b); walls made of more compact graphitic sheets can be seen in the inner walls of CNTs, unlike the outer walls, which are made up of amorphous or turbostratic carbon less compact, sponge-like structure.

On the other hand, sample ACF3-CNT-AT1 was also analyzed, where damage or erosion can be seen on the external walls of the CNTs. This can be attributed to the

gasification of labile carbon, leaving a heterogeneous surface on the walls of CNTs (Figure 3.5 c) and d). This resulted in a higher specific surface area, as will be explained in section 3.3.2.2, and more importantly, in the increase of highly reactive edge sites of the graphitic sheets that make up the CNT that serve as active sites to adsorb CO_2 [284,285]. In addition, the arrangement of two different walls disappeared (Figure 5 d), leaving mostly the inner wall that has the highest carbon density.

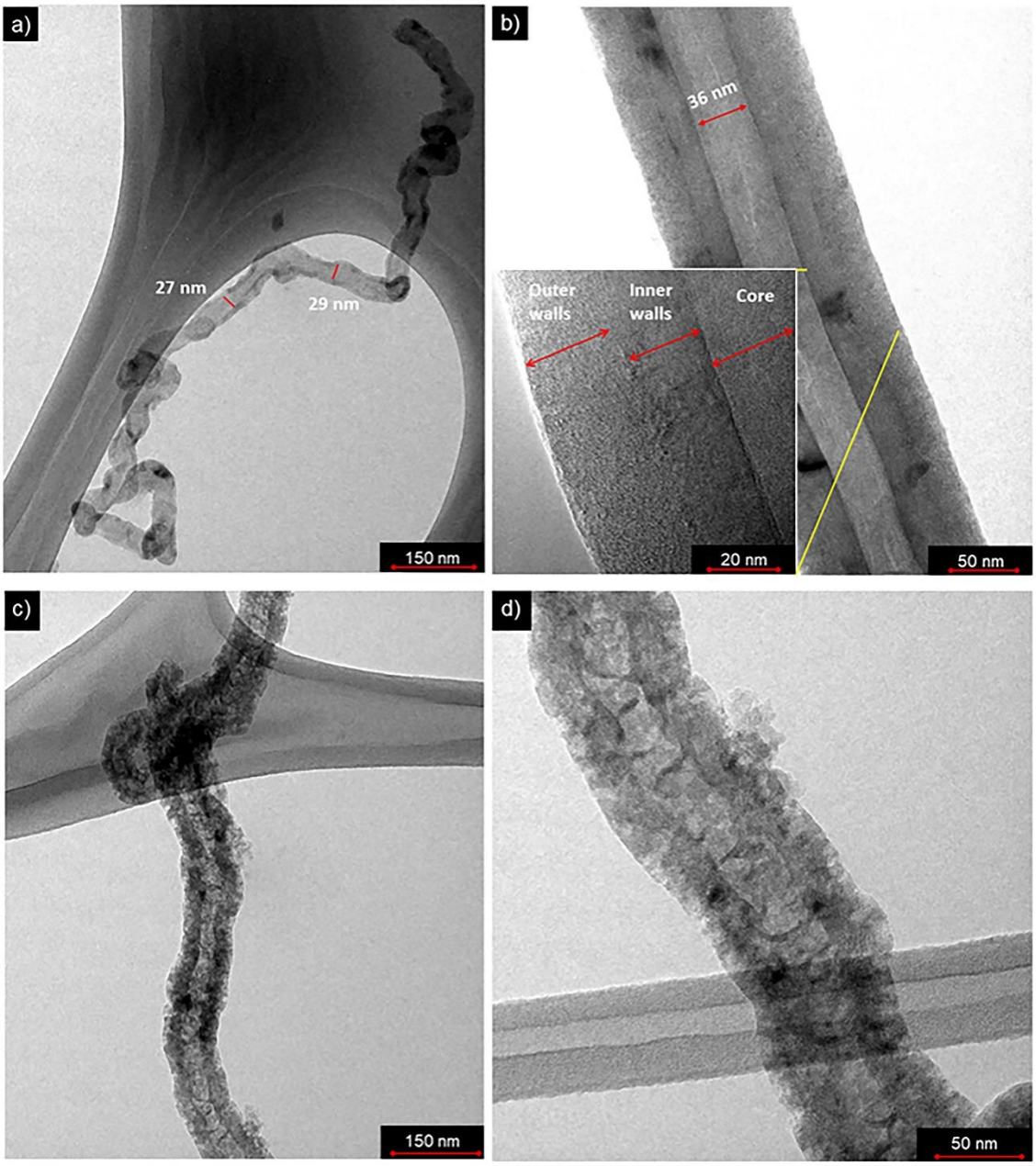

Figure 3.5 *Representative TEM images of CNT from ACF3-CNT: a) curved CNT, b) arrangement of two different CNT walls, c) and d) CNT from ACF3-CNT-AT1.*

The ACF, ACF3-CNT and ACF3-CNT-AT1 samples were characterized by Raman spectroscopy (Figure 3.6), where the bands D (~1320 cm^{-1}), G (~1580 cm^{-1}) and the 2D band (~2700 cm^{-1}) were identified. The G band (graphitic band) is associated with vibrations in the planes of the graphene sheets, that is, with the interlayer E_{2g}-

mode graphite symmetry that reflects the structural integrity of the sp^2-hybridized carbon atoms. The D band (defect or disorder band) is related to defects in the CNT sidewalls, that is, with disordered carbon atoms with CNT sp^2 hybridizations containing vacancies, impurities, or other symmetry-breaking defects [194,286]. The 2D band is attributed to the overtone of the D band, but with the difference that it does not activate due to its proximity to the defects. It is active for graphite crystals through the double resonance process involving phonons with opposite wave vectors [287].

Pristine ACFs show peaks with widths of approximately 255 cm^{-1} (D band) and 99 cm (G band). After the CVD process (ACF-CNT), the width of the peak corresponding to the D band remained at 255 cm^{-1} with respect to the ACF, while the width of the peak of the G band decreased to 84 cm^{-1}. Finally, after treatment with air at 300 °C (ACF3-CNT-AT1) the peaks presented widths of 133 cm^{-1} (D band) and 77 cm^{-1} (G band): this decrease in the peak width has been related to the increase in the number of ordered graphitic structures [288], and to the disappearance of additional peaks at 1180, 1500 and 1620 cm^{-1}, which are related to impurities, amorphous carbon, and disordered carbon, respectively [289].

On the other hand, in Raman spectra, the ratio of the D and G (I_D/I_G) bands can be considered as a measure of the crystalline order of carbon materials and provides a good estimate of the defect level [286-288,290]. For the analyzed samples, I_D/I_G ratios of 0.82, 0.86 and 0.93 were obtained for ACF, ACF3-CNT and ACF3-CNT-AT1, respectively. The increase in the intensity of the D band and therefore the increase in the I_D/I_G index of the ACF with CNTs with respect to the pristine material,

confirms the current defective curly structure of the CNTs [288], as can be seen in the SEM micrographs (Figure 3.2 d) and 3.3 h)). In addition, the ACF3-CNT and ACF3-CNT-AT1 indices agree with the results found by TEM micrographs, since the AT1 treatment increased the number of defects (CNT texture) as well as the I_D/I_G index value. It is worth mentioning that for the sample ACF3-CNT-AT1 the band around 2700 cm^{-1} was defined, which has been attributed to the presence of graphitic structures with few layers [291].

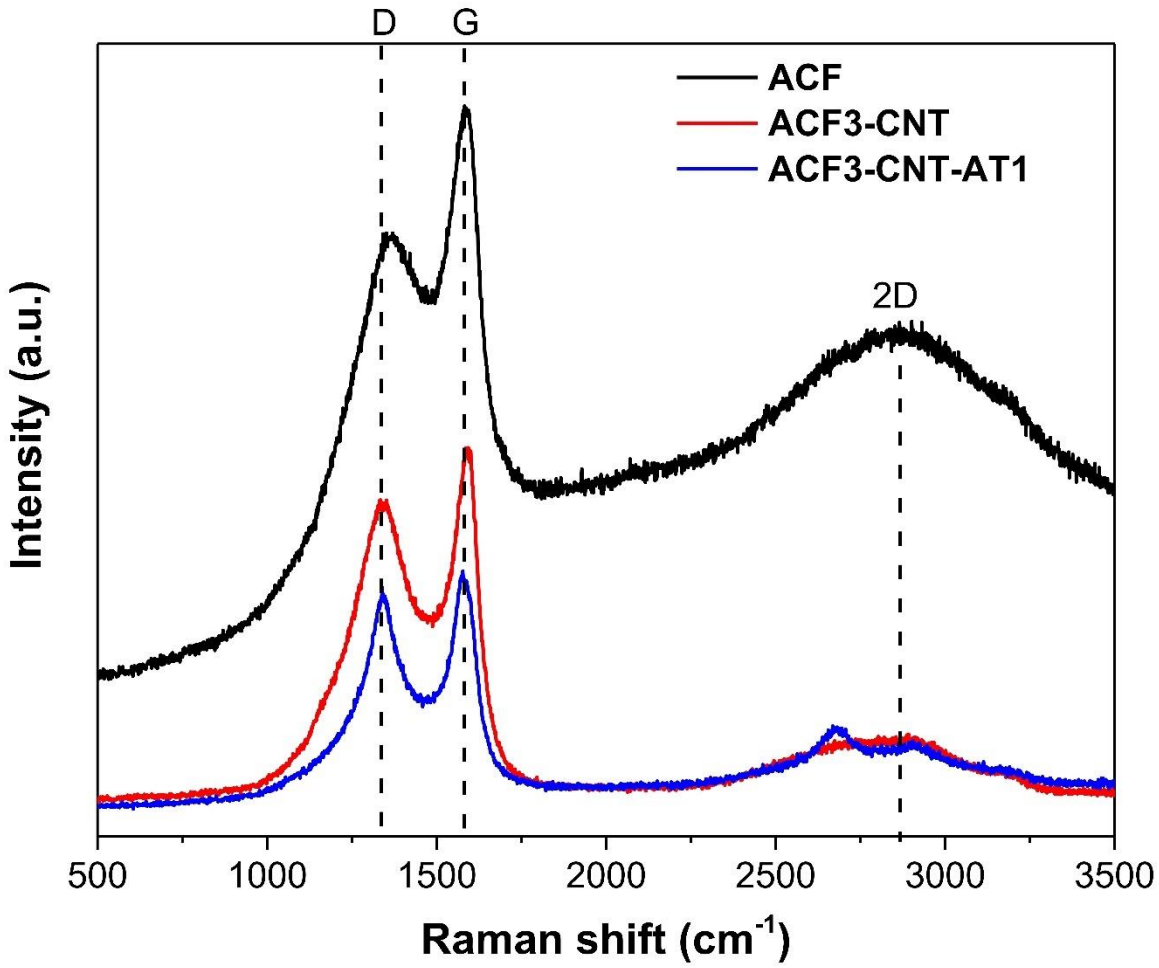

Figure 3.6 *Raman spectrum of ACF, ACF3-CNT and ACF3-CNT-AT1.*

3.3.2.2 Textural proprieties and surface chemistry

The specific surface area and pore size distribution of ACF, ACF1-CNT, ACF3-CNT and ACF3-CNT-AT1 (Table 3.2) were obtained by N_2 physisorption. Figure 3.7 a) shows the N_2 adsorption isotherms of carbon materials, where it was observed that ACF presented a type (II) isotherm according to the IUPAC classification, characteristic of non-porous or macroporous materials. Also, the samples modified with CNT present a type (I) isotherm characteristic of microporous materials [292]. Regarding the pore size distribution (PSD) of the studied materials (Figure 3.7 b), the ACF presented mainly mesoporous with pores between 15 nm and 45 nm without the presence of micropores. The ACF1-CNT sample mainly presented low mesoporosity between 20 and 37 nm. The ACF3-CNT and ACF3-CNT-AT1 sample showed a small amount of mesopores between 25 and 60 nm and great microporosity of <2 nm. Accordingly, there was a significant increment on the specific surface area of ACF sample, from 2 to 104 m^2/g (ACF1-CNT), and up to 252 m^2/g when increasing the catalyst content (ACF3-CNT). Particularly, the volume of the micropores was significantly increased after CNTs deposition, which is attributed to the homogeneous growth of CNT (Figure 3.3 g), through increasing the exposed area of the CNTs. Finally, after the thermal treatment of sample ACF3-CNT, the specific surface area of the material increased even more, up to 452 m^2/g. This significant increase in specific surface area was attributed to the rough texture of CNTs, as shown in TEM micrographs (Figure 3.5 c) and d). The increase in specific surface area and pore volume due to the rise in defects in the external walls of CNT has been previously reported when these are activated with KOH or NaOH [293,294].

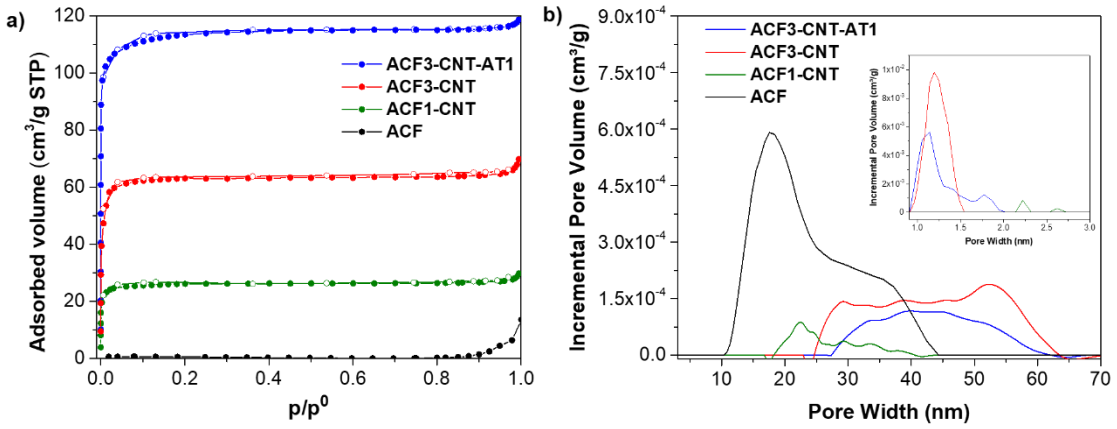

Figure 3.7 *a) Experimental N_2 adsorption isotherms at 77 K and b) pore size distribution of ACF, ACF1-CNT, ACF3-CNT and ACF3-CNT-AT1 calculated with Quenched solid density functional theory (QSDFT).*

Table 3.2 *Textural properties of ACF, ACF1-CNT, ACF3-CNT and ACF3-CNT-AT1.*

Sampler	S_{BET}	V_{total}	V_{macro}	V_{meso}	V_{micro}
	(m^2/g)	(cm^3/g)			
ACF	2	0.009	0.009	0	0
ACF1-CNT	104	0.038	0.037	0.001	0
ACF3-CNT	252	0.096	0.002	0.002	0.092
ACF3-CNT-AT1	452	0.168	0.001	0.001	0.166

By using FTIR and potentiometric titrations, the changes in surface chemistry of the pristine (ACF) and modified materials with CNTs (ACF3-CNT-AT1) were identified (Figure 3.8). Bands between 871-711 cm^{-1} corresponding to benzene groups related to the fiber's graphitization were identified in both samples. Also, the bands at 1137 and 1043 cm^{-1} attributed to C-O and C-OH vibrations of acid groups were found mainly in ACF. Signals corresponding to C=C and C=O vibrations between 1550 and 1750 cm^{-1} of the aromatic ring of the phenolic structure were identified for ACF3-CNT-AT1 (Figure 3.8 a) [255,256]. This increase in the signal for sp^2 hybridizations

(C=C), associated with the growth of CNTs, contributes to the capture of CO_2 through pi-pi bonds [295].

On the other hand, by potentiometric titrations (Figure 3.8 b), a pH_{pzc} of 6.05 was obtained for ACF and 8.05 for ACF3-CNT-AT1, which is relevant since it has been reported that the adsorption of CO_2 in carbon materials is associated with the presence of functional groups and surfaces of a basic nature [296]. Moreover, a considerable number of functional groups was introduced into the ACF3-CNT-AT1 sample, which is evident when comparing the proton binding curve of this sample with the pristine one. The increase in functional groups can be attributed to the surface vacancies and increase in texture of the air treated CNTs observed in Figure 3.5 c) and d). Vacancies on the surface of carbon materials, such as CNTs, have been reported to exhibit high reactivity towards CO_2 through Van der Waals interactions [284,285].

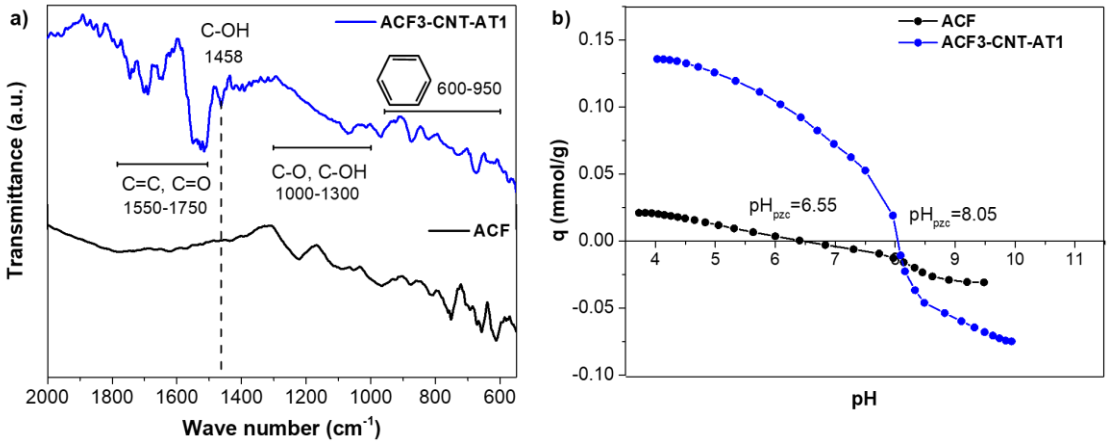

Figure 3.8 *FTIR (a) and proton binding curves (b) of ACF and ACF3-CNT-AT1 samples.*

The change in elemental composition of materials after CNT modification was determined by EDS (Figure 3.9). The composition of ACF was C (77.19 %), O (20.42 %), Mg (0.5 %), Si (0.32 %), Cl (0.56 %) and Ca (1.02 %), whereas for ACF3-CNT-AT1 was C (81.88%), O (4.66%), Ca (1.16%) and Fe (12.3%). From these values, a decrease in the amount of oxygen and an increase in the amount of carbon were observed, attributed to the growth of CNT.

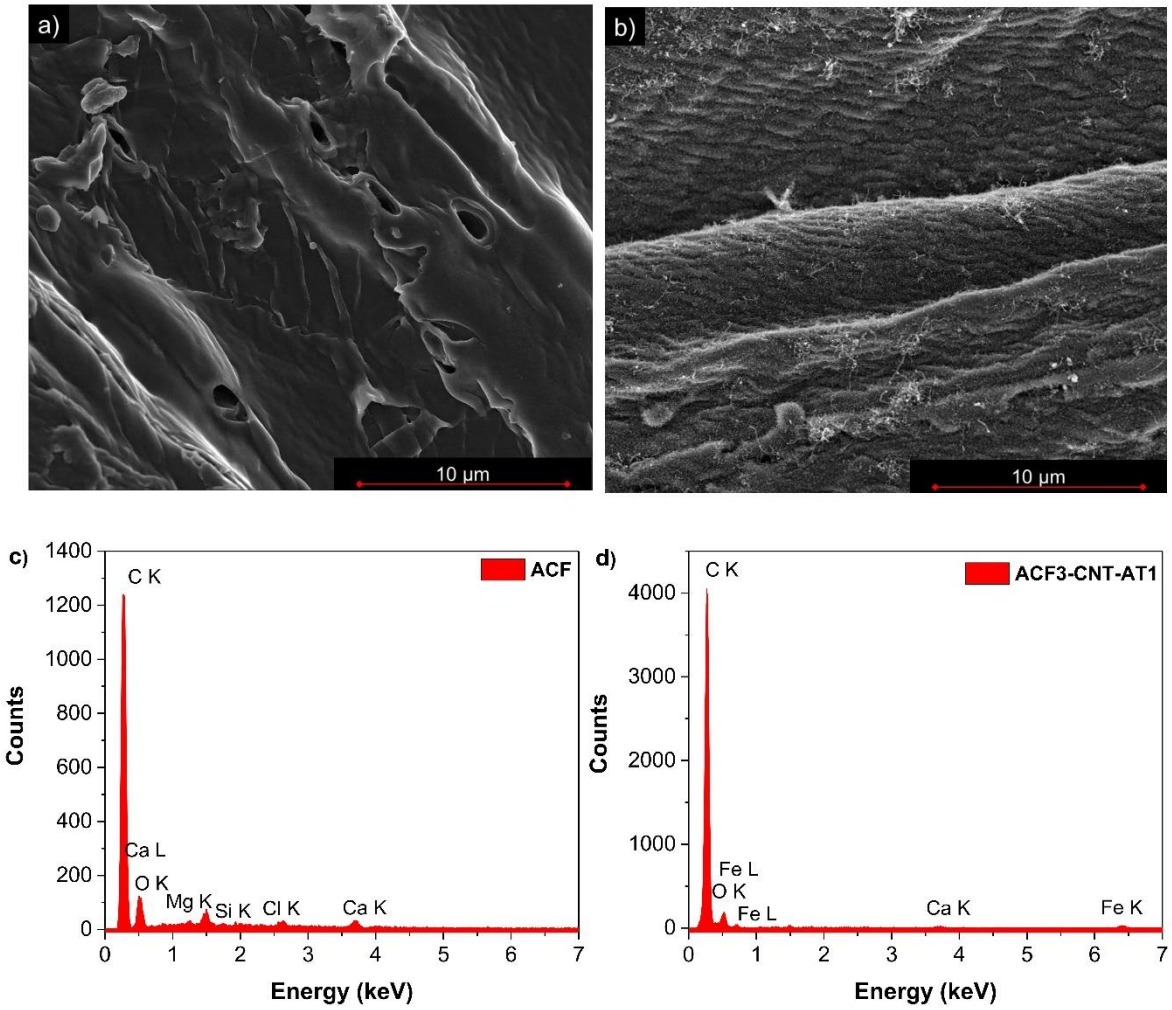

Figure 3.9 *SEM secondary electrons images of a) ACF, b) ACF3-CNT and EDS analysis of c) ACF and d) ACF3-CNT-AT1 of presented images.*

3.3.3 CO_2 capture in pristine and modified ACF samples

The CO_2 capture kinetics is presented in Figure 3.10 where, the average capture rate was calculated by dividing the capture capacity by the time within the first 50 min. The maximum CO_2 capture capacity for the pristine material (ACF) was 1.16 mmol/g with a CO_2 capture rate of 0.023 mmol/g·min. This result agrees with what was previously reported by our research group for this material [185]. Additionally, the CO_2 capture capacity of ACF3-CNT was 1.21 mmol/g, with a CO_2 capture rate of 0.024 mmol/g·min; and 1.43 mmol/g (23% more than ACF) at 90 min. Moreover, the heat-treated modified adsorbent (ACF3-CNT-AT1) captured 1.61 mmol/g CO_2 at a rate of 0.032 mmol/g·min. In this way, it was possible to further increase the CO_2 capture capacity by almost 40% with respect to the pristine material (ACF) while maintaining fast kinetics. In addition, two kinetic models were used to describe the CO_2 capture rate of ACF, ACF3-CNT and ACF3-CNT-AT1. According to the correlation coefficients (R^2), see Table 3.3, the experimental data of the materials were slightly better described by the pseudo first order model. This model assumes that the limiting step in an adsorption process is the mass transfer of the adsorbate to the surface of the adsorbent [297]. The theoretical values of q_e obtained from the pseudo first order model agree with q_e (exp) and the capture rate constants (k_1) were 0.066, 0.026 and 0.06 min^{-1} for ACF, ACF3-CNT and ACF3-CNT-AT1, respectively. The considerable increase in the k_1 constant for ACF3-CNT-AT1 corroborates the improvement in kinetics, even though the q_e values were similar.

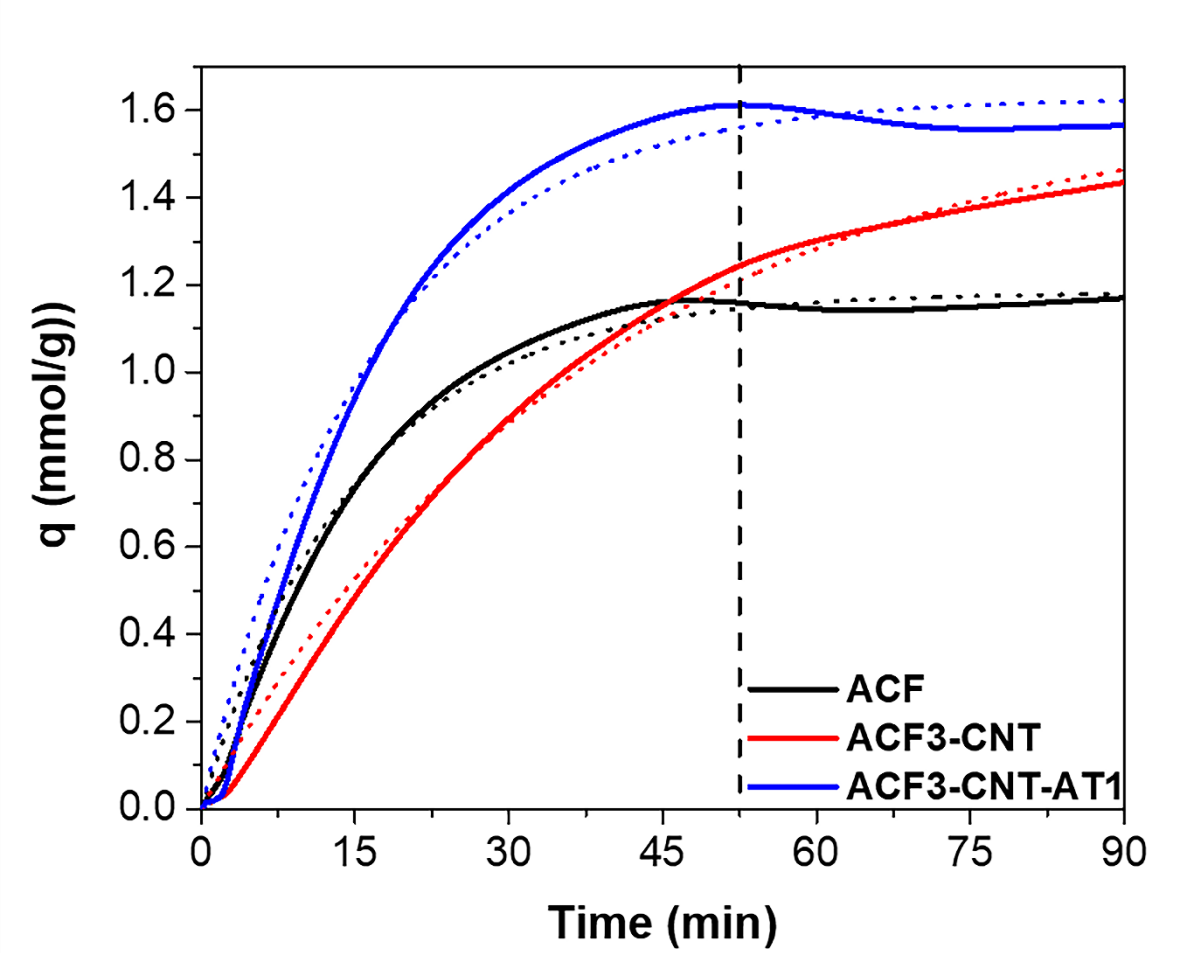

Figure 3.10 *CO_2 capture kinetics of ACF, ACF3-CNT and ACF3-CNT-AT1 at 25° C and 1 bar, using a pure CO_2 flow of 30 mL/min. Experimental data (solid lines) and the pseudo first-order model fit (dotted lines).*

Table 3.3 *Kinetic constants for CO_2 capture of ACF, ACF3-CNT and ACF3-CNT-AT1.*

Equation parameters	**ACF**	**ACF3-CNT**	**ACF3-CNT-AT1**
Pseudo first-order			
k_1 (min^{-1})	0.066	0.026	0.060
q_e (mmol/g)	1.18	1.61	1.62
R^2	0.98	0.99	0.97
Pseudo second-order			
k_2 (g/(mmol·min))	112.6	0.008	0.033
q_e(mmol/g)	0.11	2.31	1.97
R^2	0.96	0.98	0.94

Fast CO_2 capture kinetics have been reported as one of the desirable criteria for a good CO_2 capture material [137]. Furthermore, the increase in CO_2 capture capacity at atmospheric pressure or low pressure is mostly controlled by the surface chemistry of the material and not by its textural properties as previously reported [155]. Therefore, the increase in highly reactive edge sites formed during air treatment have been reported to be able to physisorb CO_2 by Van Der Waals interactions [284,285]. In addition, the increase of basic groups by the growth of CNT, reflected in the surface charge distribution and FTIR analysis (Figure 3.8), also contributed to CO_2 capture through pi-pi interactions on the surface of carbon materials derived from graphitic sheets (Figure 3.11) [295,296].

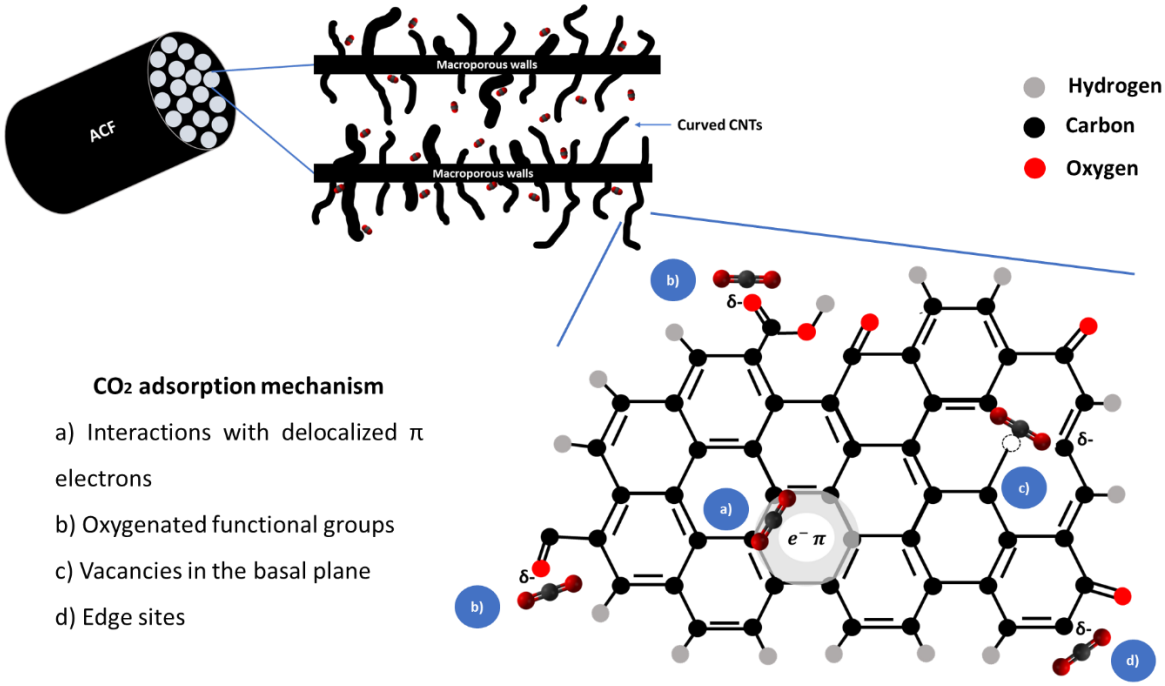

Figure 3.11 *Suggested CO_2 capture mechanism of CNT-modified ACFs [284,285,295,296].*

CO_2 capture isotherms were performed for ACF and for the sample that showed the best CO_2 capture capacity (ACF3-CNT-AT1) in the kinetic experiments (Figure 3.12

a). The static CO_2 capture capacity at 25 °C of ACF and ACF3-CNT-AT1 reached capacities of 1.33 and 1.71 mmol/g at 1 bar and 2.30 and 3.51 mmol/g at 10 bar, respectively. At atmospheric pressure the static CO_2 capture performance improved by almost 28.5%. At higher pressures, the CNT-modified material improved its performance over the pristine material, up to 52.6 % at 10 bar. The increase in CO_2 capture capacity at low pressure is mostly controlled by the surface chemistry of the material and the improvement at higher pressures has been reported to be related to the increase in specific specific area [155].

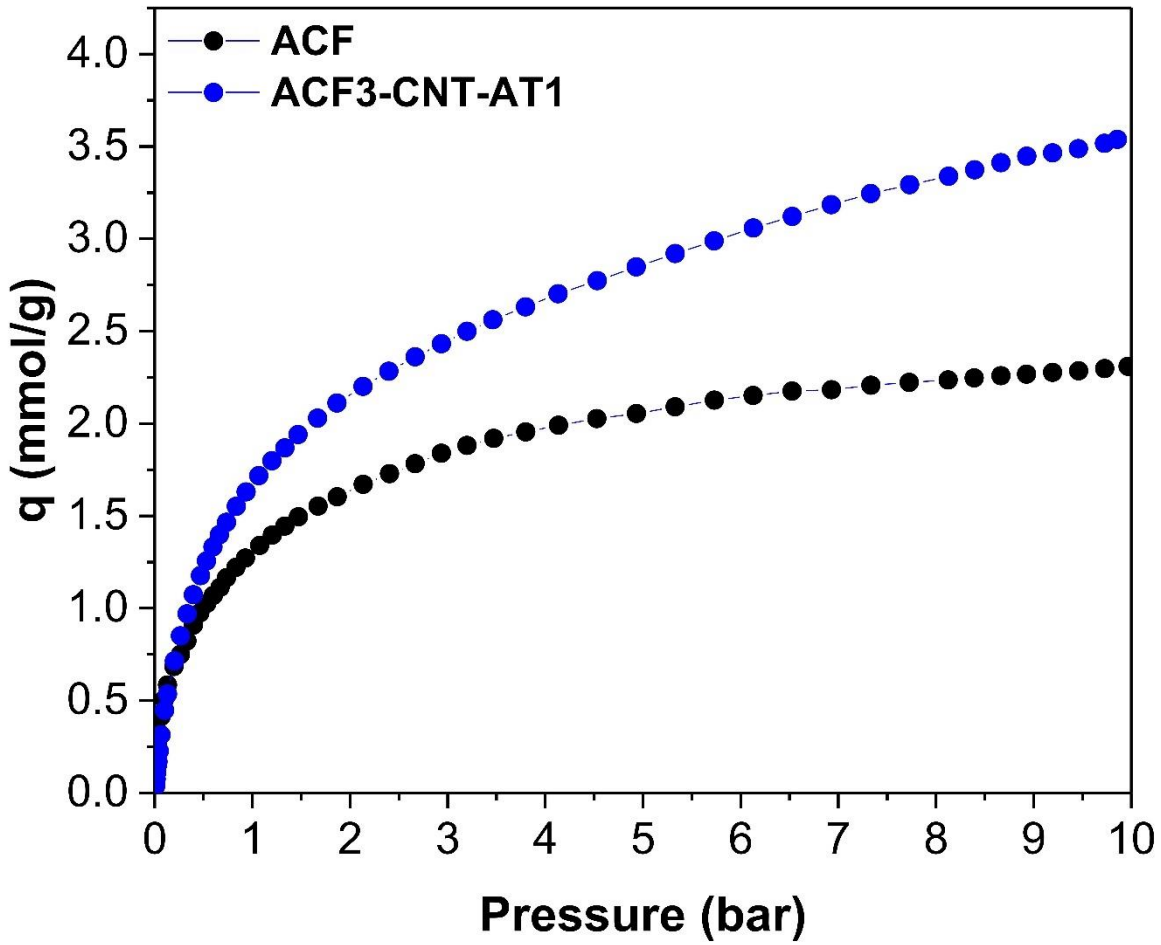

Figure 3.12 *a) CO_2 adsorption isotherms at 25 °C and pressures up to 10 bar from ACF and ACF3-CNT-AT1.*

In addition, CO_2 capture isotherms at different temperatures (25, 50 and 75 °C) of ACF and ACF3-CNT-AT1 (Figure 3.13 a) were realized to calculate the isosteric heat of adsorption (Figure 3.13 b). For both materials, the isosteric heat values were similar and the CO_2 adsorption was carried out by physisorption [236]. The ACF3-CNT-AT1 sample presented constant values of around 26 kJ/mol throughout the range of the CO_2 adsorbed. The constant value of isosteric heat can be interpreted as homogeneity in the interaction between the adsorbent and the CO_2 molecules [298]. Moreover, for ACF, the isosteric heat values decreased from 28 to 26 kJ/mol as the amount of CO_2 increased. The decrease in isosteric heat has been attributed to the disappearance of favorable adsorption sites [236].

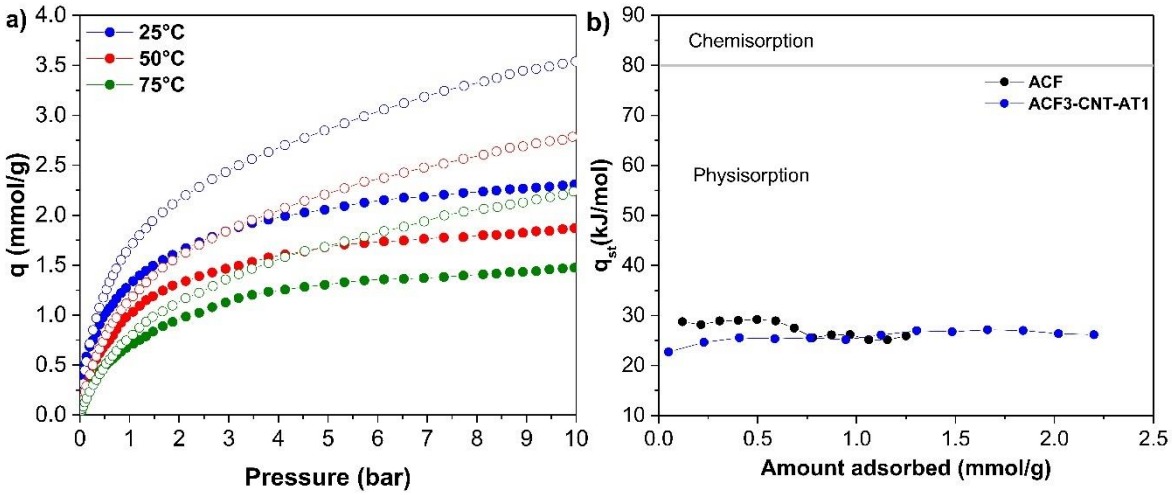

Figure 3.13 *a) CO_2 adsorption isotherms at different temperatures (25, 50 and 75°C) and pressures up to 10 bar for ACF (solid points) and ACF3-CNT-AT1 (empty points) and b) Isosteric heat of adsorption.*

The CO_2 capture capacity of the materials developed during this work was compared with that of similar carbon materials reported in the literature (Table 3.4). The capacities for the CNT-modified fibers were similar and even higher than materials

with larger specific surface areas, which indicates that not only the textural properties are relevant.

Table 3.4 *CO_2 capture capacity of different carbon materials.*

Material	Sorption capacity (mmol/g)	Adsorption conditions	BET specific surface area (m^2/g)	Ref.
ACF	1.33	25 °C, 1 bar	2	This work
ACF	2.30	25 °C, 10 bar	2	This work
ACF3-CNT-AT1	1.71	25 °C, 1 bar	452	This work
ACF3-CNT-AT1	3.51	25 °C, 10 bar	452	This work
Bagasse-based activated carbon	0.45	30 °C, 1 bar	923	[299]
Rice husk carbon (RHC)	0.7	25 °C, 1 bar	249	[300]
RHC modified with potassium citrate	1.55	25 °C, 1 bar	1343	[300]
Pine sawdust biochar	1.35	30 °C, 1 bar	582	[301]
Sugarcane bagasse and hickory wood	0.25-1.67	25°C, 1 bar	-	[302]
Sawdust	0.95	25 °C, 1 bar	524	[303]
Sawdust activated with urea phosphate	1.34	25 °C, 1 bar	1189	[303]
N-Doped Porous Carbon	3.3	25 °C, 1 bar	1658	[304]
Water chestnut shell-derived N/S-doped carbons	4.54	25 °C, 1 bar	1353	[305]
Potassium Bitartrate-derived porous carbon	3.55	25 °C, 1 bar	947	[306]

Three CO_2 sorption-desorption cycles were performed by ACF and ACF3-CNT-AT1 (Figure 3.14) with 50 min of CO_2 capture and 30 min of CO_2 desorption. For ACF, capture capacities of 1.17, 1.16 and 1.16 mmol/g were obtained for the first 3 sorption cycles, respectively, with a reversibility of 99%. On the other hand, ACF3-CNT-AT1 captured 1.61, 1.53 and 1.54 mmol/g for the first 3 sorption cycles, respectively, with a regeneration capacity of 95%. These results are of great relevance since both materials have a high regeneration capacity, which make evident that the main CO_2 capture mechanism is by physisorption. In addition, the CO_2 capture kinetics remain constant during 3 cycles (0.023 and 0.032 mmol/g·min for ACF and ACF3-CNT-AT1, respectively).

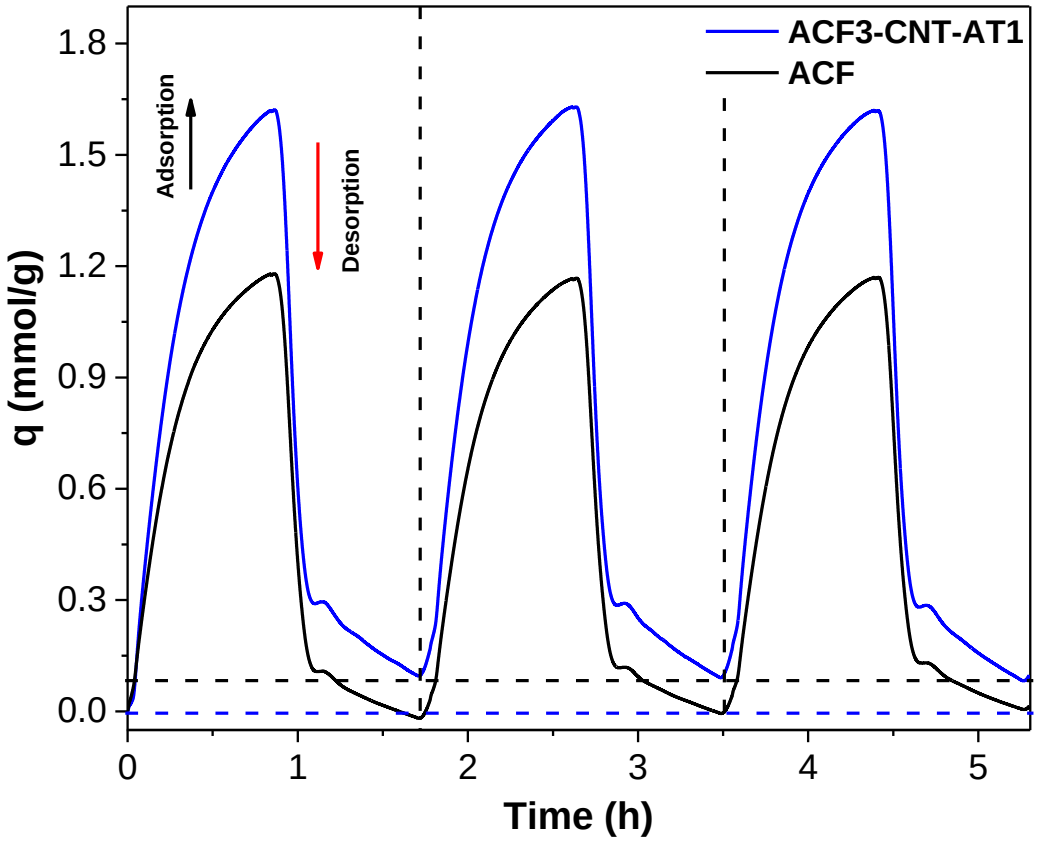

Figure 3.14 *Sorption (black arrow)-desorption (red arrow) cycles of ACF and ACF3-CNT-AT1 at 25 °C and 1 bar using a flowrate of pure CO_2 of 30 mL/min.*

CO_2 capture tests were carried out also at 80 °C (Figure 3.15 a), a temperature similar to the gases emitted by a combustion engine. A decrease in CO_2 capture capacity was observed, achieving a capacity of 0.27 and 0.46 mmol/g at 50 min (77 and 72% lower) and 0.32 and 0.53 mmol/g at 90 min (63 and 67% lower) for ACF and ACF3-CNT-AT1, respectively. This decrease in the CO_2 capture capacity is most likely due to the increase of the CO_2 kinetic energy which causes dispersion and/or Van der Waals forces to be less efficient [273,284].

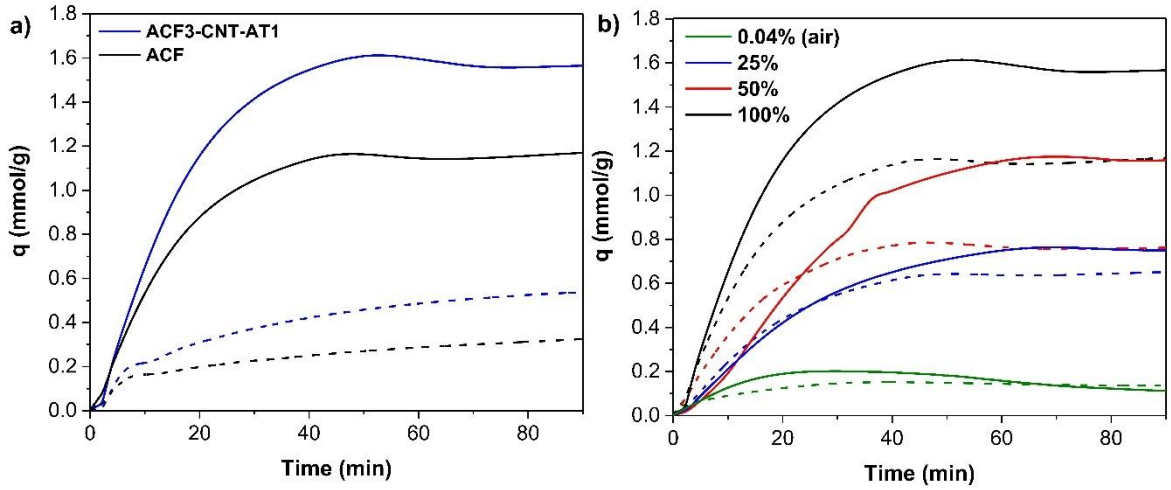

Figure 3.15 *a) Capture kinetics of CO_2 (flowrate of pure CO_2 of 30 mL/min) at 25 °C (solid line) and 80 °C (dotted line) of ACF and ACF3-CNT-AT1 and b) CO_2 capture kinetics at concentrations of 100%, 50%, 25% and 0.04% (air) of ACF (dotted lines) and ACF3-CNT-AT1 (solid lines) at 1 bar and 25 °C.*

The effect of CO_2 concentration (100%, 50%, 25% and air (0.04%)) on CO_2 capture capacity of samples was evaluated (see Figure 3.15 b). The CO_2 capture capacity of ACF and ACF3-CNT-AT1 decreased as the CO_2 concentration decreased to 50 and 25%, showing slower kinetics (equilibrium approx. 70 min). It has been reported that the decrease in kinetics as CO_2 concentration decreases can be attributed to CO_2 dilution [307]. For ACF, the CO_2 capture rate decreased from 0.023 mmol/g·min

with pure CO_2 to 0.017 and 0.012 mmol/g·min with 50 and 25% CO_2, respectively. For ACF3-CNT-AT1, the CO_2 capture rate decreased from 0.032 mmol/g·min with pure CO_2 to 0.017 and 0.011 mmol/g·min with 50 and 25% CO_2, respectively (Table 3.5).

The capture capacity of ACF3-CNT-AT1 when using a concentration of 50% CO_2, decreased 28%, from 1.61 to 1.17 mmol/g, and 33%, from 1.16 to 0.78 mmol/g, for ACF. For the experiment with 25% CO_2 concentration, a capacity of 0.76 mmol/g for ACF3-CNT-AT1 (53% lower) and 0.64 mmol/g for ACF (45% lower) was obtained. Finally, for the experiment with air containing 0.04% of CO_2, a capture capacity of 0.2 mmol/g for ACF3-CNT-AT1 (88% less) and 0.15 mmol/g for ACF (88% less) was achieved. This non-linear decrease in the CO_2 capture capacity, with respect to the concentration of this gas, showed a certain selectivity towards CO_2. The apparent selectivity (Q_{CO_2}/Q_{N_2}) reported values at 25 °C and 1 bar of 1.65 and 2.48 for ACF and ACF3-CNT-AT1, respectively, which indicates that the improved adsorbent with CNT was more selective for CO_2.

Table 3.5 *CO_2 capture kinetics and capacities of ACF and ACF3-CNT-AT1 at 25 °C, 1 bar and different CO_2 percentage.*

Material	**CO_2 percentage (%)**	**Q_{max} (mmol/g)**	**$Q_{max,\ time}$ (min)**	**Capture rate at $Q_{max,\ time}$ (mmol/g·min)**
ACF	100	1.16	50	0.023
	50	0.78	45	0.017
	25	0.64	50	0.012
	Air	0.15	35	0.004
ACF3-CNT-AT1	100	1.61	50	0.032

Table 3.5 (Continuation)			
50	1.17	68	0.017
25	0.76	66	0.011
Air	0.2	26	0.007

3.4 Conclusions

This work demonstrates that it is possible to homogeneously grow CNT on carbonized bagasse fibers, from the mezcal industry, and efficiently apply them to capture CO_2. A concentration of iron salts of $FeCl_3$ and $FeCl_2$ of 6 and 3 g/L, respectively, homogeneously impregnate magnetite nanoparticles (< 25 nm) on ACF for CNT growth (ACF3-CNT). Curved CNTs with 2 different types of wall array with an inner diameter of 20-40 nm are synthesized, which increases the specific surface area of the modified ACF from 2 to 252 m^2/g. Subsequently, when treating the CNTs - modified ACF with air at 300 °C for 1 minute (ACF3-CNT-AT1), a change in the CNTs texture is observed, which increases the specific surface area more than 220 times (up to 452 m^2/g) compared to the pristine material (2 m^2/g). The dynamic CO_2 capture capacity of ACF3-CNT-AT1 increases almost 40% (from 1.16 to 1.61 mmol/g), that is mainly attributed to the increase of both basic groups and highly reactive edge sites, as suggested by potentiometric titrations, FTIR and TEM analysis. Also, the static CO_2 capture capacity of ACF3-CNT-AT1 improves 28.5% (from 1.33 to 1.71 mmol/g) at 1 bar and 52.6% (from 2.30 to 3.51 mmol/g) at 10 bar, attributed to the increase in specific surface area. In addition, fast adsorption kinetics are maintained during the first 50 min, regeneration capacities of 95% are achieved in three sorption-desorption cycles, and apparent selectivity index (CO_2/N_2) of 2.48

was obtained for ACF3-CNT-AT1. Finally, this work demonstrates the feasibility of improving the rapid CO_2 capture capacity of a material of natural origin, such as carbonized bagasse fibers, through the homogeneously growth of CNT on its surface.

Chapter 4:

Growth of carbon nanofibers on a macroporous biochar to improve its CO_2 capture capacity.

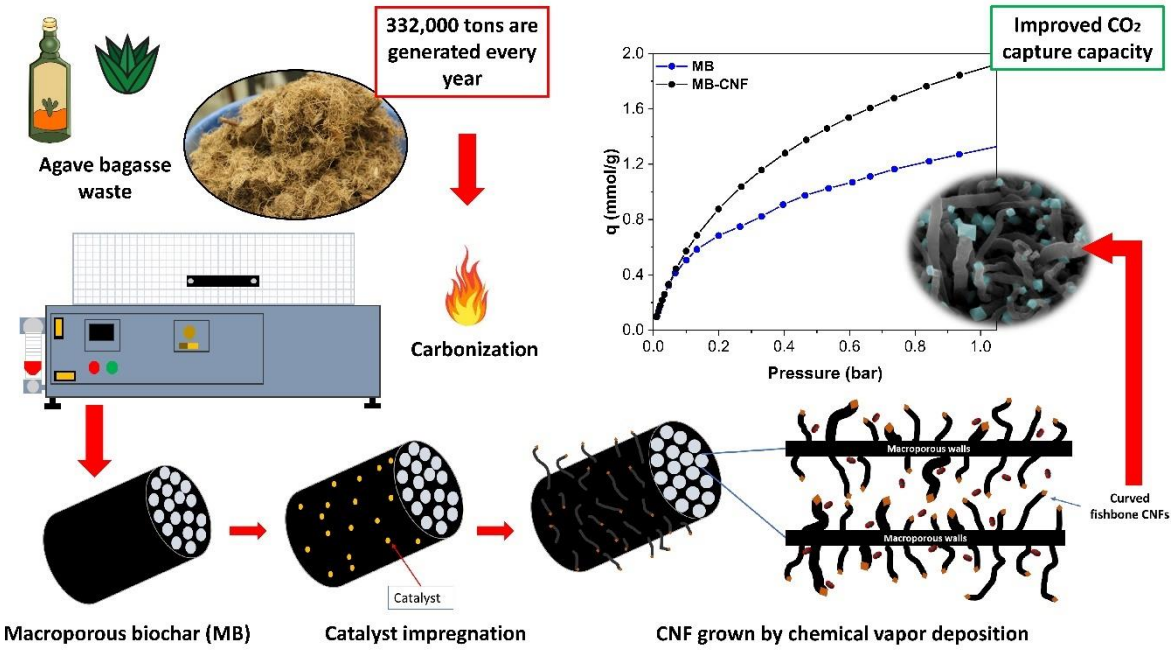

ABSTRACT

CO_2 capture through porous solids, such as carbon materials, presents an excellent low-cost and energy-consuming option as a replacement for liquid amines currently used in CO_2 capture systems. Furthermore, modification through carbon nanostructures, such as carbon nanofibers, could improve the CO_2 capture capacity without reducing kinetics, which is an essential factor in CO_2 capture processes. Therefore, in this work a new hybrid carbon material was prepared by modifying a macroporous biochar (MB) with fishbone carbon nanofibers (CNF) to improve its CO_2 capture capacity. The growth of CNF was carried out by chemical vapor deposition (CVD) for 1 min at 700 °C by using octahedral-shaped magnetite nanoparticles as a catalyst and acetylene as a carbon source. MB and CNF-modified MB (MB-CNF) were characterized by N_2 physisorption, X-ray photoelectron spectroscopy (XPS), potentiometric titrations, Raman spectroscopy, and scanning and transmission electron microscopy. The CO_2 capture kinetics were obtained with a thermogravimetric analyzer (TGA) and the CO_2 capture was obtained by adsorption isotherms at pressures of up to 10 bar and temperatures of 0-75 °C. In addition, the isosteric heat of adsorption was calculated with the Clausius-Clapeyron equation. CNFs were homogeneously grown on the surface of the MB, which increased the specific surface area from 2 to 422 m^2/g. Furthermore, through the growth of CNF, it was possible to increase the CO_2 capture capacity more than 40%, from 2.3 to 3.25 mmol/g at 25 °C and 10 bar, maintaining rapid capture kinetics (0.028 mmol/g·min). This result is mainly attributed to the increase in basic groups, reactive edge sites, and increase in specific surface area. A constant value of

isosteric heat of adsorption of MB-CNF of around 29 kJ/mol and excellent regeneration capacity of more than 97% for 3 desorption-desorption cycles were obtained. The rapid sorption-desorption kinetics and excellent regeneration capacity of CNF-modified MB makes this material suitable to be used in CO_2 capture systems.

4.1 Introduction

Since the beginning of the industrial era, the burning of fossil fuels to generate energy, livestock processes, industrial processes, waste management and the extraction of oil, gas and minerals have contributed to most carbon dioxide emissions (CO_2) and other greenhouse gases [9,308]. The growing emission of CO_2 has caused a rapid increase in global warming and climate change, in consequence different strategies have been sought to reduce the concentration of this gas in the atmosphere [309,310]. CO_2 capture and storage are considered one of the most promising and mature technologies to reduce CO_2 emissions and concentration in the atmosphere [310,311]. However, the most used method currently is the post-combustion capture of CO_2 by using liquid amines, which have important disadvantages such as the need of very large equipment, they are corrosive, require high-energy consumption for their regeneration and have a high toxicity [312-314]. Due to this, the capture of CO_2 through porous solids, such as carbons materials, has received greater attention due to their lower cost, low energy consumption for their regeneration, are non-corrosive, and possess high thermal and mechanical stability [315-317]. For the generation of carbon materials, different raw materials have been used such as petroleum coke, organic polymers, biomass, including others [318-321]. Among the different porous materials that have been investigated,

carbons from sustainable sources (e.g., agricultural waste) are of greater interest due to their low cost and by the fact that a waste is used to produce materials with added value [104]. Currently, most studies on carbon materials have focused on improving the CO_2 capture capacity increasing the specific surface area by chemical or physical activation [149,322,323]. However, this process generates micro and mesopores in which the CO_2 must diffuse into meso and micropores to be adsorbed, which makes the adsorption kinetics relatively slow at low pressures. In this sense, carbon nanofibers (CNF) have great specific surface area readily available and high reactivity due to the border and basal planes that form the graphite sheets, which can react with CO_2 through electrostatic interactions [324]. Therefore, in this work the effect of the growth of fishbone-type carbon nanofibers (CNF) in a macroporous biochar (MB), from the tequila and mezcal industry, in the CO_2 capture performance will be evaluated.

4.2 Experimental Section

4.2.1 Reagents and precursor

All the chemicals used in this research were reagent grade. $FeCl_3 \cdot 6\ H_2O$, $FeCl_2 \cdot 4\ H_2O$, HNO_3, H_2SO_4, 0.1 N NaOH and 0.1 N HCl were obtained from Sigma Aldrich. Deionized water was used for the preparation of all solutions. The precursor (agave bagasse fibers from *Agave salmiana* plant) was provided by a distillery located in San Luis Potosi, Mexico.

4.2.2 Carbonization of bagasse fibers

The methodology used for the carbonization of the bagasse fibers is a modification of a previous study [184]. The agave bagasse fibers were washed, dried at 90 °C for 48 h and evenly fractionated at ~ 0.5 cm. Subsequently, the fibers were carbonized in a Barnstead Thermolyne 21100 tube furnace under an inert atmosphere of N_2 at a temperature of 600 °C for 2 h to favor the formation of macroporous channels in the bagasse fibers [184]. The biochar obtained was then sieved (35x60 USA Standard test sieve) and washed with HCl to reduce ash content as mentioned below. 1 g of biochar was placed in a polypropylene tube, then 40 mL of 3M HCl solution was added and stirred at 100 rpm on an orbital incubator for 72 h. Subsequently, the residue was decanted, and the biochar was rinsed with deionized water until no variations in pH were measured. The material was dried at 90 °C for 48h and stored in a N_2 atmosphere. The material named as ACF in chapter 3, was named as macroporous biochar (MB) in this chapter to avoid ambiguities.

4.2.3 Impregnation of iron nanoparticles in MB

Chemical vapor deposition (CVD) was used to grow carbon nanofibers (CNF) onto the MB surface. The methodology for the impregnation of the iron catalyst is a modification of the chemical precipitation of iron salts in an alkaline environment known as the Massart process [277,278]. The chemical reaction to synthesize magnetite nanoparticles (Fe_3O_4) can be formulated according to Equation 4.1 [279].

$$Fe^{2+} + 2Fe^{3+} + 8OH^- \rightarrow Fe_3O_4 + 4\ H_2O \qquad (\textit{Equation 4.1})$$

For the impregnation of the iron nanoparticles, solutions of $FeCl_3 \cdot 6\ H_2O$ and $FeCl_2 \cdot 4\ H_2O$ were prepared with a concentration of 6 and 3 g/L, respectively. 5 mL of each solution were mixed under constant stirring and 100 mg of MB were added. The suspension was mixed under a N_2 atmosphere, and the pH was adjusted to 12. It was then placed in a microwave reactor (Anton Paar model "Monowave 400") at 160 °C for 10 min. Finally, MB impregnated with catalyst was washed with deionized water and dried at 90 °C for 48 h.

4.2.4 CNF growth by CVD

After impregnation of the MB with the iron catalyst, carbon nanofibers (CNF) were grown by chemical vapor deposition or CVD in a Barnstead Thermolyne 21100 model tube furnace. A certain amount of catalyst-impregnated MB was used, and a temperature of 700 °C was established with a heating ramp of 25 °C/min and a N_2 flow of 40 mL/min. Acetylene (C_2H_2) was used as a carbon source, which was injected for 1 min at a constant flow rate of 10 mL/min once the growth temperature was reached. Afterwards, the temperature and the N_2 flow were kept constant for 10 min. Finally, a post-treatment was carried out to remove amorphous carbon as described below: heating ramp of 15 °C/min and N_2 flow of 40 mL/min up to 300 °C. Once the temperature was reached, the atmosphere was changed to air with a flow of 20 mL/min for 1 min. This sample was named as MB-CNF.

4.2.5 Physicochemical characterization of materials

The morphology of MB and MB-CNF was analyzed by a scanning electron microscope (SEM), HELIOS NANOLAB 600i SEM. Before analysis, samples were

immobilized on a carbon tape retained in a SEM sample holder. A Transmission electron microscope (TEM, FEI's Tecnai F-30 operated at 300 kV) was used to further analyze the morphology and determine the type of CNF grown. The sample was suspended in isopropanol and then sonicated for 10 min. Finally, the sample was mounted on lacey carbon coated copper grids.

X-ray photoelectron spectroscopy (PHI 5000 VersaProbe II XPS, Physical Electronics) with a monochromatic Al-Kα (1486.6 eV) radiation was utilized to study the elemental composition and chemical state of the samples. The deconvolution of the spectra was processed using MultiPak 9.3 (or XPSPEAK 4.1) software. XRD patterns were obtained using a D8 Bruker Advance diffractometer with Cu-Kα radiation operated at 35 kV from 2θ range of 10-80° with steps of 0.02°. The CNFs structure was analyzed by Raman spectroscopy (Renishaw with Leica DM LM), which was performed between 500 and 3500 cm^{-1}, with a scan duration of 60 s and a microscope magnification of 50x, providing a resolution of 1 μm.

The surface area and pore size distribution were determined from the nitrogen adsorption isotherm at 77 K through a Micromeritics ASAP 2020 physisorption equipment. The specific surface area was determined by using the Breunaer-Emment-Teller (BET) equation and the pore size distribution was obtained with the density functional theory (DFT). The surface charge distribution and the point of zero charge (pH_{pzc}) were determined by potentiometric titration using a METTLER TOLEDO T70 automatic titrator, with 0.1 N NaOH and 0.1 N HCl as the titration system. The values obtained in the potentiometric titration were analyzed using the SAEIUS-pK-dist program © 1994 software.

4.2.6 CO_2 capture experiments

The CO_2 capture kinetics were carried out using a thermogravimetric analyzer (TGA) model SETSYS EVOLUTION TGA-DTA/DSC from Setaram Instrumentation. A stabilization stage was carried out as described below; The sample was exposed to a flow of 30 mL/min of N_2 and the temperature was increased from room temperature to 105 °C and kept constant for 30 min, and then the temperature decreased to 25 °C. Afterwards, the CO_2 capture kinetics were carried out with CO_2 of 99.98% purity and a flow of 30 mL/min for 90 min. The weight change of the samples during CO_2 exposure was attributed to the mass of CO_2 captured, and this was estimated per gram of material (Equation 4.2). Furthermore, the equilibrium time was determined.

$$Q = \frac{m_t - m_i}{m_0(PM)} \quad \textit{(Equation 4.2)}$$

Where Q is the CO_2 capture capacity in mmol/g material, m_t and m_i is the difference in mass (mg), m_0 (g) the initial mass of the adsorbent material and PM is the molecular weight of CO_2 (mg/mmol).

The CO_2 capture isotherms (at 0, 25, 50 and 75 °C) of MB and MB-CNF were studied in a Micromeritics ASAP 2050 automatic manometric sorptometer up to a pressure of 10 bar. Before measurements, the materials were degassed at 150 °C for 8 hours under vacuum. Three sorption-desorption cycles of MB-CNF were performed, where the desorption was carried out by evacuating the system until reaching a pressure of approximately 5 μmHg.

In addition, the isosteric heat of adsorption (q_{st}) was calculated from the isotherms at 25, 50 and 75 °C. This value represents the strength of interaction between

adsorbate-adsorbent, the degree of heterogeneity on the surface of the material, as well as whether the CO_2 sorption process is by chemisorption or physisorption. This study was carried out from the analysis of the q_{st} curve (kJ/mol) vs. amount of CO_2 adsorbed (mmol/g) using the Clausius-Clapeyron equation:

$$q_{st} = R\left[\frac{\delta \ln p}{\delta\,(1/T)}\right]_{n_{ads}} \quad \textit{(Equation 4.3)}$$

where p (kPa) is the equilibrium pressure, T (K) is the adsorption temperature and R (8.314 kJ/mol·K) is the ideal gas constant. The equilibrium pressure (p) for each amount of CO_2 adsorbed (n_{ads}) was estimated by non-linear interpolation from the data of the experimental isotherms at different temperatures. The slope of the straight line of adsorption (ln p vs. 1/T) corresponds to the isosteric enthalpy of CO_2 adsorption for a defined amount of CO_2 adsorbed.

4.3 Results and Discussion

4.3.1 Characterization of the macroporous biochar (MB) and catalyst impregnation

The morphology of the MB was analyzed by scanning electron microscopy (SEM). Figure 4.1 a) shows the macroporous channels with a diameter between 2-30 µm, which are naturally related to their vascular layers [184]. Furthermore, in Figure 4.1 b) it was appreciated the rough surface of the MB made up of channels parallel to fibers with some pores along their entire length.

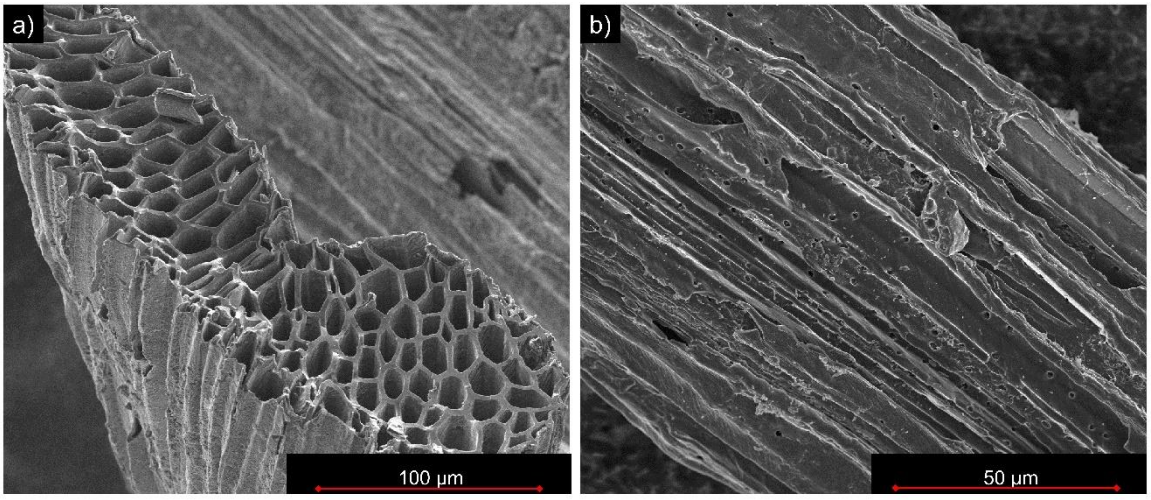

Figure 4.1 *SEM secondary electrons images of a) MB tip and b) MB surface.*

Figure 4.2 a) shows the MB impregnated with the metal catalyst, where the lightest points are the iron spheric nanoparticles, which are uniformly distributed on the surface of the MB. The good distribution of the catalyst can be attributed to a good interaction between the substrate (MB) and the catalyst (iron nanoparticles) as large particle aggregates do not appear, which means that there are many catalytic sites for the growth of CNF [227]. In addition, the diameter of 60 nanoparticles from micrograph reported in Figure 4.2 b) was measured using the ImagenJ program, and the size distribution was presented by a histogram in Figure 4.2 c). It was observed that the impregnated particles on MB have a size distribution between 12 and 33 nm with an average of 21 nm, which is an ideal size for the growth of CNF [229,230].

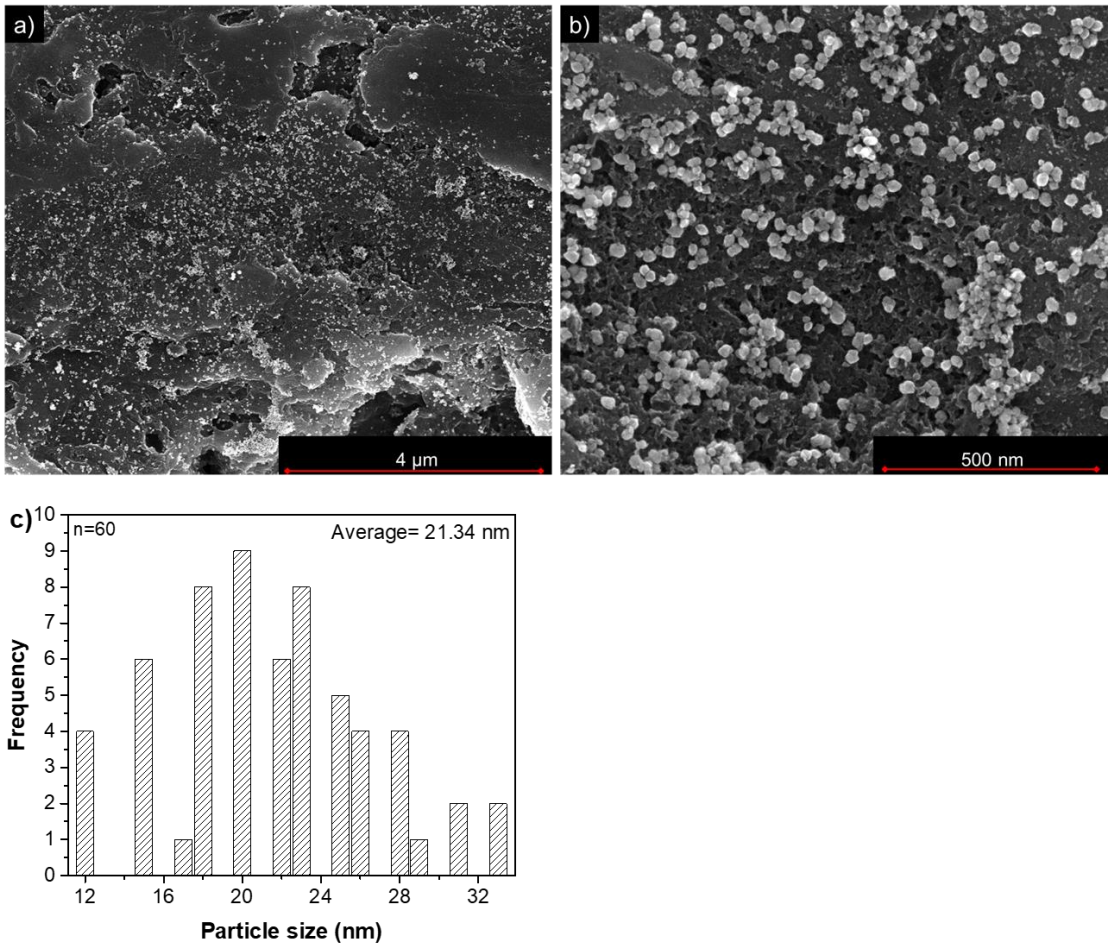

Figure 4.2 *SEM secondary electron images of a, b) catalyst-impregnated MB and c) size histogram of impregnated catalyst (n=60).*

4.3.2 Growth and characterization of CNF

4.3.2.1 Structural characterization of CNFs grown onto MB

Figures 4.3 a) and b) show the homogeneous growth of curved CNFs on the MB in two different areas. In Figures 4.3 c) and d), it was observed that the catalyst is located at the tip of the CNF, which indicates tip growth, where the carbon atoms displace the catalyst during the growth of the CNF [218]. Furthermore, it can be observed that the morphology of the catalyst changed during the CVD process, which is attributed to the sintering of the spherical particles to form octahedral or

diamond-shaped nanoparticles (Figure 4.3 e) and f). Also, it can be noted that the size of the catalyst governed the diameter of the nanofibers, as it has been commonly reported for the growth of this type of structures [217,325]. On the other hand, it was found that the catalyst has a lateral arrangement in the tip of the CNF, so it is assumed that the CNFs grow preferably on two of the faces of the octahedral catalyst. It has been reported that the nucleation of graphitic sheets grown during the CVD process largely depends on the crystal orientation of the metal particles and certain crystalline planes of the metal nanoparticles can be prioritized [325,326].

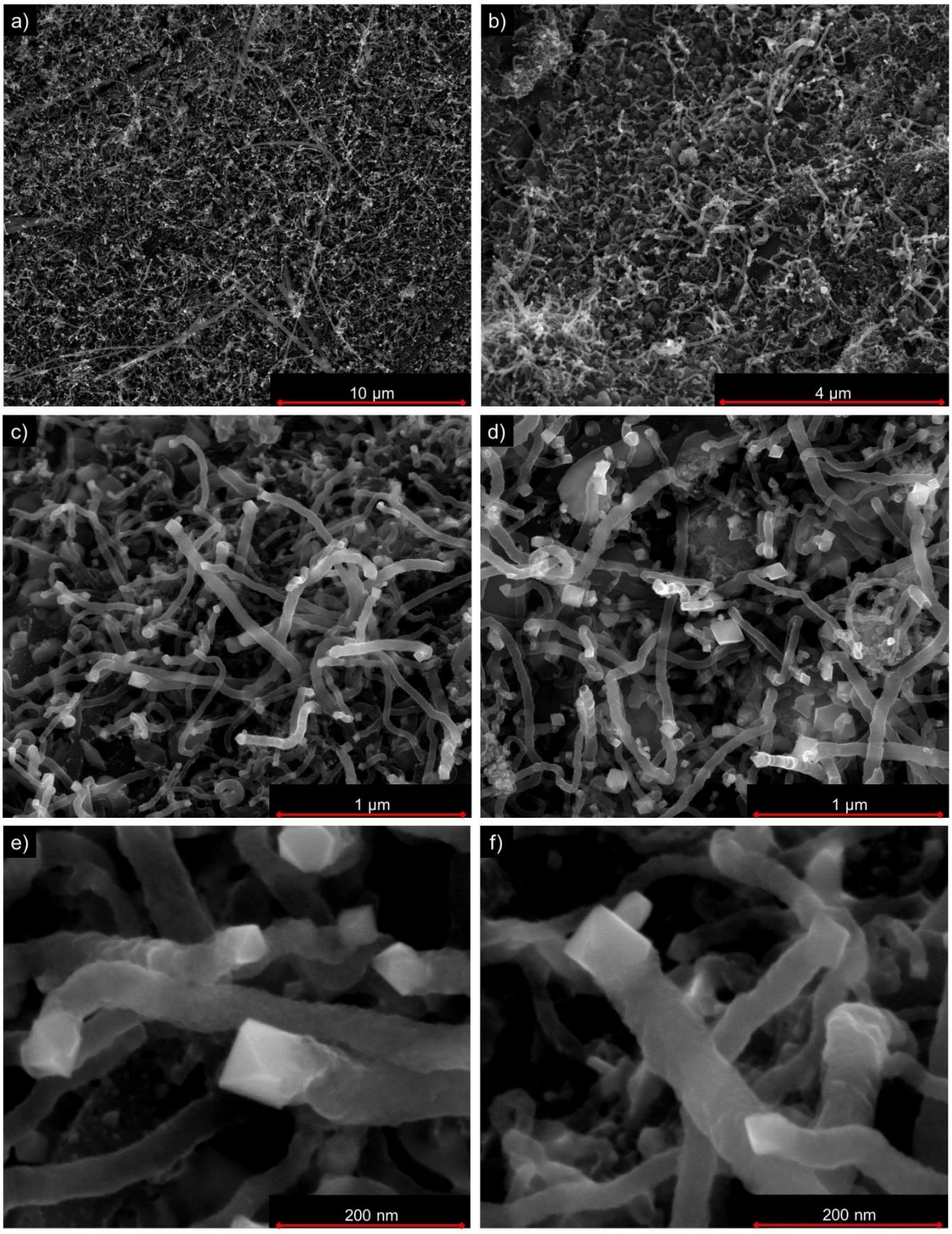

Figure 4.3 *a-f) Secondary electron SEM images of different zones and magnifications of MB-CNF.*

The CNF grown on the MB was analyzed by transmission electron microscopy to estimate the type of CNF that was grown. TEM micrographs of the CNF body are presented in Figure 4.4 a) and b), where curved CNFs with diameters between 30-50 nm were observed. Figures 4.5 a) shows the interface between the octahedral catalyst and the graphitic sheets that make up the CNF and Figure 4.5 b) reports the tail of the CNF. The red arrows represent the orientation of the growth of the carbon nanofibers and the red lines the orientation of the graphitic sheets. From this, it was concluded that fishbone-type CNFs were grown because in this type of structure the graphene layers are arranged in the shape of a cone with angles that range between 0 and 90° with respect to the growth direction of the fiber [205,327,328], as observed in Figures 4.4 c) and d).

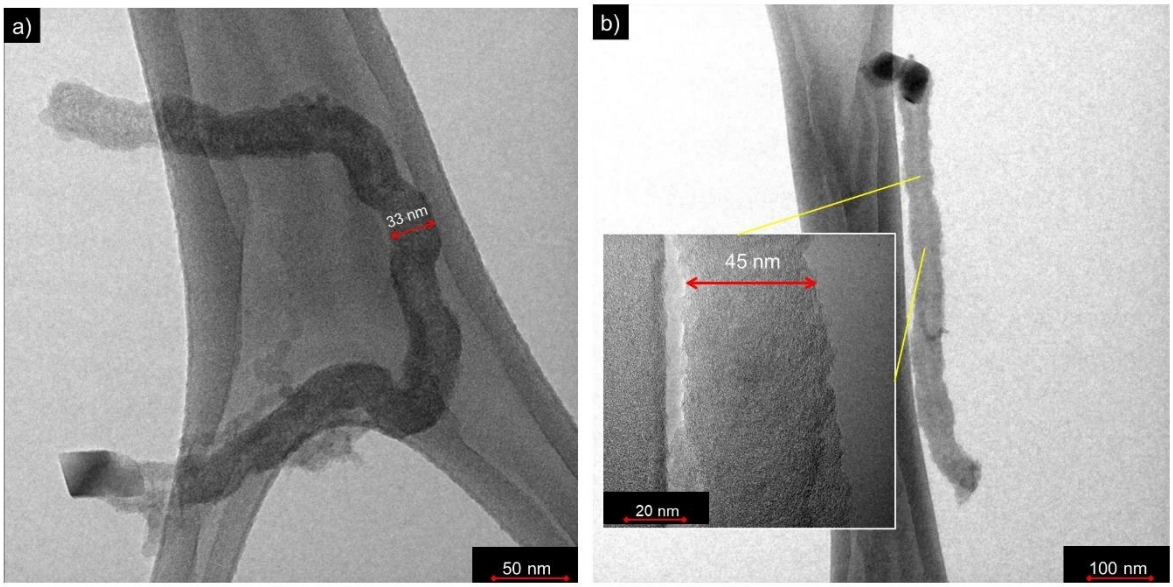

Figure 4.4 *Representative TEM images of CNF from a) and b) MB-CNF.*

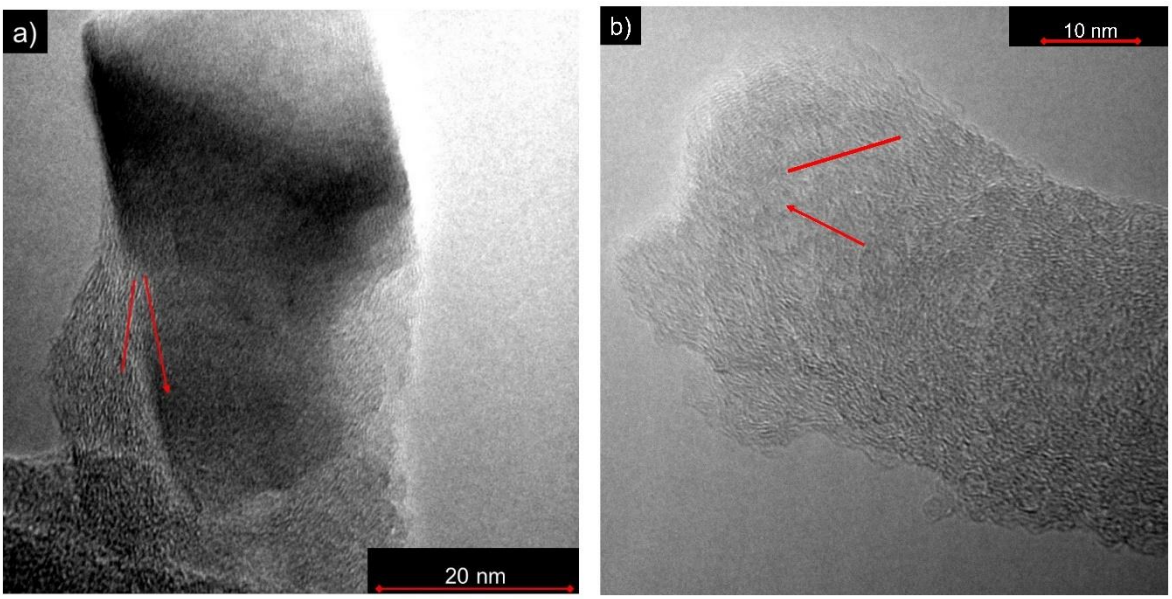

Figure 4.5 Representative TEM images of CNF from MB-CNF: a) CNF tip and b) CNF tail (**red line**= direction of graphic planes of CNF and **red arrow**= direction of fiber axis).

Through Raman spectroscopy, the MB and MB-CNF were analyzed where (Figure 4.6), the D bands (~1320 cm^{-1}), G (~1580 cm^{-1}) and the 2D band (~ 2700 cm^{-1}) were identified. The G band (graphite band) is associated with in-plane vibrations of graphene sheets, that is, with the interlayer E_{2g} mode graphite symmetry that reflects the structural integrity of sp^2 hybridized carbon atoms. The D band (defect or disorder band) is related to defects in the walls of CNFs, with vacancies, impurities or other defects that break the vibration symmetry [194,286]. The 2D band is attributed to the overtone of the D band, but with the difference that it does not appear due to its proximity to the defects [287].

The MB showed bands with widths of approximately 293 cm^{-1} (D band) and 96 cm^{-1} (G band), whereas for MB-CNF these band withs were smaller, 287 cm^{-1} for D band and 81 cm^{-1} for G band. This decrease in bandwidths has been related to the increase in the number of ordered graphitic structures [288], and to the

disappearance of additional peaks related to impurities, amorphous carbon, and disordered carbon [289]. In addition, the I_D/I_G ratio was calculated, which is widely considered as a measure of the crystalline order of carbon materials and provides a good estimate of the level of defects [286-288]. Through the growth of CNF, the I_D/I_G ratio decreased from 0.82 for MB to 0.75 for MB-CNF, which has been attributed to fewer defects in carbon materials [291].

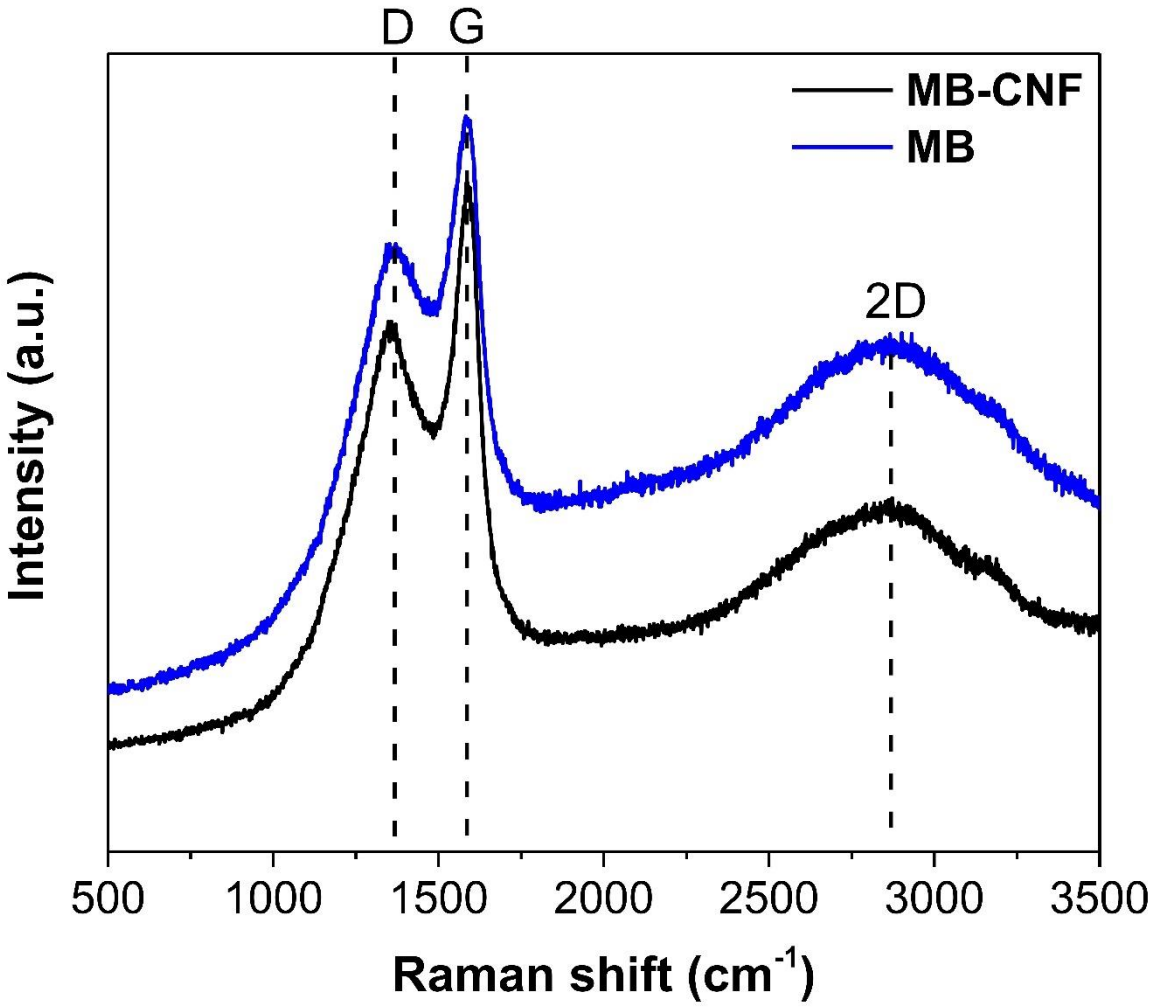

Figure 4.6 *Raman spectrum of MB and MB-CNF.*

4.3.2.2 Iron catalyst characterization in MB-CNF

EDS analysis of two zones corresponding to metallic nanoparticles were carried out at the tip of the CNFs of the MB-CNF sample (Figure 4.7), where the presence of C, O, Fe, Na, Ca and Si was detected in an average concentration of 78.5, 15.2, 4.9, 0.7, 0.4 and 0.3 (wt.%), respectively. Although this result does not prove the crystalline phase of the catalyst, it does provide an idea of its chemical composition, in which, if we omit the obvious presence of C and O, the element in majority is Fe.

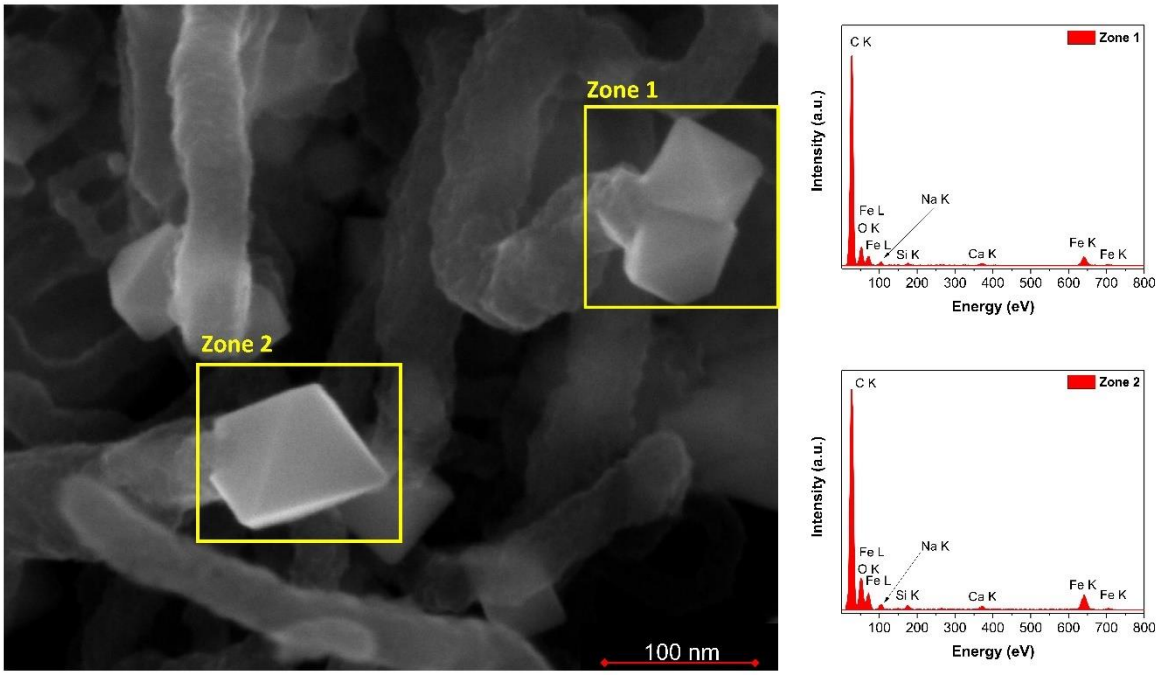

Figure 4.7 *SEM secondary electrons images of the catalyst at the tip of the CNF grown on MB, and EDS of the two areas marked with yellow boxes.*

X-ray diffraction (XRD) corroborated the crystalline phase of the catalyst impregnated on the MB before and after the CVD process. Figure 4.8 a) shows the diffractograms corresponding to the MB sample impregnated with catalyst and MB-CNF. Firstly, a wide band can be observed with a maximum 2θ value of 22.8 and 23.3° for MB-CNF and MB, respectively. This band has been reported for

lignocellulosic materials, attributed to a low degree of graphitization and presence of amorphous carbon [329-332]. Furthermore, immersed in this broadband, it can be distinguished a diffraction peak corresponding to the (002) plane of graphite (00-056-0159), and the (100) plane of graphite was also identified around 42° of a broadband present in both samples. The crystalline phase of the catalyst impregnated on the MB was identified as magnetite (01-080-6402). In both samples, the peaks located at 35.44, 43.07, 56.96 and 62.55° coincided with the mentioned crystallographic chart and, specifically for the MB-CNF sample, additional peaks could be identified at 30.09 and 54.44°.

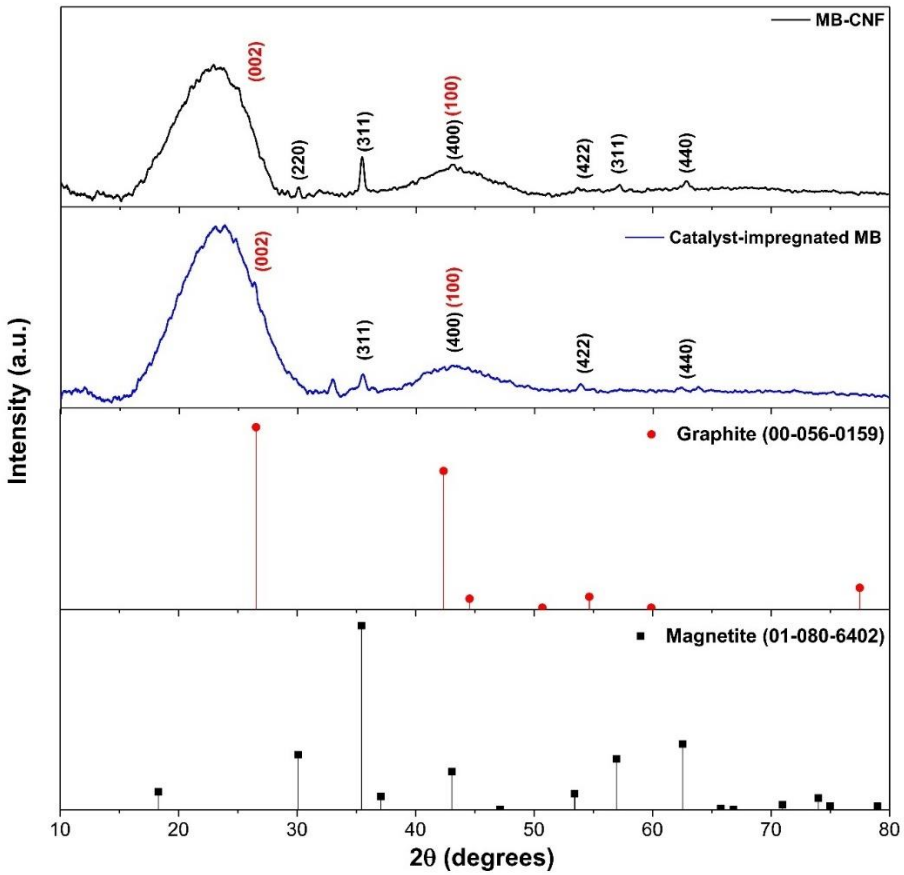

Figure 4.8 *X-ray diffraction patterns of MB-CNF and catalyst-impregnated MB.*

Because the magnetite signals in the diffractogram of Figure 4.8 might be inconclusive, deconvolution of the Fe2p signal from the XPS spectrum of MB-CNF was performed to corroborate the crystalline phase of the catalyst (Figure 4.9). The Fe2p peak was resolved into four peaks; 710.6 and 723.7 eV were assigned to the +2 oxidation state and 711.7 and 725.6 eV to the +3 oxidation state [333]. Based on the integrated areas of these subpeaks, the proportion of Fe^{2+} and Fe^{3+} was determined from the peaks of Fe2p1/2 and Fe2p3/2 where it was found that the ratio of Fe^{2+}/Fe^{3+} was 34/66 which almost corresponds to the 1:2 molar ratio that magnetite has in its structure (Fe_3O_4 =$Fe^{2+}Fe^{3+}{}_2O_4$) [333,334]. Furthermore, it has been reported that Fe_3O_4 does not have a satellite peak between the peaks of Fe2p1/2 and Fe2p3/2 unlike hematite or maghemite [335-337].

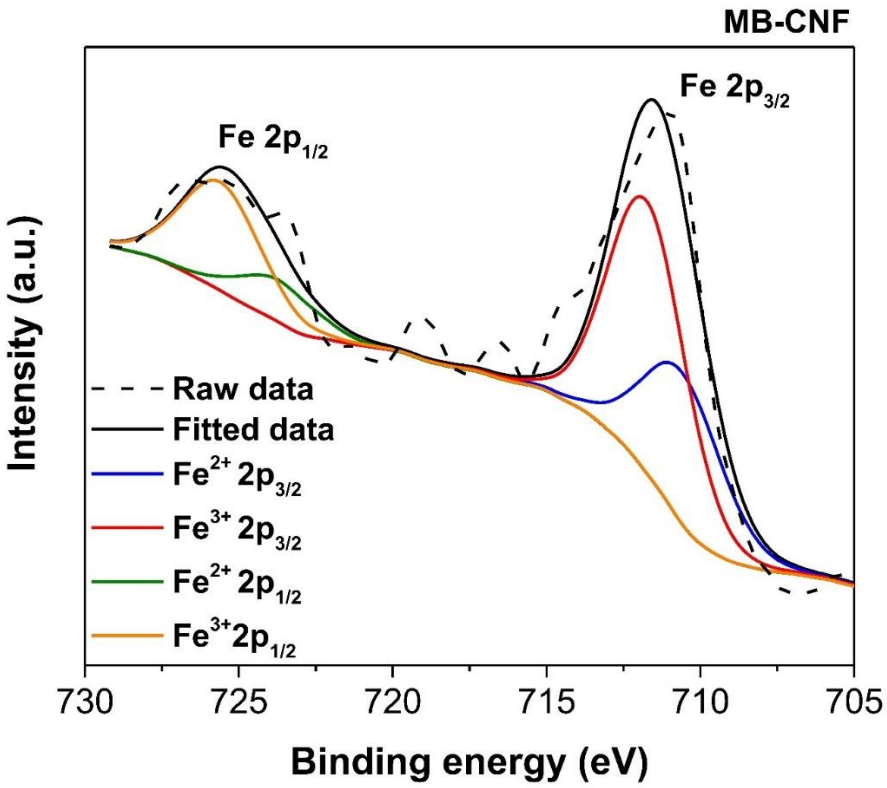

Figure 4.9 *Deconvolution high-resolution XPS of Fe $2p_{1/2}$ and Fe $2p_{3/2}$ spectra of MB-CNF.*

4.3.2.3 Texture proprieties and surface chemistry

The specific surface area and pore size distribution of MB and MB-CNF (Table 4.1) were obtained from the N_2 physisorption isotherms (Figure 4.10). It was observed that the MB presented a type (II) isotherm according to the IUPAC classification, characteristic of non-porous or macroporous materials. Furthermore, for the sample modified with CNF, a type (I) isotherm characteristic of microporous materials was identified [229]. Through the growth of CNF on the surface of the MB, the specific surface area was increased from 2 to 422 m^2/g. The significant increase in specific surface area is mainly attributed to the rough walls of the CNFs as observed in SEM micrographs (Figure 4.3 e) and f)). The pore volume also increased considerably (Table 4.1), from 0.009 cm^3/g to 0.152 cm^3/g for MB and MB-CNF, respectively. The MB presented a pore size distribution (PSD) mainly of mesopores between 10 and 45 nm, without the presence of micropores, whereas MB-CNF reported a low volume of meso- and macropores (0.003 cm^3/g) between 25 and 60 nm and a large volume of micropores (149 cm^3/g), which can contribute to the capture of CO_2 [149].

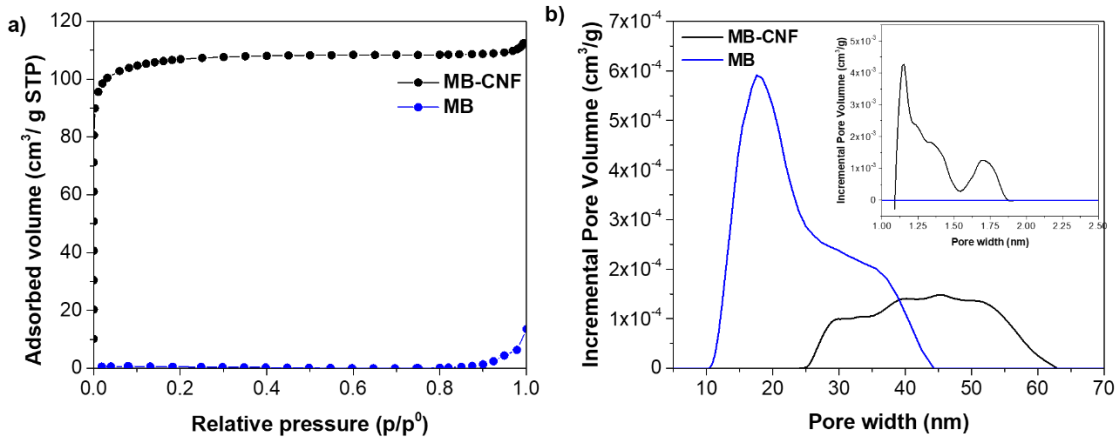

Figure 4.10 *a) Experimental N_2 adsorption isotherms at 77 K and b) pore size distribution of MB and MB-CNF calculated with Quenched solid density functional theory (QSDFT).*

Table 4.1 *Textural properties of MB and MB-CNF.*

Sample	S_{BET}	V_{total}	V_{macro}	V_{meso}	V_{micro}
	(m^2/g)	(cm^3/g)			
MB	2	0.009	0.009	0	0
MB-CNF	422	0.152	0.001	0.002	0.149

Changes in surface chemistry upon CNF growth were estimated by potentiometric titrations and pH_{pzc} was calculated (Figure 4.11). The MB presented a pH_{pzc} of 6.55 and this was shifted to 8.4 for MB-CNF. This indicates that CNF contributed to the increase of functional groups of basic nature, which could improve the CO_2 adsorption capacity in carbon materials [155,338].

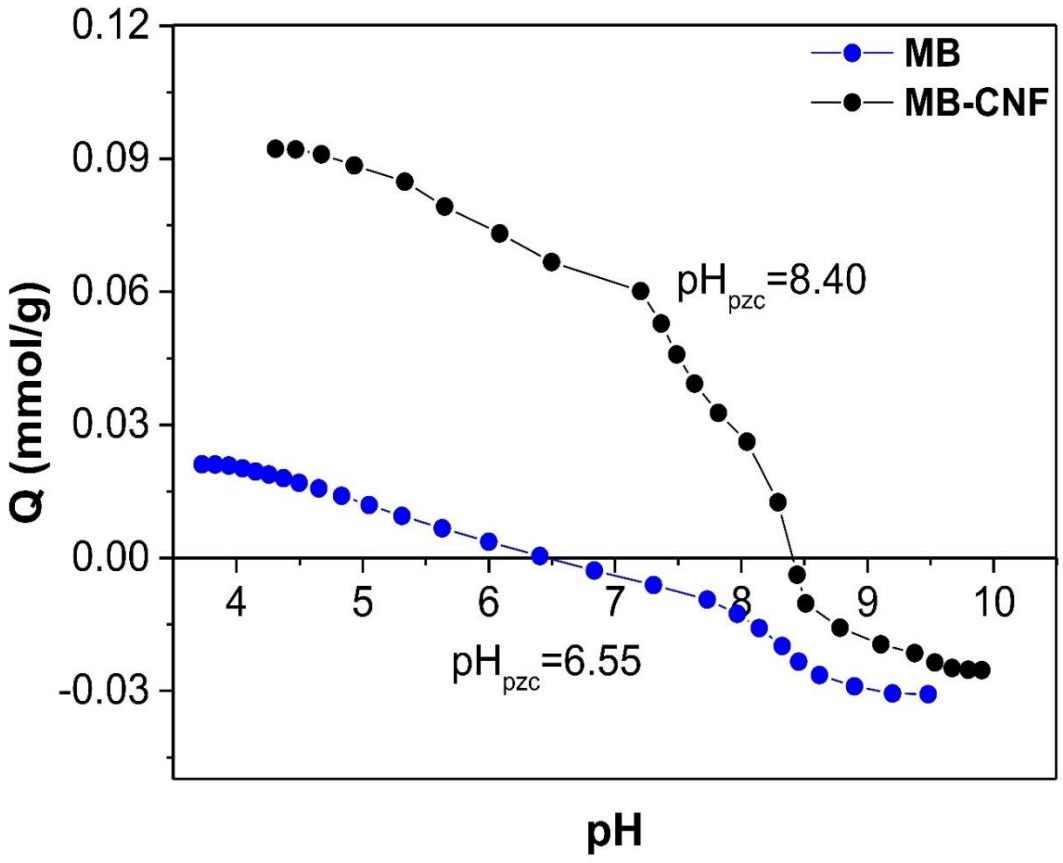

Figure 4.11 *Proton binding curves of MB and MB-CNF samples.*

The overall XPS spectrum (Figure 4.12) was obtained to derive the elemental composition of MB and MB-CNF and the data obtained were condensed in Table 4.2. A very similar carbon content of (~84.5%) was obtained for both samples and elements such as Na, Si and Ca from the precursor (agave bagasse) were also identified, which agrees with EDS results. In addition, elements of the catalyst impregnation process such as Cl and Fe were found. Among the main differences before and after the growth of CNF was the increase of almost 3% in N and the decrease of almost 4% in O. The increase in N content could help to increment the basic active sites concentration, as it was obtained by potentiometric titrations, and with this, improve the interaction strength with CO_2 and it removal [338].

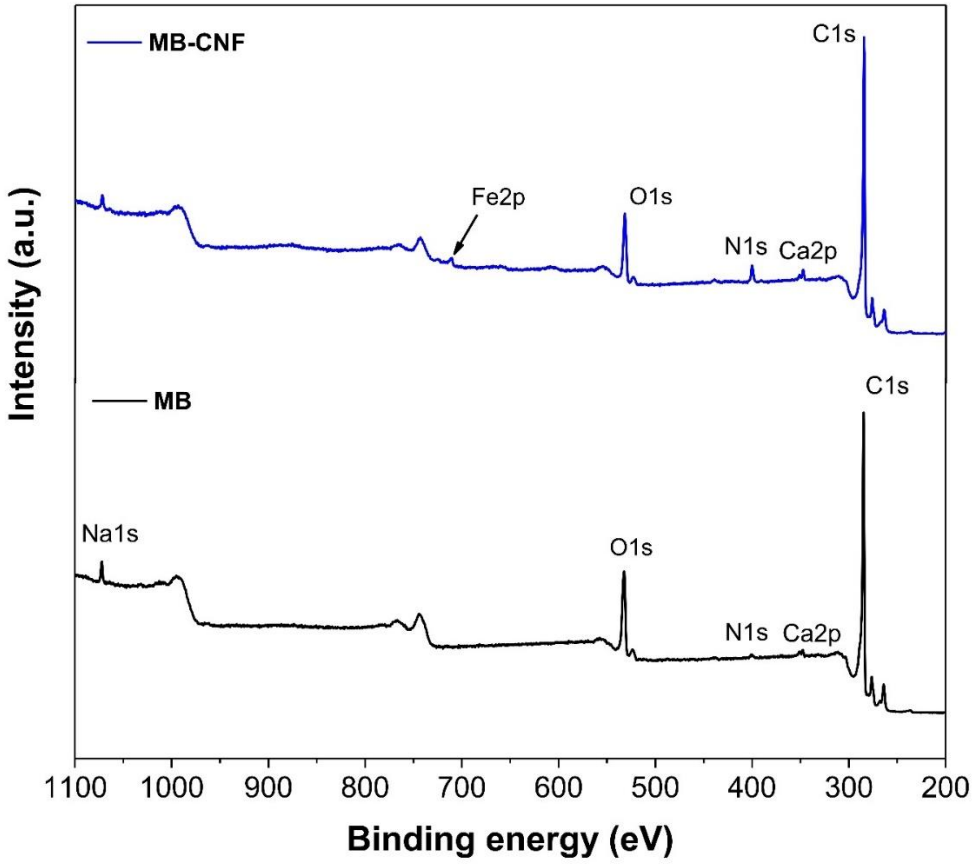

Figure 4.12 *XPS survey spectra of MB and MB-CNF.*

Table 4.2 *Element composition (atomic %) of MB and MB-CNF.*

	Atomic content (%)							
	C1s	**N1s**	**O1s**	**Na1s**	**Si2p**	**Cl2p**	**Ca2p**	**Fe2p3**
MB	84.44	0.46	13.47	1.01	0.06	0	0.55	0
MB-CNF	84.8	3.28	9.82	1	0.15	0.33	0.61	0.02

The contributions of carbon, oxygen, and nitrogen (Figure 4.13) were obtained by deconvolution of the high-resolution spectra of the energy levels of each element of the MB and MB-CNF samples (Table 4.3). For C, the samples exhibited signals corresponding to C=C sp^2 (284.2 eV), C-C sp^3 (284.8 eV), ketone or quinone groups C=O (286.3 eV), carboxylic groups, carbonyls, or esters O-C=O (287.1 eV) and pi-pi interactions (290 eV). For O, signals of carbonyl or ketone groups C=O (531.3 eV), carboxylic groups COOH (532.5 eV) and ether groups C-O (533.9 eV) were identified for both samples. Only MB showed the signal corresponding to absorbed H_2O (535.7 eV) and only MB-CNF exhibited the Fe-O signal (530.3 eV). Finally, for N the samples showed signals of N-pyridinic (398.6 eV), N-pyrrolic (400.2 eV), quaternary N (401.6 eV) and NOx (403.5 eV) groups [339]. Among the most notable results obtained from the deconvolutions, it can be observed that the growth of CNF increased about 8% and 4% the amount of C=C sp^2 and C=O, respectively. Also, MB-CNF did not report the signal attributed to H_2O, which could be attributed to a more hydrophobic nature. Finally, for N it was found that for MB the content of pyrrolic and pyridinic groups was similar (~39%) while for MB-CNF N mainly contributed to pyrrolic groups follow by quaternary, pyridinic and NOx groups. Therefore, it is expected that CNFs will contain defects, edge sites and curvatures related mainly to nitrogenous groups (mostly pyrrolic) and oxygenated groups

(mostly carbonyl, ketone or carboxylic) that provide greater reactivity to the material towards CO_2 [155,162,164].

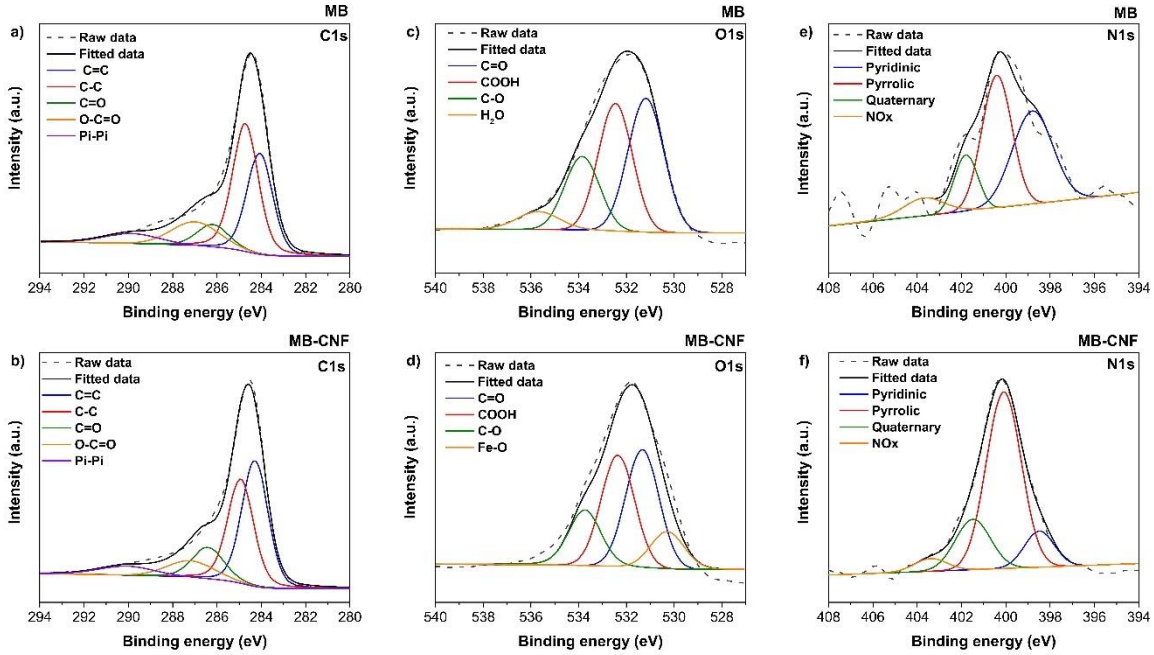

Figure 4.13 *Deconvolution of high-resolution XPS spectra of samples MB and MB-CNF: a) and b) for C1s, c) and d) for O1s, e) and f) for N1s.*

Table 4.3 *Relative and absolute abundance (%) of the different peaks assigned to C1s, O1s and N1s from the XPS spectra deconvolution for MB and MB-CNF.*

	Relative abundance of C1s (%)					**Absolute abundance of C1s (%)**				
Sample	**C=C**	**C-C**	**C=O**	**O-C=O**	**π-π**	**C=C**	**C-C**	**C=O**	**O-C=O**	**π-π**
MB	30.9	40.3	8.9	13	6.8	26.1	34.02	6.83	10.98	5.74
MB-CNF	38.8	33.3	12.5	9.1	6.3	32.9	28.23	10.6	7.71	5.34
	Relative abundance of O1s (%)					**Absolute abundance of O1s (%)**				
	C=O	**COOH**	**C-O**	**H_2O**	**Fe-O**	**C=O**	**COOH**	**C-O**	**H_2O**	**Fe-O**
MB	38.5	34.7	20.5	6.3	0	5.18	4.67	2.77	0.85	0
MB-CNF	36.1	34	17.9	0	12	3.56	3.35	1.76	0	1.19
	Relative abundance of N1s (%)					**Absolute abundance of N1s (%)**				
	Pyri	**Pyrr**	**Quat**	**NOx**		**Pyri**	**Pyrr**	**Quat**	**NOx**	

Table 4.3 (Continuation)								
MB	38.4	40.3	13.2	8.1	0.18	0.19	0.06	0.03
MB-CNF	11.4	65.5	18.7	4.4	0.37	2.15	0.61	0.14
Pyri= Pyridinic/ Pyrr=Pyrrolic/ Quat=Quaternary								

4.3.3 CO_2 capture of MB and MB-CNF

CO_2 capture isotherms of the materials were carried out at different temperatures (0, 25, 50 and 75 °C) and pressures ≤10 bar (Figure 4.14, Table 4.4). For all the temperatures tested the CNF growth on MB had a positive effect on the CO_2 capture capacity, which was slightly more noticeable at higher pressures. At 1 bar, the MB-CNF presented a CO_2 capture capacity of 2.65, 1.93, 1.32 and 0.87 mmol/g at 0, 25, 50 and 75 °C, respectively, which represents an improvement from 22 to 45% compared to MB. Furthermore, at 10 bar and 0 °C the CO_2 capture capacity was improved 28% through the growth of CNF (from 3.75 to 2.92 mmol/g), while at higher temperatures the increase was more than 40% (from 2.3, 1.86 and 1.47 mmol/g to 3.25, 2.61 and 2.15 mmol/g at 25, 50 and 75 °C, respectively).

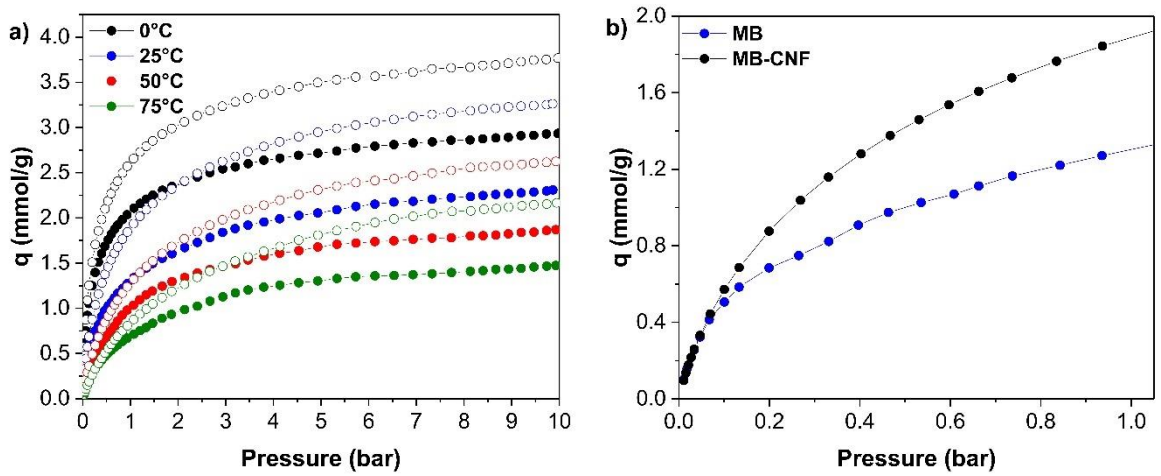

Figure 4.14 *a) CO_2 adsorption isotherms at different temperatures (25, 50 and 75°C) and pressures up to 10 bar for MB (solid points) and MB-CNF (empty points) b) CO_2 adsorption isotherms at 25 °C and 1 bar.*

Table 4.4 *CO_2 capture capacities of MB and MB-CNF at 0, 25, 50 and 75 °C and pressure of 1-10 bar.*

	CO_2 capture capacity (mmol/g)							
	0 °C		**25 °C**		**50 °C**		**75 °C**	
Sample	**1 bar**	**10 bar**	**1 bar**	**10 bar**	**1 bar**	**10 bar**	**1 bar**	**10 bar**
MB	2.1	2.92	1.33	2.3	1.03	1.86	0.71	1.47
MB-CNF	2.65	3.75	1.93	3.25	1.32	2.61	0.87	2.15

It has been reported that the CO_2 capture capacity at pressures less than 5 bar is governed mostly by surface chemistry, while as the pressure increases the specific surface area and pore size have greater relevance [155]. Therefore, increasing the specific surface area and modifying the surface chemistry of the MB through increasing the basic sites by CNF (Figure 4.15), it was possible to improve the CO_2 capture capacity in the entire range of tested pressures, with the greatest effect at the highest pressure.

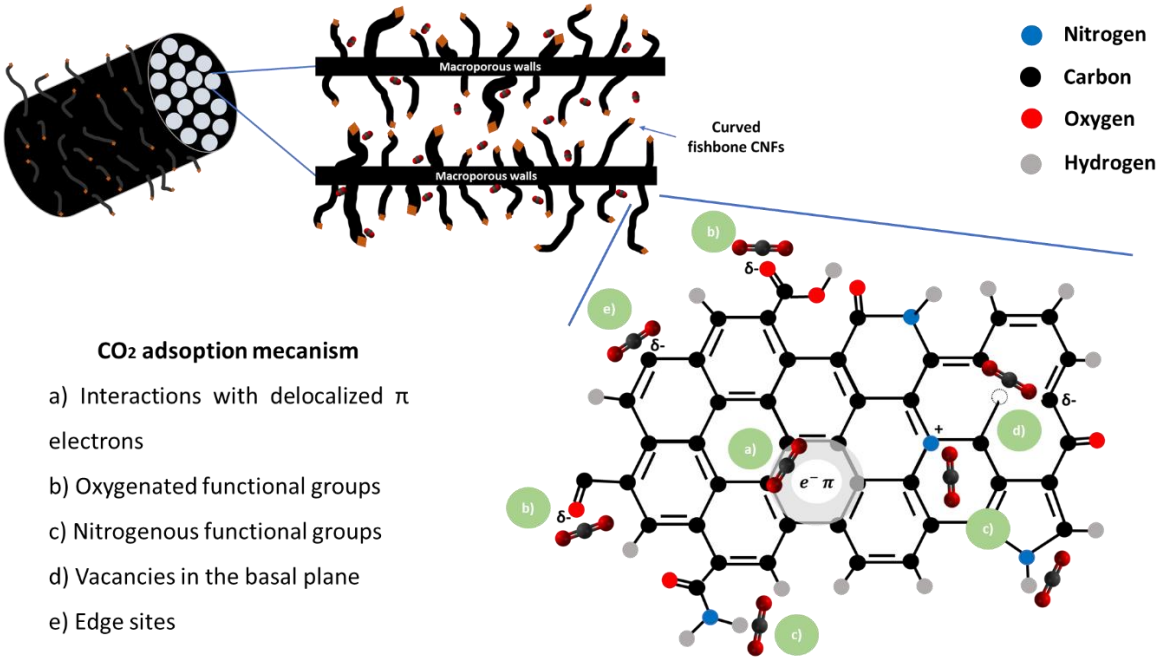

Figure 4.15 *Suggested CO_2 capture mechanisms of MB-CNF [155,162,164].*

From the isotherms at 25, 50, and 75 °C, the isosteric heat of adsorption was calculated by using the Clausius–Clapeyron equation (Figure 4.16 a). For MB-CNF, constant values of around 29 kJ/mol were obtained throughout the range of CO_2 adsorbed, which can be interpreted as a homogeneity in the active sites energy of the adsorbent material [299]. For MB the isosteric heat values decreased from 28 to 25 kJ/mol as the amount of CO_2 increased, which is attributed to the disappearance of favorable adsorption sites [236].

The CO_2 capture kinetics are presented in Figure 4.16 b) and the average capture rate was calculated by dividing the capture capacity by 50 minutes. The maximum CO_2 capture capacity for the pristine material (ACF) was 1.16 mmol/g with a CO_2 capture rate of 0.023 mmol/g·min, while the CO_2 capture capacity of MB-CNF was 1.40 mmol/g with a CO_2 capture rate of 0.028 mmol/g·min. It was possible to increase the capture capacity and the CO_2 capture rate by 20% compared to the

MB, maintaining the same equilibrium time (50 min). Additionally, two kinetic models were used to describe the CO_2 capture rate of the materials. According to the correlation coefficients (R^2), see Table 4.5, the experimental data of the materials were slightly better described by the pseudo-first-order model, where the theoretical values of q_e obtained from the pseudo-first-order model agree with the experimental data obtained. This model assumes that the limiting step in an adsorption process is the mass transfer of the adsorbate to the adsorbent surface [297]. This result is of great importance because it was proven that by growing CNF, the CO_2 capture capacity can be improved without affecting the kinetics of the material, so it can be concluded that the area provided by the CNF is readily available to interact with CO_2. This agrees with the constant value of the isosteric heat of adsorption, as there is no diffusion through the pores, all the active sites are directly available, and they have very similar energy. Contrary to what happens with most activated carbons (AC), where the isosteric heat of adsorption value normally decreases as the adsorbed amount increases [236,318,338].

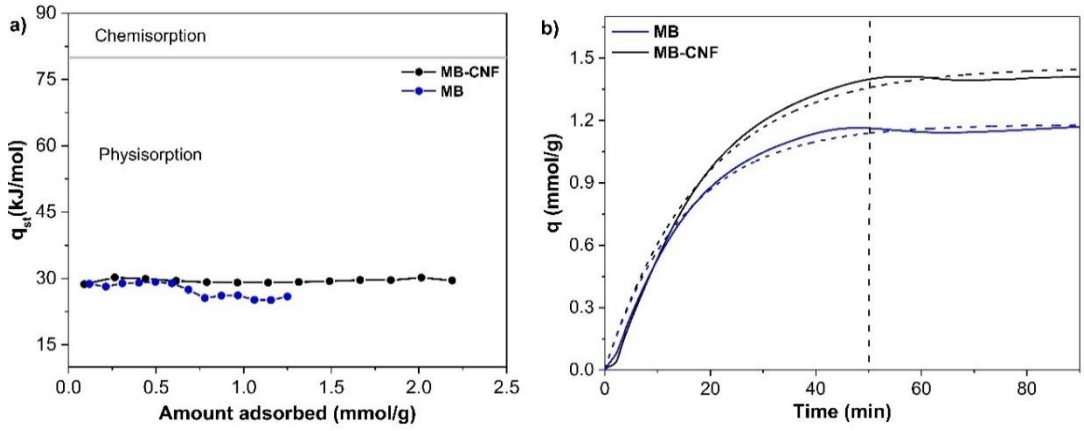

Figure 4.16 *a) Isosteric heat of adsorption and b) CO_2 capture kinetics (1 bar, CO_2 flowrate of 30 mL/min) of MB and MB-CNF. Experimental data (solid lines) and the pseudo first-order model fit (dotted lines).*

Table 4.5 *Kinetic constants for CO_2 capture by MB and MB-CNF.*

Equation parameters	MB	MB-CNF
Pseudo first-order		
k_1 (min^{-1})	0.066	0.053
q_e (mg/g)	1.18	1.45
R^2	0.98	0.98
Pseudo second-order		
k_2 (g/(mg·min))	112.6	160.44
q_e(mg/g)	0.11	0.106
R^2	0.96	0.96

Finally, the regeneration capacity of MB-CNF was tested through CO_2 sorption-desorption cycles at 25 °C (Figure 4.17), where the desorption was carried out by a pressure change. The CO_2 capture capacities at 1 bar were 1.92, 1.91 and 1.92 mmol/g whereas at 10 bar were 3.25, 3.15 and 3.19 mmol/g from cycles 1 to 3, respectively. Therefore, at 1 bar the regeneration capacity was practically 100%, while at 10 bar the regeneration capacity was 97 and 98% for the second and third cycles, respectively. This result is of great relevance for industrial application and provides evidence that the CO_2 capture mechanism is by physisorption. Also, it should be noted that desorption in this system occurred due to a change in pressure where at the end of the CO_2 capture isotherm the equipment was evacuated and, to carry out the next sorption cycle, the equipment requires reaching 5 μmHg, so the desorption process takes around 5 hours.

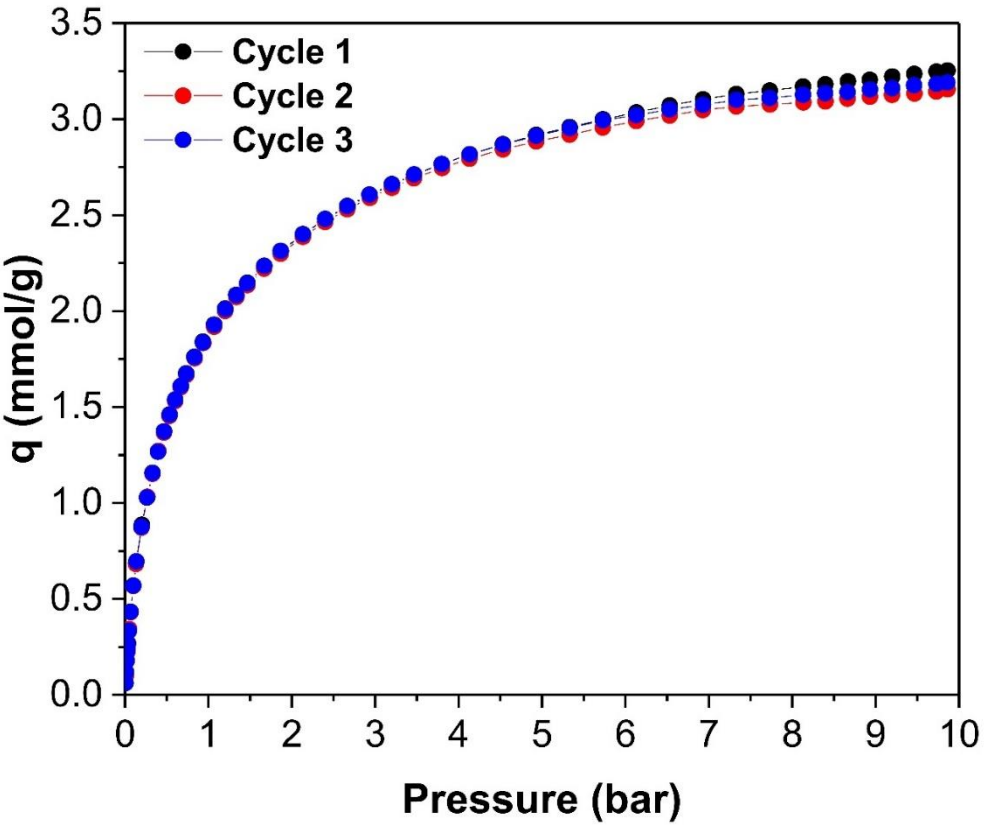

Figure 4.17 *Multi-cycles of CO_2 adsorption isotherms of MB-CNF at 25 °C.*

4.4 Conclusions

In this work, it was demonstrated the feasibility to grown fishbone-type CNF on the surface of a macroporous biochar, from the tequila and mezcal industry, to improve its CO_2 capture capacity. Through octahedral magnetite nanoparticles, curved fishbone-type CNFs with diameters between 30 and 50 nm were grown, which has not been previously reported. The growth of CNF increases the specific surface area of MB from 2 to 422 m^2/g and the pore volume from 0.009 to 0.152 cm^3/g. The CO_2 capture capacity increases more than 40% (from 1.33 and 2.3 mmol/g to 1.93 and 3.25 mmol/g at 25 °C and 1 and 10 bar, respectively) attributed to the increase in basic groups, the highly reactive edge sites and to the increase in the specific surface area, as it was proved by potentiometric titrations, XPS spectrum

deconvolutions, SEM, and N_2 physisorption analysis. The constant value of the isosteric heat of adsorption of MB-CNF (29 kJ/mol) indicates homogeneity in the adsorption active sites. Furthermore, the growth of CNF do not affect the equilibrium time in the CO_2 capture kinetics (50 min), the CO_2 capture rate was improved by 20% (from 0.023 to 0.028 mmol/g min) and regeneration capacities of more than 97% were achieved during three sorption-desorption cycles. Finally, this work demonstrates the possibility of improving the rapid CO_2 capture capacity of a macroporous biochar through the growth of CNF on its surface, without affecting its kinetics and with excellent regeneration capacity which is ideal for industrial applications.

Chapter 5:

Efficient use of ionic liquid in CO_2 capture through its dispersion in a carbon nanofibers/macroporous biochar composite

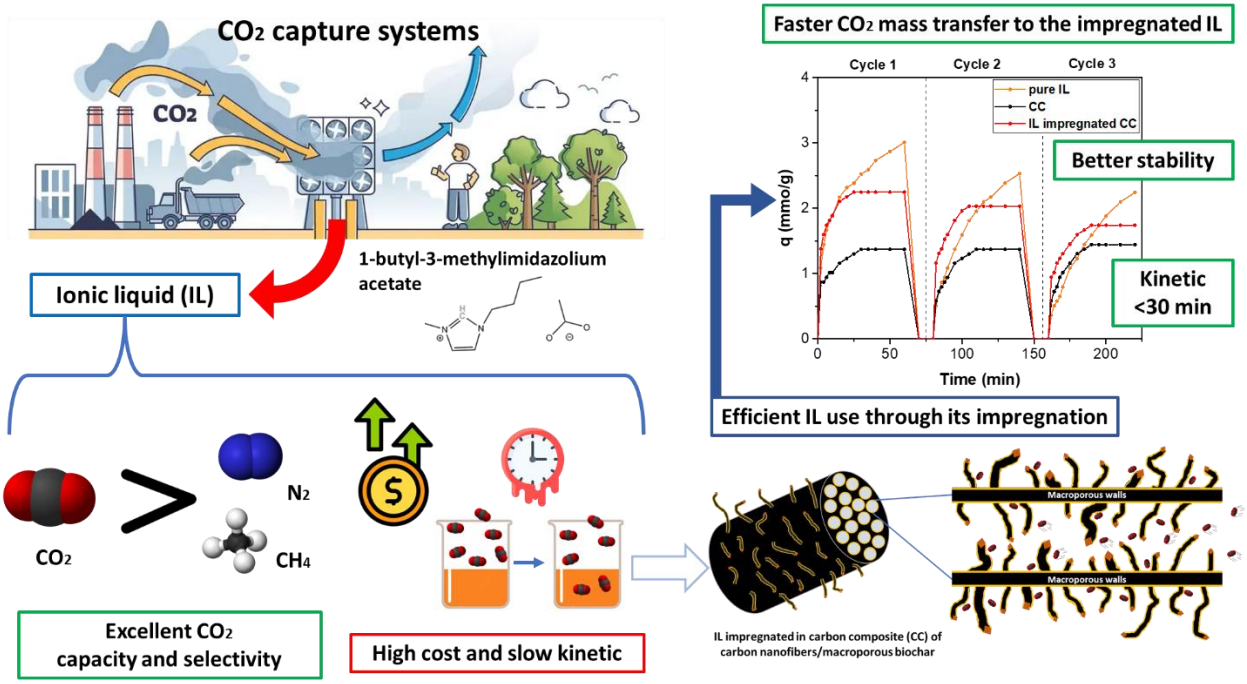

ABSTRACT

The CO_2 capture with liquid amines is the most used method industrially to reduce CO_2 emissions into the atmosphere. However, important disadvantages such as their high energy consumption, toxicity and corrosiveness have led to the search for new absorbents to replace them. Among them, ionic liquids present important advantages for their application in CO_2 capture, but their slow kinetics due to their high viscosity have limited their use. Therefore, in this research a new hybrid material was prepared to make more efficient the CO_2 capture capacity and kinetics of an ionic liquid supported on a carbon composite (CC) conformed of a macroporous biochar modified with carbon nanofibers. CNF growth was obtained uniformly by CVD over the entire surface of the MB. The surface area increased from 2 to 422 m^2/g after CNF growth providing more rapidly available area to impregnate the IL. The ionic liquid (IL) used was 1-butyl 3-methylimidadolium acetate ([BMIM][Ac]), which has a great affinity for CO_2. The selected materials were characterized by SEM, N_2 Physisorption, FTIR and TGA. CO_2 capture at different pressures (1-8 bar) and sorption-desorption cycles at 8 bar were evaluated for pure IL, CC and IL-impregnated CC using a mass ratio from 1:0.05 to 1:0.1. The sample impregnated with a mass ratio of 1:0.05 (CC-IL1:0.05) showed the most efficient use of IL and the best CO_2 capture performance. The CO_2 capture capacity of CC improved from 0.41 and 1.37 mmol/g to 0.81 and 2.46 mmol/g of CC-IL1:0.05 for 1 and 8 bar, respectively. The equilibrium time of CC-IL1:0.05 was less than 20 min for all the pressures tested and the CO_2 capture rate was improved around double (from 0.02 and 0.06 mmol/g·min for CC to 0.04 and 0.12 mmol/g·min for CC-IL1:0.05 at 1 and

8 bar, respectively) for all pressures tested, compared to the pristine material. Finally, the CO_2 capture and desorption cycles (80 °C, 10 min) showed regeneration capacities of 84.33 and 73.81% for IL and 90.32 and 77.41 for CC-IL1:0.05 for the second and third cycle, respectively. The considerable improvement in kinetics, CO_2 capture capacity, and regeneration of IL-impregnated CC demonstrated its viability for CO_2 capture systems.

5.1 Introduction

Climate change and global warming are priority issues of global interest due to the increasing emission of greenhouse gases [1]. This considerable increase has been attributed mainly to human activities such as the consumption of fossil fuels, deforestation, and the rapid expansion of agriculture [340]. Among the greenhouse gases, CO_2 is one of the main ones, which has reached concentrations in the atmosphere of more than 400 ppm [4].

Different strategies have been proposed to reduce CO_2 concentrations in the atmosphere, such as absorption [341], adsorption [342,343], membrane separation [344], storage of underground rocks [345] and the conversion of CO_2 into fuels and chemicals [345,346]. Among them, the CO_2 capture through liquid amines is one of the most widely used methods at the industrial level because of its fast absorption rate, excellent capture capacity and low cost [341,348]. However, these materials have some disadvantage like solvent volatilization, equipment corrosion, and high energy consumption for adsorbent regeneration [349-351]. Consequently, new materials have been investigated for CO_2 capture that been efficient, non-toxic, more economical and with low energy consumption such as ionic liquids, which have been

of great interest in different areas such as catalysis, electrochemistry, biochemistry and gas separation [352-354].

Ionic liquids (IL) are liquid salts at room temperature and are composed of an organic cation and a weak inorganic or organic base anion with a diffuse negative charge [345,355]. Among the ILs used for CO_2 capture, those formed by the imidazolium cation stand out [82,85]. This cation can form carboxylates, and the reversible reaction shifts to the product at low CO_2 partial pressures and room temperature [82,83,85]. Nevertheless, ILs have certain disadvantages such as high cost and low mass transfer due to their high viscosity, causing the capacity and speed of capture to decrease, which prevent their use on a large scale [356,357]. One of the strategies studied to improve the use of IL has been to immobilize them in solid porous materials [345,358]. Different materials have been used as support to impregnate the IL, such as mesoporous silica [359], graphene oxide [360], granular carbon [280], and bio-carbons [361,362].

Particularly, our research group has previously worked with macroporous biochar (MB), obtained from pyrolysis of mezcal industry waste, as support to impregnate 1-butyl-3-methylimidadolium acetate IL [185]. In this previous study, it was obtained that the mass ratio of $1:1x10^{-3}$ (wt MB: wt IL) was the one that presented the best CO_2 capture performance through the formation of a thin layer of IL on the biocarbon macropores. However, the biochar used had low specific surface area, so the amount of IL that could be impregnated without affecting the rapid CO_2 capture kinetics was limited. Therefore, in this study it is proposed to increase the available

surface of MB through the growth of carbon nanofibers (CNF) to improve the mass transfer from CO_2 to IL, making it more efficient.

5.2 Experimental Section

5.2.1 Reagents and precursor

All the chemicals used in this research were reagent grade. $FeCl_3 \cdot 6\ H_2O$, $FeCl_2 \cdot 4\ H_2O$, and ionic liquid (1-butyl-3-methylimidazolium acetate) were obtained from Sigma Aldrich. Deionized water was used for the preparation of all solutions. The precursor (agave bagasse fibers from *Agave salmiana* plant) was provided by a distillery located in San Luis Potosi, Mexico.

5.2.2 Carbon composite synthesis

5.2.2.1 Macroporous biochar production

For the synthesis of the carbon composite, carbonized agave bagasse fibers modified with carbon nanofibers on their surface were used. The methodology used for the carbonization of the agave bagasse fibers is a modification of a previous work [184]. The agave bagasse fibers were washed with distilled water, dried at 90 °C for 48 h and fractionated at ~ 0.5 cm. Subsequently, the precursor was carbonized in a Barnstead Thermolyne 21100 tube furnace under an inert atmosphere of N_2 at a temperature of 600 °C for 2 h. The macroporous biochar obtained was then sieved (35x60 USA Standard test sieve) and washed with HCl to reduce the ash content as mentioned below. 40 mL of 3 M HCl solution was mixed with 1 g of biochar and stirred at 100 rpm in an orbital incubator for 72 h. Subsequently, the residue was decanted, and the biochar was rinsed with deionized water until the pH was constant.

Finally, the biochar was dried at 90 °C for 48h and stored in a N_2 atmosphere to prevent oxidation of the material. This material was named as macroporous biochar (MB).

5.2.2.2 Carbon nanofibers growth

Chemical vapor deposition (CVD) was used to grow carbon nanofibers (CNF) onto the MB surface. To promote the growth of CNF, iron nanoparticles were impregnated on MB by using a modification of the chemical precipitation of iron salts in an alkaline environment known as the Massart process [277,278]. For the impregnation of the metallic catalyst, solutions of $FeCl_3 \cdot 6\ H_2O$ and $FeCl_2 \cdot 4\ H_2O$ were prepared with a concentration of 6 and 3 g/L, respectively. 5 mL of each solution were mixed under constant stirring and 100 mg of MB were added. The suspension was mixed under a N_2 atmosphere, and the pH was adjusted to 12. Afterwards, it was placed in a microwave reactor (Anton Paar model Monowave 400) at 160 °C for 10 min. Finally, the catalyst-impregnated MB was washed with deionized water and dried at 90 °C for 48 h.

The growth of CNF on the MB was carried out in a Barnstead Thermolyne 21100 model tube furnace. Approximately 1 g of catalyst-impregnated MB was used, the temperature was raised to 700 °C with a heating ramp of 25 °C/min and a flowrate of N_2 of 40 ml/min. Once the temperature was reached, acetylene (carbon source) was injected for 1 min at a constant flow of 10 ml/min, and the temperature and N_2 flowrate were kept constant for 10 min. Finally, a post-treatment was carried out to remove amorphous carbon deposited during the synthesis; A heating ramp of 15 °C/min and a N_2 flowrate of 40 ml/min up to 300 °C were used. At this temperature,

the atmosphere was changed to air at 20 ml/min for 1 min. This sample made up of CNF-modified MB was named as carbon composite (CC).

5.2.3 Impregnation of carbon composite with ionic liquid

The impregnation of the ionic liquid (IL) 1-butyl-3-methylimidazolium acetate, [BMIM][Ac], on the CC was performed based on a modification of a previously reported method [185]. First, 1200 µL of deionized water was mixed with the corresponding volume of IL to obtain an impregnation mass ratio of 1:0.05 to 1:0.1 (wt CC: wt IL). Then, the IL- deionized water mixture was stirred for 8 min at 80 °C, 60 mg CC was added and stirred for 2 more min under the same temperature. Afterwards, the suspension was stirred at 90 rpm on an orbital incubator for 24 hrs. Finally, the solvent was removed by evaporation at 80 °C for 48 h and stored in N_2 atmosphere. The samples were named as CC-ILx, where x is the mass ratio of the IL used (1:0.05, 1:0.075 and 1:0.1).

5.2.4 Physicochemical characterization of impregnated carbon composite

The surface area and pore size distribution were determined from the nitrogen adsorption isotherm at 77 K using a Micromeritics ASAP 2020 physisorption equipment. The surface area was determined using the Breunaer-Emment-Teller (BET) equation and the pore size distribution was obtained using the density functional theory (DFT). For the identification of functional groups, FTIR studies were conducted in a Nicolet 1S50 FTIR equipment, from Thermo Scientific, in the spectral range of 500 to 2000 cm^{-1}, in attenuated total reflectance (ATR) mode with 64 scans with a resolution of 4 cm^{-1}. The degree of IL impregnation was obtained from the loss

of mass until 290 °C in a thermogravimetric analyzer (SETSYS Evolution TGA-DTA/DSC, SETARAM Instrumentation), based on the thermogravimetric curve resulting from pure IL. A heating ramp of 10 °C/min from 25 to 700 °C in a N_2 atmosphere and atmospheric pressure was used. The distribution of the CNF and the impregnation of the IL were analyzed under a HELIOS NANOLAB 600i SEM with high resolution field emission source and secondary electron detector. Before analysis, the samples were immobilized on a carbon tape retained in an SEM sample holder.

5.2.5 CO_2 capture experiments

The kinetics and CO_2 capture capacity experiments at room temperature and different manometric pressures were performed in a 25 ml high-pressure reactor (4704, Parr Instrument), adapted with a digital manometer (ASHCROFT DG25 with a previously used methodology [363]). CO_2 capture tests were performed at 1, 3, 5 and 8 bar of CC, IL and impregnated CC. A mass of 0.1 g was used, where the amount of gas captured was attributed to the change in pressure during the CO_2 capture experiments. To calculate the CO_2 capture capacity of the materials, the ideal gas law was used, considering the compressibility constant of CO_2 (ζ_{CO_2}). The equation used is presented below:

$$q_{CO_2} = \frac{(V)(\Delta P)}{(\zeta_{CO_2})(R)(T)(m_0)} \qquad \textit{(Equation 5.1)}$$

Where, q_{CO_2} is the CO_2 capture capacity (mmol of CO_2/g of material), P is the difference between the initial pressure and the equilibrium pressure (bar), R is the

ideal gas constant (0.083 L bar/ K mol), V is the volume of equipment (mL), T is the temperature (K) and ζ_{CO_2} is the compressibility constant.

For sorption-desorption cycles, first the sorption process was conducted at certain pressure and then this was reduced to atmospheric pressure, the system was heated at 80 °C during 10 min through a water bath and subsequently, the equipment was cooled down to 25 °C to repeat the CO_2 capture process.

The reversibility was calculated based on the following equation:

$$Reversibility = \left(\frac{q_{i+1}}{q_1}\right)(100\%) \qquad \textit{(Equation 5.2)}$$

Where q is the capture capacity (mmol/g) obtained in 60 min in the sorption-desorption cycle number i = 1 to 3.

5.3 Results and Discussion

5.3.1 Composite characterization

Representative SEM images of MB and CC samples are presented in Figure 5.1. A significant in texture can be observed between the pristine MB (Figure 5.1 a) and the one that has CNF (Figure 5.1 b): it can be observed that the growth of the nanostructures occurred uniformly over the entire surface of MB. Figure 5.1 c) and d) showed that the CNFs formed a complex matrix of curved tubular structures with diameters ranging from 15 to 50 nm. In addition, it was possible to identify the catalyst at the tip of the CNFs (Figure 5.1 d), which follows a tip growth model, where carbon atoms displace the catalyst during the CVD process [218].

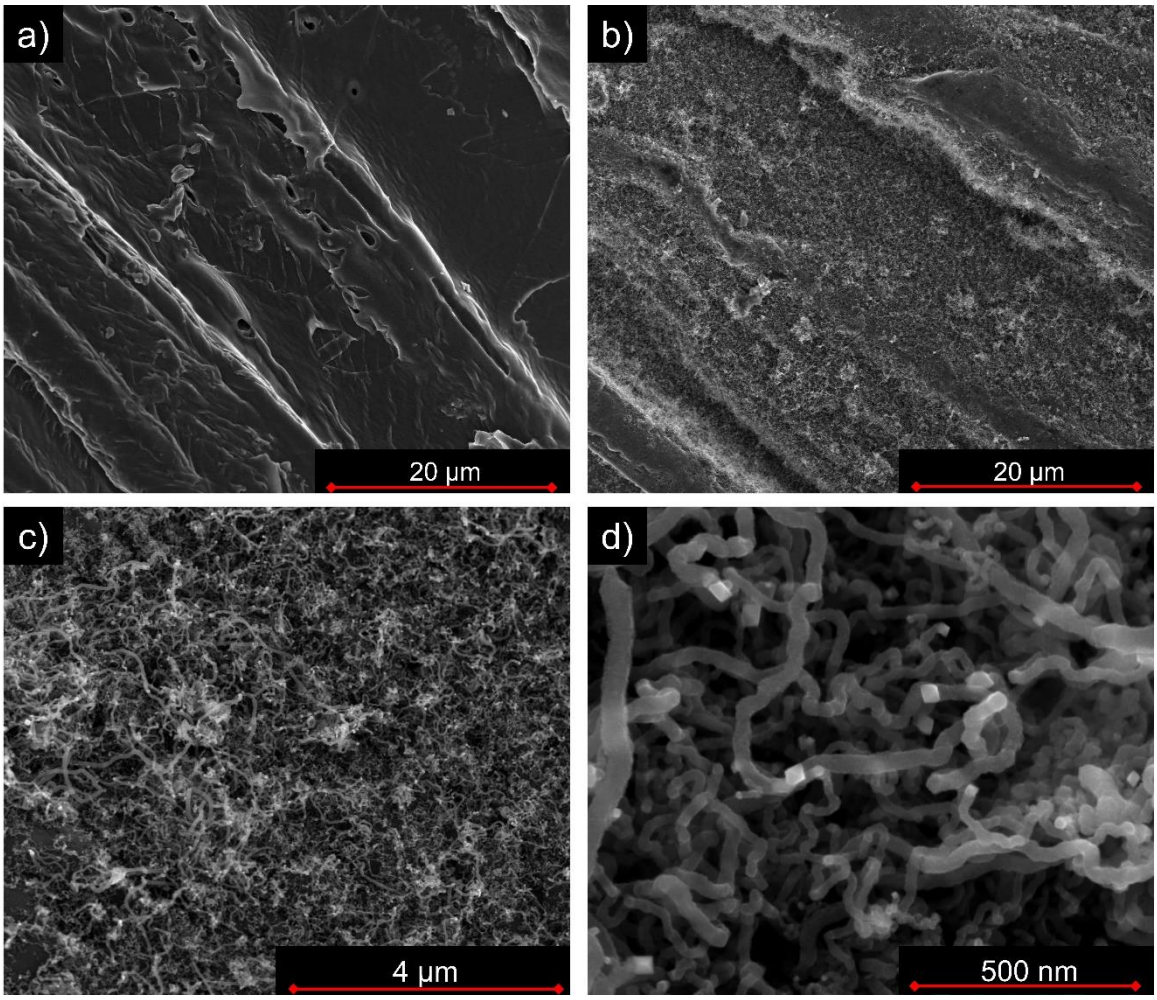

Figure 5.1 *SEM secondary electrons images of a) MB surface, b) CC surface, c) and d) CNF grown on the surface of MB.*

Figure 5.2 shows the N_2 adsorption isotherms of carbon materials, where it is possible to observe that the MB sample presents a type (II) isotherm characteristic of non-porous or macroporous adsorbent materials. In addition, CC presents a type (I) isotherm characteristic of microporous materials [36]. The pore area and volume data were condensed in Table 5.1. The MB has a specific surface area of 2 m^2/g and a pore volume of 0.009 cm^3/g, which corresponds to what was previously reported by our research group [292]. On the other hand, through the growth of CNF (CC) it was possible to considerably increase the specific surface area up to 422 m^2/g with a pore volume of 0.152 cm^3/g. This provides more rapidly available area

where IL can be impregnated without the disadvantage of blocking pores, as occurs with materials with compound porosity such as activated carbons [364].

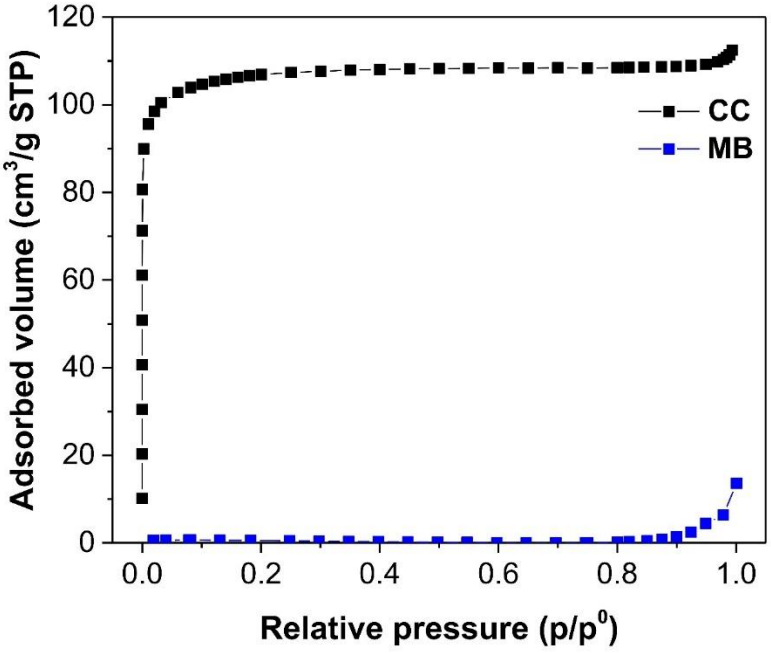

Figure 5.2 *Experimental isotherms of N_2 adsorption at 77 K of MB and CC calculated with Quenched solid density functional theory (QSDFT).*

Table 5.1 *Textural properties of MB and CC.*

Sample	S_{BET}	V_{total}	V_{macro}	V_{meso}	V_{micro}
	(m^2/g)	(cm^3/g)			
MB	2	0.009	0.009	0	0
CC	422	0.152	0.001	0.002	0.149

5.3.2 Characterization of the impregnated carbon composite

The effect of IL impregnation on CC was analyzed by SEM (Figure 5.3). In the first instance, it can be observed that the distribution as well as the definition of the pristine CNFs grown on MB (Figure 5.1 c) change with the IL impregnation (Figure 5.3 a)-c)). As the degree of impregnation increased, larger IL clusters were observed. In addition, the definition between each CNF decreased as the IL-

impregnated ratio increased, even CNFs with diameters smaller than 30 nm could not be perceived for any IL ratio (Figure 5.3 d)-f)). This can cause part of the IL-impregnated surface to be inaccessible to CO_2, leading to a less efficient use of IL [359,364,365]. Because of this, impregnation tests with high IL ratios were not performed. On the other hand, it has been reported that [BMIM][Ac] IL can interact with carbon materials through hydrogen bonding and electrostatic interactions [250,368].

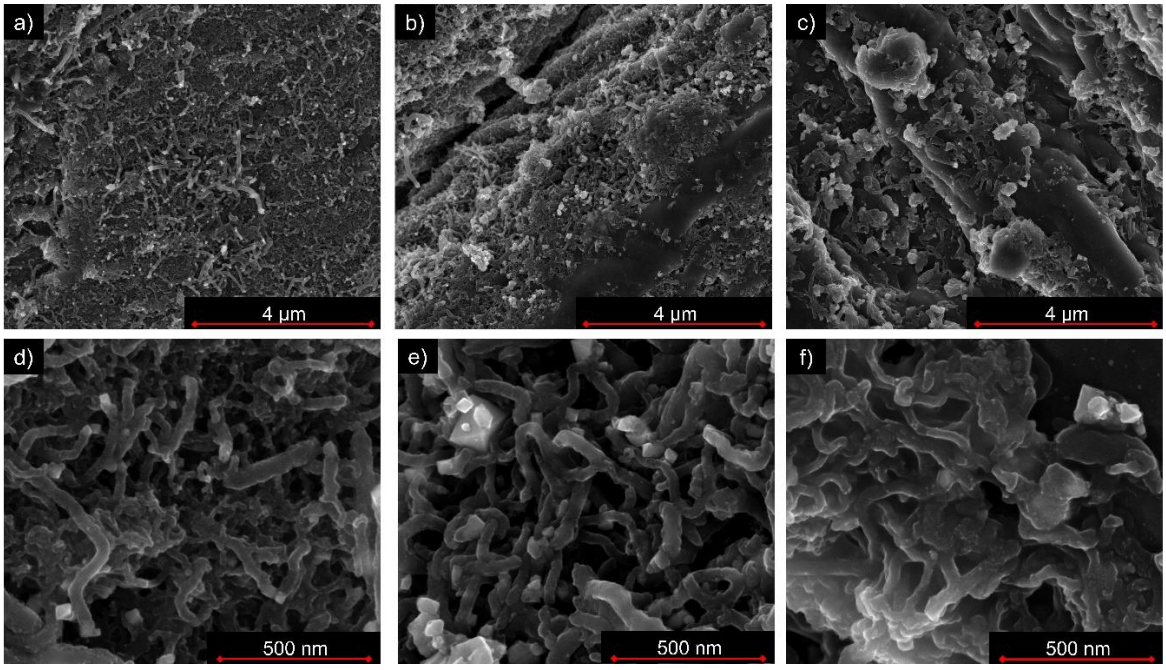

Figure 5.3 *SEM secondary electrons images of a) CC-IL1:0.05, b) CC-IL1:0.075, c) CC-IL1:0.1, zoom of the IL-impregnated CNF of d) CC-IL1:0.05, e) CC-IL1:0.075 and, CC-IL1:0.1.*

The functional groups related to the IL and CC were identified (Figure 5.4). Firstly, CC show bands between 600-950 cm^{-1} corresponding to -OH and =CH stretching phenolic groups. Also, bands at 1000-1300 cm^{-1} attributed to C-O and C-OH vibrations of phenolic groups structure were found. Signals corresponding to C=C and C=O vibrations between 1550-1750 cm^{-1} of the aromatic ring of the phenolic

structure were identified. Finally, a band at 1458 cm^{-1} corresponding to C-OH vibration of aliphatic structure groups were found [255,256]. On the other hand, the main bands attributed to [BMIM][Ac] IL were identified: these were sharper as the amount of IL impregnated increased. In ~1600 cm^{-1} a band attributed to C=N stretch incorporated into the imidazole ring was identified. Also, bands at ~1390 and 1160 cm^{-1} are attributed to C=O and C-O vibrations of the acetate anion [76,250] and the bands between 600-750 cm^{-1} are associated with stretching vibrations of C-H and $C\text{-}H_3$ of aliphatic chains of the cation [76,366].

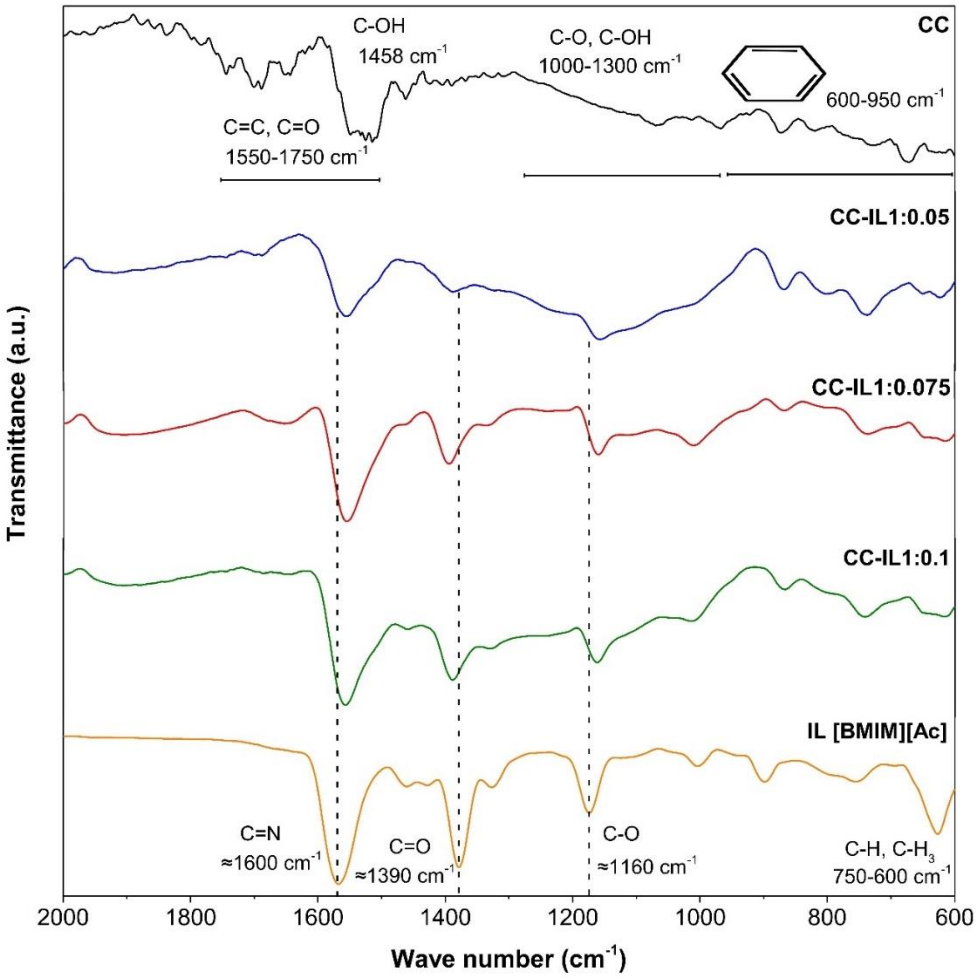

Figure 5.4 *FTIR spectra of CC, pure [BMIM][Ac] IL and CC impregnated with different IL mass ratio.*

5.3.2.1 Thermal stability and impregnation level

The thermal stability of CC and IL [BMIM][Ac] was evaluated in nitrogen atmosphere to study their CO_2 uptake and regeneration (Figure 5.5). The IL presented a mass loss of 14.5 % from 25-140 °C attributed to moisture [367]. In addition, the IL began to degrade after 140 °C, where the greatest mass loss occurred around 215 °C until obtaining a residual mass of 1.66% at 290 °C, which coincides with previous reports [85,185]. For CC, excellent thermal stability is observed over the entire tested temperature range. For temperatures below 290 °C, a mass loss of 2.5% was obtained, mainly attributed to moisture. These values were considered to calculate the degree of experimental IL impregnation.

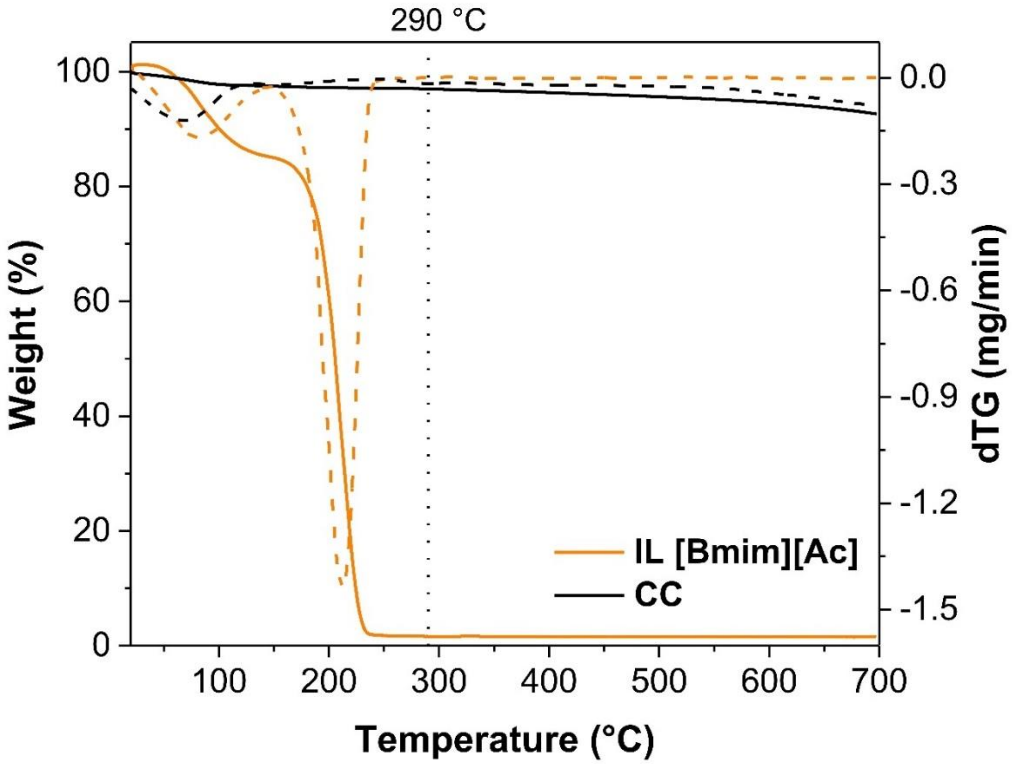

Figure 5.5 *Non-isothermal thermogravimetric analysis under N_2 atmosphere at a heating rate of 10 °C/min until 700 °C, thermogravimetric (solid line) and differential thermogravimetric (dTG, dashed line) curves of CC (black) and [BMIM][Ac] IL (orange).*

For the IL impregnations on the CC, different mass ratios were tested, from 1:0.05 to 1:0.1 (wt CC: wt IL). These ratios were chosen because it has been reported than CO_2 capture kinetics were significantly affected with higher ratios of impregnated IL [341,352]. Figure 5.6 showed the thermogravimetric curves of the different impregnation experiments, and the data of the impregnation degree were condensed in Table 5.2. The impregnation of the IL was carried out adequately since it was observed that the weight loss associated with moisture and decomposition of the IL (T<290 °C) was proportional to the degree of impregnation of each sample, corresponding with the calculated values from the mass ratio.

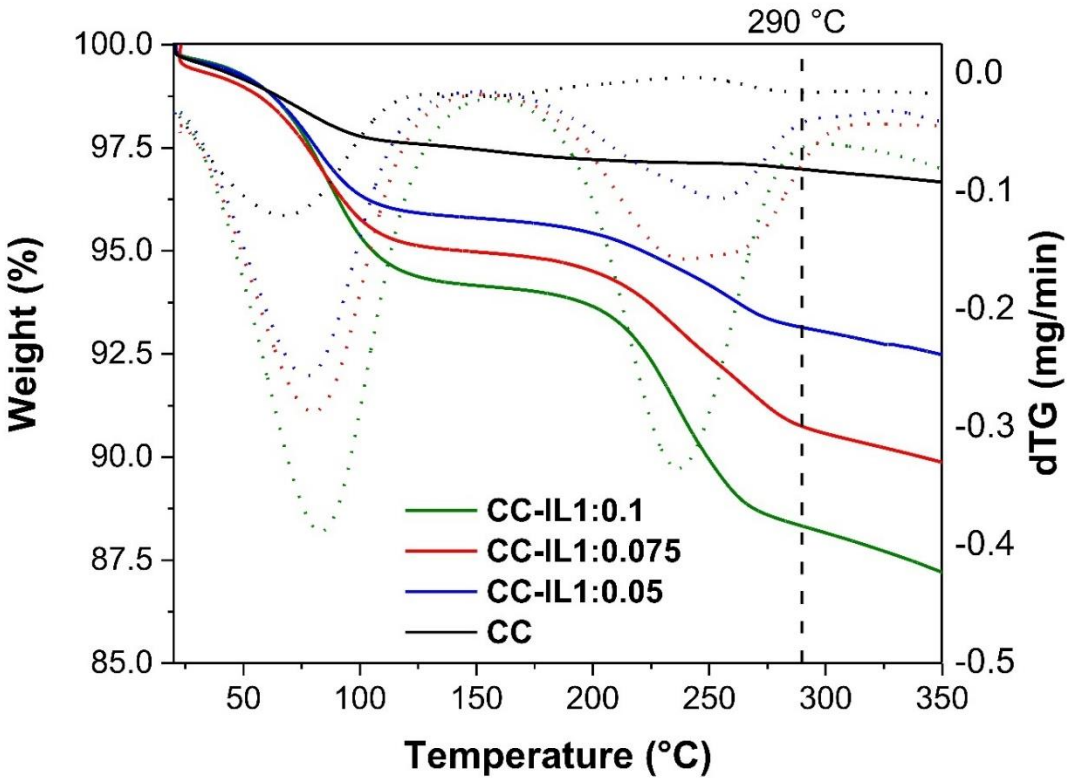

Figure 5.6 *Non-isothermal thermogravimetric analysis under N_2 atmosphere at a heating rate of 10 °C/min until 350 °C, thermogravimetric (solid line) and differential thermogravimetric (dTG, dashed line) curves of CC impregnated with different IL mass ratio.*

Table 5.2 *Ionic liquid and moisture concentration in impregnated CC calculated from TGA analysis.*

Samples	Moisture (%)	Ionic liquid content (%)	
		Calculated from mass ratio	Measured in TGA
CC	2.50	-	-
IL	14.5	100	98.34
CC-IL1:0.05	4.17	5.26	4.34
CC-IL1:0.075	4.98	7.88	6.75
CC-IL1:0.1	5.79	10.44	9.17

5.3.3 CO_2 capture experiments

In Figure 5.7 the kinetics at different pressures of IL, CC and CC impregnated with IL were presented. CO_2 capture capacities, kinetics, and capture rate were condensed in Table 5.3. The sample with the lowest mass ratio, 1:0.05 (wt CC:wt IL), presented the best IL use efficiency and therefore better CO_2 capture capacity. Through IL impregnation, the CO_2 capture capacity of the CC was improved from 0.41, 0.56, 0.85 and 1.37 mmol/g to 0.81, 1.53, 1.86 and 2.46 mmol/g for CC-IL1: 0.05 at 1, 3, 5 and 8 bar, respectively. This represented an improvement between 80-170% for CC-IL1:0.05 over the pristine material (CC). In addition, if the CO_2 capture capacity of CC-IL1:0.05 is calculated considering the amount of IL and compared with that of pure IL at 60 min, an improvement of more than 15 times at 1 bar (from 1.27 to 19.59 mmol/g IL) and up to almost 20 times at 8 bar (from 3.06 to 59.37 mmol/g IL) was obtained.

The considerable improvement in the efficient use of impregnated IL in CO_2 capture was largely attributed to its good dispersion in CC observed in the SEM micrographs

(Figure 5.3 d), leds to a significant improvement in the CO_2 mass transfer rate due to the increase in the gas-liquid contact area [352,369,370]. The improvement in the CO_2 capture rate (<10 min) for the impregnated materials was observed at a pressure of 3 and 5 bar, because at this pressure the gas interacts rapidly with the impregnated IL, unlike at 8 bar where the pressure contributes to the CO_2 being absorbed more quickly by the pure IL. The CO_2 capture rate improved from 0.121 and 0.156 mmol/g·min for pure IL to 0.141 and 0.172 mmol/g·min for CC-IL1:0.05 at 3 and 5 bar, respectively. Moreover, it has been reported that the saturation time of IL at 1 bar can be as long as 20 hours [85] compared to 20 minutes for CC-IL1:0.05. These results indicate that CO_2 capture in impregnated IL is controlled by mass transfer rather than reaction kinetics [85,352].

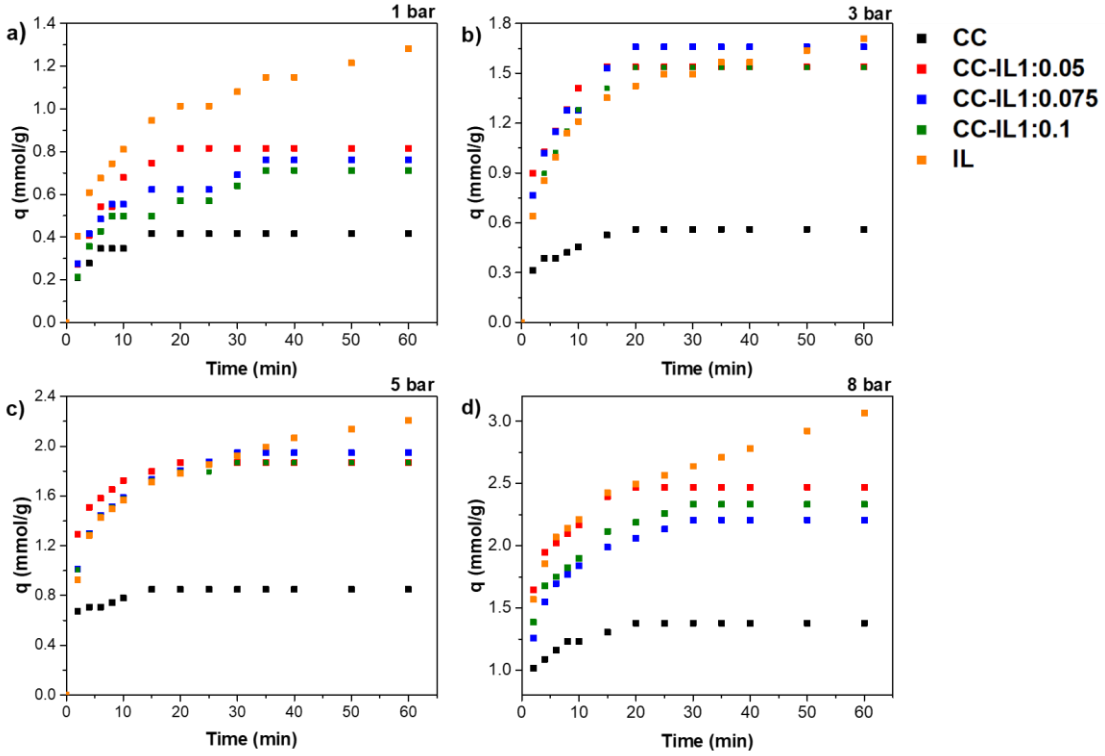

Figure 5.7 *CO_2 capture kinetics of CC, IL and CC impregnated with IL at 25 °C and pressure of a) 1 bar, b) 3 bar, c) 5 bar and d) 8 bar.*

Table 5.3 *CO_2 capture kinetics and capacities of IL, CC and CC impregnated with IL at 25 °C and pressure of 1, 3, 5 and 8 bar.*

Samples	Pressure (bar)	q_{max} (mmol/g)	q_{max} (mmol/g IL)	Saturation time (min)	Capture rate at 10 min (mmol/g·min)
IL	1	1.27	-	60	0.081
	3	1.7	-	60	0.121
	5	2.21	-	60	0.156
	8	3.06	-	60	0.221
CC	1	0.41	-	20	0.034
	3	0.56	-	20	0.045
	5	0.85	-	15	0.077
	8	1.37	-	20	0.123
CC-IL1:0.05	1	0.81	19.59	20	0.068
	3	1.53	36.98	15	0.141
	5	1.86	44.90	20	0.172
	8	2.46	59.37	20	0.217
CC-IL1:0.075	1	0.75	12.03	35	0.055
	3	1.65	26.23	20	0.127
	5	1.94	30.81	30	0.158
	8	2.20	34.89	30	0.184
CC-IL1:0.1	1	0.7	8.47	35	0.049
	3	1.53	18.29	20	0.128
	5	1.86	22.22	30	0.157
	8	2.33	27.78	30	0.189

q_{max} taken at saturation time, for IL at 60 min.

Regarding the CO_2 capture mechanism, it has been widely reported from experimental techniques and computational methods [92,185,371] that the interaction between IL and CO_2 occurs as a reversible reaction between the C2 of the $[BMIM]^+$ ring to form a carboxylate complex (Figure 5.8), where the reaction moves towards the products side at low partial pressures [372].

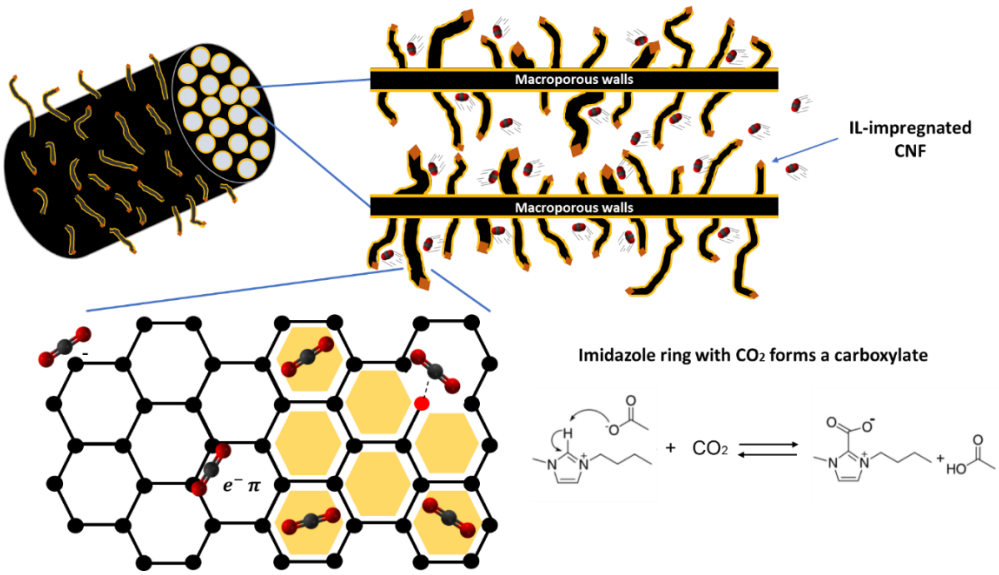

Figure 5.8 *Suggested CO_2 capture mechanism of impregnated IL [92,185,371,372].*

Three sorption-desorption cycles were performed to assess the feasibility of using the impregnated materials in a CO_2 capture system. The reversibility capacity of pure IL, CC and the materials impregnated with IL was calculated with CO_2 capture times of 60 min and a pressure of 8 bar (Figure 5.9). The results of these sorption-desorption tests were condensed in Table 5.4. For IL, capacities of 3, 2.53 and 2.24 mmol/g IL were obtained with reversibility of 84.33 and 73.81% for the 2nd and 3rd cycle, respectively. The decrease in IL regenerability has been attributed to the formation of complexes between CO_2 and IL, which makes IL regeneration more difficult causing a partial reversibility [366]. On the other hand, the CC presented a regenerability of 100% with a CO_2 capture capacity of 1.37 mmol/g for the 3 cycles, where the CO_2 capture rate as well as the kinetics remained practically the same (0.0685 mmol/g·min and 20 min, respectively). These results indicate that the CC did not present diffusion problems in CO_2 sorption-desorption cycles.

Corresponding to IL-impregnated materials, it was found that as the degree of IL impregnation increased, the degree of reversibility was similar to that of pure IL. This indicates that the diffusion of CO_2 was better at low mass ratios of IL, as previously reported [85,185,373], since as the amount of IL is higher, a worse dispersion and formation of IL agglomerates was observed (Figure 5.3). The material that presented the best performance was CC-IL1:0.05 with CO_2 capture capacities of 2.24, 2.03 and 1.74 mmol/g (first to third cycle) and with reversibility capacities of 90.32 and 77.41% for the 2nd and 3rd cycle, respectively. Previously, reversibility capacities in the second cycle of 77 and 54% at 8 bar were reported for MB impregnated with IL with mass ratios of $1:1x10^{-3}$ and 1:0.075, respectively [363]. The considerable improvement in the reversibility in the capture of CO_2 indicates that the growth of CNF on the MB contributed to improve the impregnation of the IL on a carbon matrix, allowing it to sorb-desorb CO_2 more efficiently.

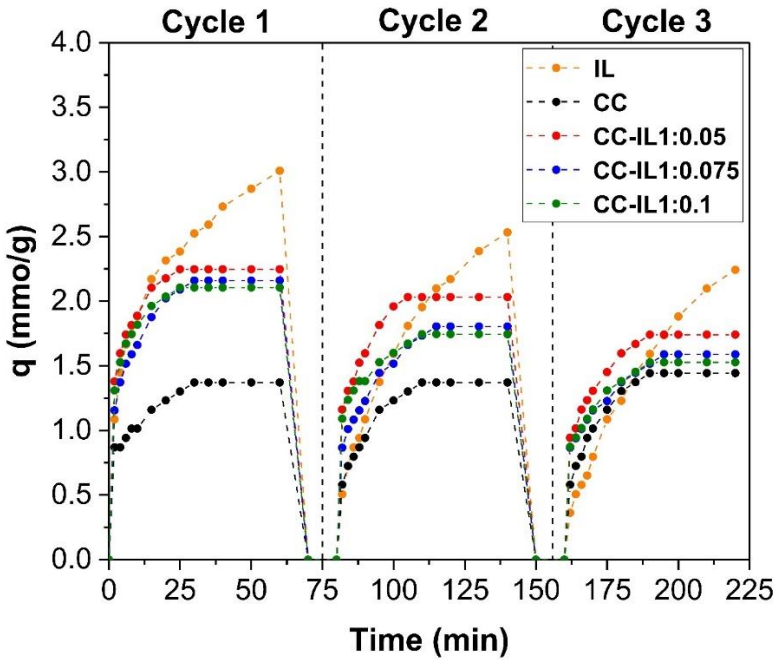

Figure 5.9 *Sorption-desorption cycles of CC, IL and CC impregnated with IL at 25 °C and 8 bar.*

Table 5.4 *CO_2 capture capacity and regenerability of 3 sorption-desorption cycles of IL, CC and CC impregnated with IL at 25 °C and 8 bar.*

Samples	q (mmol/g)			Regeneration capacity (%)	
	C1	C2	C3	C2	C3
IL	3.00	2.53	2.24	84.33	73.81
CC	1.37	1.37	1.37	100	100
CC-IL1:0.05	2.24	2.03	1.74	90.32	77.41
CC-IL1:0.075	2.16	1.80	1.58	83.32	73.31
CC-IL1:01.1	2.10	1.74	1.52	82.74	72.41
C means Cycle					

5.4 Conclusions

This work demonstrates that it is possible to considerably improve the efficiency of CO_2 capture of the ionic liquid [BMIM][Ac] through its impregnation in a carbon composite, CNF-modified macroporous biochar. The surface of the MB increases from 2 to 422 m^2/g through the growth of CNF, which allows improving the accessible surface where the IL can be impregnated. The TGA results show that the methodology used to impregnate the CC is adequate, since the weight loss associated with the decomposition of IL (T <290 ° C) was proportional to the degree of impregnation of each sample. The sample CC-IL1:0.05 presents the most efficient use of IL and therefore, the best capture CO_2 performance. Through a better IL dispersion, corroborated by SEM, mass transfer improves the contact area between CO_2 and IL. The CO_2 capture capacity of the CC improves from 0.41 and 1.37 mmol/g to 0.81 and 2.46 mmol/g for CC-IL1:0.05 for 1 and 8 bar, respectively. In addition, the impregnation of the IL drastically improves the CO_2 capture kinetics. For all pressures used during the experiments, the equilibration time of CC-IL1:0.05 is less than 20 min and the CO_2 capture rate improves almost twofold, from 0.02-

0.06 mmol/g·min for CC to 0.04 and 0.12 mmo/g·min for CC-IL1:0.05 at 1 and 8 bar, respectively. Furthermore, the calculated CO_2 capture capacity of the impregnated IL is up to 20 times greater than that for pure IL. The enormous improvement in the CO_2 capture capacity of the IL is attributed to the good dispersion in the CC, increasing the gas-liquid contact area. These results indicate that CO_2 capture of the impregnated IL is mainly controlled by mass transfer and not by reaction kinetics between CO_2 and IL. Finally, for sorption-desorption cycles it is observed that as the degree of impregnation of IL increases, the reversibility is similar to that of pure IL. The CC impregnated with the least ratio of IL (1:0.05) presents the best regeneration capacities of 90.32 and 77.41 % for the second and third cycle, respectively. Therefore, the considerable improvement in kinetics and CO_2 capture capacity of the IL-impregnated CC, as well as its high regenerability, demonstrates its viability for CO_2 capture systems.

Chapter 6:

Highly selective separation of CO_2 from the CO_2/CH_4 gas mixture using carbonized bagasse fibers modified with carbon nanotubes.

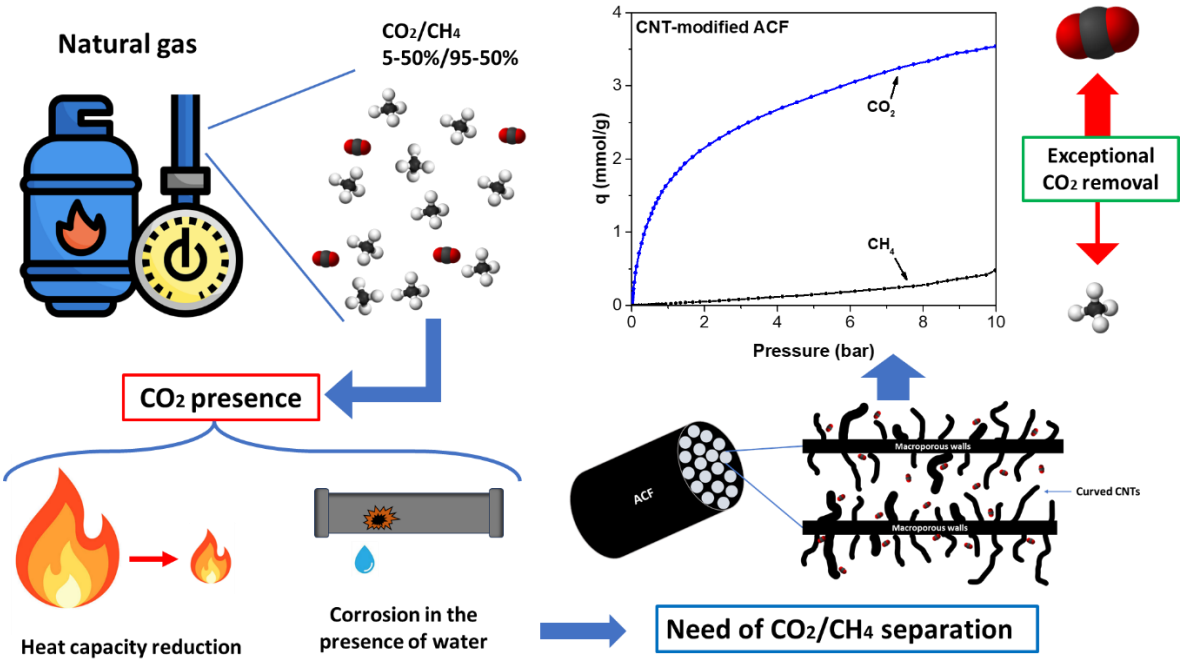

ABSTRACT

Global climate change has led to the need to transition towards renewable energy sources, such as methane. However, this gas is usually found combined with other gases, mainly CO_2, reducing its heat capacity. Therefore, the selective separation of CO_2 from a CO_2/CH_4 mixture is of great importance. Accordingly, in this work carbonized agave bagasse fibers modified with carbon nanotubes (ACF3-CNT-AT1) were evaluated as a selective CO_2 adsorbent on the CO_2/CH_4 gas mixture. The growth of carbon nanotubes (CNT) was carried out by chemical vapor deposition (CVD) at 700 °C, using magnetite particles as catalyst and acetylene as carbon source. The texture properties and surface chemistry of carbonized bagasse fibers (ACF) and CNT-modified ACF were characterized by scanning electron microscopy (SEM), N_2 adsorption isotherms at 77 K, CO_2 isotherms at 273 K and X-ray photoelectron spectroscopy (XPS). The CO_2 and CH_4 adsorption capacities were obtained by adsorption isotherms at pressures of up to 10 bar and temperatures of 25, 50 and 75 °C. The isosteric heat of adsorption (q_{st}) was calculated by using the Clausius-Clapeyron equation and the CO_2/CH_4 selectivity was calculated by the ideal adsorbed solution theory (IAST). Through the homogeneous growth of CNT on the surface of the ACF, the specific area was increased from 2 to 452 m^2/g and the micropore volume from 0.009 to 0.168 cm^3/g. Furthermore, the C content increased, and the O content decreased with respect to the pristine ACF; most of the oxygenated groups were attributed to carbonyl, ketone, and carboxylic. Additionally, the CNT-modified ACF presented CO_2 and CH_4 adsorption capacities of 3.53 and 0.47 mmol/g at 25 °C and 10 bar, respectively, and an isosteric heat of adsorption

for CO_2 of 26 kJ/mol and 11-3 kJ/mol for CH_4. Finally, the IAST selectivity of ACF3-CNT-AT1 for the binary mixture CO_2/CH_4 (10:90) presented one of the highest values reported in the literature (330.3). These results indicate that through the growth of CNT on the surface of ACF, it is possible to considerably improve the CO_2 selectivity in the CO_2/CH_4 gas mixtures, which makes it viable for its application in methane purification. Consequently, methane can increase its heat capacity and its commercial value and decrease the disadvantages of being in a mixture with other gases.

6.1 Introduction

The growing concern about global climate change and energy demand has led to increased interest in the transition to renewable or lower greenhouse gas emissions energy sources [374]. One of the alternatives is the use of biofuels as an alternative to fossil fuels, which present a considerable reduction in hydrocarbons, SO_x and CO_2 emissions [375-377]. Methane (CH_4) has been considered, in addition to a greenhouse gas, a source of clean and cheap energy, which can be produced from anaerobic digestion or obtained from coal and natural gas deposits [378-381]. However, CH_4 is usually found combined with other gases (mainly CO_2), which reduce its heating value and there is a risk of corrosion in pipes in the presence of water [382-384]. Therefore, the separation of carbon dioxide (CO_2) to improve the methane purity is of great importance. The most commonly used technologies have been absorption with liquid amines [385,386], membrane separation [387-389], cryogenic distillation [390-392] and adsorption [393-395]. Absorption with liquid amines has been the most used due to its high level of development [396]. However,

the significant energy demand for their regeneration has led to the investigation of other methodologies such as adsorption in porous solids [34]. Adsorption presents important advantages such as relatively low cost and low energy consumption, where the main materials tested have been zeolites, metal-organic structures (MOFs) and carbons [316,397-401]. Carbon materials are of great interest because they have good CO_2 adsorption capacity, fast kinetics, hydrophobic character, good chemical and thermal stability and relatively low production and regeneration costs [402-404]. Furthermore, when carbon materials are produced, the precursors are sought to be cheap, accessible, and highly available [405]; Agricultural by-products are therefore particularly attractive. In this sense, the mezcal and tequila industry produces more than 370,000 tons per year of bagasse waste [171], which can be carbonized to generate macroporous biochar [184]. Because the materials used for the biogas CH_4 purification must present high selectivity towards CO_2, guaranteed by their adequate textural properties (specific surface area and pore size distribution) and surface chemistry [406], in this work carbonized agave bagasse fibers were modified with carbon nanotubes (CNT) to increase the specific surface area and polar surface groups that improve selectivity towards CO_2 [407].

6.2 Experimental Section

The materials studied in this chapter were named ACF and ACF3-CNT-AT1 in chapter 2 and their synthesis is widely described in section 3.2 of that chapter.

6.2.1 Physicochemical characterization of materials

The morphology of the materials was observed under a HELIOS NANOLAB 600i SEM with high resolution field emission source and secondary electron detector. Before analysis, the samples were immobilized on a carbon tape retained in an SEM sample holder. The specific surface area and pore size distribution were determined from the nitrogen adsorption isotherm at 77 K using a Micromeritics ASAP 2020 physisorption equipment. The specific surface area was determined by using the Breunaer-Emment-Teller (BET) equation and the pore size distribution (PSD) was obtained by using the density functional theory (DFT). Also, CO_2 isotherms at 0 °C obtained by a Micromeritics ASAP 2050 automatic manometric sorptometer were used to calculate the micropore size distribution using the non-localized density functional theory (NLDFT). Finally, X-ray photoelectron spectroscopy (PHI 5000 VersaProbe II XPS, Physical Electronics) with a monochromatic Al-Kα (1486.6 eV) radiation was utilized to study the elemental composition and chemical state of the samples. The deconvolution of the spectra was processed with the help of the MultiPak 9.3 (or XPSPEAK 4.1) software.

6.2.2 CO_2 and CH_4 capture experiments

The CO_2 and CH_4 adsorption isotherms (at 25, 50 and 75 °C) of the materials were obtained in a Micromeritics ASAP 2050 automatic manometric sorptometer up to a pressure of 10 bar. Before measurements, the materials were degassed at 150 °C for 8 hours under vacuum. In addition, the isosteric heat of adsorption (q_{st}) was calculated, which is a value that characterizes the adsorbate-adsorbent interaction strength, the type of adsorption (chemisorption or physisorption) and the degree of

heterogeneity of the material surface. This study was carried out from the analysis of the q_{st} curve (kJ/mol) vs. the amount of CO_2 or CH_4 adsorbed (mmol/g), where the q_{st} values were obtained from the data of the CO_2 or CH_4 adsorption isotherms measured at different temperatures, and by using the Clausius-Clapeyron equation (Equation 6.1):

$$q_{st} = R\left[\frac{\delta \ln p}{\delta\,(1/T)}\right]_{n_{ads}} \qquad \textit{(Equation 6.1)}$$

where p (kPa) is the equilibrium pressure, T (K) is the adsorption temperature and R (8.314 kJ/mol·K) is the ideal gas constant. The equilibrium pressure (p) for each amount of CO_2 or CH_4 adsorbed (n_{ads}) was estimated by non-linear interpolation from the data of the experimental isotherms at different temperatures. The slope of the straight line of adsorption (ln p vs. 1/T) corresponds to the isosteric enthalpy of CO_2 or CH_4 adsorption for a defined amount of CO_2 or CH_4 adsorbed.

The selectivity of the materials was calculated by the ideal adsorbed solution theory (IAST), which is the most widely used method to predict the selectivity of binary gases from single-component isotherms [338,408-410]. To apply the IAST method, first the CO_2 and CH_4 isotherms at 25 °C were fitted to the Langmuir model (Equation 6.2).

$$q = \frac{q_{sat} bp}{1+bp} \qquad \textit{(Equation 6.2)}$$

where, q is the amount of gas adsorbed (mmol/g), q_{sat} is the maximum adsorption capacity of the gas, b is the Langmuir constant and p is pressure (bar).

For the CO_2/CH_4 gas mixtures (10:90), (30:70) and (50:50), the IAST selectivity was calculated by using the following equation:

$$S = \frac{q_1/q_2}{p_1/p_2} \qquad \textit{(Equation 6.3)}$$

where q_1 and q_2 are the adsorbed amounts of CO_2 and CH_4 (in mmol/g) and p_1 and p_2 are the partial pressure of CO_2 and CH_4, respectively.

6.3 Results and Discussion

6.3.1 Physicochemical characterization

Through SEM characterization, the CNT growth was described widely in chapter 3. SEM micrographs of the ACFs before and after the CNT growth are presented in Figure 6.1. For the ACF, a rough morphology was observed with channels parallel to the fibers, where the surface is mostly smooth with pores throughout their surface (Figure 6.1 a) and b)). For the modified ACF, a homogeneous growth of CNT was obtained on the entire surface despite its roughness (Figure 6.1 c) and d)). Figure 6.1 e) showed curved CNTs with a similar outer diameter, which form a complex matrix. Finally, Figure 6.1 f) showed a representative TEM micrograph of the grown CNTs, where the hollow core of the CNTs and an inner diameter of 20-30 nm were confirmed, as it was observed in chapter 3.

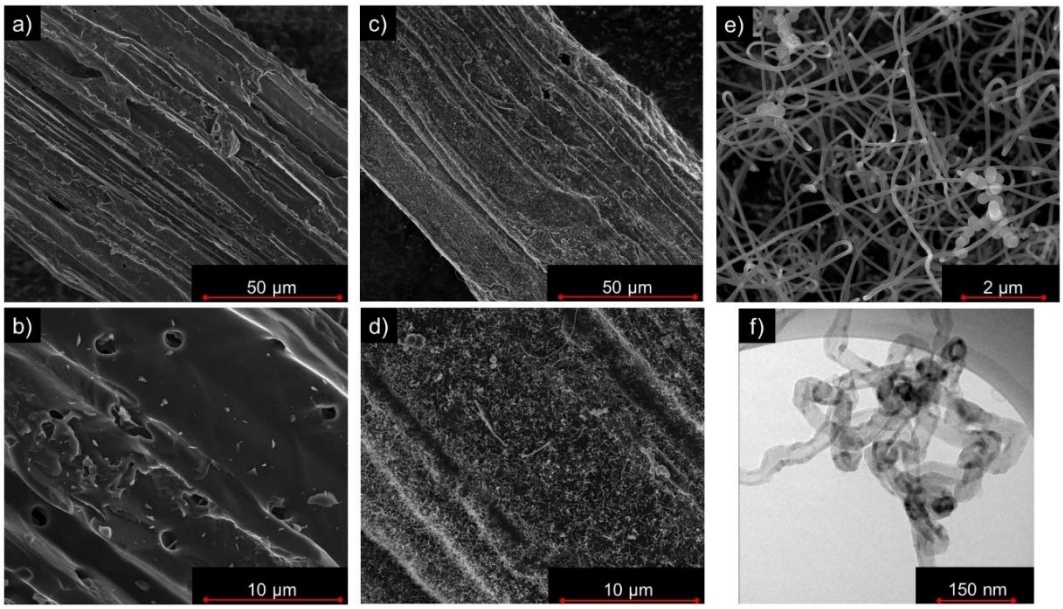

Figure 6.1 *SEM secondary electrons images of a) and b) ACF, d)-e) ACF3-CNT-AT1 and f) representative TEM image of CNT from ACF3-CNT-AT1.*

Through the isotherms of N_2 at 77 K and CO_2 at 273 K, the textural properties of the ACF and ACF modified with CNT were obtained. The ACF showed a type (II) N_2 isotherm according to the IUPAC classification characteristic of non-porous or macroporous materials and ACF3-CNT-AT1 revealed a type (I) isotherm (Figure 6.2 a)) characteristic of microporous materials [292]. Furthermore, through the growth of CNT it was possible to increase the specific surface area from 2 to 452 m^2/g, with a considerable increase in pore volume from 0.009 to 0.168 cm^3/g, mainly in micropores (Table 6.1). The PSD of the materials from N_2 and CO_2 isotherms is reported in Figure 6.2 b) and Figure 6.2 d, respectively.

From the N_2 isotherms, it can be said that ACF presented low mesoporosity (between 10-45 nm) without the presence of micropores and for ACF3-CNT-AT1 it was found that the sample mainly presents microporosity (predominantly < 1.4 nm). On the other hand, through the CO_2 isotherms at 273 K, ACF presented a micropore volume of 0.131 cm^3/g, attributed mostly to ultrarmicropores (0.099 cm^3/g) with a

pore size between 0.35 to 0.5 nm. Furthermore, ACF3-CNT-AT1 presented a micropore volume of 0.156 cm^3/g, mainly attributed to ultramicropores (0.114 cm^3/g) with pore size between 0.45 to 0.55 nm. Ultramicropores have been reported to contribute to CO_2 capture at low pressures, while supermicropores become more important as pressure increases [155]. It is important to mention that these results should be taken with caution because it has been reported that the PSD obtained from CO_2 isotherms with NLDFT exhibit insensitivity in the ultramicropore region and the results may not be entirely correct to differentiate between microporous materials [411].

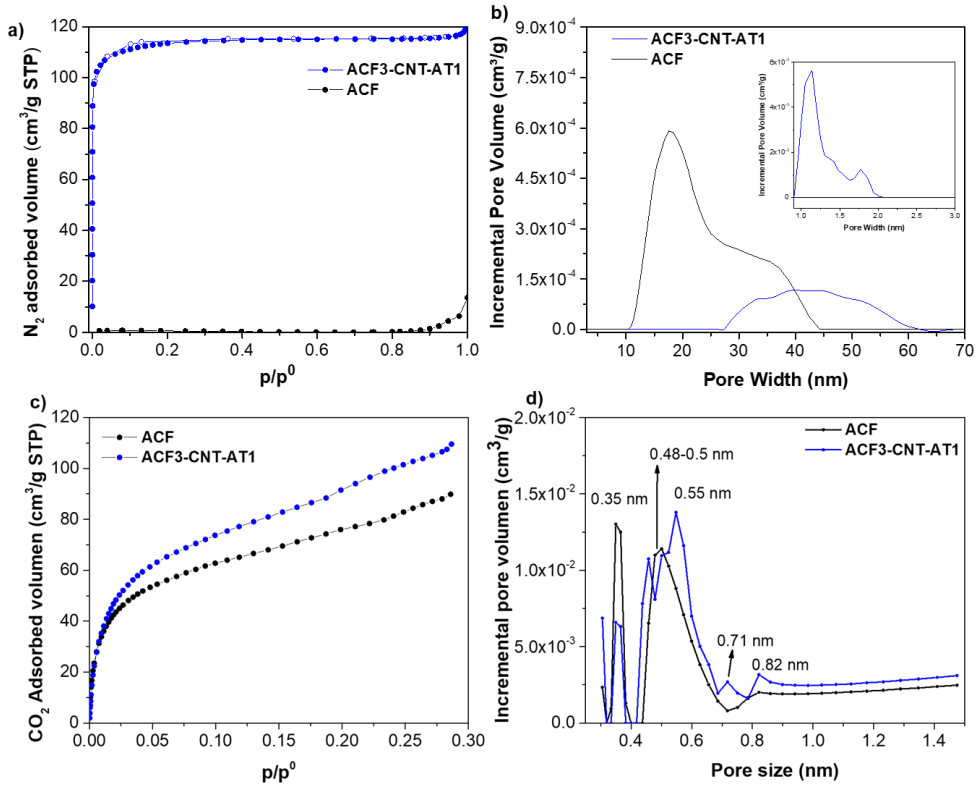

Figure 6.2 *a) Experimental N_2 adsorption isotherms at 77 K and b) pore size distribution calculated from N_2 isotherms with Quenched solid density functional theory (QSDFT), c) Experimental CO_2 adsorption isotherms at 273 K and d) pore size distribution calculated from CO_2 isotherms with nonlocal density functional theory (NLDFT).*

Table 6.1 *Textural properties of ACF and ACF3-CNT-AT1.*

Sample	S_{BET}	V_{total}	V_{macro}	V_{meso}	V_{micro}	V_{micro}*	V_{Super}*	V_{Ultra}*
	(m^2/g)	(cm^3/g)						
ACF	2	0.009	0.009	0	0	0.131	0.032	0.099
ACF3-CNT-AT1	452	0.168	0.001	0.001	0.166	0.156	0.042	0.114
*Calculated from CO_2 isotherms at 273 K. Super= Supermicropores from 2 to 0.7 nm. Ultra= Ultramicropores less than 0.7 nm.								

The chemical composition was analyzed through the overall XPS spectrum, and the data are presented in Table 6.2. It was obtained that through the growth of CNT by CVD, the carbon content increased from 84.44 to 88.44%, and the O content decreased from 13.47 to 8.8%. These changes correspond to what was reported in Figure 3.8, where the increase in the basic nature of the material was observed. In addition, specific elements of the precursor (agave bagasse) such as Na, Si and Ca were found. Also, a low concentration of Cl was identified that comes from the catalyst impregnation, but not Fe was found for the CNT-modified ACF. Therefore, it is considered that the impregnated iron nanoparticles may be covered with C, which makes difficult their quantification by this technique.

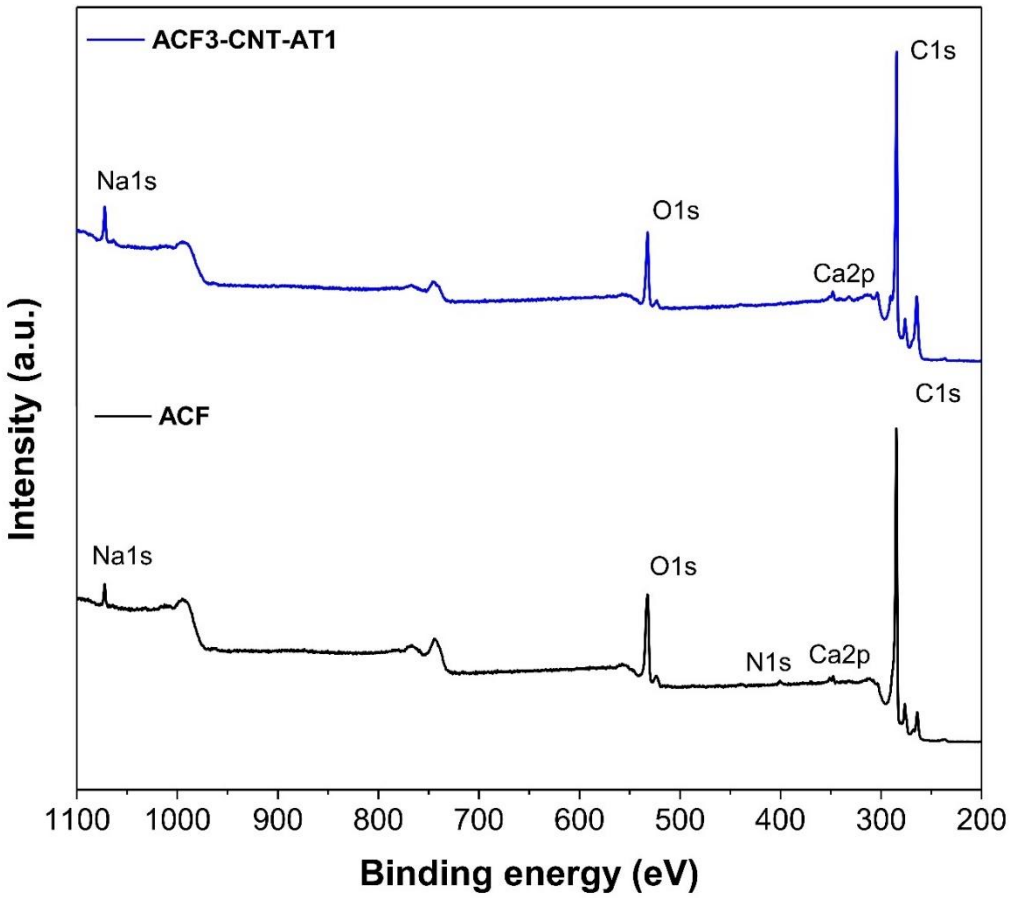

Figure 6.3 *XPS survey spectra of ACF and ACF3-CNT-AT1.*

Table 6.2 *Elemental composition (atomic %) of ACF and ACF3-CNT-AT1.*

	Atomic content (%)						
	C1s	**N1s**	**O1s**	**Na1s**	**Si2p**	**Cl2p**	**Ca2p**
ACF	84.44	0.46	13.47	1.01	0.06	0	0.55
ACF3-CNT-AT1	88.44	0	8.8	2.03	0.05	0.02	0.66

The contributions of C, O and N (Figure 6.4) were calculated by deconvolution of the high-resolution spectra of the energy levels of each element and the data are presented in Table 6.3. For carbon, the samples showed signals corresponding to C=C sp^2 (284.2 eV), C-C sp^3 (284.8 eV), ketone or quinone groups C=O (286.3 eV),

carboxylic groups, carbonyls or esters groups O-C=O (287.1 eV) and pi-pi bonds (290 eV). For oxygen, the signals of C=O carbonyl or ketone groups (531.3 eV), COOH carboxylic groups (532.5 eV), C-O ether groups (533.9 eV) and absorbed H_2O (535.7 eV) were found. Finally, for N, only ACF showed signals from N-pyridinic (398.6 eV), N-pyrrolic (400.2 eV), quaternary N (401.6 eV) and NOx (403.5 eV) groups [339]. Through the growth of CNT, the amount of C=C sp^2 increased by 6.1%, and C=O, C-C sp^3 and pi-pi around 4%, where the only signal that decreased 9.5% was the related with carboxylic, carbonyl or ester groups (O-C=O). Furthermore, only for the ACF the signal attributed to H_2O was found, which could be attribute to the fact that through the growth of nanostructures the hydrophilic nature of the ACF decreased. For the oxygenated groups, ACF3-CNT-AT1 presented mainly C=O groups (50.2%), COOH (34.1%) and C-O (15.7%), where the main change with respect to the ACF was the disappearance of the H_2O signal, the reduction of ether groups (C-O) and the considerable increase of C=O groups. Therefore, the defects and curvature of the CNTs observed in Figures 6.1 e) and f) must be mainly related to oxygenated groups (mainly carbonyl, ketone, and carboxylic groups), which provide greater reactivity towards CO_2 [301].

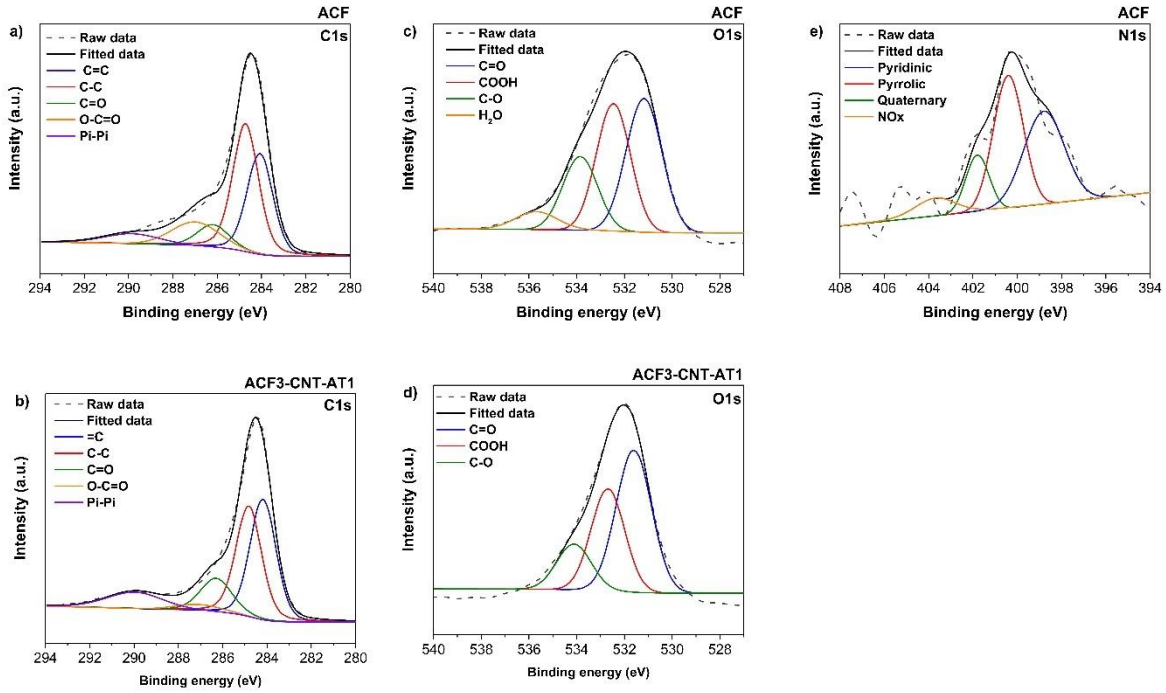

Figure 6.4 *Deconvolution of high-resolution XPS of samples ACF and ACF3-CNT-AT1: a) and b) for C1s, c) and d) for O1s and e) for N1s high resolution spectra.*

Table 6.3 *Relative and absolute abundance (%) of the different peaks assigned from the deconvolution of the central energy level of C1, O1 and N1 for ACF and ACF3-CNT-AT1.*

	Relative abundance of C1s (%)					**Absolute abundance of C1s (%)**				
Sample	**C=C**	**C-C**	**C=O**	**O-C=O**	**π-π**	**C=C**	**C-C**	**C=O**	**O-C=O**	**π-π**
MB	30.9	40.3	8.9	13	6.8	26.1	34.02	6.83	10.98	5.74
ACF3-CNT-AT1	37	35.1	13.3	3.5	11.1	32.72	31.04	11.76	3.1	9.81
	Relative abundance of O1s (%)					**Absolute abundance of O1s (%)**				
	C=O	**COOH**	**C-O**	**H_2O**	**Fe-O**	**C=O**	**COOH**	**C-O**	**H_2O**	**Fe-O**
MB	38.5	34.7	20.5	6.3	0	5.18	4.67	2.77	0.85	0
ACF3-CNT-AT1	50.2	34.1	15.7	0	0	4.41	3	1.32	0	0
	Relative abundance of N1s (%)					**Absolute abundance of N1s (%)**				
	Pyri	**Pyrr**	**Quat**	**NOx**		**Pyri**	**Pyrr**	**Quat**	**NOx**	

Table 6.3 (Continuation)0								
MB	38.4	40.3	13.2	8.1	0.18	0.19	0.06	0.03
ACF3-CNT-AT1	0	0	0	0	0	0	0	0
Pyri= Pyridinic/ Pyrr=Pyrrolic/ Quat=Quaternary								

6.3.2 CO_2 adsorption capacity and selectivity.

Figure 6.5 shows the CO_2 and CH_4 isotherms at 25 °C and pressure up to 10 bar. For ACF, CO_2 and CH_4 adsorption capacities of 1.33 and 0.57 mmol/g at 1 bar and 2.30 and 1.54 mmol/g at 10 bar were obtained from the isotherms of each pure gas, respectively. While for ACF3-CNT-AT1, CO_2 and CH_4 adsorption capacities of 1.71 and 0.02 mmol/g at 1 bar and 3.53 and 0.47 mmol/g at 10 bar were obtained, respectively. For both materials, CO_2 was preferentially adsorbed on top of CH_4 due to the greater quadrupole moment of CO_2, which promotes a stronger attraction between adsorbate and adsorbent [404,405,412]. However, the affinity of ACF3-CNT-AT1 was considerably higher, which has been attributed to the higher surface polarity given by the presence of heteroatoms, especially O, the increase in microporosity and specific surface area, and even to the hydrophobic nature of the material [413,414]. For ACF3-CNT-AT1, no presence of nitrogenous groups was found, so the high polarity of the material was attributed to oxygenated groups, mainly carbonyl, ketone, and carboxylic, as obtained by XPS. In this way, the results indicate the opposite of what was reported through computational studies, where it has been reported that higher content of oxygenated groups, specifically C=O and COOH, improve CO_2 selectivity [415,416]. For ACF, an absolute content of C=O and

COOH groups of 9.86% was found and 7.43% for ACF3-CNT-AT1. Therefore, other proprieties of ACF3-CNT-AT1 such as the higher hydrophobic character, the availability of these oxygenated groups, the available specific surface area and the pore size distribution must be contributing to the exceptional CO_2 selectivity of ACF3-CNT-AT1. Actually, the sorption behavior of these gases has been predicted using simplified local density models, where it was found that pores <0.42 nm adsorb more easily CH_4 [415,417]. This agrees with our results, since according to the PSD through the CO_2 isotherms at 273 K it was found that the pore volume <0.42 nm of ACF3-CNT-AT1 is 0.019 cm^3/g whereas that for ACF is 0.03 cm^3/g, that is 58% higher.

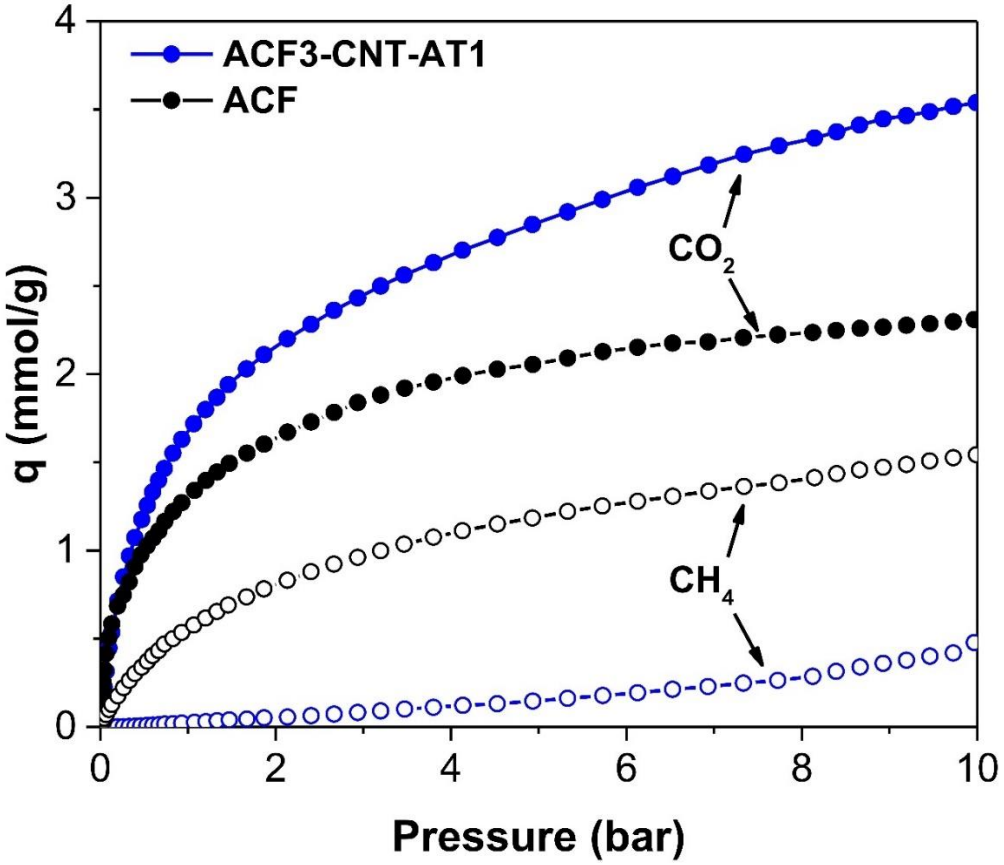

Figure 6.5 *CO_2 and CH_4 adsorption isotherms at 25 °C and pressures up to 10 bar of ACF and ACF3-CNT-AT1.*

For CO_2 molecules, the atoms of the oxygenated groups act as basic adsorption sites, which serve as Lewis bases by providing electrons to the acidic carbon atoms of the CO_2 molecule. Specifically, O atoms in the C=O and COOH functional groups have been reported to confer electronegativity by gaining electrons from surrounding atoms (0.45 and 0.455 e^-). The electronegativity of these O atoms enhances the interaction energy with CO_2 by up to 35.74 kJ/mol [415]. On the other hand, for CH_4 molecules the negatively charged functional groups slightly attract the H atoms (because the CH_4 molecule forms a regular tetrahedron). However, the atoms of the oxygenated groups exert a repulsive force between the atoms with negative charges in the functional groups and the carbon atom of CH_4, which makes the CH_4 poorly adsorbed (Figure 6.6). Likewise, the electropositive atoms of the functional groups that act as Lewis acids, also provide an positive effect on the selective capture of CO_2 through weak interactions with the oxygen atoms of CO_2 [415]. The positive partial charges in the graphite sheets are mainly given by functional groups that alter the charge distribution and it has also been reported that positive partial charges may exist at the edge sites [415,418].

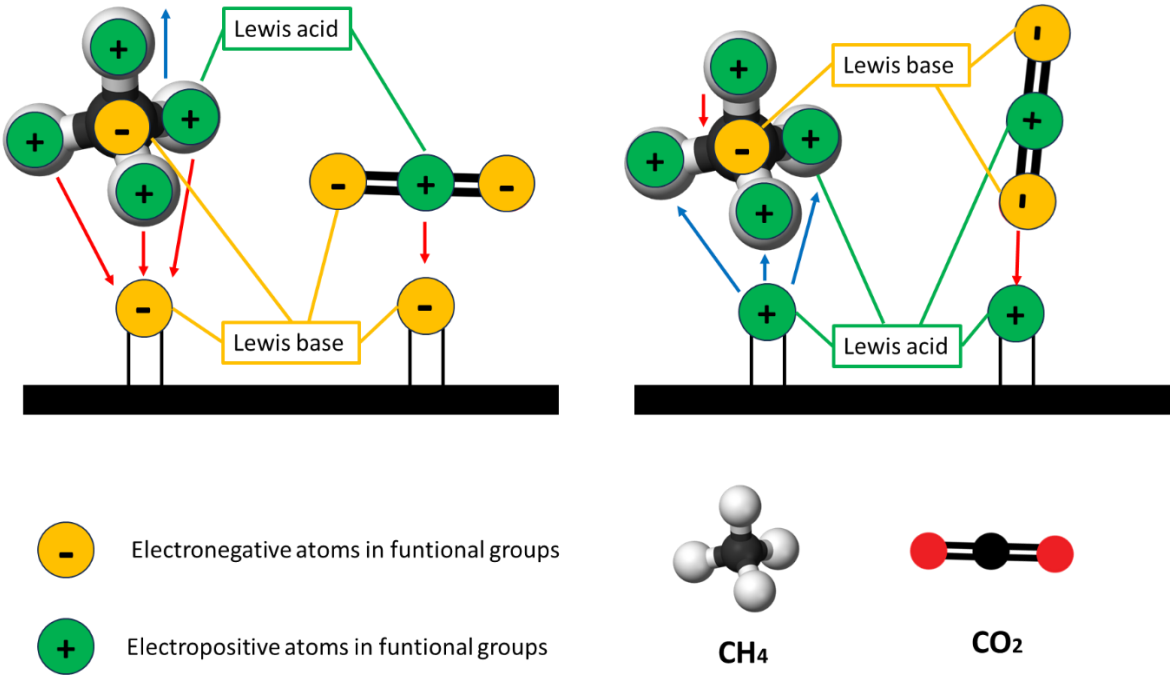

Figure 6.6 *Schematic representation of the interaction between gas molecules and charged atoms in the functional groups, modified from [415].*

CO_2 and CH_4 capture tests of ACF3-CNT-AT1 were carried out at different temperatures (Figure 6.7 a) and the isosteric heat of adsorption for both gases was obtained from the Clausius-Clapeyron equation (Figure 6.7 b). Maximum CO_2 capture values of 3.53, 2.78 and 2.23 mmol/g at 10 bar were obtained at 25, 50 and 75°C, respectively. For CH_4, the maximum adsorption values obtained at 10 bar were 0.47, 0.37 and 0.30 mmol/g, 7.5 times less than the values for CO_2. Regarding the isosteric heat of adsorption (q_{st}), for CO_2 a relatively constant value of about 26 kJ/mol was obtained for the entire range of adsorbed gas and for CH_4 a maximum value of 11 kJ/mol was obtained and then dropped rapidly to 3 kJ/mol as the amount adsorbed increased. The isosteric heat constant value for CO_2 can be interpreted as homogeneity in the interaction between the adsorbent and CO_2 molecules [298]. On the contrary, the rapid decrease in q_{st} value for CH_4 indicates the absence of active

sites to adsorb this molecule [405]. These results corroborate the strong affinity of ACF3-CNT-AT1 towards CO_2, which is of great interest for applications such as in natural gas purification [34,395].

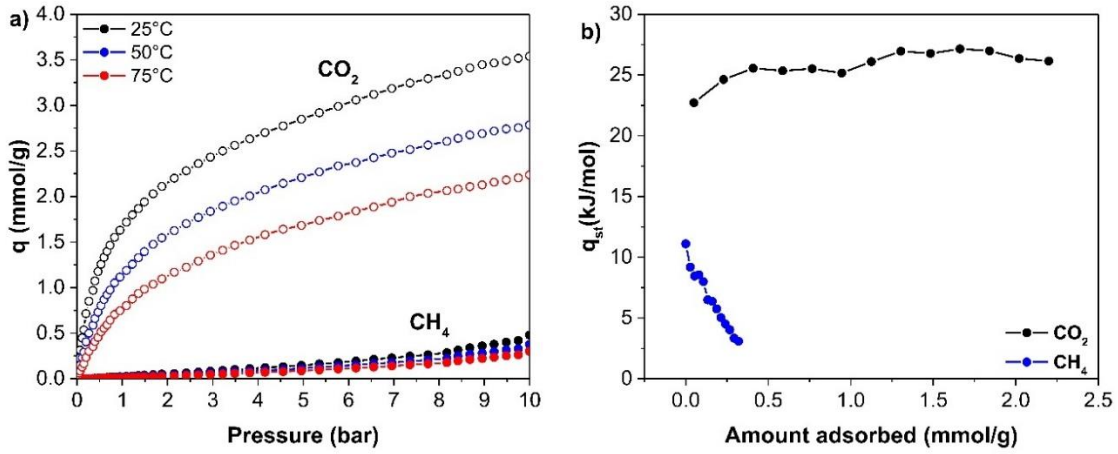

Figure 6.7 *a) CO_2 (empty points) and CH_4 (solid points) adsorption isotherms at 25, 50 and 75 °C and pressure up to 10 bar and b) Isosteric heat of adsorption of CO_2 and CH_4 of ACF3-CNT-AT1.*

To calculate the IAST selectivity CO_2/CH_4 at 25 °C of ACF3-CNT-AT1, the isotherms of pure CO_2 and CH_4 were fitted to the Langmuir model (Figure 6.8), as previously reported [419]. The model fitted adequately (R^2>0.96) and the q_{max} values correspond to those obtained experimentally (Table 6.4).

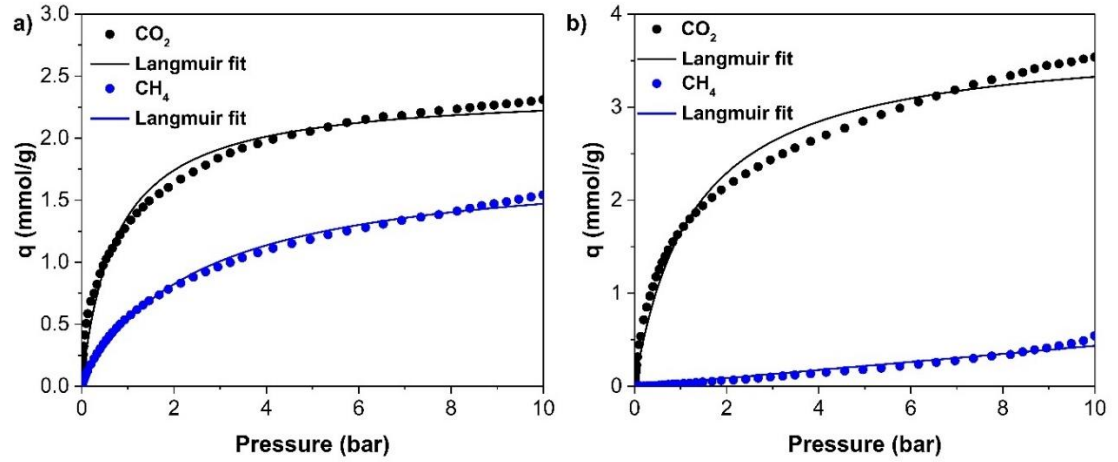

Figure 6.8 *CO_2 and CH_4 adsorption isotherms of a) ACF and b) ACF3-CNT-AT1, and Langmuir model (solid line).*

Table 6.4 *Parameters of the Langmuir isotherms model for CO_2 and CH_4 adsorption of ACF and ACF3-CNT-AT1 at 25 °C and pressure up to 10 bar.*

Sample	CO_2			CH_4		
	q_{max} (mmol/g)	b	R^2	q_{max} (mmol/g)	b	R^2
ACF	2.38	1.35	0.982	1.83	0.41	0.995
ACF3-CNT-AT1	3.75	0.78	0.985	0.43	0.0004	0.967

The IAST selectivity curves for ACF and ACF3-CNT-AT1 (Figure 6.9) were calculated for 3 different CO_2/CH_4 ratios (10:90, 30:70 and 50:50) because it has been reported that non-conventional natural gas, such as biogas and landfill gas, can have a CO_2 concentration of 30-50% [394,395], which could drastically reduce the heating value of natural gas and cause corrosion in pipes in the presence of water. Furthermore, a CH_4 concentration greater than 90% is required in a gas pipeline [396], so these relationships are important for industrial processes with natural gas. The CO_2/CH_4 selectivity of ACF3-CNT-AT1 increased considerably with respect to the pristine material (Table 6.5). At 1 bar the CO_2/CH_4 selectivity increased more than 14 times for ratios 10:90 (from 22.8 to 330.3) and 30:70 (from 5.9 to 85.6) and 22 times higher for the ratio of 50:50 (from 2.5 to 55). At 10 bar, the CO_2/CH_4 selectivity of ACF3-CNT-AT1 were 5 to 7 times higher than those for ACF (for ratios of 10:90, 30:70 and 50:50 improved from 13.5 to 68.8, from 3.5 to 17.8 and 1.5 to 11.4, respectively). It has been reported that selectivity values are usually bigger at low pressure and decrease rapidly as pressure increases until reaching an almost constant value [338,420]. Basically, at low pressures the strong electrostatic interaction between CO_2 and the functionals groups of the carbon material causes

CO_2 to adsorb more easily, compared to CH_4, where there are no strong interactions, so it is adsorbed less, only in spaces unoccupied by CO_2 [415]. The excellent selectivity values obtained for ACF3-CNT-AT1 are one of the highest reported for carbon materials, which makes it very attractive for the purification of natural gas at industrial level.

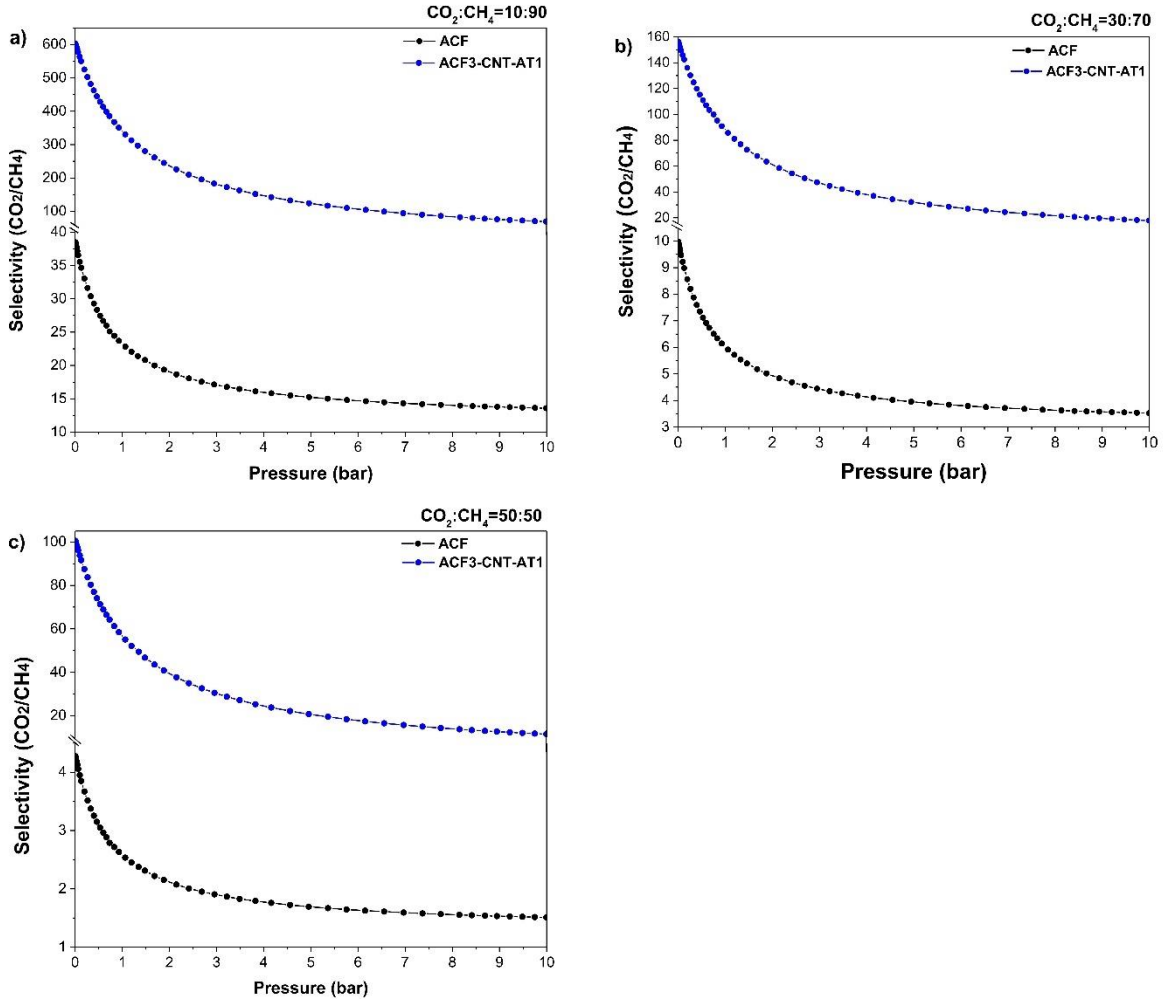

Figure 6.9 *IAST selectivity values of ACF and ACF3-CNT-AT1 for a CO_2/CH_4 binary mixture of a) 10:90, b) 30:70 and c) 50:50 at 25 °C and pressure up to 10 bar.*

Table 6.5 *IAST selectivity values at different CO_2/CH_4 ratios of ACF and ACF3-CNT-AT1 at 25 °C and pressure 1-10 bar.*

	IAST Selectivity CO_2/CH_4					
	(10:90)		(30:70)		(50:50)	
Sample	1 bar	10 bar	1 bar	10 bar	1 bar	10 bar
ACF	22.8	13.5	5.9	3.5	2.5	1.5
ACF3-CNT-AT1	330.3	68.8	85.6	17.8	55	11.4

6.4 Conclusions

This research demonstrates the feasibility of using carbonized agave bagasse fibers modified with CNTs for the effective separation of CO_2 from a CO_2/CH_4 mixture. The samples were characterized by SEM and TEM microscopy, where homogeneous growth of curved CNTs with an inner diameter of 20-30 nm is observed. The textural properties of the materials were analyzed through N_2 adsorption isotherms at 77 K, where the specific surface area increases from 2 to 452 m^2/g and the pore volume from 0.009 to 0.168 cm^3/g with the growth of CNT. Furthermore, the micropore PSD obtained from the CO_2 isotherms at 273 K shows that more than 70% of the micropore volume is attributed to ultramicropores (<0.7 nm), for ACF 0.099 cm^3/g and for ACF3-CNT-AT1 0.11 cm^3/g. By using XPS, the decrease in the oxygenated groups and the increase in the hydrophobic character of ACF3-CNT-AT1 with respect to the pristine material is determined from the disappearance of the signal corresponding to H_2O. The pristine ACF shows CO_2 and CH_4 adsorption capacity of 2.3 and 1.54 mmol/g at 10 bar, respectively. Furthermore, ACF3-CNT-AT1 demonstrates excellent CO_2 adsorption capacity (3.53 mmol/g) with respect to the low CH_4 adsorption (0.47 mmol/g) at 10 bar, accordingly. This important CO_2

selectivity of ACF3-CNT-AT1 is attributed to various factors such as: higher relative abundance of C=O groups which polarize CO_2, adsorbing it preferentially; the hydrophobic character given by the CNTs that promotes their interplay with CO_2 by pi-pi interactions; and the decrease in pores <0.42 nm that more easily adsorb CH_4. The calculated isosteric heat value of CO_2 and CH_4 of ACF3-CNT-AT1 presents a constant value of approximately 26 kJ/mol for CO_2, which is indicative of the homogeneity in the active sites. For CH_4, a maximum isosteric heating value of 11 kJ/mol is obtained, which decreases rapidly to 3 kJ/mol as the amount of adsorbed CH_4 increases, indicating the absence of active sites for its adsorption. Furthermore, ACF3-CNT-AT1 shows excellent IAST selectivity values of up to 22 times higher than those for ACF, up to 330.3 for a CO_2/CH_4 10:90 ratio at 1 bar. Finally, the high CO_2 selectivity of ACF3-CNT-AT1 makes this hybrid material very promising for applications in natural gas purification systems.

Chapter 7:

Final remarks

Since the beginning of the industrial era, greenhouse gas emissions have increased considerably, and carbon dioxide is the main one since contributes to more than 70% of these emissions followed by methane. Because of the increasing concentration of CO_2 in the atmosphere, methodologies have been sought to reduce its concentration and emissions. Absorption through liquid amines is the most widely used method despite its various disadvantages such as corrosion of equipment and high energy demand. On the other hand, there are ionic liquids as a possible substitute for liquid amines, which despite having interesting properties for CO_2 capture, present important limitations such as high cost, viscosity, and slow kinetics.

A strategy of great interest to improve the use of liquid absorbents is through their impregnation in porous solids, which makes them more efficient, improves their capture kinetics, thermal and chemical stability. In this sense, using carbon materials coming from agricultural waste, such as carbonized bagasse fibers (CBF), as support of IL can improve the CO_2-absorber interaction. Additionally, the increase in the specific surface area of CBF through tubular carbon nanostructures, such as CNTs or CNFs, is of interest since they have a considerable available surface on

which to impregnate liquid absorbents. Furthermore, nanostructures can contribute to CO_2 capture due to their surface chemistry and textural properties.

The results shown in Chapter 2 demonstrated the feasibility of efficiently using TEPA amine impregnated on carbonized bagasse fibers to improve the CO_2 capture capacity as well as the thermal stability of the amine. It was observed that by impregnating a low amount of amine (CBF-TEPA5%) the CO_2 capture capacity was very similar to that of pure TEPA during the tests carried out at 1-10 bar. Furthermore, the equilibrium time of the impregnated material was less than 30 min. It was observed that low concentrations of TEPA were correctly impregnated into the CBF channels, which led to improve the CO_2 capture capacities and kinetics by increasing the CO_2-TEPA contact area. Additionally, the regeneration capacity of CBF-TEPA5% improved considerably with respect to pure TEPA from the 3rd sorption-desorption cycle, where the regeneration remained constant for 4th cycles. The CO_2 capture mechanism was also described, where TEPA interacts with CO_2 through individual amine sites, to form carbamate, and physical interactions.

In Chapter 3, the specific surface area of the ACF was increased by the growth of CNT to upgrade the area where liquid absorbents can be impregnated. This strategy was chosen since CNTs have accessibly surface area and avoid the diffusion of CO_2 through tuortuous porosity improving the adsorption kinetics, unlike chemical or physical activation. Furthermore, the microporosity generated by activation can be easily blocked by the liquid absorbent, which limits the amount of absorbent impregnated and therefore the capture capacity. Prior to CNT growth, the CBFs were washed with hydrochloric acid to remove inorganic content (mainly $CaCO_3$) that

could interfere with the good dispersion of the metal catalyst. CNT growth was carried out by CVD and the precipitation of iron salts at different concentrations (modification of the Massart process) was used to impregnate magnetite nanoparticles used as a catalyst. The $FeCl_3$:$FeCl_2$ concentration of 6:3 g/L was the one that presented the highest performance of CNT growth because of the uniform distribution of nanoparticles smaller than 30 nm. Curved CNTs with an inner diameter of 20-30 nm were grown, with the catalyst at the tip and, after AT1 post-treatment, an eroded surface was obtained. The growth of CNT notably increased the specific surface area and provided a basic nature to the ACF which contributed to the capture of CO_2. In this sense, the rapid CO_2 capture kinetics of ACF was not affected by the growth of CNT, even the capture rate and the capture capacity improved around 40% for the different pressures (1-10 bar), temperatures (25 -80 °C) and CO_2 concentrations (100%, 50%, 25% and 0.04%) tested. Furthermore, the calculated isosteric heat of adsorption of the CNT-modified ACFs showed constant values for the entire range of adsorbed CO_2, which can be interpreted as homogeneity in the active sites to adsorb CO_2. Additionally, regeneration capacities of 95% were achieved during 3 sorption-desorption cycles. From these results, it was proposed that the CO_2 capture mechanism of CNT-modified ACFs was through physisorption, Van der Waals forces, and pi-pi interactions given by the eroded surface of the grown curved CNTs.

In Chapter 4, it was tried to escalate the CNT growth in a rotary tubular furnace (1 g of ACF per batch), where the catalyst impregnation methodology and growth temperature (700 °C) were conserved and the contact time with the carbon source

(from 3.5 to 1 min) and the acetylene flow (5 to 10 mL/min) was modified. In this case, the CVD process did not result in the growth of CNT, but fishbone-type CNFs were grown homogeneously, where the catalyst changed its structure from spherical to octahedral or diamond-shaped, something that has not been previously reported, to the best of our knowledge, on heterogeneous surfaces such as ACF. The change in the morphology of the catalyst and in the type of grown nanostructure is still uncertain, but it is expected to carry out more tests to elucidate the change of grown CTS. It has been reported that during the growth of CNF, conditions such as the atmosphere, substrate, reaction temperature and pressure or flow of the carbon-containing gas can modify the concentration and diffusion of C in the catalyst that can result in changes on the size and shape of the catalyst particle [195,205,421]. Therefore, depending on the nature and shape of the catalyst and the orientation of its faces, CTS with different structures can be formed [202,203,422-424], as observed in this work.

The grown CNFs presented the catalyst at the tip of the nanofibers with a diameter of 30-50 nm. The specific surface area presented a similar value to the CNT-modified material (422 m^2/g) as well as the surface charge distribution and the point of zero charge. The surface chemistry of the CNF-modified ACF was changed by the increase of nitrogen groups and the decrease of oxygenated groups with respect to the pristine ACF: the biggest contribution was by pyrrolic groups (65.5% relative abundance), carbonyl, ketone and carboxylic (70.1% relative abundance). In the same way as for CNT-modified ACF, the CO_2 capture capacity increased more than 30% for the pressures (1-10 bar) and temperatures tested (0-75 °C), where the

increase in specific surface area and the increase in the basic nature of the material contributed to improving CO_2 capture. Furthermore, the calculation of the isosteric heat of adsorption showed constant values of about 29 kJ/mol, slightly higher than for ACF modified with CNT, which indicates homogeneity in the active sites to adsorb CO_2 and stronger interaction strength, possibly because of the presence of nitrogenous groups. Furthermore, the adsorption kinetics were not affected either, reaching equilibrium in 50 min, which indicates that the active sites to adsorb CO_2 are readily available. CNFs grown in ACFs contain defects, edge sites and curvature that can be related mainly with nitrogenous groups (mainly pyrrolic) and oxygenated groups (mainly carbonyl, ketone, and carboxylic) that provide greater reactivity towards CO_2, improving their capture capacity without affecting its kinetics.

In Chapter 5, the increase in the specific surface area given by the growth of CNF was taken as advantage to impregnate the IL 1-butyl-3-methylimidazolium acetate, which has good selectivity, capture capacity and thermal stability, but its kinetics are slow due to its high viscosity. Therefore, impregnating the IL in a porous material that has readily available specific surface area resulted in a composite with better capture kinetics than pristine IL and better CO_2 capture capacity than the carbon composite (CNF-modified ACF). In this chapter, the impregnation conditions previously used in the research group [185,249] were considered, where mass ratios of support and IL higher than 1:0.1 presented a reduction in the kinetics of the ACF and the capture capacity did not improve significantly. For CC, it was also found that mass ratios below 1:0.1 worked adequately, specifically the ratio 1:0.05 was the one that presented the best CO_2 capture capacities. The CO_2 capture capacity was

almost doubled with respect to the pristine material for all pressures tested (1-8 bar) and, by calculating the amount of IL impregnated in the CC, the CO_2 capture capacity of the IL was more than 15 times higher than that of pure IL. Additionally, the capture kinetics of impregnated IL was considerably improved, where equilibrium was reached in 20 min and the capture rate was more than doubled (0.04 and 0.12 mmol/g·min for CC-IL1:0.05 at 1 and 8 bar, respectively).

The good impregnation of the IL, observed by SEM, provided a larger gas-liquid contact area. Sample CC-IL1:0.05 presented better dispersion of the IL in the CNFs and, consequently, better capture capacities and faster kinetics. Furthermore, this relationship was the only one that showed improvement in the regeneration capacity during the 3 sorption-desorption cycles. Therefore, it was demonstrated that, by impregnating a liquid absorbent such as TEPA or IL [BMIM][Ac] with different characteristics, the capture capacity, kinetics and regeneration capacity can be substantially improved. In this sense, the use of the liquid absorbents can be made more efficient, making their use more viable for application in CO_2 capture, storage, or reuse systems.

It is worth mentioning that it was also tried to impregnate TEPA in the CC (Figure A1 and A2), however, the conditions used for impregnation did not allow to considerably increase the CO_2 capture capacity. Also, by SEM it was observed that TEPA covered the CNFs instead of being distributed on the body of the nanostructures, which possibly caused that the CO_2 capture capacity to not be benefited in the same way as for IL. Consequently, in future works different methodologies could be implemented to improve the TEPA´s impregnation.

On the other hand, the CO_2 capture tests in Chapter 2 and 5 were carried out through a high-pressure reactor (Described in section 2.2.5 and Figure 2.1). The main difficulties that the impregnated materials presented were that, prior to the CO_2 capture test, it is necessary to carry out a degassing process where contaminants or water are removed using relatively high vacuum. Through these processes, the impregnated absorbent could modify its distribution and concentration in the support, which is why the data obtained during the tests carried out in the sorptometer were not completely reliable (Figure A3). However, the tests carried out in the high-pressure reactor for the impregnated materials present advantages such as the greater similarity with conventional CO_2 capture systems as they do not have the need to heat or vacuum prior to CO_2 capture, although the results cannot be directly compared with those obtained using a sorptometer. Therefore, the results obtained can be considered closer to a real process than those obtained by a sorptometer, where ideal conditions are used.

Finally, in Chapter 6, the CO_2/CH_4 selectivity of the CNT-modified ACF was determined, which is another possible application of the synthesized materials. In this sense, the selective adsorption of CO_2 for the purification of a natural gas flow is another possible application of great interest because the presence of CO_2 reduces the heat capacity of CH_4 and in contact with humidity it can corrode the pipes. The ACF modified with CNT had good CO_2 capture capacity, but very low CH_4 capture capacity (1.71 and 3.53 mmol/g from CO_2 and 0.02 and 0.47 mmol/g from CH_4 at 1 and 10 bar, respectively). In general, it has been reported that due to the quadrupole moment of CO_2, it is adsorbed with higher force than methane. However,

the high CO_2 capture capacity of ACF modified with CNT compared to that of CH_4 has been attributed to the presence of functional groups that can polarize CO_2 more strongly and, therefore, have preference towards this gas. Specifically, it has been reported that the groups that contain C=O favor the selectivity of CO_2 over CH_4 to a greater extent. In this sense, the relative abundance of C=O groups in CNT-modified ACF increased from 70 % of pristine material to 85%. Also, the higher hydrophobic character, availability of oxygenated groups, exposed specific surface area and pore size distribution (less pores volume <0.42 nm) contributed to the exceptional CO_2 selectivity of ACF3-CNT-AT1. Furthermore, the high selectivity of this material was corroborated by the calculation of the isosteric heat of adsorption for CO_2 and CH_4, where the q_{st} of CO_2 presented a constant value of about 26 kJ/mol throughout the range of adsorbed quantity, unlike the q_{st} of CH_4 which presented a value of 11 kJ/mol and quickly dropped to 3 kJ/mol, which is attributed to the absence of active sites to adsorb this gas. In addition, the IAST selectivity value was calculated for different CO_2/CH_4 ratios of interest for the purification of natural gas, where CNT-modified ACF presented values of up to 22 and 7 times higher than ACF at 1 and 10 bar, respectively. In addition to the surface chemistry, which was essential to obtain the highest values reported for CO_2/CH_4 selectivity, the rapid availability of functional groups given by CNTs made it possible for their functionality to be very efficient, unlike materials such as activated carbon. The diffusion through the pores of the activated carbons can cause that, although the surface chemistry could be similar to that of the CNT-modified ACF, the pore volume (specifically pores <0.42 nm) contributes more to CH_4 adsorption and consequently the selectivity is reduced.

Also, CO_2/CH_4 selectivity tests were also carried out for CNF-modified ACF (Figure A5 and Table A2), where the selectivity was slightly benefited compared to that of ACF, specifically at higher pressures. It is curious that the modification with CNT has contributed enormously to the CO_2/CH_4 selectivity, but with CNF practically not as they have apparently similar characteristics. However, the main difference between the grown CNTs and CNFs was the distribution of oxygenated groups, where the CNFs have a 70% of relative abundance of C=O-containing groups unlike the 85% of the CNTs. Therefore, by having a distribution of functional groups similar to the pristine ACF, only with a higher amount of nitrogen, the CO_2/CH_4 selectivity was not benefited in the same way as for CNT-modified ACF.

The results presented in this thesis demonstrated the great potential of the modification of ACF with tubular nanostructures such as CNT and CNF for the selective capture of CO_2, as well as its usefulness to impregnate ionic liquid and generate a composite with excellent CO_2 capture capacity and fast kinetics. This represents a great advance in the development of highly efficient materials for the selective CO_2 capture.

Chapter 8:

8.1 Final conclusions

The urgent need to reduce CO_2 emissions and its concentration in the atmosphere due to climate change has created the need to generate new and more efficient hybrid materials for CO_2 capture. Liquid absorbents impregnated on porous solids has been one of the most promising strategies to generate materials with outstanding CO_2 capture capacity, high selectivity, regeneration capacity and fast kinetics.

In this study it was demonstrated that it is possible to grow CTS on carbonized agave bagasse fibers through CVD with magnetite nanoparticles as catalyst, which allowed to improve the CO_2 capture capacity and to increase the specific surface area where IL could be impregnated. It was found that a low concentration of iron (0.3%), distributed in the ACF in the form of magnetite nanoparticles smaller than 30 nm, was suitable to grow CNT uniformly in a TGA and fishbone-type CNF in a rotary tube furnace. Furthermore, the ACF modification with CTS showed a considerable increase in the basic nature of the ACF as well as in the specific surface area (2 m^2/g to more than 400 m^2/g). These changes in the textural properties and surface chemistry of the material allowed to improve the CO_2 capture capacity of ACF up to 40% for the different conditions of pressure (1-10 bar), temperature (0-75 °C) and

CO_2 concentation (100, 50, 25 and 0.04%) tested. It was proposed that the increase in the specific surface area, micropore volume and the basic nature of the materials improved the CO_2 capture capacity through weak interactions such as Van der Waals forces, π-π and electrostatic interactions. Furthermore, the fast kinetics in 50 min (0.032 mmol/g·min) and the high regeneration capacity of >95% were maintained.

The increase in specific surface area given by the growth of CNF also provided higher area where the IL [BMIM][Ac] can be impregnated and improve the CO_2 capture capacity. The impregnation of a small amount of IL (CC:IL of 1:0.05) on the ACF-CNF produced an increase on the CO_2 capture capacity and kinetics of approximately double at all pressures tested (1-8 bar). Also, the time to reach equilibrium was drastically increased to less than 20 min and the regeneration capacity of the IL was improved through its impregnation on the carbon material. It was proposed that the CO_2 capture mechanism of IL was through the reversible reaction with the C2 of the $[BMIM]^+$ ring to form a carboxylate complex. In this way, the feasibility of impregnating IL [BMIM][Ac] in a carbon composite such as CNF-modified ACF was demonstrated, which make the use of IL considerably more efficient.

Finally, the CO_2/CH_4 selectivity of CTS-modified materials and pristine ACFs was tested as another possible application. The growth of CNF slightly improved the CO_2/CH_4 selectivity of the material, possibly due to the higher concentration of nitrogen groups, which provides a greater capacity to polarize the CO_2 molecule and, therefore, greater affinity towards this gas. On the other hand, CNT growth

considerably improved the CO_2/CH_4 selectivity, up to 22 times higher than ACF. The great CO_2 selectivity of the CNT-modified ACF was attributed to the higher amount of C=O groups, its hydrophobic character and the reduction of pores <0.42 nm that adsorb more easily CH_4. Furthermore, the readily available functional groups given by the CNTs made it possible for their functionality to be highly efficient and drastically reduce the volume contribution of micropores to adsorb CH_4.

Finally, carbonized bagasse fibers modified with carbon nanostructures show to be excellent materials for CO_2 capture under different conditions of pressure, temperature and CO_2 concentration. These also possess notable CO_2 selectivity in a CO_2/CH_4 mixture. In addition, this carbon composite material also proved to be a remarkable support to impregnate liquid absorbents with which the kinetics of CO_2 capture and its regeneration capacity were improved. In this way, these materials present advantages and properties of great interest for their implementation in pilot and industrial scale.

PERSPECTIVES

The results presented in this doctoral thesis demonstrated the possible application of carbonized bagasse fibers modified with carbon nanostructures and impregnated with liquid absorbents for their application in CO_2 capture systems. However, there are different aspects that can be carried out to generate other materials, possibly more efficient to selectively capture CO_2. In this thesis, it was possible to improve the CO_2 capture capacity and regeneration capacity of CBF through impregnation with TEPA without affecting its kinetics. However, it is still necessary to find a methodology to impregnate this same amine onto CNF-modified ACF with more positive results.

Additionally, we believe that carbonized bagasse fibers are a very versatile material and an excellent precursor to test different types of physical or chemical modifications and improve their CO_2 capture properties. The impregnation of other types of amines or ILs on pristine ACF or those modified with CNF can be studied to compare the effectiveness of the impregnated absorbent and determine which combination of materials present the best cost-benefit to apply them in large-scale capture systems. Also, the modification of the surface chemistry plays an important role in the selective capture of CO_2, especially at low pressures, so the incorporation of nitrogen groups may be another alternative to improve the CO_2 capture capacity. In addition, it has been reported that the specific surface area and micropore volume is an important factor to increase the CO_2 capture capacity at pressures >5 bar, so different chemical or physical activation methodologies should be tested, as well as

combining these with impregnation of a liquid absorbent or the incorporation of nitrogenous groups.

On the other hand, elucidating the key parameters for the growth of CNF or CNT can be an important contribution to nanomaterials science. In addition, it is necessary to optimize the methodologies to carry out CO_2 capture tests of the impregnated materials at different temperatures and CO_2 concentrations. Obtaining adsorption isotherms and being able to calculate important parameters such as the isosteric heat of adsorption is very importance to compare directly with works reported by other research groups. Additionally, testing the capture capacity of pure or combined gases of environmental interest such as CH_4, N_2 and H_2 can expand the application of the materials developed in this thesis work.

Bringing this type of research closer to an industrial or larger-scale application under the understanding of the phenomena that occur at each stage must be a priority. In this sense, it is necessary to carry out CO_2 capture tests under the effect of humidity and estimate the stability of the materials developed under these conditions. Furthermore, performing continuous testing through packed bed columns can be considered the next step towards the application of these materials.

SCIENTIFIC PRODUCTS

Publication

L.E. Rios-Saldaña, K. Sapag, C. Nieto-Delgado, M. Avalos-Borja, J.R. Rangel-Mendez, Enhancing the CO_2 capture capacity of natural macroporous carbonized fibers by growing carbon nanotubes on their surface, Colloids and Surfaces A: Physicochemical and Engineering Aspects 669 (2023) 131524.

Attendance to conferences

National

- Participation in the “XI Simposio de avances de tesis de posgrado en Ciencias Ambientales” with the oral presentation: “Estudio de la captura de CO_2 mediante fibras de bagazo de agave carbonizadas modificadas con nanotubos de carbono e impregnadas con líquido iónico”, San Luis Potosí, México, 2022. 2nd place was obtained.
- Participation in the “Concurso institucional Three Minutes Thesis 2022” with the oral presentation: “Estudio de la captura de CO_2 mediante fibras de bagazo de agave carbonizadas modificadas con nanotubos de carbono e impregnadas con líquido iónico”, San Luis Potosí, México, 2022.
- Participation in the “XII Simposio de avances de tesis de posgrado en Ciencias Ambientales” with the oral conference: “Estudio de la captura de CO_2 mediante fibras de bagazo de agave carbonizadas modificadas con nanofibras de carbono

e impregnadas con liquido ionico", San Luis Potosí, México, 2023. 1st place was obtained.

- Participation in the "Concurso de IPI-Tesis Doctorado del XII Congreso interdisciplinario de posgrados (CONIP)" with the oral presentation: "Captura de CO_2 mediante fibras de bagazo carbonizadas modificadas con nanoestructuras de carbono e impregnada con absorbentes líquidos", San Luis Potosí, México, 2023. 2nd place was obtained.
- Participation in the "Primer congreso de adsorción de la AMDA 2023" with the poster presentation: "Fibras de bagazo carbonizadas impregnadas con tetraetilenpentamina (TEPA) para captura de CO_2", Guanajuato, México, 2023.
- Participation in the "Primer congreso de adsorción de la AMDA 2023" with the oral presentation: "Mejora de la capacidad de captura de CO_2 de fibras debagazo carbonizadas mediante el crecimiento de nanofibras de carbono en su superficie", Guanajuato, México, 2023.

International

- Participation in the "Cuarto Taller Latinoamericano de Materiales de Carbono (TLMC4)" with the oral presentation: "Crecimiento de nanotubos de carbono sobre fibras de bagazo carbonizadas para su aplicación en la captura de CO_2", San Luis Potosí, México, 2021. 3er place was obtained.
- Participation in the "V Congreso Nacional de Ciencia y Tecnología Ambiental, Argentina y Ambiente 2023 (AA2023) y 4° Simposio Iberoamericano de Adsorción (IBA-4)" with the poster presentation: "Mejora de la capacidad de captura de CO_2

de fibras de bagazo carbonizadas mediante el crecimiento de nanotubos de carbono en su superficie", San Luis, Argentina, 2023.

- Participation in the "The World Conferences on Carbon (Carbon2023)" with the oral presentation: "Improved CO_2 capture capacity by an impregnated carbon nanofibers/macroporous natural carbon composite with an ionic liquid", Cancún, Mexico, 2023.
- Participation in the "The World Conferences on Carbon (Carbon2023)" with the poster presentation: "Growth of fishbone-type carbon nanofibers on macroporous biochar and its application in CO_2 capture", Cancún, Mexico, 2023. Winner of "Walker Award" for best poster presentation by a student.

Others

- Workshop participant in the "Taller para elaborar propuestas de investigación con financiamiento", San Luis Potosí, México, 2022.
- Organizing committee participant of the "V Congreso Nacional de Ciencia y Tecnología Ambiental, Argentina y Ambiente 2023 (AA2023) y 4° Simposio Iberoamericano de Adsorción (IBA-4)", San Luis, Argentina, 2023.
- Participation in the "Escuela: Adsorción y ambiente" made during the "V Congreso Nacional de Ciencia y Tecnología Ambiental, Argentina y Ambiente 2023 (AA2023) y 4° Simposio Iberoamericano de Adsorción (IBA-4)", San Luis, Argentina, 2023.
- Participation in the "Concurso de fotografía científica del XII Congreso interdisciplinario de posgrados (CONIP)" with the photograph titled "Campo de nanoflores de diamante", San Luis Potosí, México, 2023.

- Winner in the contest “Fotografía Científica, campo Ciencia de Materiales” with the photograph titled “Crecimiento de nanofibras de carbono sobre fibras de bagazo de agave carbonizadas utilizando un catalizador de hierro con morfología de diamante” organized by “Asociación Mexicana de Microscopia y Microanalisis A.C. (AMMM)”, México, 2023.

References

[1] Chu, X., Deng, X., Jin, G., Wang, Z., Li, Z., Ecological security assessment based on ecological footprint approach in Beijing-Tianjin-Hebei region, China. Phys. Chem. Earth 101 (2017) 43–51.

[2] Ali, G., Pumijumnong, N., Cui, S., Decarbonization action plans using hybrid modeling for a low-carbon society: the case of Bangkok Metropolitan Area. J. Clean.Prod. 168 (2017) 940–951.

[3] J. Godin, W. Liu, S. Ren, C.C. Xu, Advances in recovery and utilization of carbon dioxide: A brief review, J. Environ. Chem. Eng. 9 (4) (2021), 105644.

[4] IPCC Special Report on Climate Change, Desertification, Land Degradation, Sustainable Land Management, Food Security, and Greenhouse gas fluxes in Terrestrial Ecosystems, 2019.

[5] Anderson, T.R., Hawkins, E., Jones, P.D., CO2, the greenhouse effect and global warming: from the pioneering work of Arrhenius and Callendar to today's Earth System Models. Endeavour 40 (2016) 178-187. https://doi.org/10.1016/j.endeavour.2016.07.002.

[6] Barry, J.P., Widdicombe, S., JM, Hall-Spencer. Effects of ocean acidification on marine biodiversity and ecosystem function. In: Gattuso, J.P., Hansson, L. (Eds.), Ocean Acidification. Oxford University Press, New York, (2011) 192−209.

[7] Basallote MD, Rodríguez-Romero A, Blasco J, DelValls TA, Riba I, Lethal effects on different marine organisms, associated with sediment–seawater acidification deriving from CO2 leakage. Environ. Sci. Pollut. Res. 19 (2012) 2550–2560.

[8] Elder, W. (2019). What is Climate Change? National Park Service. Recuperado de https://www.nps.gov

[9] Hussain, M., Liu, G., Yousaf, B., Ahmed, R., Uzma, F., Ali, M.U., Ullah, H., Butt, A.R., Regional and sectoral assessment on climate-change in Pakistan: social norms and indigenous perceptions on climate-change adaptation and mitigation in relation to global context. J. Clean. Prod. 200 (2018) 791-808. https://doi.org/10.1016/j.jclepro.2018.07.272.

[10] A.D. Kamkeng, M. Wang, J. Hu, W. Du, F. Qian, Transformation technologies for CO2 utilisation: Current status, challenges and future prospects, Chem. Eng. J. 409 (2021), 128138.

[11] The Production Gap Report 2020, by UN Environment Programme (UNEP), Stockholm Environment Institute (SEI), International Institute for Sustainable Development (IISD), Overseas Development Institute (ODI), and E3G, http://productiongap.org/2020report/.

[12] International Energy Agency, 2013. Technology Roadmap-Carbon Capture and Storage 2013. 1 July. [Online]. Available. https://webstore.iea.org/technology-roadmap-carbon-capture-and-storage-2013, Accessed date: 26 December 2018.

[13] Dowell, N.M., Fennell, P.S., Shah, N., Maitland, G.C., The role of CO2 capture and utilization in mitigating climate change. Nat. Clim. Chang. 7 (2017) 243–249.

[14] United States Environmental Agency, 2018. Global Greenhouse Gas Emissions Data|Greenhouse Gas (GHG) Emissions|US EPA [WWW Document]. URL. https://www.epa.gov/ghgemissions/global-greenhouse-gas-emissions-data.

[15] IPCC, 2005. Special report on carbon dioxide capture and storage. In: Metz, B., Davidson, O., Coninck, H.C., Loos, M., Meyer, L.A. (Eds.), Prepared by Working Group III of the Intergovernmental Panel on Climate Change. Cambridge University Press, Cambridge, New York, pp. 442.

[16] Taifan, W., Boily, J. F., & Baltrusaitis, J., Surface chemistry of carbon dioxide revisited. Surface Science Reports, 71(4) (2016) 595–671. https://doi.org/10.1016/j.surfrep.2016.09.001.

[17] Greenwood NN, Earnshaw A (1997). Chemistry of the Elements (2nd ed.). Butterworth-Heinemann. pp. 305–314. ISBN 978-0-08-037941-8.

[18] Atkins P, de Paula J (2006). Physical Chemistry (8th ed.). W.H. Freeman. pp. 461, 464. ISBN 978-0-7167-8759-4.

[19] Hunt, Andrew J., Emily H.K. Sin, Ray Marriott, and James H. Clark, “Generation, Capture, and Utilization of Industrial Carbon Dioxide.” ChemSusChem 3(3) (2010) 306–22.

[20] Lipei Fu, Zhangkun Ren, Wenzhe Si, Qianli Ma, Weiqiu Huang, Kaili Liao, Zhoulan Huang, Yu Wang, Junhua Li, Peng Xu, Research progress on CO2 capture

and utilization technology, Journal of CO2 Utilization 66 (2022) 102260. https://doi.org/10.1016/j.jcou.2022.102260

[21] Rodríguez-Rivas, David. 2009. Curso de Cultivos Protegidos. 1st ed. ed. David Rodriguez-Rivas. Bogotá: Sistema de Bibliotecas SENA.

[22] Sanz-Pérez, E. S., Murdock, C. R., Didas, S. A., & Jones, C. W., Direct Capture of CO2 from Ambient Air. Chemical Reviews, 116(19) (2016) 11840–11876. https://doi.org/10.1021/acs.chemrev.6b00173

[23] L. Wang, Exploration on microbial fixation of CO2 technology and its application, Biotech. World 11 (2013) 3.

[24] A. Anand, S. Raghuvanshi, S. Gupta, Trends in Carbon Dioxide (CO2) Fixation by Microbial Cultivations, Curr. Sustain. /Renew. Energy Rep. 7 (2) (2020) 40–47.

[25] J. Zheng, K. Bhatnagar, M. Khurana, P. Zhang, B.Y. Zhang, P. Linga, Semiclathrate based CO2 capture from fuel gas mixture at ambient temperature: Effect of concentrations of tetra-n-butylammonium fluoride (TBAF) and kinetic additives, Appl. Energy 217 (2018) 377–389.

[26] J. Bai, X. Zhen, K. Yan, P. Li, S. Fang, C. Chang, The effect of additive molecular diameters on the hydrate-based CO2 capture from simulated biogas, Fuel 278 (2020), 118370.

[27] L. Yang, Recovery and separation process of carbon dioxide, Mod. Econ. Inf. 15 (2017), 394-394.

[28] S.M. Safdarnejad, J.D. Hedengren, L.L. Baxter, Plant-level dynamic optimization of Cryogenic Carbon Capture with conventional and renewable power sources, Appl. Energy 149 (2015) 354–366.

[29] J.L. Li, B.H. Chen, Review of CO2 absorption using chemical solvents in hollow fiber membrane contactors, Sep. Purif. Technol. 41 (2) (2005) 109–122.

[30] Z.X. Yang, B. Lu, D.D. Guo, Z.Y. Ji, C.J. Ji, G.J. Zhang, Research Status and Progress of CO2 Capture and Separation Methods, Shandong. Chem. Ind. 49 (2020) 62–64.

[31] B. Wu, K.R. Huang, Z.J. Liu, Research progress on carbon dioxide capture by chemical absorption, Guangzhou. Chem. Ind. 45 (11) (2017) 11–14.

[32] H. Su, L. Cui, Research on absorption method and mechanism of carbon dioxide, Environ. Sci. Manag. 31 (8) (2006) 79–81

[33] A.I. Sarker, A. Aroonwilas, A. Veawab, Equilibrium and Kinetic Behaviour of CO2 Adsorption onto Zeolites, Carbon Molecular Sieve and Activated Carbons, Energy Procedia 114 (2017) 2450–2459.

[34] N.A. Rashidi, S. Yusup, An overview of activated carbons utilization for the postcombustion carbon dioxide capture, J. CO2 Util. 13 (2016) 1–16.

[35] J. Serafin, M. Ouzzine, O.F.C. Jr, J. Sre´nscek-Nazzal, I.C. G´omez, F.Z. Azar, C.A. R. Mafull, D. Hotza, C.R. Rambo, Conversion of fruit waste-derived biomass to highly microporous activated carbon for enhanced CO2 capture, Waste Manag. 136 (2021) 273–282.

[36] M. Karaszova, B. Zach, Z. Petrusova, V. Cervenka, M. Bobak, M., Syc, P. Izak, Postcombustion carbon capture by membrane separation, Review, Sep. Purif. Technol. 238 (2020), 116448.

[37] Y. Cao, E. Yang, W. Wang, Membranes for carbon dioxide separation, Spec. Petrochem. 32 (1) (2015) 53–59.

[38] C. Song, M. Xie, Y. Qiu, Q. Liu, L. Sun, K. Wang, Y. Kansha, Integration of CO2 absorption with biological transformation via using rich ammonia solution as a nutrient source for microalgae cultivation, Energy 179 (2019) 618–627.

[39] G.J. Chen, H.Y. Cheng, S.S. Fan, New separation technology through forming solid gas hydrates, Mod. Chem. Ind. 19 (7) (1999) 12–14.

[40] J. Cai, Y. Zhang, C.G. Xu, Z.M. Xia, Z.Y. Chen, X.S. Li, Raman spectroscopic studies on carbon dioxide separation from fuel gas via clathrate hydrate in the presence of tetrahydrofuran, Appl. Energy 214 (2018) 92–102.

[41] L.X. Hao, G.J. Zhang, Y. Jia, J.W. Qu, Q.T. Su, Progress of CO2 adsorption performance of solid porous materials, Mod. Chem. Ind. 36 (7) (2016) 29–34.

[42] Pera-Titus M. Porous inorganic membranes for CO2 capture: present and prospects. Chem. Rev. 114 (2014) 1413–92.

[43] A.A. Olajire, CO2 capture and separation technologies for end-of-pipe applications - A review, Energy 35 (6) (2010) 2610–2628.

[44] S.C. Sun, W. Wei, X.C. Cong, Y.F. Liu, W.B. Zhao, Progress in separation and recovery of carbon dioxide from flue gas by hydrate technology, Nat. Gas. Chem. Ind. 35 (2) (2010) 71–74.

[45] Y. Wang, D.L. Zhong, Z. Li, J.B. Li, Application of tetra-n-butyl ammonium bromide semi-clathrate hydrate for CO2 capture from unconventional natural gases, Energy 197 (2020), 117209.

[46] Z. Cheng, H. Xu, S. Wang, W. Liu, Y. Li, L. Jiang, C. Chen, Y. Song, Effect of nanoparticles as a substitute for kinetic additives on the hydrate-based CO2 capture, Chem. Eng. J. 424 (2021), 130329.

[47] Khalik Mohamad Sabil, Behzad Partoon, Recent advances on carbon dioxide capture through a hydrate-based gas separation process, Current Opinion in Green and Sustainable Chemistry, 11 (2018) 22–26. https://doi.org/10.1016/j.cogsc.2018.03.006

[48] Turgut M. Gür, Carbon Dioxide Emissions, Capture, Storage and Utilization: Review of Materials, Processes and Technologies, Progress in Energy and Combustion Science 89 (2022) 100965. https://doi.org/10.1016/j.pecs.2021.100965

[49] A. Hart, N. Gnanendran, Cryogenic CO2 capture in natural gas, Energy Procedia 1 (1) (2009) 697–706.

[50] M.A. Moreira, A.M. Ribeiro, A.F. Ferreira, A.E. Rodrigues, Cryogenic pressure temperature swing adsorption process for natural gas upgrade, Sep. Purif. Technol. 173 (2017) 339–356.

[51] Gottlicher G, Pruschek R. Comparison of CO_2 removal systems for fossil fuelled power plants. Energy Convers. Manag 38 (1997)173–8.

[52] Khalilpour, R., Mumford, K., Zhai, H., Abbas, A., Stevens, G., Rubin, E.S., Membrane-based carbon capture from flue gas: a review. J. Clean. Prod. 103 (2015) 286-300. https://doi.org/10.1016/j.jclepro.2014.10.050

[53] Lonsdale HK. The growth of membrane technology. J. Membrane Sci., 10 (1982) 81–181.

[54] Ansaloni, L., Salas-Gay, J., Ligi, S., Baschetti, M.G., Nanocellulose-based membranes for CO2 capture. J. Membr. Sci. 522 (2017) 216-225. https://doi.org/10.1016/j.memsci.2016.09.024

[55] Kang, C.A., Brandt, A.R., Durlofsky, L.J., Jayaweera, I., Assessment of advanced solvent-based post-combustion CO2 capture processes using a bi-objective optimization technique. Appl. Energy 179 (2016) 1209–1219.

[56] Yamasaki A. An overview of CO2 mitigation options for global warming-Emphasizing CO2 sequestration options. J. Chem. Engr. Japan 36 (2003) 361–75.

[57] Abdul Hai Alami, Abdullah Abu Hawili, Muhammad Tawalbeh, RitaHasand, Lana Al Mahmoud, Sara Chibib, Anfal Mahmood, Kamilia Aokal, Pawarin Rattanapanya, Materials and logistics for carbon dioxide capture, storage and utilization, Science of the Total Environment 717 (2020) 137221. https://doi.org/10.1016/j.scitotenv.2020.137221

[58] S. Xiao, H. Liu, H. Gao, M. Xiao, X. Luo, R. Idem, P. Tontiwachwuthikul, Z. Liang, Kinetics and mechanism study of homogeneous reaction of CO2 and blends of diethanolamine and monoethanolamine using the stopped-flow technique, Chem. Eng. J. 316 (2017) 592–600.

[59] Rafay Ahmed, Guijian Liu, Balal Yousaf, Qumber Abbas, Habib Ullah, Muhammad Ubaid Ali, Recent advances in carbon-based renewable adsorbent for selective carbon dioxide capture and separation-A review, Journal of Cleaner Production 242 (2020) 118409. https://doi.org/10.1016/j.jclepro.2019.118409

[60] Knudsen, J.N., Jensen, J.N., Vilhelmsen, P.-J., Biede, O., Experience with CO2 capture from coal flue gas in pilot-scale: testing of different amine solvents. Energy Procedia 1 (2009) 783-790. https://doi.org/10.1016/j.egypro.2009.01.104

[61] Wu, X., Yu, Y., Qin, Z., Zhang, Z., The advances of post-combustion CO2 capture with chemical solvents: review and guidelines. Energy Procedia 63 (2014) 1339–1346.

[62] Wilberforce, T., Baroutaji, A., Soudan, B., Hai Al-Alami, A., Ghani Olabi, A. Outlook of carbon capture technology and challenges. Sci. Total Environ. 657 (2019) 56–72.

[63] Zhang, Z., Li, Y., Zhang, W., Wang, J., Soltanian, M.R., Olabi, A.G. Effectiveness of amino acid salt solutions in capturing CO2: a review. Renew. Sust. Energ. Rev. 98 (2018)179–188.

[64] Y.S.Wang, T. Du, Y.L. Song, S. Che, X. Fang, L.F. Zhou, Amine-functionalized mesoporous ZSM-5 zeolite adsorbents for carbon dioxide capture, Solid State Sci. 73 (2017) 27–35.

[65] G. Zhou, K. Wang, R. Liu, Y. Tian, B. Kong, G. Qi, Synthesis and CO2 adsorption performance of TEPA-loaded cellulose whisker/silica composite aerogel, Colloids Surf. A: Physicochem. Eng. Asp. 631 (2021), 127675.

[66] Huangyu Yan, Guojie Zhang, Jun Liu, Guoqiang Li, Ying Wang, Highly efficient CO2 adsorption by imidazole and tetraethylenepentamine functional sorbents: Optimization and analysis using response surface methodology, Journal of Environmental Chemical Engineering 9 (2021) 105639. https://doi.org/10.1016/j.jece.2021.105639

[67] National Center for Biotechnology Information (2023). PubChem Compound Summary for CID 8197, Tetraethylenepentamine. Retrieved December 18, 2023 from https://pubchem.ncbi.nlm.nih.gov/compound/Tetraethylenepentamine.

[68] Barzagli F, Giorgi C, Mani F, Peruzzini M. Reversible carbon dioxide capture by aqueous and non-aqueous amine-based absorbents: a comparative analysis carried out by 13C NMR spectroscopy. Appl Energy 220 (2018) 208–19.

[69] Farid Shakerian, Ki-Hyun Kim, Jan E. Szulejko, Jae-Woo Park, A comparative review between amines and ammonia as sorptive media for post-combustion CO2 capture, Applied Energy 148 (2015) 10–22. http://dx.doi.org/10.1016/j.apenergy.2015.03.026

[70] Yu B, Yu H, Li K, Yang Q, Zhang R, Li L, et al. Characterization and kinetic study of carbon dioxide absorption by an aqueous diamine solution. Appl Energy 208 (2017) 1308–17.

[71] Coleman, Fergal, “Lead(Ii) Chloride Ionic Liquids and Organic/Inorganic Hybrid Materials – a Study of Chloroplumbate(Ii) Speciation.” Dalton Transactions 42(14) (2013) 5025.

[72] Kirchner, Barbara, Topics in Current Chemistry Topics in Current Chemistry - Ionic Liquids (2010).

[73] Angell CA, Ansari Y, Zhao Z. Ionic liquids: past, present and future. Faraday Discuss 154 (2012) 9–27.

[74] Yu G, Zhao D, Wen L, Yang S, Chen X. Viscosity of ionic liquids: database, observation, and quantitative structure-property relationship analysis. AIChE Journal 58 (2012) 2885–99.

[75] Zhang S, Sun N, He X, Lu X, Zhang X. Physical properties of ionic liquids: database and evaluation. J. Phys. Chem. Ref. Data 35 (2006) 1475–517.

[76] Bogolitsyn, K. G., T. E. Skrebets, and T. A. Makhova, "Physicochemical Properties of 1-Butyl-3-Methylimidazolium Acetate." Russian Journal of General Chemistry 79(1) (2009) 128–31. https://doi.org/10.1134/S1070363209010198

[77] Pérez del Pino, Angel et al, "Synthesis of Graphene-Based Photocatalysts for Water Splitting by Laser-Induced Doping with Ionic Liquids." Carbon 130 (2018) 48–58.

[78] Figueroa JD, Fout T, Plasynski S, McIlvried H. Advances in CO2 capture technology – The U.S. Department of Energy's carbon sequestration program. Intern. J. Greenhouse Gas Control 2 (2008) 9–20.

[79] Ramdin M, de Loos TW, Vlugt TJH. State-of-the-art of CO2 capture with ionic liquids. Ind. Eng. Chem. Res. 51 (2012) 8149–77.

[80] Pennline HW, Luebke DR, Jones KL, Myers CR, Morsi BI, Heintz YJ, Ilconich JB. Progress in carbon dioxide capture and separation research for gasification-based power generation point sources. Fuel Process. Technol. 89 (2008) 897–907.

[81] Cadena C, Anthony JL, Shah JK, Morrow TI, Brennecke JF, Maginn EJ. Why is CO2 soluble in imidazolium-based ionic liquids? J. Am. Chem. Soc.126 (2004) 5300–8.

[82] Zhou, Lingyun, Xiaomin Shang, Jing Fan, and Jianji Wang, "Solubility and Selectivity of CO2 in Ether-Functionalized Imidazolium Ionic Liquids." Journal of Chemical Thermodynamics 103 (2016) 292–98.

[83] Congmin Wang, Huimin Luo, Xiaoyan Luo, Haoran Li and Sheng Dai, Equimolar CO2 Capture by Imidazolium-Based Ionic Liquids and Superbase Systems, Green Chem.12 (2010) 2019-2023. https://doi.org/10.1039/C0GC00070A

[84] Santiago, R. et al., "From Kinetics to Equilibrium Control in CO2 Capture Columns Using Encapsulated Ionic Liquids (ENILs)." Chemical Engineering Journal 348 (2018) 661–68.

[85] Moya, Cristian et al., “Encapsulated Ionic Liquids for CO2 Capture: Using 1-Butyl-Methylimidazolium Acetate for Quick and Reversible CO2 Chemical Absorption.” ChemPhysChem 17(23) (2016) 3891–99.

[86] Junaid Haider, Saad Saeed, Muhammad Abdul Qyyum, Bilal Kazmi, Rizwan Ahmad, Ayyaz Muhammad, Moonyong Lee, Simultaneous capture of acid gases from natural gas adopting ionic liquids: Challenges, recent developments, and prospects. Renewable and Sustainable Energy Reviews, 123 (2020) 109771. https://doi.org/10.1016/j.rser.2020.109771

[87] Mark B. Shiflett and A. Yokozeki, Chemical Absorption of Sulfur Dioxide in Room-Temperature Ionic Liquids, nd. Eng. Chem. Res. 49, 3 (2010) 1370–1377. https://doi.org/10.1021/ie901254f

[88] G. Gurau, H. Rodriguez, S. P. Kelley, P. Janiczek, R. S. Kalb, R. D. Rogers, Demonstration of Chemisorption of Carbon Dioxide in 1,3 Dialkylimidazolium Acetate Ionic Liquids, Angew Chem. Int. Ed. 50 (2011) 12024–12026; Angew. Chem. 123 (2011) 12230–12232.

[89] Cabaço, M. I., Besnard, M., Danten, Y., & Coutinho, J. A. P., Carbon dioxide in 1-butyl-3-methylimidazolium acetate. I. Unusual solubility investigated by Raman spectroscopy and DFT calculations. Journal of Physical Chemistry A, 116(6) (2012) 1605–1620. https://doi.org/10.1021/jp211211n

[90] Besnard, M., Cabaço, M. I., Chávez, F. V., Pinaud, N., Sebastião, P. J., Coutinho, J. A. P., & Danten, Y., On the spontaneous carboxylation of 1-butyl-3-methylimidazolium acetate by carbon dioxide. Chemical Communications, 48(9) (2012) 1245–1247. https://doi.org/10.1039/c1cc16702b

[91] M. Besnard, M. I. Cabaco, F. Vaca Chavez, N. Pinaud, P. J. Sebastiao, J. A. Coutinho, J. Mascetti, Y. Danten, CO2 in 1-butyl-3-methylimidazolium acetate. 2. NMR investigation of chemical reactions, J. Phys. Chem. A, 116 (2012) 4890 – 4901. https://doi.org/10.1021/jp211689z

[92] W. Shi, R. L. Thompson, E. Albenze, J. A. Steckel, H. B. Nulwala, D. R. Luebke, Contribution of the Acetate Anion to CO2 Solubility in Ionic Liquids: Theoretical Method Development and Experimental Study, J. Phys. Chem. B, 118 (2014) 7383–7394. https://doi.org/10.1021/jp502425a

[93] C. GRAHAM D. A. IMRIE R. E. RAAB, Measurement of the electric quadrupole moments of CO_2, CO, N_2, Cl_2 and BF_3, Molecular Physics, 93:1 (1998) 49-56. https://doi.org/10.1080/002689798169429

[94] Berger, A.H., Bhown, A.S., Comparing physisorption and chemisorption solid sorbents for use separating CO2 from flue gas using temperature swing adsorption. Energy Procedia 4 (2011) 562-567. https://doi.org/10.1016/j.egypro.2011.01.089.

[95] Samanta A, Zhao A, Shimizu GKH, Sarkar P, Gupta R. Post-combustion CO2 capture using solid sorbents: a review. Ind. Eng. Chem. Res. 51 (2012) 1438–63.

[96] T.L. Dantas, F.M.T. Luna, I.J. Silva Jr, D.C. de Azevedo, C.A. Grande, A. E. Rodrigues, R.F. Moreira, Carbon dioxide–nitrogen separation through adsorption on activated carbon in a fixed bed, Chem. Eng. J. 169 (1–3) (2011) 11–19.

[97] A. Pereira, A.F. Ferreira, A.E. Rodrigues, A.M. Ribeiro, M.J. Regufe, Additive manufacturing for adsorption-related applications—A review, J. Adv. Manuf. Process. 4 (1) (2022), 10108.

[98] W.M. Verdegaal, K. Wang, J.P. Sculley, M. Wriedt, H.C. Zhou, Evaluation of Metal-Organic Frameworks and Porous Polymer Networks for CO2-Capture Applications, ChemSusChem 9 (6) (2016) 636–643.

[99] Choi S, Drese JH, Jones CW. Adsorbent materials for carbon dioxide capture from large anthropogenic point sources. ChemSusChem 2 (2009) 796–854.

[100] Chaffee AL, Knowles GP, Liang Z, Zhang J, Xiao P, Webley PA. CO2 capture by adsorption: materials and process development. Int. J. Greenhouse Gas Control 1 (2007) 11–8.

[101] P.P. Zhang, H.R. Xiao, J.Y. Chen, W. Shu, X. Wang, Review of Modification Method of Activated Carbon and its Technology Progress and Development, Trend Anhui Agric. Sci. Bull. 23 (11) (2017) 99–103.

[102] J.R. Li, Y. Ma, M.C. McCarthy, J. Sculley, J. Yu, H.K. Jeong, P.B. Balbuena, H. C. Zhou, Carbon dioxide capture-related gas adsorption and separation in metalorganic frameworks, Coord. Chem. Rev. 255 (15–16) (2011) 1791–1823

[103] Y. Wang, J.H. Li, Z.Y. Huang, Y. Zhao, Y. Yang, R.X. Dong, Research progress on synthesis and application of mesoporous molecular sieves, Tianjin. Chem. Ind. 30 (4) (2016) 1–8.

[104] Mohsen Karimi, Mohammad Shirzad, Jose A.C. Silva, Alírio E. Rodrigues, Biomass/Biochar carbon materials for CO2 capture and sequestration by cyclic adsorption processes: A review and prospects for future directions, Journal of CO2 Utilization 57 (2022) 101890.

[105] Database of Zeolite Structures, Structure Commission of the International Zeolite Association (IZA-SC), http://www.iza-structure.org/databases/(accessed Dec. 22, 2023).

[106] West RC. CRC handbook of chemistry and physics. CRC Press; 1967.

[107] E. Davarpanah, M. Armandi, S. Hern´andez, D. Fino, R. Arletti, S. Bensaid, M. Piumetti, CO2 capture on natural zeolite clinoptilolite: Effect of temperature and role of the adsorption sites, J. Environ. Manag. 275 (85) (2020), 111229.

[108] S.J. Chen, M. Zhu, Y. Fu, Y.X. Huang, Z.C. Tao, W.L. Li, Using 13X, LiX, and LiPdAgX zeolites for CO2 capture from post-combustion flue gas, Appl. Energy 191 (2017) 87–98.

[109] K. Adil, P.M. Bhatt, Y. Belmabkhout, S.M.T. Abtab, H. Jiang, A.H. Assen, A. Mallick, A. Cadiau, J. Aqil, M. Eddaoudi, Valuing Metal–Organic Frameworks for Postcombustion Carbon Capture: A Benchmark Study for Evaluating Physical Adsorbents, Adv. Mater. 29 (2017), 1702953.

[110] Y.L. Li, Y.W. Zhao, C.X. Wang, Advances in Adsorption and Separation of CO2 by MOFs Materials, J. Zhongzhou. Univ. 37 (1) (2020) 112–116.

[111] R. Sabouni, H. Kazemian, S. Rohani, Carbon dioxide capturing technologies: a review focusing on metal organic framework materials (MOFs), Environ. Sci. Pollut. Res. 21 (8) (2014) 5427–5449.

[112] Schnobrich JK, Koh K, Sura KN, Matzger AJ., A framework for predicting surface areas in microporous coordination polymers. Langmuir 26 (2010) 5808.

[113] L. Lei, Y. Cheng, C. Chen, M. Kosari, Z. Jiang, C. He, Taming structure and modulating carbon dioxide (CO2) adsorption isosteric heat of nickel-based metal organic framework (MOF-74(Ni)) for remarkable CO2 capture, J. Colloid Interface Sci. 612 (2022) 132–145

[114] Liu J, Tian J, Thallapally PK, McGrail BP., Selective CO2 capture from flue gas using metal-organic frameworks – A fixed bed study. J. Phys. Chem. C 116 (2012) 9575–81.

[115] Jiang L, Gonzalez-Diaz A, Ling-Chin J, Roskilly AP, Smallbone AJ. Postcombustion CO2 capture from a natural gas combined cycle power plant using activated carbon adsorption. Appl. Energy 245 (2019) 1–15.

[116] Harry, M., Reinoso, F.R., 2006. Activated Carbon. Elsevier Ltd.

[117] Rana M, Subramani K, Sathish M, Gautam UK. Soya derived heteroatom doped carbon as a promising platform for oxygen reduction, supercapacitor and CO2 capture. Carbon 114 (2017) 679–89.

[118] Sevilla M, Parra JB, Fuertes AB. Assessment of the role of micropore size and N doping in CO2 capture by porous carbons. Appl. Mater. Interfaces 5 (2013) 6360–8.

[119] Ello, A.S., De Souza, L.K.C., Trokourey, A., Jaroniec, M., Coconut shell-based microporous carbons for CO2 capture. Microporous Mesoporous Mater. 180 (2013) 280–283. https://doi.org/10.1016/j.micromeso.2013.07.008

[120] Gonzalez, A.S., Plaza, M.G., Rubiera, F., Pevida, C., Sustainable biomass-based carbon adsorbents for post-combustion CO2 capture. Chem. Eng. J. 230 (2013) 456–465. https://doi.org/10.1016/j.cej.2013.06.118.

[121] Abbas, A.F., Ahmed, M.J., Mesoporous activated carbon from date stones (Phoenix dactylifera L.) by one-step microwave assisted K2CO3 pyrolysis. J. Water Process Eng. 9 (2016) 201–207. https://doi.org/10.1016/j.jwpe.2016.01.004.

[122] Ozdemir, I., Sahin, M., Orhan, R., Erdem, M., Preparation and characterization of activated carbon from grape stalk by zinc chloride activation. Fuel Process. Technol. 125 (2014) 200–206. https://doi.org/10.1016/j.fuproc.2014.04.002

[123] Bouchelta, C., Medjram, M.S., Bertrand, O., Bellat, J.P., Preparation and characterization of activated carbon from date stones by physical activation with steam. J. Anal. Appl. Pyrolysis 82 (2008) 70–77. https://doi.org/10.1016/j.jaap.2007.12.009

[124] Ceyhan, A.A., S¸ahin, ¨O., Baytar, O., Saka, C., Surface and porous characterization of activated carbon prepared from pyrolysis of biomass by two stage

procedure at low activation temperature and it's the adsorption of iodine. J. Anal. Appl. Pyrolysis 104 (2013) 378–383. https://doi.org/10.1016/j.jaap.2013.06.009.

[125] Ogungbenro, A.E., Quang, D.V., Al-Ali, K.A., Vega, L.F., Abu-Zahra, M.R.M., Physical synthesis and characterization of activated carbon from date seeds for CO2 capture. J. Environ. Chem. Eng. 6 (2018) 4245–4252. https://doi.org/10.1016/j.jece.2018.06.030.

[126] Rashidi, N.A., Yusup, S., A review on recent technological advancement in the activated carbon production from oil palm wastes. Chem. Eng. J. 314 (2017) 277–290. https://doi.org/10.1016/j.cej.2016.11.059

[127] Yang DP, Li Z, Liu M, Zhang X, Chen Y, Xue H, et al. Biomass-derived carbonaceous materials: recent progress in synthetic approaches, advantages, and applications. ACS Sustainable Chem Eng 7 (2019) 4564–85.

[128] Bejoy T, Midhun CR, Athira KB, Rubiyah MH, Jithin J, Audrey M. Nanocellulose, a versatile green platform: from biosources to materials and their applications. Chem Rev118 (2018)11575–625.

[129] Xiao R, Wang JJ, Gaston LA, Zhou B, Park JH, Li R, et al. Biochar produced from mineral salt-impregnated chicken manure: fertility properties and potential for carbon sequestration. Waste Manag 78 (2018) 802–10.

[130] Gao A, Guo N, Yan M, Li M, Wang F, Yang R. Hierarchical porous carbon activated by CaCO3 from pigskin collagen for CO2 and H2 adsorption. Microporous Mesoporous Mater 260 (2018) 172–9.

[131] Thines KR, Abdullah EC, Mubarak NM, Ruthiraan M. Synthesis of magnetic biochar from agricultural waste biomass to enhancing route for waste water and polymer application: a review. Renew Sustain Energy Rev 67 (2017) 257–76.

[132] Wiedner K, Rumpel C, Steiner C, Pozzi A, Maas R, Glaser B. Chemical evaluation of chars produced by thermochemical conversion (gasification, pyrolysis and hydrothermal carbonization) of agro-industrial biomass on a commercial scale. Biomass Bioererg 59 (2013) 264–78.

[133] Tsang YF, Kumar V, Samadar P, Yang Y, Lee J, Ok YS, et al. Production of bioplastic through food waste valorization. Environ Int 127 (2019) 625–44.

[134] Koottatep T, Fakkaew K, Tajai N, Pradeep SV, Polprasert C. Sludge stabilization and energy recovery by hydrothermal carbonization process. Renew Energy 99 (2016) 978–85.

[135] Nada Abuelnoor, Ahmed AlHajaj, Maryam Khaleel, Lourdes F. Vega, Mohammad R.M. Abu-Zahra, Activated carbons from biomass-based sources for CO2 capture applications, Chemosphere 282 (2021) 131111.

[136] Jiang, C., Yakaboylu, G.A., Yumak, T., Zondlo, J.W., Sabolsky, E.M., Wang, J., Activated carbons prepared by indirect and direct CO2 activation of lignocellulosic biomass for supercapacitor electrodes. Renew. Energy 155 (2020) 38–52. https://doi.org/10.1016/j.renene.2020.03.111

[137] Gonzalez-García, P., Activated carbon from lignocellulosics precursors: a review of the synthesis methods, characterization techniques and applications. Renew. Sustain. Energy Rev. 82 (2018) 1393–1414. https://doi.org/10.1016/j.rser.2017.04.117

[138] Macedo, J.S., Otubo, L., Ferreira, O.P., Gimenez, I. de F., Mazali, I.O., Barreto, L.S., Biomorphic activated porous carbons with complex microstructures from lignocellulosic residues. Microporous Mesoporous Mater. 107 (2008) 276–285. https://doi.org/10.1016/j.micromeso.2007.03.020.

[139] Jung, S., Park, Y.K., Kwon, E.E., Strategic use of biochar for CO2 capture and sequestration. J. CO2 Util. 32 (2019) 128–139. https://doi.org/10.1016/j.jcou.2019.04.012.

[140] Antunes E, Jacob MV, Brodie G, Schneider PA. Microwave pyrolysis of sewage biosolids: dielectric properties, microwave susceptor role and its impact on biochar properties. J Anal Appl Pyrol 129 (2018) 93–100.

[141] Bamdad H, Hawboldt K, MacQuarrie S. A review on common adsorbents for acid gases removal: focus on biochar. Renew Sustain Energy Rev 81 (2018) 1705–20.

[142] Zhang Z, Zhu Z, Shen B, Liu L. Insights into biochar and hydrochar production and applications: a review. Energy 171 (2019) 581–98.

[143] Singh G, Lakhi KS, Sil S, Bhosale SV, Kim I, Albahily K, et al. Biomass derived porous carbon for CO2 capture. Carbon 148 (2019) 164–86.

[144] Yuan X, Suvarna M, Low S, Dissanayake PD, Lee KB, Li J, et al. Applied machine learning for prediction of CO2 adsorption on biomass waste-derived porous carbons. Environ Sci Technol 2021.

[145] Wang T, Zhai Y, Zhu Y, Li C, Zeng G. A review of the hydrothermal carbonization of biomass waste for hydrochar formation: process conditions, fundamentals, and physiochemical properties. Renew Sustain Energy Rev 90 (2018) 223–47.

[146] Osman AI, Hefny M, Maksoud MA, Elgarahy AM, Rooney DW. Recent advances in carbon capture storage and utilisation technologies: a review. Environ Chem Lett 19 (2021) 797–849.

[147] Chen Y, Zhang X, Chen W, Yang H, Chen H. The structure evolution of biochar from biomass pyrolysis and its correlation with gas pollutant adsorption performance. Bioresour Technol 246 (2017) 101-1.

[148] Enrique García-Díez, Sebastien Schaefer, Angela Sanchez-Sanchez, Alain Celzard, Vanessa Fierro, M. Mercedes Maroto-Valer, and Susana García, Novel Porous Carbons Derived from Coal Tar Rejects: Assessment of the Role of Pore Texture in CO2 Capture under Realistic Postcombustion Operating Temperatures, ACS Appl. Mater. Interfaces 11(40) (2019) 36789–36799.

[149] Seul-Yi Lee, Soo-Jin Park, Determination of the optimal pore size for improved CO2 adsorption in activated carbon fibers, J. of Colloid and Interface Sci. 389 (2013) 230-235. https://doi.org/10.1016/j.jcis.2012.09.018

[150] Jiacheng Wang, Andreas Heerwig, Martin R. Lohe, Martin Oschatz, Lars Borchardta and Stefan Kaskel, Fungi-based porous carbons for CO2 adsorption and separation, J. Mater. Chem. 22 (2012) 13911-13913. https://doi.org/10.1039/C2JM32139D

[151] Liwei Wang, Linli Rao, Binbin Xia, Linlin Wang, Limin Yue, Yuqing Liang, Herbert DaCosta, Xin Hu, Highly efficient CO2 adsorption by nitrogen-doped porous carbons synthesized with low-temperature sodium amide activation, Carbon 130, (2018) 31-40. https://doi.org/10.1016/j.carbon.2018.01.003

[152] Jun Han, Li Zhang, Bo Zhao, Linbo Qin, Yu Wang, Futang Xing, The N-doped activated carbon derived from sugarcane bagasse for CO2 adsorption, Industrial

Crops and Products, 128 (2019) 290-297. https://doi.org/10.1016/j.indcrop.2018.11.028

[153] Liu Shenfang, Rao Linli, Yang Pupu, Wang Xinyi, Wang Linlin, Ma Rui, Yue Limin, Hu Xin, Superior CO2 uptake on nitrogen doped carbonaceous adsorbents from commercial phenolic resin, Journal of Environmental Sciences 93 (2020) 109-116. https://doi.org/10.1016/j.jes.2020.04.006

[154] M.G. Plaza, C. Pevida, A. Arenillas, F. Rubiera, J.J. Pis, CO2 capture by adsorption with nitrogen enriched carbons, Fuel 86 (14) (2007) 2204-2212. https://doi.org/10.1016/j.fuel.2007.06.001

[155] R. L. S. Canevesi, S. Schaefer, M. T. Izquierdo, A. Celzard, and V. Fierro, Roles of Surface Chemistry and Texture of Nanoporous Activated Carbons in CO2 Capture, ACS Appl. Nano Mater. 5(3) (2022) 3843–3854. https://doi.org/10.1021/acsanm.1c04474

[156] T.J. Bandosz, M.J. Biggs, K.E. Gubbins, Y. Hattori, Y. Liyama, K. Kaneko, J. Pikunic, K.T. Thomson, (L.R. Radovic and P.A. Thrower, eds.), Chemistry and Physics of Carbon, 28, Marcel Dekker, New York, 2001, p. 41.

[157] R. T. Yang, (P.A. Thrower, ed.), Chemistry and Physics of Carbons, 19, Marcel Dekker, New York, 1984, p. 163.

[158] Bandosz, T. J., & Ania, C. O. (2006). Surface chemistry of activated carbons and its characterization. In Activated Carbon Surface in Environmental Remediation (Vol. 7, pp. 159–229).

[159] Ljubiša R. Radović, Philip L. Walker Jr., Robert G. Jenkins, Importance of carbon active sites in the gasification of coal chars, Fuel, 62 (7) (1983) 849-856. https://doi.org/10.1016/0016-2361(83)90041-8

[160] J.S. Noh and J.A. Schwarz, Effect of HNO3 treatment on the surface acidity of activated carbons, Carbon, 28 (1990) 675. https://doi.org/10.1016/0008-6223(90)90069-B

[161] Montes-Morán, M. A., Suárez, D., Menéndez, J. A., & Fuente, E., On the nature of basic sites on carbon surfaces: An overview. Carbon, 42(7) (2004) 1219–1225. https://doi.org/10.1016/j.carbon.2004.01.023

[162] Shafeeyan, M. S., Mohd, W., Wan, A., Houshmand, A., & Shamiri, A., A review on surface modification of activated carbon for carbon dioxide adsorption. Journal of Analytical and Applied Pyrolysis, 89(2) (2010) 143–151. https://doi.org/10.1016/j.jaap.2010.07.006

[163] Boehm, H. P., Some aspects of the surface chemistry of carbon blacks and other carbons. Carbon, 32(5) (19947 59–769. https://doi.org/10.1016/0008-6223(94)90031-0

[164] Liu, Y., & Wilcox, J., Molecular simulation of CO2 adsorption in micro- and mesoporous carbons with surface heterogeneity. International Journal of Coal Geology, 104 (2012) 83–95. https://doi.org/10.1016/j.coal.2012.04.007

[165] S. Biniak, G. Szymanski, J. Siedlewski and A. Swiatkowski, The characterization of activated carbons with oxygen and nitrogen surface groups, Carbon, 35 (1997) 1799. https://doi.org/10.1016/S0008-6223(97)00096-1

[166] J. Lahaye, G. Nanse, A. Bagreev and V. Strelko, Porous structure and surface chemistry of nitrogen containing carbons from polymers, Carbon, 37 (1999) 585.

[167] K. Kaneko, T. Suzuki, Y. Fujiwara and K. Nishikawa, (Rodriguez-Reinoso F. et al. eds.) Characterization of Porous Solids II, Elsevier Sci. Pub., Amsterdam, 1991, p. 389.

[168] Shi, J., Yan, N., Cui, H., Liu, Y., & Weng, Y., Sulfur doped microporous carbons for CO2 adsorption. Journal of Environmental Chemical Engineering 5(5) (2017) 4605–4611. https://doi.org/10.1016/j.jece.2017.09.002

[169] F.M. Mpatani, R. Han, A.A. Aryee, A.N. Kani, Z. Li, L. Qu, Adsorption performance of modified agricultural waste materials for removal of emerging microcontaminant bisphenol A: a comprehensive review, Sci. Total Environ. (2021), 146629.

[170] M. Shirzad, H.K.S. Panahi, B.B. Dashti, M.A. Rajaeifar, M. Aghbashlo, M. Tabatabaei, A comprehensive review on electricity generation and GHG emission reduction potentials through anaerobic digestion of agricultural and livestock/slaughterhouse wastes in Iran, Renew. Sustain. Energy Rev. 111 (2019) 571–594.

[171] Rodolfo Palomo-Briones, Irma López-Gutiérrez, Fabiola Islas-Lugo, Karen Lizeth Galindo-Hernández, Dendera Munguía-Aguilar, Jack Andrés Rincón Pérez, Miguel Ángel Cortés-Carmona, Felipe Alatriste-Mondragón, Elías Razo-Flores, Agave bagasse biorefinery: processing and perspectives, Clean Techn Environ Policy 20 (2018) 1423–1441. https://doi.org/10.1007/s10098-017-1421-2

[172] M. Parascanu, M. Puig-Gamero, G. Soreanu, J. Valverde, L. Sanchez-Silva, Comparison of three Mexican biomasses valorization through combustion and gasification: environmental and economic analysis, Energy 189 (2019), 116095.

[173] https://www.atlasbig.com/en-in/countries-by-olive-production, 2020.

[174] D. Bajwa, G. Pourhashem, A.H. Ullah, S. Bajwa, A concise review of current lignin production, applications, products and their environmental impact, Ind. Crops Prod. 139 (2019), 111526.

[175] https://www.statista.com/statistics/1040499/world-coconut-production-by-leading-producers/, 2019.

[176] https://www.atlasbig.com/en-ie/countries-by-almond-production, 2020.

[177] C. Liu, L. Chen, W. Tang, S. Peng, M. Li, N. Deng, Y. Chen, Predicting potential distribution and evaluating suitable soil condition of oil tea Camellia in China, Forests 9 (8) (2018) 487.

[178] https://www.statista.com/statistics/255945/top-countries-of-destination-for-us-rice-exports-2011/, 2021.

[179] 97] D. Hoyle, P. Levang, Oil palm development in Cameroon, Citeseer (2012).

[180] T. Silalertruksa, S.H. Gheewala, Competitive use of sugarcane for food, fuel, and biochemical through the environmental and economic factors, Int. J. Life Cycle Assess. 25 (7) (2020) 1343–1355.

[181] M. Meghana, Y. Shastri, Sustainable valorization of sugar industry waste: status, opportunities, and challenges, Bioresour. Technol. 303 (2020), 122929.

[182] C. Reimann, R.T. Ottesen, M. Andersson, A. Arnoldussen, F. Koller, P. Englmaier, Element levels in birch and spruce wood ashes—green energy? Sci. Total Environ. 393 (2-3) (2008) 191–197.

[183] SAGARPA, secretaria de agricultura, ganadería, desarrollo rural, pesca y alimentación, AGAVE TEQUILERO Y MEZCALERO Mexicano Planeación Agrícola Nacional. Ciudad de México, (2017).

[184] Nieto-Delgado, C., Rangel-Méndez, J.R., Production of activated carbon from organic by-products from the alcoholic beverage industry: Surface area and hardness optimization by using the response surface methodology 34 (2011) 1528–1537.

[185] E.D. Isaacs-Páez, A.J. García-Pérez, C. Nieto-Delgado, Luis F. Chazaro Ruiz, J.R. Rangel-Mendez, Enhanced CO2 capture kinetics by using macroporous carbonized natural fibers impregnated with an ionic liquid, Journal of Molecular Liquids 350 (2022) 118602.

[186] Nazrul Hsana, Pradip K. Duttaa, Santosh Kumarb, Neeladri Dasc, Joonseok Koh, Capture and chemical fixation of carbon dioxide by chitosan grafted multiwalled carbon nanotubes, Journal of CO_2 Utilization 41 (2020) 101237.

[187] Xin Hea, Jing Liua, Yuwei Jianga, Muhammad Yaseena, Haoyu Guana, Jianhua Suna, Xuemin Cui, Dankui Liao, Zhangfa Tong, 'Useful' template synthesis of N-doped acicular hollow porous carbon/ carbon-nanotubes for enhanced capture and selectivity of CO2, Chemical Engineering Journal 361 (2019) 278–285.

[188] Fan Wu, Zheng Zhou, Sila Temizel-Sekeryan, Ramin Ghamkhar, Andrea L. Hicks, Assessing the environmental impact and payback of carbon nanotube supported CO2 capture technologies using LCA methodology, Journal of Cleaner Production 270 (2020) 122465.

[189] Seyyed Alireza Mousavi and Hosna Janjani, Antibiotics adsorption from aqueous solutions using carbon nanotubes: a systematic review, Toxin reviews, 39 (2020) 87-98. https://doi.org/10.1080/15569543.2018.1483405

[190] Manisha Byakodi, Narlawar Sagar Shrikrishnaa, Riya Sharmaa, Shekhar Bhansali, Yogendra Mishra, Ajeet Kaushik, Sonu Gandhi, Emerging 0D, 1D, 2D, and 3D nanostructures for efficient point-of-care biosensing, Biosensors and Bioelectronics: X, 12 (2022) 100284. https://doi.org/10.1016/j.biosx.2022.100284

[191] O.G. Apul, T. Karanfil, Adsorption of synthetic organic contaminants by carbon nanotubes: A critical review, Water Res. 8 (2014) 34–55.

[192] R.B. Mathur, S. Chatterjee, B.P. Singh, Growth of carbon nanotubes on carbon fibre substrates to produce hybrid/phenolic composites with improved mechanical properties, Compos. Sci. Technol. 68 (7–8) (2008) 1608–1615.

[193] Alberto G. Albesa, Andrés A. García Blanco, Débora A. Soares Maia, Jhonny Villarroel-Rocha, José L. Vicente, Karim Sapag, Texture and surface sites of treated and as-prepared SWNT using experimental and simulation methods, Adsorption 27 (2021) 909–923. https://doi.org/10.1007/s10450-021-00317-9

[194] Fengsheng Su, Chungsying Lu, Wenfa Cnen, Hsunling Bai, Jyh Feng Hwang, Capture of CO2 from flue gas via multiwalled carbon nanotubes, Science of the Total Environment 407 (2009) 3017–3023.

[195] Xuezhi Duan, Gang Qian, Jinghong Zhou, Xinggui Zhou, De Chen, Weikang Yuan, Flat interface mediated synthesis of platelet carbon nanofibers on Fe nanoparticles, Catalysis Today 186 (2012) 48– 53.

[196] M. Terrones, SCIENCE AND TECHNOLOGY OF THE TWENTY-FIRST CENTURY: Synthesis, Properties, and Applications of Carbon Nanotubes, Annual Review of Materials Research, 33 (2003) 419-501.

[197] Alessandro Sanginario,Beatrice Miccoli, and Danilo Demarchi, Carbon Nanotubes as an Effective Opportunity for Cancer Diagnosis and Treatment, Biosensors, 7(1), (2017) 9 . https://doi.org/10.3390/bios7010009

[198] K. Hata, D. N. Futaba, K. Mizuno, T. Namai, M. Yumura, and S. Iijima, Water-Assisted Highly Efficient Synthesis of Impurity-Free Single-Walled Carbon Nanotubes, Science 306 (2004) 1362.

[199] Dresselhaus G, Dresselhaus M, Avouris P. Carbonnanotubes: Synthesis, structure, properties and applications. Springer-Verlag 2001, Berlin.

[200] Y. Nie, Surface Silanization of Carbon Nanofibers and Nanotubes for Altering the Properties of Epoxy Composites, (2012).

[201] F. Jérôme, S. Valange, Rational Design of Nanostructured Carbon Materials: Contribution to Cellulose Processing: Applications in the Chemical Industry, Energy Development, and Environment Protection (2017) 627–654.

[202] M.S. Kim, N.M. Rodriguez, R.T.K. Baker, The role of interfacial phenomena in the structure of carbon deposits, J. Catal. 134 (1992) 253–268.

[203] N.M. Rodriguez, A. Chambers, R.T.K. Baker, Catalytic Engineering of Carbon Nanostructures, Langmuir 11 (1995) 3862–3866.

[204] Israf Ud Din, Maizatul S. Shaharun, A. Naeem, Mshari A. Alotaibi, Abdulrahman I. Alharthi, M. Afroz Bakht, Qazi Nasir, Carbon nanofibers as potential materials for catalysts support, a mini-review on recent advances and future perspective, Ceramics International 46 (2020) 18446–18452.

[205] Yi-An Zhu, Ying-Chun Dai, De Chen, Wei-Kang Yuan, First-principles study of carbon diffusion in bulk nickel during the growth of fishbone-type carbon nanofibers, Carbon 45 (2007) 21–27.

[206] Jourdain, V., Bichara, C., Current understanding of the growth of carbon nanotubes in catalytic chemical vapour deposition, Carbon 58 (2013) 2–39. https://doi.org/10.1016/j.carbon.2013.02.046

[207] G. Zhong, S. Hofmann, F. Yan, H. Telg, J. H. Warner, D. Eder, C. Thomsen, W. I. Milne, and J. Robertson, Acetylene: A Key Growth Precursor for Single-Walled Carbon Nanotube Forests, J. Phys. Chem. C 113 (2009) 17321.

[208] K. Hernadi, A. Fonseca, J. B. Nagy, D. Bernaerts, and A. A. Lucas, Fe-catalyzed carbon nanotube formation, Carbon 34 (1996) 1249-1257.

[209] J. Kong, A. M. Cassell, and H. Dai, Chemical vapor deposition of methane for single-walled carbon nanotubes, Chem. Phys. Lett. 292 (1998) 567-574.

[210] S. Fan, M. Chapline, N. Frankline, T. Tombler, A. M. Cassel, and H. Dai, Self-oriented regular arrays of carbon nanotubes and their field emission properties, Science 283 (1999) 512.

[211] B. C. Satiskumar, A. Govindaraj, and C. N. R. Rao, Bundles of aligned carbon nanotubes obtained by the pyrolysis of ferrocene–hydrocarbon mixtures: role of the metal nanoparticles produced in situ, Chem. Phys. Lett. 307 (1999) 158.

[212] W. Z. Li, S. Xie, L. X. Qian, B. H. Chang, B. S. Zou, W. Y. Zhou, R. A. Zhao, and G. Wang, Large-Scale Synthesis of Aligned Carbon Nanotubes, Science 274 (1996) 1701.

[213] R. Sen, A. Govindraj, and C.N.R. Rao, Carbon nanotubes by the metallocene route, Chem. Phys. Lett. 267 (1997), pp. 276–280.

[214] B. Q. Wei, R. Vajtai, Y. Jung, J. Ward, R. Zhang, G. Ramanath, and P. M. Ajayan, Organized assembly of carbon nanotubes, Nature 416 (2002) 495.

[215] P. Nikolaev, M. J. Bronikowski, R. K. Bradley, F. Rohmund, D. T. Colbert, K. A. Smith, and R. E. Smalley, Gas-phase production of carbon single-walled nanotubes from carbon monoxide via the HiPco process: A parametric study, Chem. Phys. Lett. 313 (1999) 91.

[216] O. A. Nerushev, S. Dittmar, R. E. Morjan, F. Rohmund, and E. E. B. Campbell, Particle size dependence and model for iron-catalyzed growth of carbon nanotubes by thermal chemical vapor deposition, J. Appl. Phys. 93 (2003) 4185.

[217] R. E. Morjan, O. A. Nerushev, M. Sveningsson, F. Rohmund, L. K. L. Falk, and E. E. B. Campbell, Growth of carbon nanotubes from C60, Appl. Phys. A 78 (2004) 253.

[218] Mukul Kumar and Yoshinori Ando, “Chemical Vapor Deposition of Carbon Nanotubes: A Review on Growth Mechanism and Mass Production”, Journal of Nanoscience and Nanotechnology 10 (2010) 3739–3758.

[219] R. T. K. Baker, M. A. Barber, P. S. Harris, F. S. Feates, and R. J. Waite, Nucleation and growth of carbon deposits from the nickel catalyzed decomposition of acetylene, J. Catalysis 26, 51 (1972).

[220] R. Andrews, D. Jacques, A. M. Rao, F. Derbyshire, D. Qian, X. Fan, E. C. Dickey, and J. Chen, Continuous production of aligned carbon nanotubes: a step closer to commercial realization, Chem. Phys. Lett. 303, 467 (1999).

[221] B. Kitiyanan, W. E. Alvarez, J. H. Harwell, and D. E. Resasco, Controlled production of single-wall carbon nanotubes by catalytic decomposition of CO on bimetallic Co–Mo catalysts, Chem. Phys. Lett. 317, 497 (2000).

[222] C. L. Cheung, A. Kurtz, H. Park, and C. M. Lieber, Diameter-Controlled Synthesis of Carbon Nanotubes, J. Phys. Chem. B 106, 2429 (2002).

[223] I. Willems, Z. Konya, J. F. Colomer, G. V. Tendeloo, N. Nagaraju, A. Fonseca, and J. B. Nagy, Control of the outer diameter of thin carbon nanotubes synthesized by catalytic decomposition of hydrocarbons, Chem. Phys. Lett. 317, 71 (2000).

[224] J. F. Colomer, C. Stephan, S. Lefrant, G. Van-Tendeloo, I. Willems, Z. Konya, A. Fonseca, C. Laurent, and J. B. Nagy, Large-scale synthesis of single-wall carbon

nanotubes by catalytic chemical vapor deposition (CCVD) method, Chem. Phys. Lett. 317, 83 (2000).

[225] Joel Gutierrez-Martínez, Cesar Nieto-Delgado, Miguel Avalos-Borja, Elena Basiuk, Jose Rene Rangel-Mendez, Fast benzene vapor capture by natural macroporous carbonized fibers improved with carbon nanostructures, Separation and Purification Technology 257 (2021) 117956.

[226] Jiangtao Zhu, Juncai Jia, Fung Luen Kwong, Dickon Hang Leung Ng, Sie Chin Tjong, Synthesis of multiwalled carbon nanotubes from bamboo charcoal and the roles of minerals on their growth, biomass and bioenergy 36 (2012) 12-19.

[227] N. Nagaraju, A. Fonseca, Z. Konya, and J. B. Nagy, Alumina and Silica Supported Metal Catalysts for the Production of Carbon Nanotubes, J. Mol. Catal. A 181, 57 (2002). https://doi.org/10.1016/S1381-1169(01)00375-2

[228] H. Ago, K. Nakamura, N. Uehara, and M. Tsuji, Roles of Metal−Support Interaction in Growth of Single- and Double-Walled Carbon Nanotubes Studied with Diameter-Controlled Iron Particles Supported on MgO, J. Phys. Chem. B 108, 18908 (2004).

[229] J. Y. Raty, F. Gygi, and G. Galli, Growth of Carbon Nanotubes on Metal Nanoparticles: A Microscopic Mechanism from Ab Initio Molecular Dynamics Simulations, Phys. Rev. Lett. 95, 096103 (2005). https://doi.org/10.1103/PhysRevLett.95.096103

[230] S. Hofmann, R. Sharma, C. Ducati, G. Du, C. Mattevi, C. Cepek, M. Cantoro, S. Pisana, A. Parvez, F. Cervantes-Sodi, A. C. Ferrari, R. Dunin-Borkowski, S. Lizzit, L. Petaccia, A. Goldoni, and J. Robertson, In situ observations of catalyst dynamics during surface-bound carbon nanotube nucleation, Nano Lett. 7, 602 (2007).

[231] H. Ago, T. Komatsu, S. Ohshima, Y. Kuriki, and M. Yumura, Dispersion of metal nanoparticles for aligned carbon nanotube arrays, Appl. Phys. Lett. 77, 79 (2000).

[232] F. Ding, P. Larsson, J. A. Larsson, R. Ahuja, H. Duan, A. Rosen, and K. Bolton, The importance of strong carbon-metal adhesion for catalytic nucleation of single-walled carbon nanotubes, Nano Lett. 8, 463 (2008).

[233] Kecheng Wei, Huanqin Guan, Qiang Luo, Jie He and Shouheng Sun, Recent advances in CO2 capture and reduction, Nanoscale 14 (2022) 11869–11891.

[234] Yu C-H, Huang C-H, Tan C-S. A review of CO2 capture by absorption and adsorption. Aerosol Air Quality Res 12 (2012) 745–69.

[235] Yue L, Rao L, Wang L, Wang L, Wu J, Hu X, et al. Efficient CO2 capture by nitrogen-doped biocarbons derived from rotten strawberries. Ind Eng Chem Res 56 (2017) 14115–22.

[236] Serafin J, Narkiewicz U, Morawski AW, Wrobel RJ. Highly microporous activated carbons from biomass for CO2 capture and effective micropores at different conditions. J CO2 Util 18 (2017) 73–79.

[237] Zhu M, Cai W, Verpoort F, Zhou J. Preparation of pineapple waste-derived porous carbons with enhanced CO2 capture performance by hydrothermal carbonationalkali metal oxalates assisted thermal activation process. Chem Eng Res Des 146 (2019) 130–40.

[238] Chen J, Yang J, Hu G, Hu X, Li Z, Shen S, et al. Enhanced CO2 capture capacity of nitrogen-doped biomass-derived porous carbons. ACS Sustainable Chem Eng 4 (2016) 1439–45.

[239] Plaza, M.G., Gonzalez, A.S., Pis, J.J., Rubiera, F., Pevida, C., Production of microporous biochars by single-step oxidation: effect of activation conditions on CO2 capture. Appl. Energy 114 (2014) 551–562. https://doi.org/10.1016/j.apenergy.2013.09.058

[240] Li, D., Tian, Y., Li, L., Li, J., Zhang, H., Production of highly microporous carbons with large CO2 uptakes at atmospheric pressure by KOH activation of peanut shell char. J. Porous Mater. 22 (2015) 1581–1588. https://doi.org/10.1007/s10934-015-0041-7

[241] M. Alhassan, I. Andrew, M. Auta, M. Umaru, M.U. Garba, A.G. Isah, B. Alhassan, Comparative studies of CO2 capture using acid and base modified activated carbon from sugarcane bagasse, Biofuels 9 (6) (2018) 719–728.

[242] He, S., Chen, G., Xiao, H., Shi, G., Ruan, C., Ma, Y., Dai, H., Yuan, B., Chen, X., and Yang, X. Facile preparation of N-doped activated carbon produced from rice husk for CO2 capture. J. Colloid Interface Sci. 582 (2021) 90–101.

[243] Q. Liu, Y. Shi, S. Zheng, L. Ning, Q. Ye, M. Tao, Y. He, Amine functionalized low-cost industrial grade multi-walled carbon nanotubes for the capture of carbon dioxide, J. Energy Chem. 23 (1) (2014) 111–118, https://doi.org/10.1016/S2095-4956(14)60124-8

[244] Q. Ye, J. Jiang, C. Wang, Y. Liu, H. Pan, Y. Shi, Adsorption of low-concentration carbon dioxide on amine-modified carbon nanotubes at ambient temperature, Energy Fuels 26 (4) (2012) 2497–2504, https://doi.org/10.1021/ef201699w

[245] Hyeok Joon Jun, Dong Kyu Yoo, Sung Hwa Jhung, Metal-organic framework (MOF-808) functionalized with ethyleneamines: Selective adsorbent to capture CO2 under low pressure, Journal of CO2 Utilization 58 (2022) 101932.

[246] Wang, P., Guo, Y., Zhao, C., Yan, J., Lu, P., Biomass derived wood ash with amine modification for post-combustion CO2 capture. Appl. Energy 201 (2017) 34–44.

[247] Yang, H., Wang, X., Liu, J., Liu, W., Gong, Y., Sun, Y., Amine-impregnated polymeric resin with high CO2 adsorption capacity for biogas upgrading. Chem. Eng. J. 430 (2022) 132899.

[248] Kasikamphaiboon, P., Khunjan, U., CO2 adsorption from biogas using aminefunctionalized MgO. Int. J. Chem. Eng. 1–8 (2018) 2018.

[249] Paola Arjona-Jaime, Elizabeth D. Isaacs-Paez, Cesar Nieto-Delgado, Luis F. Chazaro-Ruiz, Rene Rangel-Mendez, Insight into the effect of pressure on the CO2 capture capacity and kinetics by a biochar-ionic liquid composite, Journal of Environmental Chemical Engineering 12 (2024) 111804. https://doi.org/10.1016/j.jece.2023.111804

[250] Mohanned Mohamedali, Hussameldin Ibrahim, Amr Henni, Imidazolium based ionic liquids confined into mesoporous silica MCM-41 and SBA-15 for carbon dioxide capture, Microporous and Mesoporous Materials 294 (2020)109916.

[251] N. Wu, X. Ji, W. Xie, C. Liu, X. Feng, X. Lu, Confinement Phenomenon Effect on the CO2 Absorption Working Capacity in Ionic Liquids Immobilized into Porous Solid Supports, Langmuir. 33 (2017) 11719–11726. https://doi.org/10.1021/acs.langmuir.7b02204

[252] M. Mohamedali, A. Henni, H. Ibrahim, Investigation of CO2 capture using acetate-based ionic liquids incorporated into exceptionally porous metal–organic frameworks, Adsorption. 25 (2019) 675–692. https://doi.org/10.1007/s10450-019-00073-x

[253] M. Asif, M. Suleman, I. Haq, S.A. Jamal, Post-combustion CO2 capture with chemcial adsorption and hybrid system: current status and challenges: review: hybrid systems for post-combustion CO2 capture, Greenhouse Gas Sci. Technol. 8 (2018) 998–1031.

[254] Peiyu Zhao, Yanchao Yin, Wei Cheng, Xianmang Xu, Deliang Yang, Wenpeng Yuan, Development of facile synthesized mesoporous carbon composite adsorbent for efficient CO2 capture. Journal of CO2 Utilization 50 (2021) 101612.

[255] Salame, I.I., Bandosz, T.J., Surface chemistry of activated carbons: combining the results of temperature-programmed desorption, Boehm, and potentiometric titrations. J. Colloid Interface Sci. 240 (2001) 252–258.

[256] Shim, Jae-Woon, Soo-Jin Park, and Seung-Kon Ryu, “Effect of Modification with HNO3 and NaOH on Metal Adsorption by Pitch-Based Activated Carbon Fibers.” Carbon 39(11) (2001) 1635–42.

[257] X. Li, Y. Ding, L. Guo, Q. Liao, X. Zhu, H. Wang, Non-aqueous energy-efficient absorbents for CO2 capture based on porous silica nanospheres impregnated with amine, Energy 171 (2019) 109–119.

[258] P. Zhao, G. Zhang, Y. Xu, Y. Lv, Z. Yang, H. Cheng, Development of aminefunctionalized silica foams with hierarchical pore structure for CO2 capture, Energy Fuels 33 (2019) 3357–3369.

[259] G. Socrates, Infrared and Raman Characteristic Group Frequencies, third ed., John Wiley & Sons, Chichester, UK, 2001.

[260] Hao Su, Huilin Zhang, Guansheng Qi, Wei Lu, Mingjun Wang, Preparation and CO2 adsorption properties of TEPA-functionalized multi-level porous particles based on solid waste, Colloids and Surfaces A: Physicochemical and Engineering Aspects 653 (2022) 130004.

[261] Huangyu Yan, Guojie Zhang, Ying Xu, Qiqi Zhang, Jun Liu, Guoqiang Li, Yuqiong Zhao, Ying Wang, Yongfa Zhang, High CO2 adsorption on amine-

functionalized improved macro-/ mesoporous multimodal pore silica, Fuel 315 (2022) 123195.

[262] J.L. Figueiredo, M.F.R. Pereira, M.M.A. Freitas, J.J.M. Orfao, Modification of the surface chemistry of activated carbons, Carbon 37 (1999) 1379–1389.

[263] Hidayu, A. R., & Muda, N., Preparation and Characterization of Impregnated Activated Carbon from Palm Kernel Shell and Coconut Shell for CO2 Capture. Procedia Engineering 148 (2016) 106–113.

[264] Bachelor TT, Toochinda P. Development of low-cost amine-enriched solid sorbent for CO2 capture. Environ Technol 33 (2012) 2645–51.

[265] K. Hori, T. Higuchi, Y. Aoki, M. Miyamoto, Y. Oumi, K. Yogo, S. Uemiya, Effect of pore size, aminosilane density and aminosilane molecular length on CO2 adsorption performance in aminosilane modified mesoporous silica, Microporous Mesoporous Mater. 246 (2017) 158–165, https://doi.org/10.1016/j.micromeso.2017.03.020

[266] Wilfong WC, Srikanth CS, Chuang SS. In situ ATR and DRIFTS studies of the nature of adsorbed CO2 on tetraethylenepentamine films. ACS Appl Mater Interfaces 6(16) (2014)13617–26.

[267] Sayari A, Belmabkhout Y, Dana E. CO2 Deactivation of Supported Amines: Does the Nature of Amine Matter? Langmuir 28(9) (2012) 4241–7.

[268] Zhao P, Zhang G, Sun Y, Xu Y. CO2 Adsorption Behavior and Kinetics on Amine- Functionalized Composites Silica with Trimodal Nanoporous Structure. Energy Fuels 31(11) (2017) 12508–20.

[269] Shao ZD, Cheng X, Zheng YM. Facile co-precursor sol-gel synthesis of a novel amine-modified silica aerogel for high efficiency carbon dioxide capture. J Colloid Interface Sci 530 (2018) 412–23.

[270] Rao AB, Rubin ES, A technical, economic, and environmental assessment of amine-based CO_2 capture technology for power plant greenhouse gas control. Environ Sci Technol 36 (2002) 4467–75. https://doi.org/10.1021/es0158861

[271] Mahsa Javidi Nobarzad, Maryam Tahmasebpoor, Mehri Imani, Covadonga Pevida, Saeed Zeinali Heris, Improved CO2 adsorption capacity and fluidization behavior of silica-coated amine-functionalized multi-walled carbon nanotubes,

Journal of Environmental Chemical Engineering 9 (2021) 105786. https://doi.org/10.1016/j.jece.2021.105786

[272] Shuangjun Li, Xiangzhou Yuan, Shuai Deng, Li Zhao, Ki Bong Lee, A review on biomass-derived CO_2 adsorption capture: Adsorbent, adsorber, adsorption, and advice, Renewable and Sustainable Energy Reviews 152 (2021) 111708. https://doi.org/10.1016/j.rser.2021.111708

[273] M. Karimi, J.A.C. Silva, C.Nd.P. Gonçalves, J.L. Diaz de Tuesta, A.E. Rodrigues, H. T. Gomes, CO_2 capture in chemically and thermally modified activated carbons using breakthrough measurements: experimental and modeling study, Ind. Eng. Chem. Res. 57 (32) (2018) 11154–11166. https://doi.org/10.1021/acs.iecr.8b00953

[274] L. Espinal, D.L. Poster, W. Wong-Ng, A.J. Allen, M.L. Green, Measurement, standards, and data needs for CO_2 capture materials: a critical review, Environ. Sci. Technol. 47 (21) (2013) 11960–11975. https://doi.org/10.1021/es402622q

[275] Kiara Montiel-Centeno, Deicy Barrera, Jhonny Villarroel-Rocha, M. Sergio Moreno, Karim Sapag, Hierarchical nanostructured carbons as CO_2 adsorbents, Adsorption 25 (2019) 1287–1297. https://doi.org/10.1007/s10450-019-00089-3

[276] Yuhang Zhang, Jiaming Sun, Jia Tan, ChunHui Ma, Sha Luo, Wei Li, Shouxin Liu, Multi-walled carbon nanotubes/carbon foam nanocomposites derived from biomass for CO_2 capture and supercapacitor applications, Fuel 305 (2021) 121622. https://doi.org/10.1016/j.fuel.2021.121622.

[277] Khalafalla, S.E. and Reimers, G.W., Preparation of Dilution-Stable Aqueous Magnetic Fluids. IEEE Transactions on Magnetics, 16 (1980) 178-183. http://dx.doi.org/10.1109/TMAG.1980.1060578

[278] R. Massart, Preparation of aqueous magnetic liquids in alkaline and acidic media IEEE Trans. Magn. 17 (1981) 1247–1248. http:// 10.1109/TMAG.1981.1061188

[279] M. Fang, V. Strom, R.T. Olsson, L. Belova, K.V. Rao, Particle size and magnetic properties dependence on growth temperature for rapid mixed co-precipitated magnetite nanoparticles, Nanotechnology (2012) 23 145-601. http:// http://dx.doi.org/10.1088/0957-4484/23/14/145601

[280] Ghosh Saunab, Sevilla, M., Fuertes, A. B., Andreoli, E., Ho, J., & Barron, A. R. Defining a performance map of porous carbon sorbents for high-pressure carbon dioxide uptake and carbon dioxide-methane selectivity. Journal of Materials Chemistry A, 4(38) (2016) 14739–14751. https://doi.org/10.1039/c6ta04936b.

[281] Joan J. Manyà, Belén Gonzáleza, Manuel Azuarab, Gabriel Arner, Ultra microporous adsorbents prepared from vine shoots-derived biochar with high CO2 uptake and CO2/N2 selectivity, Chemical Engineering Journal 345 (2018) 631–639. https://doi.org/10.1016/j.cej.2018.01.092

[282] J.A. Perez-Pimienta, et al., Characterization of agave bagasse as a function ofionic liquid pretreatment, Biomass Bioenergy 75 (2015) 180–188. https://doi.org/10.1016/j.biombioe.2015.02.026

[283] P. J. Vikesland, R. L. Rebodos, J. Y. Bottero, J. Rose and A. Masion, Aggregation and sedimentation of magnetite nanoparticle clusters, Environ. Sci.: Nano 3 (2016) 567. https://doi.org/10.1039/c5en00155b

[284] Roxana M. del Castillo, Alipio G. Calles, Raúl Espejel-Morales, Hector Hernandez-Coronado, Adsorption of CO_2 on graphene surface modified with defects, Computational Condensed Matter 16 (2018) e00315. https://doi.org/10.1016/j.cocom.2018.e00315

[285] Liu, X., Sun, C., Liu, H., Tan, W. H., Wang, W., & Snape, C. Developing hierarchically ultra-micro/mesoporous biocarbons for highly selective carbon dioxide adsorption. Chemical Engineering Journal, 361 (2019) 199–208. https://doi.org/10.1016/j.cej.2018.11.062

[286] C. Herrero-Latorre, J. Álvarez-Méndez, J. Barciela-García, S. García-Martín, R.M. Peña-Crecente, Characterization of carbon nanotubes and analytical methods for their determination in environmental and biological samples: A review, Analytica Chimica Acta 853 (2015) 77–94. https://doi.org/10.1016/j.aca.2014.10.008

[287] N. Larouche, B.L. Stansfield, Classifying nanostructured carbons using graphitic indices derived from Raman spectra, Carbon NY 48 (3) (2010) 620–629. https://doi.org/10.1016/j.carbon.2009.10.002

[288] Niels De Greef, Luman Zhang, Arnaud Magrez, László Forró, Jean-Pierre Locquet, Ignaas Verpoest, Jin Won Seo, Direct growth of carbon nanotubes on

carbon fibers: Effect of the CVD parameters on the degradation of mechanical properties of carbon fibers, Diamond & Related Materials 51 (2015) 39–48. http://dx.doi.org/10.1016/j.diamond.2014.11.002

[289] H.J. Seong, A.L. Boehman, Evaluation of Raman Parameters Using Visible Raman Microscopy for Soot Oxidative Reactivity, Energy Fuels 27 (2013) 1643–11624. https://doi.org/10.1021/ef301520y

[290] S.K. Pillai, S.S. Ray, M. Moodley, Purification of multi-walled carbon nanotubes, J. Nanosci. Nanotechnol. 8 (2008) 1–21. https://doi.org/10.1166/jnn.2008.345

[291] L. Escobar-Alarcon, et al., Two-dimensional carbon nanostructures obtained by laser ablation in liquid: effect of an ultrasonic field, Appl. Phys. A Mater. Sci. Process. 124 (2) (2018) 1–7. https://doi.org/10.1007/s00339-018-1559-8

[292] M. Thommes, K. Kaneko, A.V. Neimark, J.P. Olivier, F. Rodriguez-Reinoso, J. Rouquerol, K.S.W. Sing, Physisorption of gases, with special reference to the evaluation of surface area and pore size distribution (IUPAC Technical Report), Pure Appl. Chem. 87 (9–10) (2015) 1051–1069.

[293] Raymundo-Pinero E, Azais P, Cacciaguerra T, Cazorla-Amorós D, Linares-Solano A, Béguin F. KOH and NaOH activation mechanisms of multiwalled carbon nanotubes with different structural organisation. Carbon 43 (2005) 786–95. https://doi.org/10.1016/j.carbon.2004.11.005

[294] Maryam Irani, Andrew T. Jacobson, Khaled A.M. Gasem, Maohong Fan, Modified carbon nanotubes/tetraethylenepentamine for CO_2 capture, Fuel 206 (2017) 10–18. https://doi.org/10.1016/j.fuel.2017.05.087

[295] Hee Wook Yoon, Tae Hoon Lee, Cara M Doherty, Tae Hwan Choi, Ji Soo Roh, Hyo Won Kim, Young Hoon Cho, Si-Hyun Do, Benny D Freeman, Ho Bum Park, Origin of CO_2-philic Sorption by Graphene Oxide Layered Nanosheets and Their Derivatives. Journal of Physical Chemistry Letters, 11 (2020) 2356–2362. https://doi.org/10.1021/acs.jpclett.0c00204

[296] Boujibar O, Souikny A, Ghamouss F, Achak O, Dahbi M, Chafik T., CO_2 capture using N-containing nanoporous activated carbon obtained from argan fruit shells. J Envrion Chem Eng 6 (2018)1995–2002. https://doi.org/10.1016/j.jece.2018.03.005

[297] Y.S. Ho, G. McKay, A Comparison of Chemisorption Kinetic Models Applied to Pollutant Removal on Various Sorbents, Process Safety and Environmental Protection 76(4) (1998) 332-340. https://doi.org/10.1205/095758298529696

[298] Shi, W.W., Wang, R.Z., Liu, H.L., Chang, B.B., Yang, B.C., Zhang, Z.L. Biowaste derived 3D honeycomb-like N and S dual-doped hierarchically porous carbons for high-efficient CO2 capture. RSC Adv. 9 (2019) 23241–23253. https://doi.org/10.1039/C9RA03659H

[299] A. Boonpoke, S. Chiarakorn, N. Laosiripojana, S. Towprayoon, A. Chidthaisong, Investigation of CO_2 adsorption by bagasse-based activated carbon, Korean J. Chem. Eng. 29 (1) (2012) 89–94. https://doi.org/10.1007/s11814-011-0143-0

[300] Fengli Gan, Bangda Wang, Jundong Guo, Jinglin He, Shenggui Ma, Xia Jiang, Ziheng Jin, Green synthesis of porous biochar with interconnected pore architectures from typical silicon-rich rice husk for efficient CO2 capture, Separation and Purification Technology 302 (2022) 122089. https://doi.org/10.1016/j.seppur.2022.122089

[301] A. D. Igalavithana, S. W. Choi, J. Shang, A. Hanif, P. D. Dissanayake, Daniel C.W. Tsang, J. H. Kwon, K. B. Lee, Y. Sik Ok, Carbon dioxide capture in biochar produced from pine sawdust and paper mill sludge: Effect of porous structure and surface chemistry, Science of the Total Environment 739 (2020) 139845. https://doi.org/10.1016/j.scitotenv.2020.139845

[302] A.E. Creamer, B. Gao, M. Zhang, Carbon dioxide capture using biochar produced from sugarcane bagasse and hickory wood, Chem. Eng. J. 249 (2014) 174–179. https://doi.org/10.1016/j.cej.2014.03.105

[303] Q. Ma, W. Chen, Z. Jin, L. Chen, Q. Zhou, X. Jiang, One-step synthesis of microporous nitrogen-doped biochar for efficient removal of CO2 and H2S, Fuel (2021) 289. https://doi.org/10.1016/j.fuel.2020.11993

[304] Qiyun Yu, Jiali Bai, Jiamei Huang, Muslum Demir, Ahmed A. Farghaly, Parya Aghamohammadi, Xin Hu, Linlin Wang, One-Pot Synthesis of Melamine Formaldehyde Resin-Derived N-Doped Porous Carbon for CO2 Capture Application, Molecules 2023, 28(4), 1772. https://doi.org/10.3390/molecules28041772

[305] Changdan Ma, Jiali Bai, Muslum Demir, Xin Hu, Shenfang Liu, Linlin Wang, Water chestnut shell-derived N/S-doped porous carbons and their applications in CO2 adsorption and supercapacitor, Fuel 326 (2022) 125119. https://doi.org/10.1016/j.fuel.2022.125119

[306] Tingyan Lu, Jiali Bai, Muslum Demir, Xin Hu, Jiamei Huang, Linlin Wang, Synthesis of potassium Bitartrate-derived porous carbon via a facile and Self-Activating strategy for CO2 adsorption application, Separation and Purification Technology 296 (2022) 121368. https://doi.org/10.1016/j.seppur.2022.121368

[307] N.Y.M.Yusuf, M.S.Masdar, W.N.R.W.Isahak, D.Nordin, T.Husaini, E.H.Majlan, S.Y.Wu, S.A.M.Rejab, C.C.Lye, Impregnated carbon–ionic liquid as innovative adsorbent for H_2/CO_2 separation from biohydrogen. International Journal of Hydrogen Energy, 4 (2019) 3414–3424. https://doi.org/10.1016/j.ijhydene.2018.06.155

[308] S. Nanda, S.N. Reddy, S.K. Mitra, J.A. Kozinski, The progressive routes for carbon capture and sequestration, Energy Sci. Eng. 4 (2016) 232.

[309] Haszeldine RS. Carbon Capture and Storage: how green can black be? Science 325 (2009)1647–52.

[310] K.S. Lackner, S. Brennan, J.M. Matter, A.-H.A. Park, A. Wright, B.V.D. Zwaan, The urgency of the development of CO2 capture from ambient air, PNAS 109 (2012) 13156–13162.

[311] N. MacDowell, N. Florin, A. Buchard, J. Hallett, A. Galindo, G. Jackson, C. S. Adjiman, C.K. Williams, N. Shah, P. Fennell, An overview of CO2 capture technologies, Energ, Environ. Sci. 3 (2010) 1645–1669.

[312] G.T. Rochelle, Amine scrubbing for CO2 capture, Science 325 (2009) 1652–1654.

[313] Nguyen T, Hilliard M, Rochelle GT. Volatility of aqueous amines in CO2 capture. Int J Greenhouse Gas Control 4 (2011) 707–15.

[314] Wang M, Lawal A, Stephenson P, Sidders J, Ramshaw C. Post-combustion CO2 capture with chemical absorption: a state-of-the-art review. Chem Eng Res Des 89 (2011) 1609–24.

[315] Nugent P, Belmabkhout Y, Burd SD, Cairns AJ, Luebke R, Forrest K, Pham T, Ma S, Space B, Wojtas L, Eddaoudi M, Zaworotko MJ. Porous materials with optimal adsorption thermodynamics and kinetics for CO2 separation. Nature 495 (2013) 80–4.

[316] Wang Q, Luo JZ, Zhong ZY, Borgna A. CO2 capture by solid adsorbents and their applications: current status and new trends. Energy Environ Sci 4 (2011) 42–55.

[317] Xie Y, Wang TT, Liu XH, Zou K, Deng WQ. Capture and conversion of CO2 at ambient conditions by a conjugated microporous polymer. Nat Commun 4 (2013)1960–6.

[318] Y. Li, R. Xu, B.B. Wang, J.P. Wei, L.Y. Wang, M.Q. Shen, J. Yang, Enhanced N doped porous carbon derived from KOH-activated waste wool: a promising material for selective adsorption of CO2/CH4 and CH4/N2, Nanomaterials 9 (2019) 266.

[319] Y. Li, S.Y. Wang, B.B. Wang, Y. Wang, J.P. Wei, Sustainable biomass glucose derived porous carbon spheres with high nitrogen doping: as a promising adsorbent for CO2/CH4/N2 adsorptive separation, Nanomaterials 10 (2020) 174.

[320] E. Jang, S.W. Choi, K.B. Lee, Effect of carbonization temperature on the physical properties and CO2 adsorption behavior of petroleum coke-derived porous carbon, Fuel 248 (2019) 85–92.

[321] C. Ma, T. Lu, J. Shao, J. Huang, X. Hu, L. Wang, Biomass derived nitrogen and sulfur co-doped porous carbons for efficient CO2 adsorption, Sep. Purif. Technol. 281 (2022), 119899.

[322] N.P. Wickramaratne, M. Jaroniec, Activated carbon spheres for CO2 adsorption, ACS Appl. Mater. Interfaces 5 (2013) 1849–1855.

[323] Meng LY, Park SJ. Effect of heat treatment on CO2 adsorption of KOH-activated graphite nanofibers. J Colloid Interface Sci 352 (2010) 498–503.

[324] Daman Yadav, Fedi Aminib, Andrea Ehrmann, Recent advances in carbon nanofibers and their applications – A review, European Polymer Journal 138 (2020) 109963.

[325] Luis Sousa Lobo, Nucleation and growth of carbon nanotubes and nanofibers: Mechanism and catalytic geometry control. Carbon 114 (2017) 411-417.

[326] Yongzhen Yanga, Xuguang Liua, Husheng Jia, Bingshe Xua, How do vapor grown carbon nanofibers nucleate and grow from deoiled asphalt? Materials Chemistry and Physics 126 (2011) 424–431.

[327] Y.A. Zhu, Zh.J. Sui, T.J. Zhao, Y.Ch. Dai, Zh.M. Cheng, W.K. Yuan, Modeling of fishbone-type carbon nanofibers: A theoretical study. Carbon 43 (2005) 1694–1699.

[328] Soroush Soltani, Nasrin Khanian, Taha Roodbar Shojaei, Thomas Shean Yaw Choong, Nilofar Asim d, Yue Zhao, Recent trends in the design and engineering of incorporated carbon nanofiber nanocomposites and their advanced applications – A review. Materials Chemistry and Physics 286 (2022) 126111.

[329] Raissa Alvarenga Carvalho Gomide, Ana Carolina Salgado de Oliveira, Danielle Aparecida Caetano Rodrigues, Cassiano Rodrigues de Oliveira, Odílio Benedito Garrido de Assis, Marali Vilela Días, Soraia Vilela Borges, Development and Characterization of Lignin Microparticles for Physical and Antioxidant Enhancement of Biodegradable Polymers, Journal of Polymers and the Environment 28 (2020) 1326–1334.

[330] Azadeh Goudarzi, Li-Ting Lin, Frank K. Ko, X-Ray Diffraction Analysis of Kraft Lignins and Lignin-Derived Carbon Nanofibers, Journal of Nanotechnology in Engineering and Medicine 5 (2014) 021006-1. https://doi.org/10.1115/1.4028300

[331] Kubo, S., Yasumitsu, U., and Yoshihiro, S., Catalytic Graphitization of Hardwood Acetic Acid Lignin With Nickel Acetate, J. Wood Sci., 49(2) (2003) 188–192.

[332] Ansari, K. B., and Gaikar, V. G., Green Hydrotropic Extraction Technology for Delignification of Sugarcane Bagasse by Using Alkybenzen Sulfonates as Hydrotropes, Chem. Eng. Sci. (2013) 157–166.

[333] Maojiang Zhang, Minglei Wang, Mingxing Zhang, Aizezi Maimaitiming, Lijuan Pang, Yulin Liang, Jiangtao Hu, Guozhong Wu, Fe3O4 Nanowire Arrays on Flexible Polypropylene Substrates for UV and Magnetic Sensing, ACS Appl. Nano Mater. 2018, 1, 5742−5752.

[334] R. M. Cornell and U. Schwertmann, “No Title The iron oxides: structure, properties, reactions, occurrences and uses,” p. 664, 2003.
[335] Toru Yamashita, Peter Hayes, Analysis of XPS spectra of Fe2+ and Fe3+ ions in oxide materials, Applied Surface Science 254 (2008) 2441–2449.
[336] D.D. Hawn, B.M. DeKoven, Background subtraction from transition metal 2p XPS by deconvolution using ligand atom XPS: study on first transition metal cyanide complexes, Surf. Interface Anal. 10 (1987) 63.
[337] M. Muhler, R. Schlogl, The nature of the iron oxide-based catalyst for dehydrogenation of ethylbenzene to styrene 2. Surface chemistry of the active phase, G. Ertl, J. Catal. 138 (1992) 413.
[338] Yao Li, Yage Wang, Bingqing Chen, Lanyun Wang, Juan Yang a, Binbin Wang, Nitrogen-doped hierarchically constructed interconnected porous carbon nanofibers derived from polyaniline (PANI) for highly selective CO2 capture and effective methanol adsorption, Journal of Environmental Chemical Engineering 10 (2022) 108847.
[339] Ania CO, “Surface chemistry of green carbons”, in Green Carbon Materials: Advances and Applications” (T.E. Rufford, J. Zhu and Hulicova-Jurkahova D, Eds.), Chapter 1. Editorial: PAN Stanford Publishing, pp. 1-26, 2013.
[340] I. Hussain, A. Rehman, C. Isik, Using an asymmetrical technique to assess the impacts of CO_2 emissions on agricultural fruits in Pakistan, Environ. Sci. Pollut. Res. 29 (2022) 19378–19389.

[341] A. Baghban, A. Bahadori, A.H. Mohammadi, A. Behbahaninia, Prediction of CO_2 loading capacities of aqueous solutions of absorbents using different computational schemes, Int. J. Greenhouse Gas Control 57 (2017) 143–161.
[342] I.M. Saeed, P. Alaba, S.A. Mazari, W.J. Basirun, V.S. Lee, N. Sabzoi, Opportunities and challenges in the development of monoethanolamine and its blends for post-combustion CO2 capture, Int. J. Greenhouse Gas Control 79 (2018) 212–233.
[343] M. Javed, M. Zahoor, S.A. Mazari, S.S. Qureshi, N. Sabzoi, A.S. Jatoi, N.M. Mubarak, An overview of effect of process parameters for removal of CO2 using biomass-derived adsorbents, Biomass Convers. Biorefin. (2021).

[344] N.H. Solangi, A. Anjum, F.A. Tanjung, S.A. Mazari, N.M. Mubarak, A review of recent trends and emerging perspectives of ionic liquid membranes for CO2 separation, J. Environ. Chem. Eng. 9 (2021) 878–887.

[345] T.S. Marliza, M.A. Yarmo, A.H. Lahuri, Y.H. Taufiq-Yap, CO2 capture using ionic liquid hybrid sorbent: Physical and chemical adsorption-desorption study, Materials Today: Proceedings 64 (2022) 20–26. https://doi.org/10.1016/j.matpr.2022.03.471

[346] M. Usman, A. Helal, M.M. Abdelnaby, A.M. Alloush, M. Zeama, Z.H. Yamani, Trends and Prospects in UiO-66 Metal-Organic Framework for CO2 Capture, Separation, and Conversion, Chem. Rec. 21 (2021) 1771–1791.

[347] S.A. Mazari, N. Hossain, W.J. Basirun, N.M. Mubarak, R. Abro, N. Sabzoi, A. Shah, An overview of catalytic conversion of CO2 into fuels and chemicals using metal organic frameworks, Process Saf. Environ. Prot. 149 (2021) 67– 92.

[348] I. Sreedhar, T. Nahar, A. Venugopal, B. Srinivas, Carbon capture by absorption-Path covered and ahead, Renew. Sust. Energ. Rev. 76 (2017) 1080–1107. https://doi.org/10.1016/j.rser.2017.03.109

[349] K.Z. House, C.F. Harvey, M.J. Aziz, D.P. Schrag, The energy penalty of postcombustion CO2 capture & storage and its implications for retrofitting the U.S. installed base, Energy Environ. Sci. 2 (2) (2009) 193–205.

[350] J. Davis, G. Rochelle, Thermal degradation of monoethanolamine at stripper conditions, Energy Procedia 1 (2009) 327–333.

[351] N. Kladkaew, R. Idem, P. Tontiwachwuthikul, C. Saiwan, Corrosion behavior of carbon steel in the monoethanolamine-H2O-CO2-O2-SO2 system: Products, reaction pathways, and kinetics, Ind. Eng. Chem. Res. 48 (2009) 10169–10179.

[352] Nadeem Hussain Solangi, Farihahusnah Hussin, Amna Anjum, Nizamuddin Sabzoi, Shaukat Ali Mazari, Nabisab Mujawar Mubarak, Mohamed Kheireddine Aroua, M.T.H. Siddiqui, Sundus Saeed Qureshi, A review of encapsulated ionic

liquids for CO2 capture, Journal of Molecular Liquids 374 (2023) 121266. https://doi.org/10.1016/j.molliq.2023.121266

[353] N. Nasirpour, M. Mohammadpourfard, S. Zeinali Heris, Ionic liquids: Promising compounds for sustainable chemical processes and applications, Chem. Eng. Res. Des. 160 (2020) 264–300, https://doi.org/10.1016/j.cherd.2020.06.006 N

[354] M. Aryafard, B. Minofar, E. Cs´efalvay, L. Malinov´a, D. Reha, Novel room temperature ionic liquids and low melting mixtures based on imidazolium: Cheap ionic solvents for chemical and biological applications, J. Mol. Liq. 344 (2021), 117877, https://doi.org/10.1016/j.molliq.2021.117877

[355] X. Zhang, L. Bai, S. Zeng, H. Gao, S. Zhang, M. Fan, Ionic Liquids: Advanced Solvents for CO2 Capture, in: W.M. Budzianowski (Ed.), Energy Efficient Solvents for CO2 Capture by Gas-Liquid Absorption: Compounds, Blends and Advanced Solvent Systems, Springer International Publishing, Cham, 2017, pp. 153-76. https://doi.org/10.1007/978-3-319-47262-1_7

[356] W. Kunz, K. Häckl, The hype with ionic liquids as solvents, Chem. Phys. Lett. 661 (2016) 6–12.

[357] Wufeng Jiang, Xiaoshan Li, Ge Gao, Fan Wu, Cong Luo, Liqi Zhang, Advances in applications of ionic liquids for phase change CO2 capture, Chemical Engineering Journal 445 (2022) 136767. https://doi.org/10.1016/j.cej.2022.136767

[358] W.L. Xie, X.Y. Ji, X. Feng, X.H. Lu, Mass transfer rate enhancement for CO2 separation by ionic liquids: Effect of film thickness, Ind. Eng. Chem. Res. 55 (1) (2016) 366–372.

[359] K.N. Ruckart, R.A. O'Brien, S.M. Woodard, K.N. West, T.G. Glover, Porous Solids Impregnated with Task-Specific Ionic Liquids as Composite Sorbents, J. Phys. Chem. C 119 (35) (2015) 20681–20697, https://doi.org/10.1021/acs.jpcc.5b04646.

[360] Lei Huang, Yufen Jin, Li Sun, Feng Chen, Ping Fan, Mingqiang Zhong, Jintao Yang, Graphene Oxide Functionalized by Poly(Ionic Liquid)s for Carbon Dioxide Capture, Journal of Applied Polymer Science 134(11) (2017) 1–8.

[361] Sethupathi S, Zhang M, Rajapaksha AU, Lee SR, Mohamad Nor N, Mohamed AR, Al-Wabel M, Lee SS, Ok YS, Biochars as Potential Adsorbers of CH4, CO2 and H2S, Sustainability 9(1) (2017) 121.

[362] Liu, Shou-Heng, and Yi-Yang Huang, Valorization of Coffee Grounds to Biochar-Derived Adsorbents for CO2 Adsorption, Journal of Cleaner Production 175 (2018) 354–60.

[363] Arjona Jaime, A.P. (2020) Fibras de carbono como adsorbente y soporte de un líquido iónico para la captura de dióxido de carbono a alta presión (Master's Thesis) Instituto Potosino de Investigación Científica y Tecnológica, A.C., (IPICYT). San Luis Potosí, México.

[364] T. Selvam, A. Machoke, W. Schwieger, Supported ionic liquids on non-porous and porous inorganic materials-A topical review, Appl. Catal. A-Gen. 445–446 (2012) 92–101, https://doi.org/10.1016/j.apcata.2012.08.007

[365] L. Keller, B. Ohs, L. Abduly, M. Wessling, Carbon nanotube silica composite hollow fibers impregnated with polyethylenimine for CO2 capture, Chem. Eng. J. 359 (2019) 476–484, https://doi.org/10.1016/j.cej.2018.11.100

[366] Shiflett, M. B., Drew, D. W., Cantini, R. A., & Yokozeki, A., Carbon dioxide capture using ionic liquid 1-butyl-3-methylimidazolium acetate. Energy and Fuels, 24(10) (2010) 5781–5789. https://doi.org/10.1021/ef100868a

[367] Almeida, H. F., Passos, H., Lopes-Da-Silva, J. A., Fernandes, A. M., Freire, M. G., & Coutinho, J. A., Thermophysical properties of five acetate-based ionic liquids. Journal of Chemical and Engineering Data, 57(11) (2012) 3005–3013. https://doi.org/10.1021/je300487n

[368] J. Palomar, J. Lemus, M.A. Gilarranz, J.J. Rodriguez, Adsorption of ionic liquids from aqueous effluents by activated carbon, Carbon 47 (7) (2009) 1846–1856, https://doi.org/10.1016/j.carbon.2009.03.028

[369] H.-L. Peng, J.-B. Zhang, J.-Y. Zhang, F.-Y. Zhong, P.-K. Wu, K. Huang, J.-P. Fan, F. Liu, Chitosan-derived mesoporous carbon with ultrahigh pore volume for amine impregnation and highly efficient CO2 capture, Chem. Eng. J. 359 (2019) 1159–1165, https://doi.org/10.1016/j.cej.2018.11.064

[370] M. Fernández, L.A. Carreño, F. Bernard, R. Ligabue, S. Einloft, Poly(ionic liquid)s nanoparticles applied in CO2 capture, Macromol. Sy. 368 (1) (2016) 98–106, https://doi.org/10.1002/masy.201500148

[371] G. Gurau, H. Rodriguez, S. P. Kelley, P. Janiczek, R. S. Kalb, R. D. Rogers, Angew, Significant Cation Effects in Carbon Dioxide–Ionic Liquid Systems, Chem Phys Chem 14 (2013) 315 -320. https://doi.org/10.1002/cphc.201200970

[372] M. Besnard, M. I. Cabaco, F. V. Chavez, N. Pinaud, P. J. Sebastiao, J. A. P. Coutinho, Y. Danten, Chem, On the chemical reactions of carbon dioxide isoelectronic molecules CS2 and OCS with 1-butyl-3-methylimidazolium acetate, Chem. Commun 49 (2013) 11083-11085. https://doi.org/10.1039/C3CC46038J

[373] O.Y. Orhan, C.S. Ume, E. Alper, The absorption kinetics of CO2 into ionic liquid- CO2 binding organic liquid and hybrid solvents, in: W. Budzianowski (Ed.), Energy efficient solvents for CO2 capture by gas-liquid absorption, Green Energy and Technology, Springer, Cham (2017) 241–261, https://doi.org/10.1007/978-3-319-47262-1_11

[374] N. Yang, R. Wang, Sustainable technologies for the reclamation of greenhouse gas CO2, J. Clean. Prod. 103 (2015) 784-792, https://doi.org/10.1016/j.jclepro.2014.10.025

[375] E.S. Shuba, D. Kifle, Microalgae to biofuels: ‘Promising’ alternative and renewable energy, review, Renew. Sustain. Energy Rev. 81 (2018) 743-755, https://doi.org/10.1016/j.rser.2017.08.042

[376] X.F. Hao, Z. Li, H.J. Hu, X.Q. Liu, Y.Q. Huang, Separation of CH4/N2 of Low Concentrations From Coal Bed Gas by Sodium-Modified Clinoptilolite, Front. Chem. 6 (2018) 9.

[377] Y. Liu, G.P. Liu, C. Zhang, W.L. Qiu, S.L. Yi, V. Chernikova, Z.J. Chen, Y. Belmabkhout, O. Shekhah, M. Eddaoudi, W. Koros, Enhanced CO2/CH4 Separation

Performance of a Mixed Matrix Membrane Based on Tailored MOFPolymer Formulations, Adv. Sci. 5 (2018) 5.

[378] G. Goula, V. Kiousis, L. Nalbandian, I. V Yentekakis, Catalytic and electrocatalytic behavior of Ni-based cermet anodes under internal dry reforming of CH4/CO2 mixtures in SOFCs, Solid State Ionics 177 (2006) 2119-2123, https://doi.org/10.1016/j.ssi.2006.03.040

[379] A.A. Pavlov, J.F. Kasting, L.L. Brown, K.A. Rages, R. Freedman, Greenhouse, warming by CH4 in the atmosphere of early Earth, J. Geophys. Res. Planets 105 (2000) 11981–11990.

[380] Y.F. Makogon, S.A. Holditch, T.Y. Makogon, Natural gas-hydrates - a potential energy source for the 21st century, J. Pet. Sci. Eng. 56 (2007) 14–31.

[381] J. Wang, R. Krishna, X. Wu, Y. Sun, S. Deng, Polyfuran-derived microporous carbons for enhanced adsorption of CO2 and CH4, Langmuir 31 (2015) 9845–9852.

[382] I. Duran, N. Alvarez-Gutierrez, F. Rubiera, C. Pevida, Biogas purification by means of adsorption on pine sawdust-based activated carbon: impact of water vapor, Chem. Eng. J. 353 (2018) 197-207, https://doi.org/10.1016/j.cej.2018.07.100

[383] K. Morishige, Adsorption and separation of CO2/CH4 on amorphous silica molecular sieve, J. Phys. Chem. C 115 (2011) 9713–9718.

[384] S. Cavenati, C.A. Grande, A.E. Rodrigues, Separation of mixtures by layered pressure swing adsorption for upgrade of natural gas, Chem. Eng. Sci. 61 (2006) 3893–3906.

[385] B.P. Spigarelli, S.K. Kawatra, Opportunities and challenges in carbon dioxide capture, J. CO2 Util. 1 (2013) 69-87, https://doi.org/10.1016/j.jcou.2013.03.002

[386] S. Rasi, J. Läntelä, A. Veijanen, J. Rintala, Landfill gas upgrading with countercurrent water wash, Waste Manag. 28 (2008) 1528–1534.

[387] A.G. Chmielewski, A. Urbaniak, K. Wawryniuk, Membrane enrichment of biogas from two-stage pilot plant using agricultural waste as a substrate, Biomass Bioenergy 58 (2013) 219–228.

[388] L. Deng, M.-B. Hägg, Techno-economic evaluation of biogas upgrading process using CO2 facilitated transport membrane, Int. J. Greenhouse Gas Control 4 (2010) 638–646.

[389] P. Shao, M. Dal-Cin, A. Kumar, H. Li, D.P. Singh, Design and economics of a hybrid membrane–temperature swing adsorption process for upgrading biogas, J. Membr. Sci. 413–414 (2012) 17–28.

[390] K. Maqsood, A.H. Ali, A.B.M. Shariff, S. Ganguly, Techno-economic evaluation of cryogenic networks for separation of CO2 from natural gas, Applied Mechanics and Materials (2014) 635–638.

[391] K. Maqsood, J. Pal, D. Turunawarasu, A.J. Pal, S. Ganguly, Performance enhancement and energy reduction using hybrid cryogenic distillation networks for purification of natural gas with high CO2 content, Korean J. Chem. Eng. 31 (2014) 1120–1135.

[392] X. Li, J. Li, B. Yang, Design and control of the cryogenic distillation process for purification of synthetic natural gas from methanation of coke oven gas, Ind. Eng. Chem. Res. 53 (2014) 19583–19593.

[393] Y.-S. Bae, K.L.Mulfort, H. Frost, P. Ryan, S. Punnathanam, L.J. Broadbelt, J.T. Hupp, R.Q. Snurr, Separation of CO2 from CH4 using mixed-ligand metal–organic frameworks, Langmuir 24 (2008) 8592–8598.

[394] G.D. Pirngruber, L. Hamon, S. Bourrelly, P.L. Llewellyn, E. Lenoir, V. Guillerm, C. Serre, T. Devic, A method for screening the potential of MOFs as CO2 adsorbents in pressure swing adsorption processes, ChemSusChem 5 (2012) 762–776.

[395] A. Alonso-Vicario, J.R. Ochoa-Gómez, S. Gil-Río, O. Gómez-Jiménez Aberasturi, C.A. Ramírez-López, J. Torrecilla-Soria, A. Domínguez, Purification and upgrading of biogas by pressure swing adsorption on synthetic and natural zeolites, Microporous Mesoporous Mater. 134 (2010) 100–107.

[396] R. Ben-Mansour, M.A. Habib, O.E. Bamidele, M. Basha, N.A.A. Qasem, A. Peedikakkal, T. Laoui, M. Ali, Carbon capture by physical adsorption: materials, experimental investigations and numerical modeling and simulations- a review, Appl. Energy 161 (2016) 225-255, https://doi.org/10.1016/j.apenergy.2015.10.011

[397] S. Cavenati, C.A. Grande, A.E. Rodrigues, C. Kiener, U. Müller, Metal organic framework adsorbent for biogas upgrading, Ind. Eng. Chem. Res. 47 (2008) 6333-6335.

[398] M.W. Ackley, S.U. Rege, H. Saxena, Application of natural zeolites in the purification and separation of gases, Microporous Mesoporous Mater. 61 (2003) 25–42.

[399] Y. Li, H. Yi, X. Tang, F. Li, Q. Yuan, Adsorption separation of CO2/CH4 gas mixture on the commercial zeolites at atmospheric pressure, Chem. Eng. J. 229 (2013) 50–56.

[400] J.A.C. Silva, A.F. Cunha, K. Schumann, A.E. Rodrigues, Binary adsorption of CO2/CH4 in binderless beads of 13X zeolite, Microporous Mesoporous Mater. 187 (2014) 100–107.

[401] J. Yang, R. Krishna, J. Li, J. Li, Experiments and simulations on separating a CO2/CH4 mixture using K-KFI at low and high pressures, Microporous Mesoporous Mater. 184 (2014) 21–27.

[402] F. Dreisbach, R. Staudt, J.U. Keller, High pressure adsorption data of methane, nitrogen, carbon dioxide and their binary and ternary mixtures on activated carbon, Adsorption 5 (1999) 215-227, https://doi.org/10.1023/A:1008914703884

[403] J. McEwen, J.-D. Hayman, A. Ozgur Yazaydin, A comparative study of CO2, CH4 and N2 adsorption in ZIF-8, Zeolite-13X and BPL activated carbon, Chem. Phys. 412 (2013) 72-76, https://doi.org/10.1016/j.chemphys.2012.12.012

[404] M. Alvarez-Gutierrez, N. Victoria Gil, F. Rubiera, C. Pevida, Cherry-stonesbased activated carbons as potential adsorbents for CO2/CH4 separation: effect of the activation parameters, Greenh. Gases Sci. Technol. 5 (2015) 812-825, https://doi.org/10.1002/ghg.1534

[405] N. Álvarez-Gutiérrez, M.V. Gil, F. Rubiera, C. Pevida, Adsorption performance indicators for the CO2/CH4 separation: Application to biomass-based activated carbons, Fuel Processing Technology 142 (2016) 361–369. http://dx.doi.org/10.1016/j.fuproc.2015.10.038

[406] Y. Zhao, X. Liu, Y. Han, Microporous carbonaceous adsorbents for CO2 separation via selective adsorption, RSC Adv. 5 (2015) 30310-30330, https://doi.org/10.1039/C5RA00569H

[407] J. Park, N.F. Attia, M. Jung, M.E. Lee, K. Lee, J. Chung, H. Oh, Sustainable nanoporous carbon for CO2, CH4, N2, H2 adsorption and CO2/CH4 and CO2/ N2 separation, Energy 158 (2018) 9-16, https://doi.org/10.1016/j.energy.2018.06.010

[408] Y. Li, N. Liu, T. Zhang, B. Wang, Y. Wang, L. Wang, J. Wei, Highly microporous nitrogen-doped carbons from anthracite for effective CO2 capture and CO2/CH4 separation, Energy 211 (2020), 118561.

[409] F. Yang, J. Wang, L. Liu, P. Zhang, W. Yu, Q. Deng, Z. Zeng, S. Deng, Synthesis of porous carbons with high N-content from shrimp shells for efficient CO2-capture and gas separation, ACS Sustain. Chem. Eng. 6 (2018) 15550–15559.

[410] P. Zhang, J. Wang, W. Fan, Y. Zhong, Y. Zhang, Q. Deng, Z. Zeng, S. Deng, Ultramicroporous carbons with extremely narrow pore size distribution via in-situ ionic activation for efficient gas-mixture separation, Chem. Eng. J. 375 (2019), 121931.

[411] V. Cornette, J. Villarroel-Rocha, K. Sapag, R. Delgado Mons J.P. Toso, R.H. Lopez, Insensitivity in the pore size distribution of ultramicroporous carbon materials by CO2 adsorption, Carbon 168 (2020) 508-514. https://doi.org/10.1016/j.carbon.2020.07.011

[412] E. Buss, Gravimetric measurement of binary gas adsorption equilibria of methane carbon dioxide mixtures on activated carbon, Gas Separ. Purif. 9 (1995) 189-197, https://doi.org/10.1016/0950-4214(95)98226-B

[413] A. Torrisi, R.G. Bell, C. Mellot-Draznieks, Functionalized MOFs for enhanced CO2 capture, Cryst. Growth Des. 10 (2010) 2839–2841

[414] X. Suo, L. Xia, Q. Yang, Z. Zhang, Z. Bao, Q. Ren, Y. Yang, H. Xin, Synthesis of anion-functionalized mesoporous poly(ionic liquid)s: via a microphase separation hypercrosslinking strategy: highly efficient adsorbents for bioactive molecules, J. Mater. Chem. A 5 (2017) 14114–14123.

[415] Hongguang Sui, Fengyun Zhang, Lei Zhang, Diansheng Wang, Yudou Wang, Yongfei Yang, Jun Yao, Competitive sorption of CO2/CH4 and CO2 capture on modified silica surfaces: A molecular simulation, Science of the Total Environment 908 (2024) 168356. https://doi.org/10.1016/j.scitotenv.2023.168356

[416] Kui Dong, Zhiwei Zhai, and Aijun Guo, Effects of Pore Parameters and Functional Groups in Coal on CO2/CH4 Adsorption, ACS Omega 6 (48) (2021) 32395-32407.

[417] Rongrong Qi, Zhengfu Ning, Qing Wang, Liang Huang, Xiaojun Wu, Zhilin Cheng, Wentong Zhang, Measurements and modeling of high-pressure adsorption of CH4 and CO2 on shales, Fuel 242 (2019) 728–743.

[418] Ljubisa R. Radovic, Alvaro F. Silva-Villalobos, Alejandro B. Silva-Tapia, Fernando Vallejos-Burgos, On the mechanism of nascent site deactivation in graphene, Carbon 49 (2011) 3471–348.

[419] Kim HS, Kang MS, Lee S, Lee Y-W, Yoo WC. N-doping and ultramicroporosity controlled crab shell derived carbons for enhanced CO2 and CH4 sorption, Microporous Mesoporous Mater 272 (2018) 92-100.

[420] Y. Li, T. Zhang, Y.G. Wang, B.B. Wang, Transformation of waste cornstalk into versatile porous carbon adsorbent for selective CO2 capture and efficient methanol adsorption, J. Environ. Chem. Eng. 9 (2021), 106149.

[421] Anna Malaika, Aleksandra Możdżyńska, Damian Piwecki, Mieczysław Kozłowski, Comparative studies of the CCVD-based synthesis of carbon nanofibers – the quantitative aspect, Diamond & Related Materials 80 (2017) 125–132. http://dx.doi.org/10.1016/j.diamond.2017.10.012

[422] Ismagilov Zinfer R., Shikina Nadezhda V., Kruchinin Vladimir N., Rudina Nina A., Ushakov Vladimir A., Vasenin Nikolai T., Veringa Hubert, Development of methods of growing carbon nanofibers on silica glass fiber supports, Catalysis Today 102–103 (2005) 85–93.

[423] Takenaka, H. Ogihara, I. Yamanaka, K. Otsuka, Decomposition of methane over supported-Ni catalysts: effects of the supports on the catalytic lifetime, Appl. Catal. A Gen. 217 (2001) 101–110.

[424] R.L. Vander Wal, T.M. Ticich, V.E. Curtis, Substrate–support interactions in metalcatalyzed carbon nanofiber growth, Carbon 39 (2001) 2277–2289.

Appendix A

Supporting information

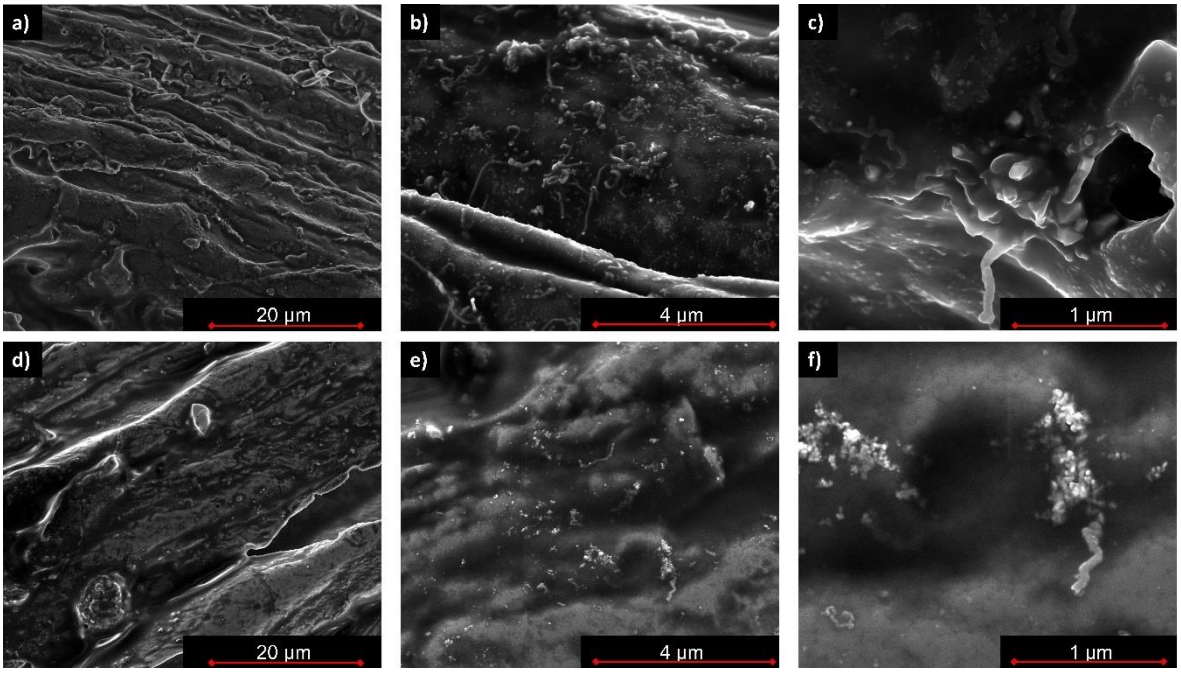

Figure A1. *SEM secondary electrons images of a)-c) MB-CNF-TEPA10% and d)-f) MB-CNF-TEPA25%.*

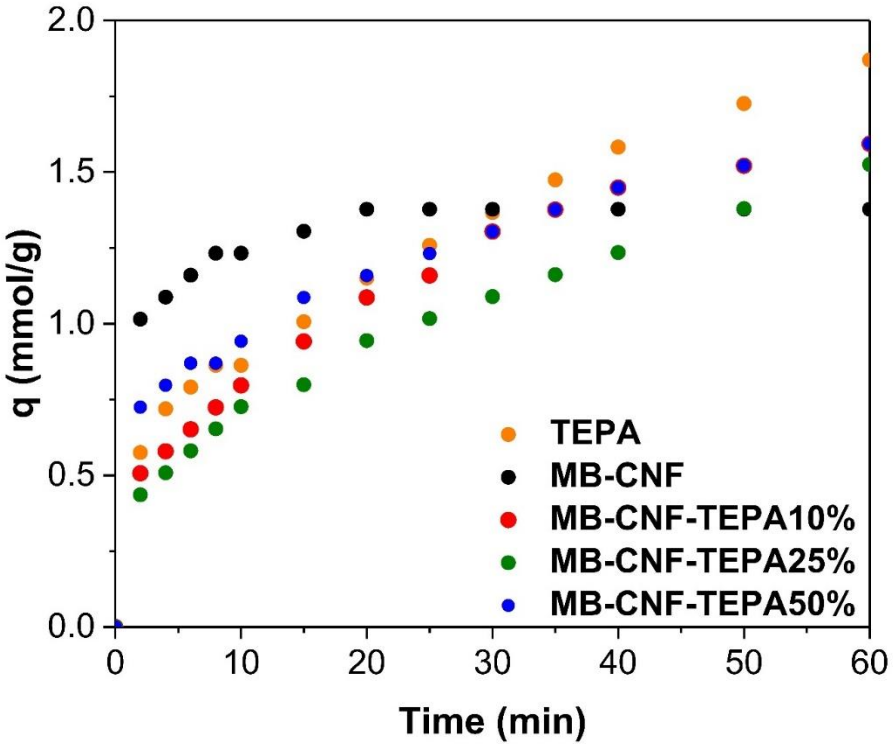

Figure A2. *CO_2 capture kinetics of TEPA, MB-CNF, and TEPA-impregnated MB-CNF at 25 °C and 8 bar.*

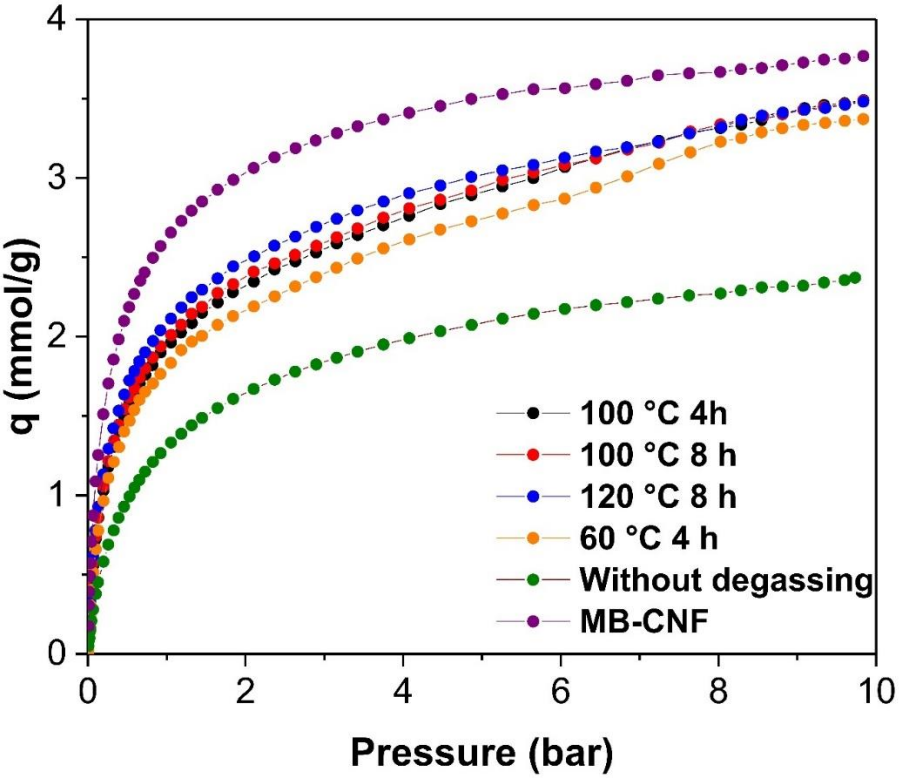

Figure A3. *CO_2 capture isotherm at 25°C and 1-10 bar of MB-CNF and MB-CNF-LI1:0.05 with different degassing times and temperatures.*

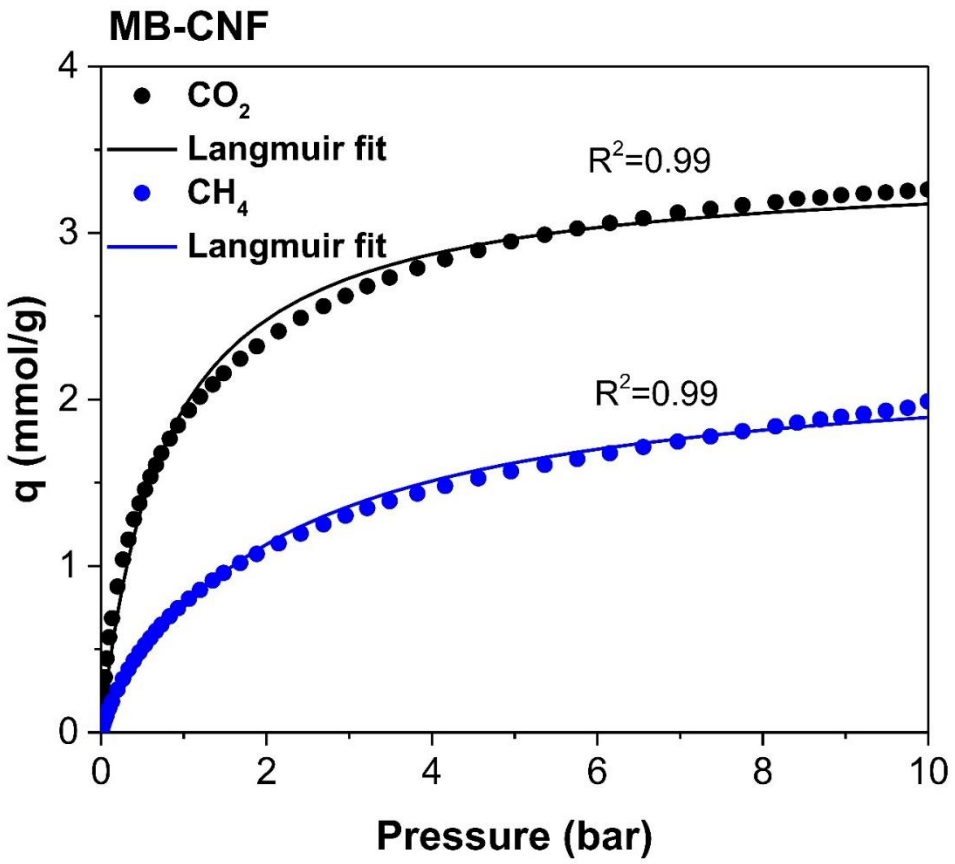

Figure A4. *CO_2 and CH_4 adsorption isotherms of MB-CNF, curves were fit to the Langmuir model (solid line).*

Table A1. *Parameters of the Langmuir isotherms model for CO_2 and CH_4 adsorption of ACF and MB-CNF at 25 °C and pressure up to 10 bar.*

Sample	CO_2			CH_4		
	q_{max} (mmol/g)	b	R^2	q_{max} (mmol/g)	b	R^2
ACF	2.38	1.35	0.982	1.83	0.41	0.995
MB-CNF	3.41	1.32	0.992	2.27	0.49	0.996

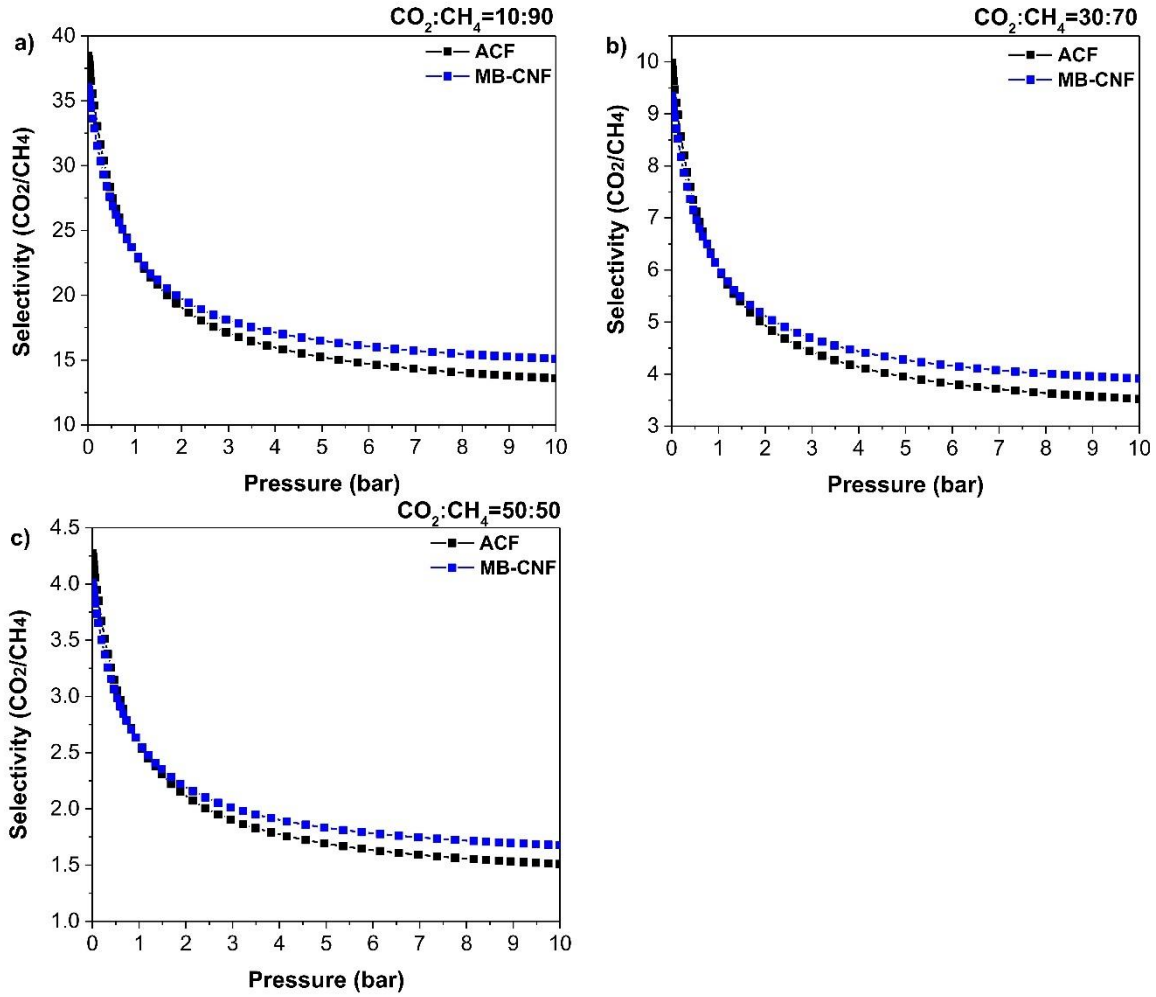

Figure A5. *IAST selectivity values of ACF and MB-CNF for a CO_2/CH_4 binary mixture of a) 10:90, b) 30:70 and c) 50:50 at 25 °C and pressure up to 10 bar.*

Table A2. *IAST selectivity values at different CO_2/CH_4 ratios of ACF and MB-CNF at 25 °C and pressure 1-10 bar.*

	IAST Selectivity CO_2/CH_4					
	(10:90)		**(30:70)**		**(50:50)**	
Sample	**1 bar**	**10 bar**	**1 bar**	**10 bar**	**1 bar**	**10 bar**
ACF	22.8	13.5	5.9	3.5	2.5	1.5
MB-CNF	22.9	15.1	5.9	3.9	2.5	1.6